TECHNISCHE UNIVERSITÄT WIEN
Vienna | Austria

AUTOMATION & CONTROL INSTITUTE
INSTITUT FÜR AUTOMATISIERUNGS- & REGELUNGSTECHNIK

Design and Evaluation of Resonant MEMS Scanning Systems for High Performance Automotive Applications

DISSERTATION

Ausgeführt zum Zwecke der Erlangung des akademischen Grades eines
Doktors der technischen Wissenschaften (Dr.techn.)

unter der Leitung von
Univ.-Prof. Dr.sc.techn. Georg Schitter

eingereicht an der
Technischen Universität Wien
Fakultät für Elektrotechnik und Informationstechnik
Institut für Automatisierungs- und Regelungstechnik

von
Dipl.-Ing. David Brunner
Matrikelnummer: 1027071

Wien, im September 2022

Technische Universität Wien
Karlsplatz 13, 1040 Wien, Österreich

Acknowledgement

This thesis summarizes the results of the research work I have conducted over the last four years at the Automation and Control Institute (ACIN) at Vienna University of Technology. Since great research is not done by individuals but in a cooperative group of researchers and supporters, I cannot claim the success of this work solely by myself. For this reason, I would like to take this opportunity to thank all the people who supported me during my studies and who played a major role in the successful completion of my doctoral thesis.
First of all, I would like to thank my supervisor Univ.-Prof. Dipl.-Ing. Dr.sc.techn. Georg Schitter for giving me the opportunity to pursue a PhD in his group and work on cutting-edge technologies, which brought interesting challenges and led to my research work, as well as for his help and support. In particular, his experience in conducting and presenting research will be of great benefit to my future career. My special thanks also go to Han Woong Yoo and Richard Schroedter, who supported me with their experience and knowledge through detailed discussions, challenging questions and a mutual friendship. Special thanks also goes to the colleagues at Infineon Thomas Thurner, Marcus Hennecke, Stephan Albert, Norbert Druml, Leonhard Niedermüller, Franz Darrer, Leonhard Kormann, Stefan Mendel and Boris Kirillov for their collaboration, fruitful discussions and support during the research projects. Furthermore, I am very grateful to my students Rene, Tobias, Severin, David and Florian for their good work, help and interest in writing their thesis on this challenging topic. I would also like to thank my colleagues at ACIN for their support and the exchange of interesting research results, as well as for the pleasant working atmosphere in the group. My very special thanks go to my parents, sister and brother, who laid the foundation for all my achievements and who have placed their trust in me ever since. Finally, my thanks go to my love Kathrin, who has always shown a lot of patience with me and has played a big part in the success of my work through her constant support and motivation.

Abstract

The potential of driver assistance systems or automated driving to avoid accidents and saving lives led to an increased demand on miniaturized low-cost optical scanning systems for applications such as light detection and ranging (lidar) sensors, augmented reality head-up displays and adaptive headlights, enabling key safety features. Micro-electro-mechanical system (MEMS) mirrors are one of the most promising scanning techniques due to their high performance and cost efficient manufacturing based on silicon technology. As the MEMS scanning system has to operate accurately even in harsh automotive environments, their influence should be analyzed and suppressed to ensure consistent safety.

In this thesis 1D resonant electrostatic MEMS mirrors are investigated, starting from the accurate modeling and parameter identification including several high order nonlinearities as well as the vibration and mode coupling mechanism implied by the lightweight mirror design using reinforcement structures. A self-sensing concept based on the displacement current caused by the mirror movement is proposed, providing precise and robust feedback signals with a simple implementation. Utilizing the full potential of the phase detection, the digital-asynchronous phase locked loop (DAsPLL) is developed, allowing fast tracking of the MEMS mirror oscillation and stabilization of open loop unstable operation points by an immediate phase compensation. For improved robustness a time-normalized PLL is proposed and designed based on a linearized MEMS mirror model, derived by a period-to-period energy conservation. A dedicated synchronization concept allows a fixed frequency ratio between two MEMS mirrors, enabling stable Lissajous scanning. Considering harsh environments, the use of linear-quadratic-gaussian (LQG) servo controllers provides superior performance compared to proportional-integral (PI) controllers achieving the targeted resolution of 0.1° even in a worst case vibration scenario by extending the automotive standard LV124. Two advanced scanning concepts are further proposed, i.e. the laser shot correction (LSC) concept reducing dynamic pixel errors by an

adaptive laser scheduling for 1D or raster scanning systems, and the adaptive Lissajous scanning to allow flexible scan pattern design, e.g. region of interest scans. The proposed advanced control and scanning concepts demonstrate superior performance even under harsh vibrations, enabling robust MEMS mirror based scanning systems for automotive applications.

Kurzfassung

Das Potenzial von Fahrerassistenzsystemen oder automatisiertem Fahren zur Vermeidung von Unfällen und zur Rettung von Menschenleben hat zu einer steigenden Nachfrage nach miniaturisierten, kostengünstigen optischen Abtastsystemen für Anwendungen wie Lidar-Sensoren (Light Detection and Ranging), Augmented-Reality-Head-up-Displays und adaptiven Scheinwerfern geführt, die wichtige Sicherheitsfunktionen ermöglichen. MEMS-Spiegel (Micro-Electro- Mechanical System) sind eine der vielversprechendsten Scantechnolgien aufgrund ihrer hohen Leistung und kosteneffizienten Herstellung auf Basis der Siliziumtechnologie. Da das MEMS-Scansystem auch in rauen Automobilumgebungen genau funktionieren muss, sollten deren Einflüsse analysiert und unterdrückt werden, um eine durchgängige Sicherheit zu gewährleisten.
In dieser Arbeit werden 1D-resonante elektrostatische MEMS-Spiegel untersucht, beginnend mit der genauen Modellierung und Parameteridentifikation einschließlich mehrerer Nichtlinearitäten höherer Ordnung sowie dem Vibrations- und Modenkopplungsmechanismus, der durch das leichte Spiegeldesign mit Verstärkungsstrukturen impliziert wird. Es wird ein Selbsterkennungskonzept vorgeschlagen, das auf dem durch die Spiegelbewegung verursachten Verschiebungsstrom basiert und präzise und robuste Rückkopplungssignale mit einer einfachen Implementierung liefert. Unter Ausnutzung des vollen Potenzials der Phasendetektion wird die digital-asynchrone Phasenregelschleife (DAsPLL) entwickelt, die eine schnelle Verfolgung der MEMS-Spiegelschwingung und die Stabilisierung instabiler Betriebspunkte durch eine sofortige Phasenkompensation ermöglicht. Zur Verbesserung der Robustheit wird eine zeitnormierte PLL vorgeschlagen und entworfen, die auf einem linearisierten MEMS-Spiegelmodell basiert, das durch eine Periode-zu-Periode-Energieerhaltung abgeleitet wird. Ein spezielles Synchronisationskonzept ermöglicht ein festes Frequenzverhältnis zwischen zwei MEMS-Spiegeln und damit einen stabilen Lissajous-Scan. Unter Berücksichtigung rauer Umgebungsbedingungen bietet der Einsatz von linear-quadratisch-gaußschen (LQG) Servor-

eglern im Vergleich zu proportional-integralen (PI) Reglern eine überlegene Performanz und erreicht die angestrebte Auflösung von 0.1° sogar in einem Worst-Case-Vibrationsszenario durch Erweiterung des Automobilstandards LV124. Darüber hinaus werden zwei fortschrittliche Scan-Konzepte vorgeschlagen, d.h. das Konzept der Laserschusskorrektur (LSC), das dynamische Pixelfehler durch eine adaptive Laserplanung für 1D- oder Rasterscansysteme reduziert, und das adaptive Lissajous-Scanning, das eine flexible Gestaltung von Scanmustern ermöglicht, z.B. für hochauflösende Scans nur von bestimmten Bereichen. Die vorgeschlagenen fortschrittlichen Regelungs- und Scankonzepte zeigen selbst bei starken Vibrationen eine überragende Performanz und ermöglichen robuste MEMS-Spiegelbasierte Scan-Systeme für Automobilanwendungen.

Contents

List of Figures

CHAPTER 1

Introduction

"*Self-driving cars are the natural extension of active safety and obviously something we should do.*" — Elon Musk, CEO of Tesla

Elon Musk's quote from 2013 addresses the potential of driver assistance or autonomous transportation to secure human lives by less accidents and to increase economic effectiveness [1, 2]. The permanent observation of the vehicle surroundings and a reliable interpretation of the scene can allow to avoid potential hazardous situations. On a higher level this information can be merged from several vehicles to build precise maps and to make traffic flow more efficient. Hence, the sensors data have to be reliable and of high definition, while the relevant information has to be properly and concisely delivered to the driver as well as to other traffic participants. This led to increasing interest of optical components in automobiles, such as lidar sensors, augmented reality head-up displays (AR HUD) and adaptive headlights to improve safety and driver assistance [3, 4]. The AR HUD as shown in Fig. 1.1a is a safety-enhancing technology that efficiently alerts the driver of potential risks without distracting the driver's vision or causing eye fatigue [5, 6]. The picture generation unit is the key element of AR HUDs and requires high illumination >10000 nit for daylight scenes and high contrast, i.e. true black, for night driving [7]. High-resolution adaptive headlights are being developed for glare protection from high beams and to project AR information on the road for pedestrians as shown in Fig. 1.1b [8, 9].
Established senors such as cameras, radar and ultrasonic are insufficient especially in providing high resolution long range data as necessary on highways as well as in environments with low lighting. Lidar is the acronym of light detection and ranging, which is an analogy of radar and is based on measuring the round trip time of light traveling from the transmitter to the object and back to the

(a) Augmented reality head-up display

(b) High-resolution adaptive headlights

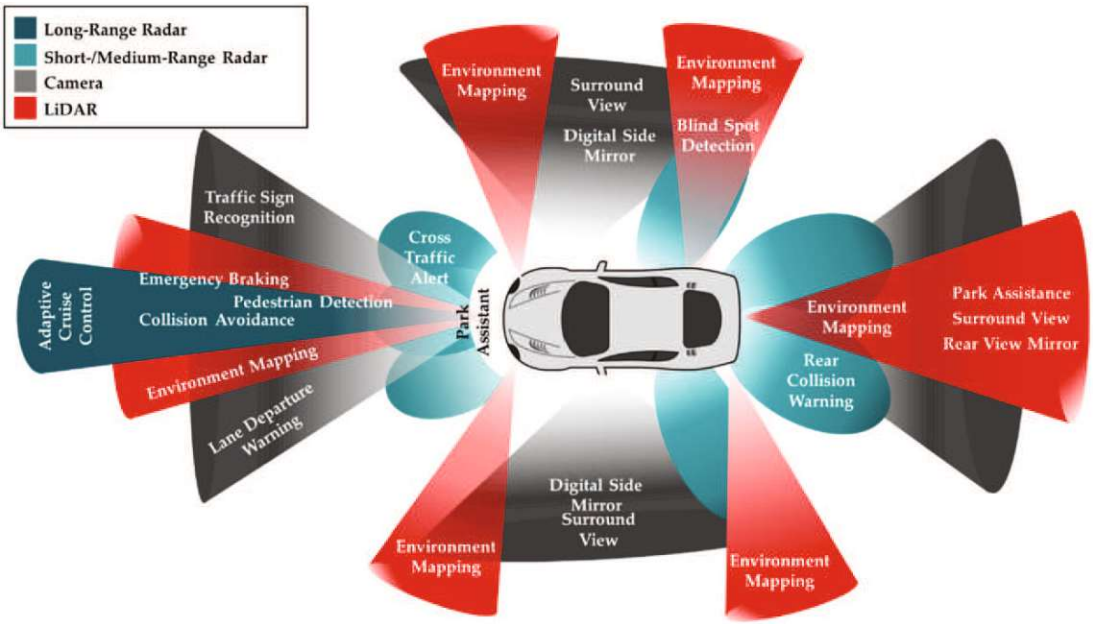

(c) Autonomous car sensor fusion and features

Figure 1.1.: (a) Use case of augmented reality, where content is projected directly into the driver's eye via the windscreen [10]. (b) Use case of high-resolution headlights for pedestrian warning [8]. (c) Sensor fusion for autonomous cars with lidar enabling safety enhancing features [11].

receiver. Lidar sensors are considered to pave the way for autonomous driving because, unlike cameras, they provide a very reliable 3D measurement of even weakly reflective objects in the most diverse environmental conditions, such as fog or rainy night, and a significantly higher resolution compared to radar [12–16]. Since the success in the DARPA robotic car races [17], various lidar sensors are developed by many vendors and commercially available in the automotive market. High level autonomous cars will be equipped with numerous sensors as shown in Fig. 1.1c, where lidar enables additional safety features such as collision detection, blind spot monitoring, object and pedestrian recognition [16,18–20] as well as environment mapping [21]. This makes automotive lidar one of the most demanding applications in terms of functional safety and robustness. Currently Google [22], BMW, Ford [23], Volvo [24] and other autonomous car developers [25] include lidar sensors in their development. Despite these attention in the automotive market last decade, the bottleneck is the unit cost. The first lidar for automotive, Velodyne HDL-64E, costs 75,000 USD, and a cheaper version, a puck lidar, still costs 8,000 USD and are both spinning scanners, i.e. the whole system including transmitter and receiver rotates which hinders the miniaturization due to bulky optical components. Many lidar manufacturers promise under 250 USD and 100 USD as a volume price, while the key lidar structure and technology for achieving such an affordable price is still unclear [13]. High angular resolution of the lidar sensors are necessary for reliable identification of potentially hazardous objects in far distance considering highway speeds. Hence, most automotive lidar manufacturers target an optical resolution of 0.1° for long range detection [26, 27]. However, lidar developers have to tackle several challenges besides cost and resolution such as size, field of view (FoV), frame rate, eye-safety and robustness, which are typically somehow contradicting.

The digital micromirror device (DMD) is currently the leading but cost-intensive technology for AR HUDs and headlights with high resolution, medium contrast ($<$ 5000:1), a fill factor $<$ 0.94 and high market prices ($\sim$120 USD for HD) [28,29]. The most commonly used for lidar are spinning scanners [27] or polygon mirrors [30], but new designs consider optical phase arrays (OPA) [31,32] and micro-electro-mechanical system (MEMS) mirrors [33–35]. MEMS mirrors show great potential thanks to their higher contrast ($>$ 80000:1 [36]), perfect fill factor, low cost and simple projection optics [37, 38]. A MEMS scanning system can use MEMS mirrors with a single axis to perform 1D line scanning [34] or two axes to allow 2D scanning, e.g. raster [39] or Lissajous [40]. As an alternative, two single axis MEMS mirrors can be combined to perform 2D scanning [37]. MEMS mirrors are a universally applicable, high-performance and cost-effective solution for mass production due to the standard CMOS manufacturing technology [35,41,42]. Automotive-qualified MEMS scanning systems enable various vehicle safety applications and long marketability up to fully automated driving. To be successful in the automotive market, the MEMS scanning system must meet

the high performance requirements of the various applications, while ensuring automotive-qualified robustness against harsh environmental conditions, such as strong vibrations and temperature fluctuations [35, 43]. The operation principles of MEMS mirrors can be resonant or non-resonant and use either electromagnetic, piezoelectric, electrothermal or electrostatic forces for actuation [44]. Resonant operation allows to benefit from the typically high quality factor enabling a large FoV scanning at frequencies of several kilohertz, while the power consumption is kept low and the control is considerably simpler [45, 46]. The electrostatic actuation is among the others the most CMOS compatible actuation principle as no unusual materials are used but only structural patterning of silicon, which minimizes cost and increases robustness [44]. Hence, considering energy consumption, cost, integrability, performance and robustness, the resonant electrostatic MEMS mirrors show high potential but typically exhibit nonlinear behavior, where the reliable operation in harsh environments has to be proven.

1.1. Scope of the thesis

To enable MEMS scanning systems to be a solution for future low cost automotive-qualified beam steering, the system has to be designed for high performance and robustness. The main goals of this thesis are:

- Investigation of the resonant electrostatic MEMS mirror dynamics by a detailed mathematical modeling and identification
- Development of robust sensing concepts and control strategies
- Demonstration of stable and high precision scanning even in harsh environments

This enables the analysis of the interrelations and interplay of resonant electrostatic MEMS mirror design choices, sensing and control. As a result the MEMS scanning system can be tailored for the individual applications taking the individual aspects into account to obtain maximum performance.

CHAPTER 2

State of the Art

This chapter provides a literature overview of the state of the art on actuation, sensing, modeling and control of resonant MEMS mirrors. It starts with a brief overview of scanning systems for automotive applications including general scanner principles and scan trajectories. Subsequently the MEMS mirrors are discussed in more detail. The most common actuation and sensing principles are reviewed and an approach to increase the dynamic performance by a lightweight mirror design is provided. The modeling and control review focuses on resonant electrostatic MEMS mirrors as they are the subject of this thesis, including their nonlinear behavior discovered in literature such as spring and damping nonlinearities, parametric excitation and mode coupling phenomena, leading to complex dynamics. Finally, this chapter identifies open challenges and missing knowledge required for enabling miniaturized high performance robust scanning systems based on resonant MEMS mirrors and formulates the research questions of this thesis.

2.1. Optical scanning systems

For high resolution AR HUD and adaptive headlights, DMDs are currently the most dominant solution [47]. They utilize several hundred thousand of small mirrors on a silicon chip that can be individually tilted to two states, i.e. 'on' and 'off'. In the 'on' state the light from the light source is directed through the projection optics and forms the image, while in the 'off' state the light is directed to an absorber. Hence, the whole image is projected at once, while the method is subtractive leading to residual stray light even when the mirrors are turned off, i.e. no true black, and a permanent high power consumption even if nothing is

projected. First researchers demonstrated the use of DMDs also for lidar, where the laser is shot during the transition between the two states of the mirrors [48], while the achieved performance is rather low. Hence, dedicated scanners tailored for fast and high resolution laser beam steering promise better performance. High performance scanning systems aim to traverse a repeating fine grid scan pattern to cover the target FoV in a minimum time to achieve fast and high resolution imaging. Considering physical limitations of the scanning devices, those two requirements of speed and spatial resolution are usually contradicting. In the following, an overview of scanner principles and scanning trajectories considered for automotive is provided.

2.1.1. Scanner principles

Spinning scanners are commonly used in commercial available automotive lidars. The transmitter and receiver module are assembled into a frame, which typically rotates continuously around the vertical axis allowing a horizontal FoV of up to 360° with high resolution. The advantage of the continuous rotation is the constant scan speed, while it requires bearings and slip rings leading to mechanical wear and therefore a reduced lifetime [49]. In order to increase the vertical FoV and resolution, multiple transmitter and receiver modules have to be included into the frame, which increases its size, complexity and cost.

Rotating mirror scanners typically perform a continuous rotation of a mirror in one direction such as monogon or polygon scanners, or oscillate, i.e. alter its scanning direction periodically as depicted in Fig. 2.1a. The continuous rotation allows a constant and fast scan speed with less moving mass compared to spinning scanners, while still mechanical wear leads to a reduced lifetime. The oscillating scanners typically use the elastic deformation of restoring springs showing less fatigue, while a constant and fast scan speed is more difficult to achieve as multiple harmonics are necessary to form the desired trajectory. For a triangular trajectory at least the first 7 harmonics have to be included, which are mainly limited by the inertia of the scanner and therefore reduce the achievable scan speed [50, 51]. To achieve non-uniform but high scan speeds the oscillating scanners can be excited at resonance, performing a single harmonic motion. In combination with high quality factors a large FoV can be achieved with a significantly reduced power consumption [45, 46]. Typical examples of oscillating scanners are galvanometer scanners [52], fast steering mirrors [53] as well as MEMS mirrors. Fast steering mirrors and galvanometer scanners allow precise scanning and a large mirror size, while they hardly achieve a large FoV at high frequencies. This is as they utilize Lorentz or reluctance forces for actuation, which requires coils and permanent magnets. Therefore, limitations of available manufacturing processes and thermal dissipation impose size constrains. In contrast, the MEMS mirrors enable a large FoV at a high frequency and long lifetime by a drastic miniaturization of

the scanning system utilizing CMOS technology with a feature size in the order of nanometer and are discussed in more detail in Section 2.2.

Optical phase arrays (OPA) receive much attention in recent years due to its potential to achieve true solid-state automotive lidar, i.e. no moving mass. In OPAs the light from a laser source is split, coupled to phase shifters using waveguides and emitted by an array of optical antennas as depicted in Fig. 2.1b. The combined wavefront of all antennas forms a beam in the far field, which can be steered by adjusting the individual phases of the emitted waves. Typically the phase is shifted by varying the refractive index of the silicon waveguides using the thermo-optic or electro-optic effect. However, the OPA technology is not yet ready to be successful in automotive as more research is needed especially for the thermal management to allow operation in various environments as well as the light source integration for a high efficiency [32]. Hence, MEMS mirrors are considered as a ready solution to achieve high performance and compact scanning systems due to its available and easily scalable technology.

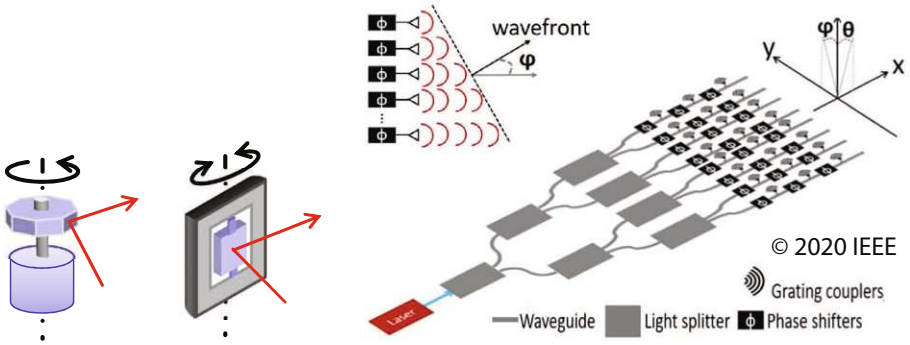

(a) Rotating scanner (b) Optical phase array scanner

Figure 2.1.: Rotating scanner principles with continuous (left) and oscillating motion in a fixed frame (right). (b) The light from the laser is split and guided to optical antennas through phase shifters, which alter the phase of the individual waves by manipulating the refractive index, resulting in a steerable laser beam [32].

2.1.2. 2D scanning trajectories

There is a variety of scanning trajectories for 2D scanning systems reported in literature including raster, Lissajous, spiral and random-access scanning. Depending on the individual scanning system and application requirement, the one or the other trajectory type allows properties such as uniform scan speed and resolution, simple scanner and control design or high flexibility in scan pattern design. In the following, raster, Lissajous as well as random-access scanning are

discussed in more detail, which are particularly attractive for automotive scanning and imaging applications.

Raster scanning

A typical scanning method is the raster scan, where one axis is significantly slower than the other to obtain an uniform scan grid. The slow axis frequency defines the scan repetition, i.e. the frame rate, while the resolution is defined by the laser repetition rate for the fast axis and the ratio of fast to slow axis frequency for the slow axis, respectively. To obtain a repeating scan pattern, the frequency ratio has to be an integer number and is typically $\gg 1$ for high resolution scanning [35]. The individual trajectories can be either of sawtooth, triangular or sinusoid shape and have to be chosen by the particular application requirements. A single-tone sinusoid trajectory simplifies the scanner and control design, while it results in a nonuniform scan speed spending a large portion of the scan time at the edges of the FoV. The triangle or sawtooth trajectories necessitate a wide control bandwidth considering scanner dynamics even for low scanning frequencies to generate multi-harmonic trajectories [51] and is therefore more susceptible to noise [45] and undesired mode excitation [2], while the scans are more uniform. A typical combination is a triangular trajectory for the slow axis, while the fast axis is a single-tone sinusoid to obtain a high resolution by maximizing the frequency ratio at a rather simple scanner design [54, 55].

Lissajous scanning

Lissajous scanning is a method, where both axes have single-tone frequencies whose ratio is a specific rational number, typically in the order of 1 [35, 56]. This method allows the scanning system to be operated at resonance to achieve fast and large amplitude scanning, especially with high Q-factors, at a low power consumption. Furthermore, the control design is rather simple as only a single frequency has to be tracked for each axis and therefore usually shows a significantly lower tracking error compared to raster scanning methods [45, 46], but provides only low flexibility in scan pattern design. A Lissajous scanning pattern is obtained by two single-tone frequencies oscillating along two orthogonal axes X and Y. Hence, the trajectory of both axes can be defined as

$$x(t) = \sin\left(2\pi f_{\mathrm{X}}\, t\right) \quad \text{and} \quad y(t) = \sin\left(2\pi f_{\mathrm{Y}}\, t\right) , \tag{2.1}$$

where f_{X} and f_{Y} are the corresponding frequencies. Without loss of generality it is assumed that $f_{\mathrm{X}} > f_{\mathrm{Y}}$ and with $\varphi_{\mathrm{X}}(t) = 2\pi f_{\mathrm{X}}\, t$ and $\varphi_{\mathrm{Y}}(t) = 2\pi f_{\mathrm{Y}}\, t$, the

evolution of the relative phase can be expressed as

$$\Delta\varphi\left(\frac{N_\mathrm{X}}{f_\mathrm{X}}\right) = \varphi_\mathrm{X}\left(\frac{N_\mathrm{X}}{f_\mathrm{X}}\right) - \varphi_\mathrm{Y}\left(\frac{N_\mathrm{X}}{f_\mathrm{X}}\right) = 2\pi N_\mathrm{X}\cdot\left(1-\frac{f_\mathrm{Y}}{f_\mathrm{X}}\right) \quad \text{and}$$
$$\Delta\varphi\left(\frac{N_\mathrm{Y}}{f_\mathrm{Y}}\right) = 2\pi N_\mathrm{Y}\cdot\left(\frac{f_\mathrm{X}}{f_\mathrm{Y}}-1\right), \tag{2.2}$$

where N_X and N_Y represent the elapsed number of X-axis or Y-axis periods, respectively. The repetition of the Lissajous scan pattern is then defined by the smallest number $K \in \mathbb{N}$ where

$$\Delta\varphi\left(\frac{N_\mathrm{X0}}{f_\mathrm{X}}\right) = \Delta\varphi\left(\frac{N_\mathrm{Y0}}{f_\mathrm{Y}}\right) = 2\pi\, K\,, \tag{2.3}$$

and $N_\mathrm{X0},\ N_\mathrm{Y0} \in \mathbb{N}$ are the total number of X-axis and Y-axis periods per Lissajous frame. Hence, $N_\mathrm{X0},\ N_\mathrm{Y0}$ and K can be calculated by the co-prime ratios given as

$$\frac{K}{N_\mathrm{X0}} = \left(1-\frac{f_\mathrm{Y}}{f_\mathrm{X}}\right) \quad \text{and} \quad \frac{K}{N_\mathrm{Y0}} = \left(\frac{f_\mathrm{X}}{f_\mathrm{Y}}-1\right), \tag{2.4}$$

where $N_\mathrm{X0} = N_\mathrm{Y0} + K$ and the period of the Lissajous frame can be calculated to

$$T_0 = \frac{1}{f_0} = \frac{N_\mathrm{X0}}{f_\mathrm{X}} = \frac{N_\mathrm{Y0}}{f_\mathrm{Y}} = \frac{K}{f_\mathrm{X}-f_\mathrm{Y}}\,. \tag{2.5}$$

As an example $f_\mathrm{X} = 2392\,\mathrm{Hz}$ and $f_\mathrm{Y} = 2366\,\mathrm{Hz}$ are considered, which result in $K = 1$, $N_\mathrm{X0} = 92$, $N_\mathrm{Y0} = 91$ and a frame rate $f_0 = 26\,\mathrm{Hz}$. The resulting resolution of the Lissajous grid is then solely defined by the number of total periods N_X0 and N_Y0 where a higher number corresponds to a higher resolution in the respective other axis as shown in Fig. 2.2. However, due to Eq. (2.5) a higher number of periods for the Lissajous scan also needs a longer time to repeat, i.e. lowers the frame rate f_0. The value K defines how fast a preview of the overall scan is provided, which is subsequently filled with scan lines until T_0. Hence, for $K = 5$ a preview is provided in $T_0/5$ seconds as shown in the figure.

In the case of N_X0 and N_Y0 are both odd integers, K is an even value, which results in overlapping scan lines and therefore a reduced resolution. This phenomenon is also discussed in [57], where an initial relative phase shift in Eq. (2.1) at $t = 0$ is proposed to avoid the overlapping. With the initial phases φ_X0 and φ_Y0 for the X- and the Y-axis, the high resolution is recovered if the following condition is met

$$(N_\mathrm{X0}\,\varphi_\mathrm{Y0} - N_\mathrm{Y0}\,\varphi_\mathrm{X0}) = \frac{\pi}{2}\,. \tag{2.6}$$

Although Lissajous scanning is simple to implement, it generates a non-

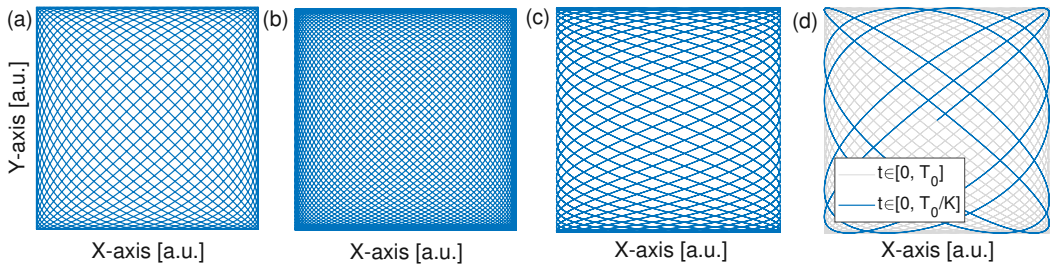

Figure 2.2.: Examples of Lissajous scan patterns. (a) Low resolution grid ($N_{X0} = 26,\ N_{Y0} = 25,\ K = 1,\ f_0 = 90\,\text{Hz}$). (b) High resolution grid ($N_{X0} = 46,\ N_{Y0} = 45,\ K = 1,\ f_0 = 52\,\text{Hz}$). (c) Asymmetric resolution grid ($N_{X0} = 26,\ N_{Y0} = 11,\ K = 15,\ f_0 = 90\,\text{Hz}$). (d) Fast preview due to $K > 1$ ($N_{X0} = 26,\ N_{Y0} = 21,\ K = 5,\ f_0 = 90\,\text{Hz}$).

uniform scan pattern, which only depends on the ratio of both scanning frequencies [45, 58]. The pattern resolution is the lowest at the center of the FoV and increases towards the edges, which is typically disadvantageous in applications. A simple resolution metric based on the scan line separation at the center is given in [45] and can be used for scanning frequency selection [59, 60]. A universal metric for the spatial resolution based on Voronoi tessellations is used in [61] to optimally select the frequencies also considering the scanner dynamics. A pixel distribution proposed in [62] generates a rectilinear grid by a constant sampling rate, which allows a better processing of the obtained image despite non-uniformity.

Dedicated resonant scanners, whose primary operation is at resonance also typically allow a simple design and reduced production cost. This assumes that the desired scanning frequency lies in a certain range around the resonance peak, i.e. the resonance bandwidth, which typically decreases with increasing Q-factor of the system [40, 58]. Not to limit the scanning frequency selection and still achieve high Q-factors, the resonance frequency of a scanning system has to be tunable. Several tuning methods are developed in literature, such as prestressing of the used suspension [46, 63, 64] or to introduce a nonlinear stiffness by a dedicated suspension design, causing the resonance frequency to depend on the system states, e.g. the amplitude, while the Q-factor can be remained high [65, 66]. Considering only a certain tuning range of the scanners, the frame rate usually contradicts with the resolution [59]. A method to obtain effective frame rates higher than the trajectory repetition rate is proposed in [67], where a model-based image reconstruction is used to estimate missing data points.

Random-access scanning

Random-access scanning systems allow arbitrary scan trajectories tailored to the specific application requirements as each pixel can be individually addressed. It is possible to define regions of interest (ROI) in the FoV, which are scanned with high resolution and more frequently in order to track objects. Traditional mechanical scanning systems do not allow true random-access scanning as its inertia is finite and the scan speed cannot be changed abruptly. Hence, ROI scans are limited by the necessary bandwidth to generate the corresponding trajectory. Inertia free scanning systems based on optical phased arrays [68,69] or acousto-optic lenses [70, 71] allow fast random-access scanning, while the system is complex.

2.2. MEMS mirrors

MEMS mirrors have been investigated in high precision scanning and projection systems last decades. The small form factor and the manufacturing with standard CMOS technology on a silicon wafer allow easy and cheap mass production [72]. In general they can be separated by their operation purpose as resonant and non-resonant. Non-resonant or quasi-static MEMS mirrors allow a static tilt of the mirror and various types of scan trajectories such as triangular or sawtooth, provided that the bandwidth is high enough. As a static tilt is achieved by the balance of the restoring springs and the actuation forces, a trade-off between actuation strength and spring stiffness has to be made to achieve large angles, resulting in typically low resonance frequencies of several hundred hertz. Resonant MEMS mirrors are typically simpler in design and can only operate at resonance, where the maximum achievable scan amplitude is given by the balance of dissipated and injected energy. They achieve large deflection angles at high frequencies of several kilohertz, while their power consumption is typically low thanks to the high Q-factor even when operated at atmospheric pressure [44, 73]. MEMS mirrors have been studied and applied for several applications such as in pico-projectors [74], optical coherence tomography [75] and automotive lidar [34, 76, 77]. In the following, typical examples of MEMS mirror actuation and position sensing principles are discussed as well as aperture size considerations and mode coupling.

2.2.1. MEMS mirror actuation principles

Depending on the application requirements the actuation principle is typically either electrostatic, electromagnetic or piezoelectric, which are compared and illustrated in Fig. 2.3 [44]. Electrothermal actuation is of less interest due to its inherent long response time at the scale of typical MEMS mirrors and low robustness against ambient temperature variations [44] and therefore not considered

here.

Electromagnetic actuation uses the Lorentz force exerted on current carrying coils in the rotating mirror and can achieve large displacements with high linearity, while it demands magnets for the magnetic field generation and a shielding to avoid electromagnetic interference (EMI), which make it more bulky, more complex to manufacture and expensive [44, 78].

Piezoelectric actuation uses materials with asymmetric dipoles, which align with an externally applied electric field, leading to an expansion or contraction of the material by applying an according voltage. This method provides high forces allowing high scanning frequencies, while the achievable displacements are low and necessitate a mechanical amplification structure to allow large angle scanning by the small movement of the actuators [79]. Furthermore, nonlinearities such as creep and hysteresis have to be taken into account especially for non-resonant scanners and the most common piezoelectric materials are not CMOS compatible [80], i.e. increasing manufacturing costs.

Electrostatic actuation uses the force between two isolated electrodes when a voltage is applied. The small dimensions, i.e. electrode gaps, of MEMS mirrors allow the electrostatic force to generate the necessary actuation, while the force is weaker compared to the other principles. To increase the actuation force, the electrode area can be maximized by using comb-drives with interdigitated fingers or the applied voltage can be increased, which can reach even 200 V and is limited by the isolation or the pull-in of the electrodes [81]. Resonant MEMS mirrors using comb-drives are the simplest to manufacture as they can be made solely by structural patterning on a silicon die without additional processing steps or materials. For the non-resonant type either sidewall and bottom electrodes [82,83] can be used or one of the comb electrodes can be shifted out-of-plane, angled or stacked to provide an asymmetry in the design, which allow a static tilt [56,84,85]. However, the electrostatic forces depend on the relative position of the comb electrodes and show no dependency on the sign of the applied voltage, resulting in a highly nonlinear actuation [86, 87]. Fig. 2.4 shows two examples of resonant MEMS mirrors using electromagnetic and electrostatic actuation.

Category	Electrostatic	Electromagnetic	Piezoelectric
Preferred Type	Comb drive	Moving coil	PZT film
Simple Fabrication	✓✓✓	✓✓✓	✓✓
Large Displacement	✓✓	✓✓✓	✓
High Force	✓	✓✓	✓✓✓
Low Power	✓✓	✓	✓✓✓
Low Voltage	✓	✓✓✓	✓✓
Compactness	✓✓✓	✓	✓✓✓
Linearity	✓	✓✓✓	✓✓

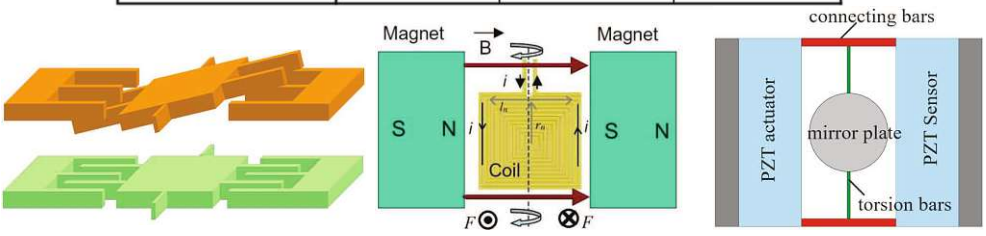

Figure 2.3.: MEMS actuation principles comparison [44] (top) and illustrations (bottom). The right illustration shows the piezoelectric actuation with torsion and connecting bars for mechanical amplification [79]. The PZT material allows to be used as an actuator or as sensor. The middle illustration shows the electromagnetic actuation, with fixed magnets and a moving coil [78]. The left illustration shows the electrostatic actuation using interdigitated comb-drives to maximize the electrode area [88].

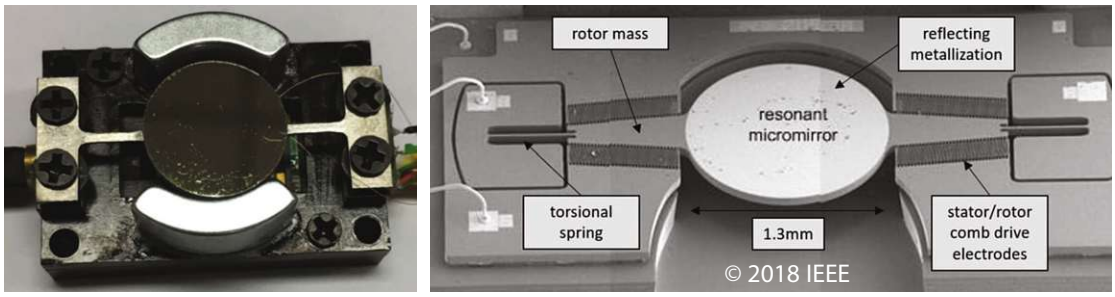

(a) Electromagnetic MEMS mirror (b) Electrostatic MEMS mirror

Figure 2.4.: Resonant MEMS mirror examples. (a) An electromagnetic MEMS mirror made with Ti-alloy structure material [89]. (b) An electrostatic MEMS mirror made from silicon [90].

2.2.2. MEMS mirror sensing principles

For stable and reliable operation of the MEMS mirror in various environmental conditions a closed loop control is necessary and therefore the position of the mirror has to be measured. Various sensing methods are proposed in literature, such as acoustic [91], piezoresistive [92, 93], piezoelectric [79, 94], optical [95, 96] and capacitive [97–100]. Angle feedback based on emitted acoustic waves is not considered since it may not be applicable for harsh environments such as in industrial or automotive applications.

Piezoresistive sensing as shown in Fig. 2.5a and **piezoelectric sensing** are based on either measuring resistance or voltage variations induced by mechanical strain due to the mirror movement and provide continuous angle feedback for closed loop control, achieving promising results [101, 102], but require the deposition and doping of materials and therefore additional processing steps in the manufacturing. Furthermore, both methods suffer from hysteresis, creep and a relatively strong temperature dependency, which have to be compensated e.g. by calibration [103–105].

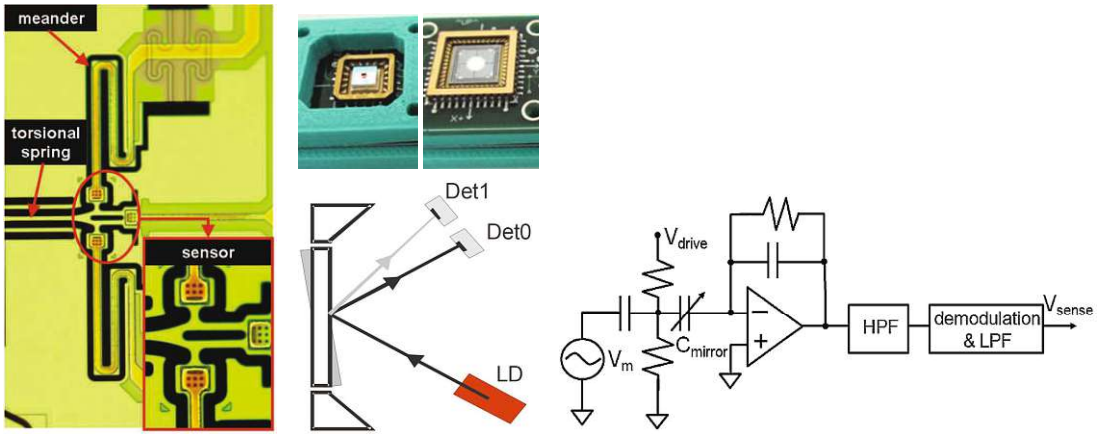

(a) Piezoresistive sensing (b) Optical sensing (c) Capacitive sensing

Figure 2.5.: (a) Piezoresistive strain sensor structure located at the torsional spring of a MEMS mirror [92]. A meander structure avoids parasitic stiffness by the sensor readout connections. (b) Optical sensing using a laser diode and a quadrant photo-detector or discrete photo diodes at the backside of the mirror [95, 96]. (c) Capacitive sensing of the position dependent comb-drive capacitance C_{mirror} [100]. The modulation signal V_{m} is superimposed onto the driving signal V_{drive}.

Optical sensing methods use a laser diode and a photo-detector on the backside of the mirror plate to measure its rotation angle as shown in Fig. 2.5b. A variant of the method uses the timing events of two photo diodes at the backside of the mirror to extract amplitude and phase of a resonant MEMS mirror, demonstrating good performance even at large ambient temperature variation [106]. However, optical components are required to be close to the MEMS mirror and the precision might be influenced by alignment errors or scattered light from the main light path.

Capacitive sensing methods use the comb-drive capacitance variations due to the MEMS mirror movement to extract the mirror trajectory or representative values such as amplitude and phase. A typical method is to use the capacitance variation induced amplitude modulation of a high frequency carrier signal superimposed onto the driving signal as shown in Fig. 2.5c [100] or frequency modulation by including the MEMS mirror in an RLC resonator [107]. Non-modulation based methods use capacitive dividers or current integrators for the extraction of the capacitance variation [108]. These concepts are referred as self-sensing concepts since the same comb-drives are used for actuation and for sensing, while no additional components or manufacturing processes are necessary. This has the drawback that the driving signal and the sensing are not independent, e.g. typically for the non-modulation based methods the sensing signal scales with the driving voltage, resulting in no sensor output for the time period where the driving voltage is zero [108]. This can be circumvented by using dedicated comb-drives only for sensing as in [56], which on the other hand adds complexity and cost. However, especially the modulation based capacitive sensing methods are rather complex and do not provide a high SNR measurement of the amplitude as the capacitance change is low when the comb-drives are fully disengaged, i.e. at large deflection small amplitude variations are hard to discriminate. Furthermore, for the typical case where the comb movement is out-of-plane and the stator as well as the rotor combs are of the same silicon layer as in Fig. 2.4b, the scanning direction cannot be determined due to the symmetry of the comb-drive capacitance for positive and negative angles. However, in applications such as automotive lidar the knowledge of the scanning direction at any time is crucial as otherwise the perceived data is unreliable and may lead to potentially hazardous situations. To overcome this problem an additional sensor or an asymmetric comb-drive design such as staggered or angular vertical combs [84] are usually necessary.

2.2.3. Reinforcement structure

Many conventional MEMS mirror designs have a rather small mirror diameter, which limits the resolution of the illuminated spot and reduces the maximum range and SNR of scanning receivers in applications such as lidar [109]. Increas-

ing the size of the MEMS mirror is not straightforward due to dynamic mirror deformations [110], causing a blurred light spot in the projection. Thicker MEMS mirrors can reduce this dynamic deformation at the cost of a strongly decreased resonance frequency by the increased inertia, which usually cannot meet the required scanning performance. A popular approach to enable large mirrors exploits reinforcement structures, e.g. thick rings or solid islands on the backside of a thin mirror, to reduce low order surface deformation with a small increase of inertia [111–114] as shown in Fig. 2.6. However, the reinforcement structures lead to an asymmetric mass distribution and can result in an undesired coupling of modes as analyzed in Section 3.4.1.

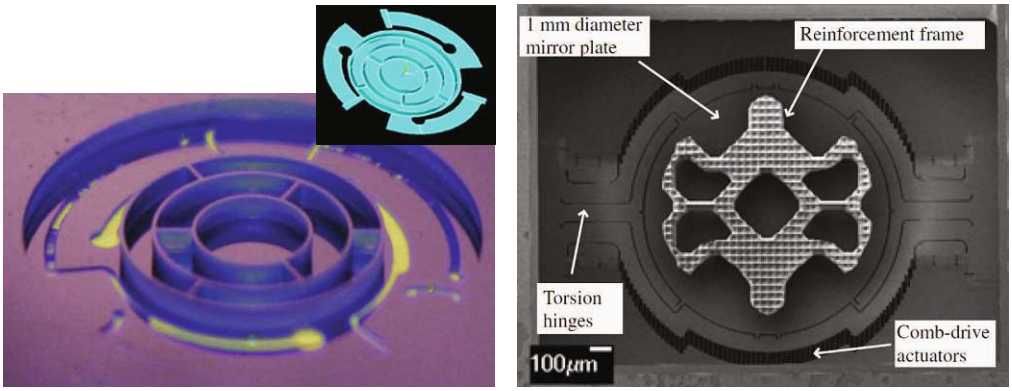

(a) (b)

Figure 2.6.: Lightweight MEMS mirror designs using reinforcement structures on the backside of a thin mirror [113, 114].

2.2.4. Mode coupling

The coupling of modes either linear or nonlinear is well known for micro- and nano-resonators and even utilized for several applications [115]. In case of large deflection oscillation of the targeted mode as for MEMS mirrors, the usual assumption of orthogonal modes may not hold. Furthermore, as electrostatic actuation is strongly dependent on the comb finger positions, introducing additional coupling mechanisms. As an example, the first two modes of an electrostatic MEMS oscillator can be excited simultaneously by applying a driving signal at the sum of both natural frequencies, called non-degenerate parametric amplification [116]. It is stated that the method allows a decoupling of driving and sensing as both frequencies are not in an integer relation, which is different from typical parametric excitation. Also nonlinearities induced by the large rotation of the resonant MEMS mirror in Fig. 2.4b lead to a simultaneous excitation of an undesired in-plane rotational mode, as illustrated in Fig. 2.7, in parametric resonance during normal operation conditions [90]. Such an in-plane rotation can

be destructive for the comb-drives as the rotor fingers may crash into their stator counterparts. Furthermore, a significant temperature dependency of the undesired mode natural frequency is observed, leading to a considerable degradation of the scanning performance due to the coupling only at ambient temperatures between 15°C and 25°C for the specific mirror. However, manufacturing tolerances may shift the individual mode frequencies, leading to coupling in different temperature regions. Hence, an undesired mode coupling during operation needs to be detected and avoided to allow mass production of robust MEMS scanning systems.

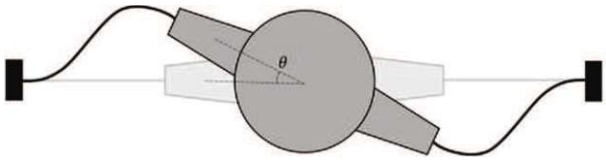

Figure 2.7.: Undesired in-plane rotational mode of the MEMS mirror in Fig. 2.4b [90].

2.3. Modeling and control of resonant electrostatic MEMS mirrors

One of the main issues in miniaturized devices such as MEMS mirrors is that nonlinear effects become more prominent and their dynamic behavior is much more changing by manufacturing tolerances [117]. For characterization and closed loop control design of the MEMS mirrors, an accurate model parametrization and estimation is critical to understand and manipulate its most dominant behavior. Although MEMS designs can have multiple degree of freedom (DoF), the dominant behavior such as the desired scanning mode is usually well separated from other eigenmodes by design, which allows modeling of the device considering only the desired DoF.

2.3.1. Mechanical modeling

Typically MEMS mirrors are modeled by a nonlinear extension of the simple harmonic oscillator considering stiffness and damping nonlinearities. Mechanical stiffness nonlinearities can be introduced by elastic deformations due to high deflections [86, 87] of the springs or by purpose using a special suspension design [118, 119]. While linear resonators usually have a distinct resonance peak whose width increases by damping, the stiffness non-linearity spreads the resonance peak over a frequency band without introducing any damping, which

can be beneficial for resonators [120]. Due to the small size of MEMS mirrors, extensive fluid dynamic calculations have to be used to analyze the damping behavior [121]. However, as the Q-factor is usually high, e.g. several hundreds even at atmospheric pressure, the highly nonlinear damping forces can hardly be measured. Hence, it is typically only observed by a nonlinear change of the dissipated energy with oscillation amplitude, i.e. an amplitude dependent Q-factor [73].

Model parameter estimation methods based on experimental data are proposed in [73] and [122], where a nonlinear analytical model is fitted to the frequency and amplitude data of a ring-down measurement, also called decay. In a similar manner, based on a decay measurement, an estimation method of the effective stiffness and damping ratio of a general nonlinear system is proposed in [123], where the parameters are identified by extracting the instantaneous amplitude and frequency and assuming a piecewise linear response. However, all those methods provide only a pure mathematical behavioral model describing the so called backbone curve of the system but with no actual physical parameters, i.e. no inertia and actuation. Furthermore, single harmonic trajectories are often assumed while it is in general no exact solution of the equation of motion in the presence of nonlinearities, especially a nonlinear stiffness.

2.3.2. Parametric excitation

The electrostatic actuation adds another non-linearity of the torque generated by comb-drives, i.e.

$$\tau_\mathrm{c} = \frac{1}{2}\frac{\mathrm{d}C(\theta_\mathrm{m})}{\mathrm{d}\theta_\mathrm{m}}\,V^2\,, \tag{2.7}$$

which is a nonlinear function of the applied voltage V and the rotation angle θ_m dependent comb-drive capacitance gradient. As resonant MEMS mirrors cannot be statically tilted and the capacitance variations are rather small and therefore hard to measure, the capacitance over rotation angle is usually obtained by an overlap approximation of the comb fingers [86] or by finite element method (FEM) simulations [124]. Fig. 2.8a depicts a typical comb-drive capacitance over the rotation angle reprinted from [124], which shows a symmetric triangular shape with the maximum at zero rotation angle and flattens at large angles [86, 97, 124–126]. As the capacitance gradient shows opposite sign of the rotation angle and the resulting torque in Eq. (2.7) is independent of the sign of the applied voltage V, the mirror can only be pulled to its rest position behaving like a voltage controllable spring with positive nonlinear stiffness. This electrostatic stiffness adds up with the mechanical stiffness of the suspension springs to the effective stiffness with which the MEMS mirror oscillates [86]. The injected energy by the comb-drives using, e.g. a square wave driving signal, depends only on the difference of the comb-drive capacitance at the points of switching on and off, i.e. is positive if

the capacitance is smaller when the driving signal is switched on. Hence, both the total effective stiffness of the system and the energy injection can be manipulated by the applied driving voltage V in a nonlinear manner. This phenomena is called parametric excitation and is typical for electrostatic resonant MEMS mirrors [124–127].

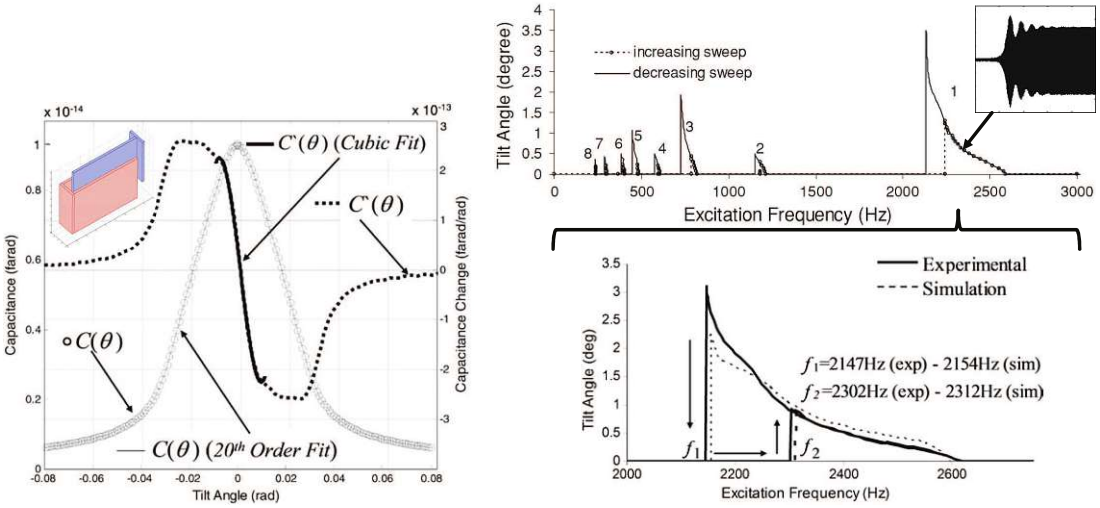

(a) Comb-drive capacitance (b) Frequency response

Figure 2.8.: (a) Comb-drive capacitance and gradient over rotation angle obtained by FEM simulation of a representative comb-drive structure [124] (see inset). (b) Frequency response by slowly sweeping an unipolar square wave driving signal [124]. (top) Total response showing up to the eighth-order parametric resonance. An inset at the right top shows a typical oscillation start over time. (bottom) Close-up at first-order parametric resonance. The point f_2 illustrates the start of oscillation at an up-sweep and f_1 the point of maximum scanning amplitude.

If the driving voltage is applied in the correct frequency and amplitude range, referred to as the stability regions, the MEMS mirror's rest position becomes unstable and it starts to oscillate. Fig. 2.8b shows a typical frequency response of a linear spring stiffness resonant MEMS mirror with electrostatic actuation obtained by slowly sweeping a square wave driving signal. An inset shows a typical transient response of the mirror trajectory envelope when it is started in the stability region. As in general any change in the driving signal triggers another dynamic envelope response, the frequency sweep needs to be slow enough to allow the transients to vanish until steady state is reached. It is found, that a resonant MEMS mirror with a natural frequency of f_m can be operated with driving frequencies located around $2f_\mathrm{m}/n$, where $n \in \mathbb{N}$ is referred as the order

of parametric resonance. Independent of the parametric order, the mirror always oscillates close to f_m, while the highest response is obtained at the first-order parametric resonance, i.e. $n = 1$, and in general scales down as n increases. The energy efficiency of the first-order parametric resonance is evident as most energy is injected if the driving voltage is switched on at maximum deflection of either direction and switched off at the zero crossing, providing the largest capacitance difference. Hence, the driving frequency is twice the mirror oscillation frequency and is mainly used in this thesis.

Other than conventional linear resonant scanners, the parametrically excited MEMS mirrors show bifurcations and can have multiple stable and unstable branches in the frequency response [65, 125, 126]. One consequence can be that a high amplitude oscillation can break down if sudden disturbances occur and no proper control is applied. In general, the high amplitude cannot be reached again by driving at the corresponding frequency, but a dedicated frequency sweep is necessary. This is shown in Fig. 2.8b as a hysteresis appears between f_1 and f_2 and the high amplitude state can only be obtained by a down sweep from frequencies $> f_2$. The analysis of the full dynamic response is in general complex and needs time consuming simulations [65]. Useful approximations can be found by applying the averaging method on the governing equation of motion [125, 126, 128].

2.3.3. Closed loop control

In an automotive application, MEMS mirrors have to operate in the desired specification even at harsh environmental conditions. Large variations of temperature or pressure, electromagnetic interference (EMI) and vibrations have to be taken into account. In order to provide precise laser synchronization signals and to maintain the MEMS mirror oscillation amplitude despite environmental influences, a phase locked loop (PLL) is usually applied [95, 100, 129]. Contrary to a conventional PLL application, where its output is synchronized to the phase of an externally applied reference signal as depicted in Fig. 2.9a, the PLL has to synchronize to the MEMS mirror oscillation, which in turn is influenced by the PLL output as shown in Fig. 2.9b. The stability of such a configuration for a nonlinear oscillator with a cubic stiffening spring is analyzed in [130], where the method of averaging is applied on the governing equation of motion. However, this approach results in complex equations already for the one cubic stiffness non-linearity, while MEMS mirrors typically show stiffness nonlinearities of higher order and the electrostatic actuation, making the analysis of the dynamics and the proper PLL design more difficult. Besides phase synchronization, also the driving voltage amplitude and duty cycle can be used to influence the dynamic behavior and steady state MEMS mirror operation points [95, 125]. A typical approach for resonant MEMS mirrors is to use a fast PLL to track the mirror's phase for stable operation and a slow amplitude controller to adjust either the

driving voltage [95] or the duty cycle [125] to reach the desired operation point.

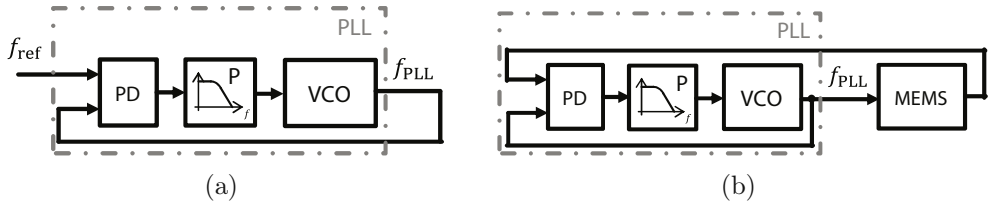

Figure 2.9.: Comparison of PLL structures. (a) Conventional PLL. The PLL adjusts a variable controlled oscillator (VCO) according to the phase detector (PD) output and the loop filter P to follow a reference signal. (b) PLL structure for MEMS mirror control. The VCO is adjusted to follow the MEMS, while the MEMS oscillation is also influenced by the PLL output in a nonlinear manner.

Although PLLs have been designed and applied in applications with MEMS mirrors, there is no analysis or guideline of how to design the loop filter or controller to meet desirable specifications, such as robustness against measurement noise and vibration. Furthermore, the interdependent influences of the driving signal manipulations such as frequency, amplitude and duty-cycle on the MEMS mirror's dynamic phase and amplitude are not taken into account. Therefore, the amplitude control has to be slow enough not to influence the phase synchronization of the PLL, allowing no optimal control of amplitude and phase simultaneously. Multiple-input-multiple-output (MIMO) controllers can deal with those interdependent influences, but were not applied to resonant MEMS mirrors yet. There are various MIMO controller design approaches such as pole placement, loop shaping or the linear-quadratic-gaussian (LQG) regulator. Compared to the others the LQG allows direct control of the system states and inputs by the definition of cost functions [131]. The LQG represents an extension of the linear-quadratic regulator (LQR), which is an optimal state feedback controller, by an optimal observer, i.e. a Kalman estimator, for state estimation from stochastic measurements.

As an alternative to feedback control, feedforward control can be considered. Iterative learning control (ILC) is widely used to compensate for errors in repeating tasks by adapting the feedforward input signals based on the errors obtained from previous iterations, also called batches [132–134]. While a feedback controller results in the same errors for each iteration, the ILC reduces the errors by time using their repeating nature. The assumption of repeating errors allows also to adjust input values for compensation of errors in the future, i.e. non-causal control. Repetitive control (RC) is also a feedforward control and its idea is similar to ILC, i.e. correcting errors from previous resulting trajectories of the repeating

reference [135]. The subtle difference is that RC considers rather a continuous correction from the measurements of a period before [136]. Due to similarity RC shares many analysis with ILC, e.g. control law and convergence criteria [132] and is mixed used in the field of scanning applications such as scanning probe microscopy [51,137–139] and optical scanning using mirrors [140–142]. For Lissajous scan, RC has been applied in atomic force microscopy (AFM) to compensate for periodic nonlinearities of piezoelectric scanners, dynamic cross-coupling of the stage [143,144], and phase errors at high frequency operation [145,146] to ensure clean tone and synchronized operation of scan axes. ILC is also applied for a video rate AFM using a rosette scan, which is generated by modulated sine scan of each axis, to improve periodic disturbances of nonlinearities in a MEMS based nanopositioner with electrostatic actuators and piezoresistive sensors [147,148]. For MEMS mirrors, both RC and ILC are reported for compensate the quasi-static actuation concepts to enhance accuracy and precision of sawtooth and the triangular scanning trajectories in raster scanning [149,150]. For MEMS mirrors and Lissajous scanning, especially additional challenges with modulation concepts, however, any feedforward learning controls such as ILC and RC has not been applied yet.

Synchronization of multiple resonant mirrors

In case of Lissajous scanning the scanning axes are typically operated in resonance at a desired frequency ratio and need to be precisely synchronized to obtain a proper scan pattern [35,40,100]. In addition, the effective receiver aperture of a lidar system can be increased by synchronizing multiple mirrors to the transmitter as in [151,152]. Therefore, the precise synchronization of individual MEMS mirrors or MEMS mirror axes becomes an important task.
A possible solution is to use elastic links between the scanning mirrors or axes to force a synchronized operation as in [153]. A different concept, presented in [151], is based on a master-slave architecture, where the individual driving frequencies of 22 receiver mirrors, i.e the slaves, are adjusted according to the measured relative phase to a transmitter mirror. With the same method, using photo-diodes at the backside of the MEMS mirrors for phase detection, a peak-to-peak phase error of 6 mrad is reported in [154]. Another master-slave concept investigated in [155] synchronizes two single axis MEMS mirrors with progressive nonlinear springs. In this concept the PLL of the slave mirror adjusts its frequency according to the measured relative phase to the PLL of the master mirror. However, robustness of the synchronization control may not be achieved in the case of sudden phase errors, e.g. caused by strong external vibrations and shocks. Hence, there is a need for modeling and stability analysis of the synchronization control concept to guarantee the proper operation in automotive environments.

The synchronization control of multiple resonant MEMS mirrors is not straight-

forward since the individual operation frequencies at the nominal amplitude may differ due to manufacturing tolerances and can shift due to pressure and temperature variations [124, 156]. Possible solutions are to use low Q-factors to achieve a reasonable resonance bandwidth [40, 58] or to tune the resonance frequency by pre-stressing the mechanical springs [63]. In case of electrostatic actuation, the frequency response can also be influenced by the driving signal shape such as voltage and duty cycle of a square wave. As reported in [151], the oscillation frequency of the used MEMS mirror can be varied by 7.5 Hz, i.e. 0.5%, at a high amplitude of 15° by changing the voltage of the square wave driving signal up to 180 V. In [86] the frequency shift by the progressive spring behavior of the torsion bars is compensated by varying the DC offset of the driving signal. Similarly, the obtained amplitude over frequency behavior can be influenced by the duty cycle, as shown in [125].

2.4. Research objectives and questions

The state of the art shows that resonant electrostatic MEMS mirrors have been investigated in various aspects, including modeling of complex dynamics and parameter identification as well as feedback sensing and control concepts. However, it also reveals that the methods and analysis have to be improved in order to allow resonant MEMS mirrors to be used in harsh automotive environments and to guarantee the target specification during the whole lifetime. Some of these issues are identified in the following and subsequently investigated in this thesis.

First, the modeling and identification methods need to be improved to gain a better understanding of the dynamic behavior of the MEMS mirror, also allowing to analyze the influence of each physical parameter. The methods proposed in literature do not include higher order nonlinearities of stiffness, damping and actuation, which are necessary to accurately reproduce the dynamic behavior of the MEMS mirror. Furthermore, identification methods that rely on the estimation of parameters using approximations or FEM simulations cannot be used for a detailed analysis of physical parameter variations caused by environmental changes or production tolerances. This leads to the first research question as follows:

Research Question 1:
Can the system dynamics of resonant electrostatic MEMS mirrors be accurately modeled and identified solely by measurement data in order to allow behavior prediction as well as monitoring of physical parameter variations?

To obtain a stable scanning motion in various environmental conditions, the PLL control for the MEMS mirror has to be properly designed considering harsh vibrations and EMI. The analysis of stability and performance of such a closed

loop system using a nonlinear model of the MEMS mirror is difficult and can be time consuming. However, in application the mirror mainly operates at its nominal operation point where the analysis actually needs to be valid. Hence, a linearization of the dynamics at the nominal operation point can provide a simple and fast approach for the controller design. Considering parameter variations the linear model should be identifiable by measurements solely to allow an accurate representation of the local dynamics in various conditions. This leads to the second research question as follows:

Research Question 2:
Can the complex nonlinear dynamics of a resonant electrostatic MEMS mirror be accurately linearized at a nominal operation point, allowing linear system theory for simple and fast control design?

Lightweight MEMS mirror designs using reinforcement structures allow improved scanning performance due to an optimized rotor structure. However, it also introduces an asymmetric mass distribution, leading to potential issues in the dynamics of the MEMS mirror or robustness in harsh automotive environments. This leads to the third research question as follows:

Research Question 3:
What can be the consequences of a lightweight MEMS mirror design using reinforcement structures to the dynamics and robustness considering harsh automotive environments?

High performance scanning using closed loop control necessitates a precise and reliable sensing concept. Considering miniaturization, mass production and cost of the total scanning system, a self-sensing concept sharing the same comb-drives for actuation and for sensing is preferable. Furthermore, as complex sensing circuits add uncertainties to the total error budget and robustness, the concept should be simple to implement. This leads to the fourth research question as follows:

Research Question 4:
Is it possible to provide accurate and precise sensing signals for closed loop control solely based on a self-sensing concept using robust circuitry?

Exciting various resonant electrostatic MEMS mirror designs in first-order parametric resonance by a control loop is not straightforward because the corresponding stability region has to be known in advance or obtained by a frequency sweep. Furthermore, the sweep may end up in a higher order of parametric resonance, which has to be detected by the sensing concept and necessitates a subsequent sweep, leading to a potentially long start-up time. Also as shown in this thesis, a progressive spring stiffness necessitates to change the sweep direction from down to up if a specific bifurcation occurs to reach high scanning amplitudes. Besides start and stabilization of the MEMS mirror by a control loop,

also a precise pixel synchronization is necessary to achieve high resolution scanning and is typically limited by the clock of the digital implementation. Hence, to evaluate the achievable resolution down to the limits of the sensing concept without clock dependency, the pixel synchronization has to be separated from the digital timing. This leads to the fifth research question as follows:

Research Question 5:
Can a closed loop control be designed to start and stabilize resonant electrostatic MEMS mirrors with unknown stiffness nonlinearities in first-order parametric resonance and to provide precise pixel synchronization to evaluate the achievable resolution limits?

Dynamic external influences such as strong vibrations disturbing the MEMS mirror or EMI increasing the sensing noise require a dedicated control design to keep the scanning motion stable. The driving signal needs to be properly adjusted to counteract the effect of vibration disturbance, while the influence of sensing noise to the mirror motion and pixel synchronization should be minimized. Furthermore, the single axis control shall be extended by a synchronized second axis to allow also robust Lissajous scanning. Advanced concepts such as optimal control have not been applied yet to resonant electrostatic MEMS mirrors in order to tackle those issues. This leads to the sixth research question as follows:

Research Question 6:
Can the control strategies of resonant electrostatic MEMS mirrors be advanced in order to achieve stable scanning motion with the targeted 0.1° resolution considering harsh environmental conditions like in automotive lidar applications?

The vibration influence suppression solely by driving signal control may not always be necessary. A possible alternative for 1D and also raster scanning can be to include the laser pulse scheduler responsible for the pixel triggering into the control concept. Hence, the pixels shall be controlled while the MEMS mirror motion is allowed to have increased errors. This leads to the seventh research question as follows:

Research Question 7:
Can the scheduling of the pixel trigger support the control concept to reduce the errors in application considering harsh environments?

In conventional Lissajous scanning both axes have fixed frequencies, resulting in a disadvantageously shaped inflexible scan pattern with a pincushion like resolution. Increasing the resolution typically comes with a decrease in frame rate, while the high resolution is not always needed in the total FoV, but only at defined ROIs. Hence, a method allowing a Lissajous scanning system to define regions with higher resolution at the cost of other regions to maintain the frame rate can be beneficial in application. This is potentially accomplished by

a dynamic modulation of the frequencies in a specific manner to design the scan pattern more flexible. In order to track the correct modulation the control concept needs to be extended, while the robustness considering harsh environments shall not be compromised. This leads to the eighth research question as follows:

Research Question 8:
Can Lissajous scanning provide flexible scan patterns with ROIs and which control concept is suitable to not compromise the robustness in harsh environments?

2.5. Outline of the thesis

To investigate the stated research questions, a resonant electrostatic MEMS mirror is accurately modeled, identified and analyzed in Chapter 3 including global and local dynamics as well as external vibration influence and mode coupling (RQ1-3). In Chapter 4 precise self-sensing concepts based on the comb-drive current feedback are discussed and analyzed regarding the achieved performance and robustness of the mirror phase, amplitude and scanning direction detection (RQ4). Subsequently, Chapter 5 describes two control concepts, where the first is able to accurately track and control the mirror motion by utilizing the full potential of the proposed sensing concept, enabling a fast start-up and stabilization of various resonant electrostatic MEMS mirror designs (RQ5). The second control concept is designed to allow robust operation of the MEMS mirror even in harsh environments by utilizing optimal control and to allow synchronization of multiple mirrors, e.g. for Lissajous scanning as discussed in Chapter 6 (RQ6). Chapter 7 provides advanced methods of scanning systems including pixel error correction by adaptive laser scheduling using the predicted mirror trajectory errors, called laser shot correction (RQ7), and the adaptive Lissajous scanning by modulation of the relative phase enabling flexible scan pattern design (RQ8). Finally, the thesis is concluded in Chapter 8, providing the answers to the aforementioned research questions and an outlook discusses further potential research extending the presented methods.

CHAPTER 3

Modeling and Identification of Resonant MEMS Mirrors[1]

The detailed understanding of the MEMS mirrors dynamic behavior is crucial in order to design reliable scanning systems. Mathematical models allow to predict the behavior before manufacturing, to monitor process variations and to design a dedicated control. Therefore, the models have to be accurate as well as identifiable with a limited effort. In this chapter, a single axis electrostatic actuated resonant MEMS mirror is modeled by a nonlinear single degree of freedom (SDoF) model and identified by measurements to accurately represent its behavior. Subsequently a linearized model valid at the nominal operation point is derived based on the period-to-period energy conservation to allow simple control design. Finally, undesired modes of the MEMS mirror are analyzed, which can occur during normal operation.

[1] Parts of this chapter are also published in
[65] D. Brunner, H. W. Yoo, T. Thurner and G. Schitter. "Data based modelling and identification of nonlinear SDOF MOEMS mirror". Proc. SPIE, 10931:269-278, 2019.
[157] D. Brunner, H. W. Yoo and G. Schitter. "Linear modeling and control of comb-actuated resonant MEMS mirror with nonlinear dynamics". IEEE Trans. Ind. Electron., 68(4):3315-3323, 2021.
[158] H. W. Yoo, R. Riegler, D. Brunner, S. G. Albert, T. Thurner and G. Schitter. "Experimental evaluation of vibration influence on a resonant MEMS scanning system for automotive lidars". IEEE Trans. Ind. Electron., 69(3):3099-3108, 2022.
[159] R. Schroedter, H. W. Yoo, D. Brunner and G. Schitter. "Charge-based capacitive self-sensing with continuous state observation for resonant electrostatic MEMS mirrors". J. Microelectromech. Syst., 30(6):897-906, 2021.

3.1. The MEMS mirror

The proposed concepts in this thesis are demonstrated by electrostatic actuated resonant MEMS mirrors with a single rotation axis R_X such as the variant in Fig. 3.1. The rotating mirrors are actuated via four comb-drives by applying an unipolar square wave voltage between the moving rotor fingers and the fixed stator fingers. The comb-drives are located at each quadrant of the mirror, where the quadrants are defined by left or right of the rotation axis and above (top) or below (bottom) the mirror in Fig. 3.1. As the comb-drive capacitance is symmetric regarding the rotation angle, the MEMS mirror exhibits electrostatic stiffness and energy injection dependent on the applied driving voltage as discussed in Section 2.3.2. As a consequence it has to be excited in first-order parametric resonance for most energy efficient operation, i.e. at twice the mirror oscillation frequency. The mechanical suspension comprises torsion bars and leaf springs for improved suppression of undesired degree of freedom movements of the mirror, which makes the design more robust and less affected by mode coupling phenomena [90]. The leaf springs are attached to the frame by relief springs and produce the main mechanical restoring force for the R_X movement, while the torsion bars mainly prevent out-of-plane movements. Due to the double sided clamped structure, the leaf springs show progressive stiffness behavior, i.e. the restoring force increases disproportionately with the rotation angle of the mirror. In order to increase the MEMS mirror performance by maximizing frequency and aperture size, dynamic deformation is one of the main limiting factors [160]. Besides mirror surface deformations, degrading the optical resolution, also the entire rotor has to be kept rigid to ensure that the device stays functional, e.g. no considerable comb-drive deformations. To overcome this, a reinforcement structure on the backside of the thin mirror is used, that makes the mirror lightweight while still dynamically flat [76, 111, 113].

Fig. 3.2 shows the mirror oscillation start, using a fixed frequency unipolar square wave driving signal switching between V_p and 0 V in the stability region. The scanning trajectory θ_m is optically measured using a position sensitive detector (PSD) [161]. After a rapid increase in amplitude, a relatively long transient envelope response in amplitude Θ_m and frequency f_m is observed until the final steady state operation point is reached. Fig. 3.2b shows how the MEMS mirror frequency varies around half the driving frequency due to the time dependent electrostatic stiffness. Similarly, if the driving signal is subsequently changed, e.g. in amplitude, frequency or duty cycle, another transient envelope response will be observed and the mirror will converge to a different steady state point. Those steady state operation points show a specific phase delay between the mirror oscillation and the driving signal whose definition is illustrated in Fig. 3.3a and determines the amount of added electrostatic stiffness and energy injection. Hence, at this point the dissipated energy is compensated and the resulting effec-

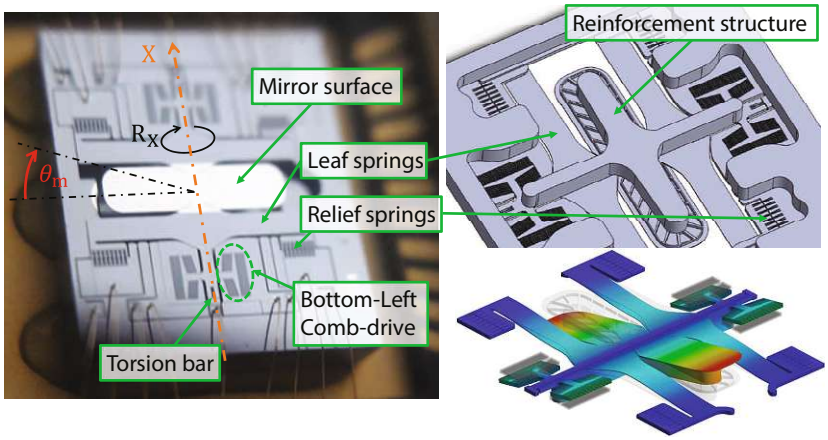

Figure 3.1.: (Left) Picture and definitions of a used comb-actuated resonant MEMS mirror with an aperture size of $3.2 \times 0.8\,\mathrm{mm}^2$ in a glass covered package under ambient pressure. The rotor suspension consists of the conventional torsion bars and additional leaf springs. (Right Top) The backside of the mirror features a reinforcement structure to prevent dynamic deformations with a lightweight design. (Right Bottom) Illustration of the desired mode R_X. (courtesy of Stephan Albert, Infineon Technologies AG)

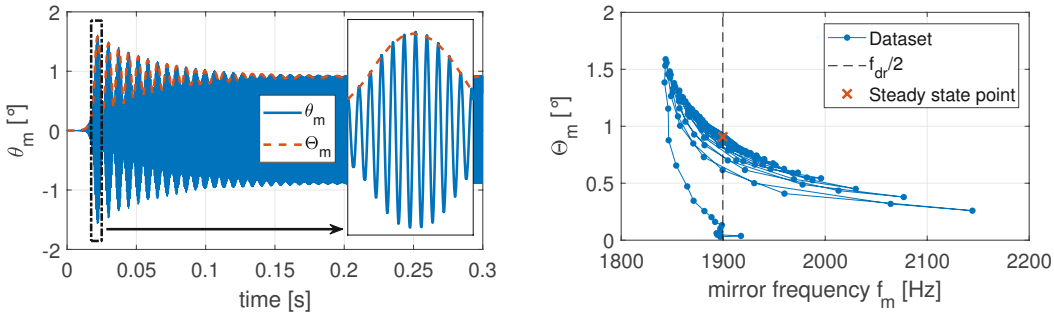

(a) (b)

Figure 3.2.: Transient start of the MEMS mirror using an unipolar square wave driving signal ($V_p = 60\,\mathrm{V}$, 50% duty cycle). (a) Mirror trajectory over time where the driving signal is applied at $t = 0\,\mathrm{s}$. (b) Mirror amplitude over frequency behavior at a transient start in the stability region.

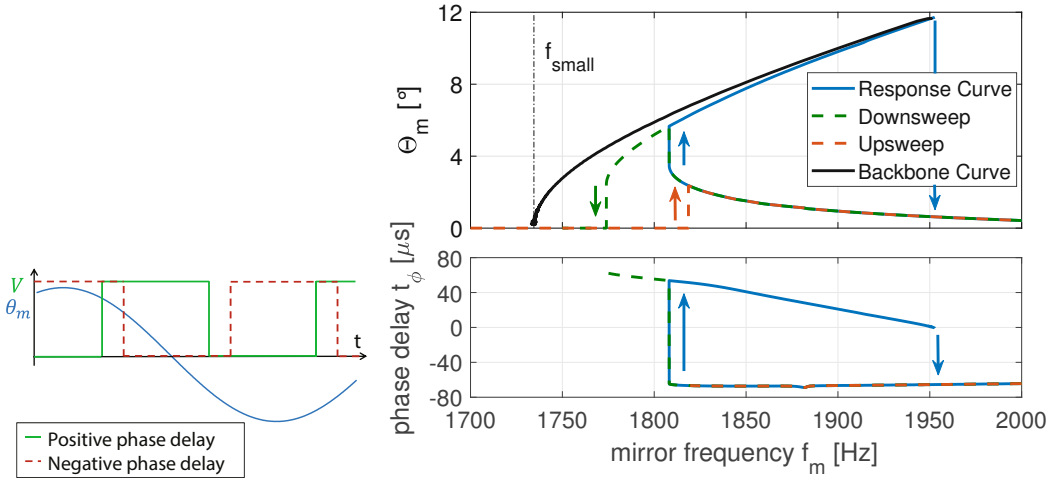

(a) (b)

Figure 3.3.: (a) Mirror trajectory and driving signal waveform illustrating the definition of the phase delay t_ϕ. (b) Measured steady state frequency response of a MEMS mirror variant using unipolar square wave driving ($V_\mathrm{p} = 60\,\mathrm{V}$, 50% duty cycle) and a backbone curve obtained by a decay measurement. The mirror shows several bifurcations (solid arrows) as well as a hardening behavior with increasing amplitude. The driving frequency is twice the mirror frequency to reach first-order parametric resonance.

tive stiffness allows the mirror to oscillate at half of the applied driving frequency in steady state.

If the driving signal frequency is slowly swept and the transients are able to vanish, a steady state frequency response can be obtained. Fig. 3.3b shows the steady state frequency response of a used MEMS mirror and its backbone curve, where the latter represents the pure mechanical behavior of the mirror obtained by a decay measurement, i.e. a ring-down from a high amplitude with the driving signal turned off. The arrows in the frequency response indicate uni-directional transitions, also called bifurcations, which cannot be passed in the other direction in a frequency sweep and highly depend on the system parameters [162]. The upper branch of the response curve can be reached by first sweeping down through the lower curve until the bifurcation leads to a jump in amplitude and phase delay. An increase in frequency then leads to increasing amplitudes, which is called stiffening behavior, until the fallback bifurcation at zero phase delay happens, where the high amplitude oscillation rapidly breaks down. The prominent stiffening is also shown by the backbone curve obtained by a decay measurement and is caused by the leaf springs in the used suspension. The small angle natu-

ral frequency of the pure mechanical system, i.e. unactuated mirror, is given by f_{small}. As the comb-drive is only able to add a positive stiffness to the system, all stable operation points are located at the right side of the backbone curve, which is different from actuators capable of applying pushing and pulling forces [87]. Operating the MEMS mirror at zero phase delay without causing a fallback, is called synchronized excitation and represents the most energy efficient operation point [163].

3.2. The nonlinear SDoF MEMS mirror model

A general SDoF model of a resonant MEMS mirror is a nonlinear extension of the simple harmonic oscillator considering nonlinear functions for the stiffness and the damping [123] as well as for the comb-drive torque. Hence, the equation of motion of the MEMS mirror can be generally written as

$$J\,\ddot{\theta}_{\text{m}} + \gamma\left(\Theta_{\text{m}}\right)\,\dot{\theta}_{\text{m}} + k\left(\theta_{\text{m}}\right)\,\theta_{\text{m}} = \tau_{\text{c}}\left(V, \theta_{\text{m}}\right)\,, \tag{3.1}$$

which allows arbitrary stiffness $k\left(\theta_{\text{m}}\right)$ and amplitude dependent damping coefficient functions $\gamma\left(\Theta_{\text{m}}\right)$, while a constant inertia J is assumed.

3.2.1. Mechanical behavioral model

For the estimation of the mechanical parameters in the left side of Eq. (3.1), the mirror is driven to a high amplitude close to the fallback and its decay is measured by turning off the actuation as shown in Fig. 3.4a. The amplitude over frequency behavior of the mirror trajectory follows the backbone curve in Fig. 3.3a, representing the pure mechanical behavior of the mirror.

Since the unactuated mirror model in Eq. (3.1) is not explicit, i.e. can be scaled by the inertia J, it is normalized by arbitrarily setting $J = 1\,\text{kg}\,\text{m}^2$ and such normalized parameters are marked with a 'n' in the subscript. This leads to a normalized mechanical equation of motion as

$$\ddot{\theta}_{\text{m}} + \gamma_{\text{n}}\left(\Theta_{\text{m}}\right)\,\dot{\theta}_{\text{m}} + k_{\text{n}}\left(\theta_{\text{m}}\right)\,\theta_{\text{m}} = 0\,. \tag{3.2}$$

The obtained backbone curve in Fig. 3.3a clearly shows a nonlinear stiffness of the mirror and furthermore Fig. 3.4b indicates a nonlinear energy dissipation as also observed in [73]. The characteristics of a simple harmonic oscillator at a decay measurement are a constant oscillation frequency and an exponentially decreasing envelope described by a single exponential term. However, at the presence of any non-linearity these simplifications are no longer valid. For example, a system with linear damping and nonlinear stiffness already leads to envelopes that cannot be

fitted by only one exponential term and therefore this characteristic can only be used as an indicator for nonlinear damping but do not prove its presence. However, at low amplitudes, the mirror response becomes almost linear, i.e. the frequency is rather constant and the envelope can be fitted by a single exponential function, i.e. $\alpha_1\, e^{-\beta_1 t}$ in Fig. 3.4b. Therefore, the normalized linear stiffness and damping coefficient can be estimated by analyzing the small angle response and are derived by

$$k_{\text{small,n}} = (2\pi f_{\text{small}})^2 \quad \text{and} \quad \gamma_{\text{small,n}} = 2\beta_1. \tag{3.3}$$

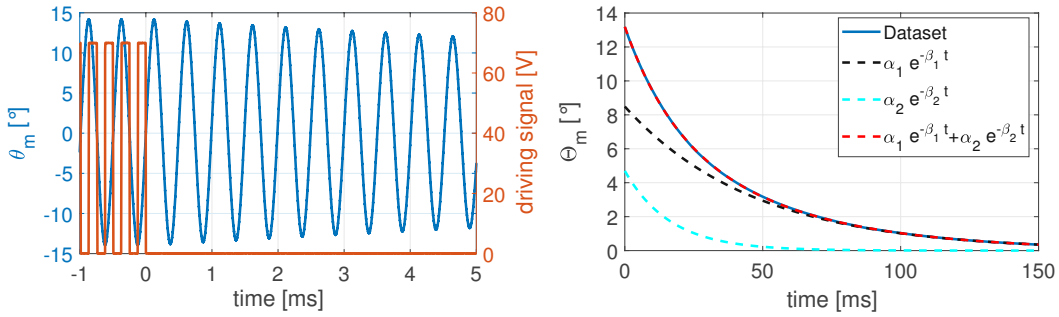

(a) (b)

Figure 3.4.: (a) Measured trajectory and driving signal at the start of the decay, where the actuation voltage is kept zero. (b) Decay envelope over time and its exponential function fits. The sum of two exponential functions is necessary to properly fit the envelope over the whole decay, indicating the presence of nonlinear energy dissipation.

Since typical MEMS mirrors have high Q-factors, the loss in energy per period during the decay can be considered small in comparison to the total energy stored in the system. Hence, each individual period can be assumed conservative such that the sum of kinetic and potential energy always equal the total stored energy, i.e.

$$\overbrace{\frac{1}{2}\dot{\theta}_{\text{m}}^2}^{\text{norm. kinetic energy}} + \overbrace{\int_0^{\theta_{\text{m}}} k_{\text{n}}\left(\theta_{\text{m}}\right)\, \theta_{\text{m}}\, \mathrm{d}\theta_{\text{m}}}^{\text{norm. potential energy}} = \overbrace{E_{\text{tot,n}}\left(\Theta_{\text{m}_i}\right)}^{\text{norm. total energy}}$$

$$= \overbrace{\int_0^{\Theta_{\text{m}_i}} k_{\text{n}}\left(\theta_{\text{m}}\right)\, \theta_{\text{m}}\, \mathrm{d}\theta_{\text{m}}}^{\text{norm. maximum potential energy}} \quad , \tag{3.4}$$

where Θ_{m_i} is the amplitude of the corresponding period i. Using Eq. (3.4) the

mirror period for a specific stiffness function can be calculated by

$$T_{\mathrm{m_i}} = \frac{1}{f_{\mathrm{m_i}}} = 4\int_0^{\Theta_{\mathrm{m}_i}} \frac{1}{\dot{\theta}_{\mathrm{m}}}\,\mathrm{d}\theta_{\mathrm{m}} = \frac{4}{\sqrt{2}}\int_0^{\Theta_{\mathrm{m}_i}} \left(\int_{\theta_{\mathrm{m}}}^{\Theta_{\mathrm{m}_i}} k_{\mathrm{n}}\left(\theta_{\mathrm{m}}\right)\,\theta_{\mathrm{m}}\,\mathrm{d}\theta_{\mathrm{m}}\right)^{-\frac{1}{2}} \mathrm{d}\theta_{\mathrm{m}}\,. \quad (3.5)$$

With numerical integration of Eq. (3.5) a normalized stiffness function can be estimated, which matches the measured decay response in amplitude and frequency. Due to the symmetry of the MEMS mirror design, the stiffness can be assumed to be an even polynomial of sufficient order, where the zero order coefficient is already given by $k_{\mathrm{small,n}}$ in Eq. (3.3). Therefore, the estimation algorithm has to only estimate the higher order coefficients. The resulting stiffness function for the used MEMS mirror is shown in Fig. 3.5a, where three coefficients are fitted to properly match the measured data.

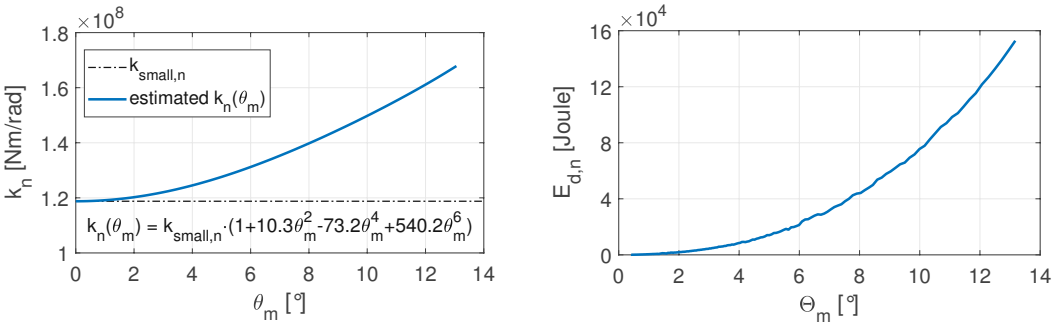

Figure 3.5.: (a) Estimated normalized spring stiffness function by matching the backbone curve using Eq. (3.5). (b) Normalized dissipated energy per mirror period over amplitude. This energy corresponds to the potential energy difference of adjacent amplitudes in the decay measurement.

Damping models of MEMS mirrors are still content of extensive research and highly depend on the geometry and the gas pressure in which they are operated [73, 164, 165]. As the damping torque is very low, it is difficult to be estimated at every time instance of the decay measurement. Therefore, the nonlinear damping is approximated by calculating an averaged damping coefficient γ_{n_i} for each mirror period along the decay and assume it is a function of the mirror amplitude Θ_{m}. This allows to model the non-linearity of the damping coefficient provided that it is relatively small and a sufficiently smooth function of the mirror amplitude.

The averaged damping coefficient can be obtained by calculating the potential

energy loss in the spring from each amplitude to the next along the decay. This corresponds to the normalized dissipated energy per cycle $E_{\mathrm{d,n}}$ shown in Fig. 3.5b and can be written as

$$E_{\mathrm{d,n}}(\Theta_{\mathrm{m}_i}) = E_{\mathrm{tot,n}}\left(\Theta_{\mathrm{m}_{i+1}}\right) - E_{\mathrm{tot,n}}\left(\Theta_{\mathrm{m}_i}\right) = \gamma_{\mathrm{n}_i} \int_{\theta_{\mathrm{m}}(t_i)}^{\theta_{\mathrm{m}}(t_{i+1})} \dot{\theta}_{\mathrm{m}}(t)\, \mathrm{d}\theta_{\mathrm{m}}\,, \tag{3.6}$$

where t_i denotes the start of the i^{th} period. Fig. 3.6a shows the calculated damping coefficient over the mirror amplitude by using the measured trajectory. The corresponding Q-factor is then calculated by

$$Q = 2\pi \frac{E_{\mathrm{tot,n}}\left(\Theta_{\mathrm{m}_i}\right)}{E_{\mathrm{d,n}}\left(\Theta_{\mathrm{m}_i}\right)}\,, \tag{3.7}$$

and is shown in Fig. 3.6b. The limited measurement SNR of the mirror trajectory leads to noisy estimations at low mirror amplitudes. However, the small amplitude values $\gamma_{\mathrm{small,n}}$ and $Q_{\mathrm{small}} = 2\pi f_{\mathrm{small}}/\gamma_{\mathrm{small,n}}$ are known from the previous analysis and have to be reached asymptotically. Hence, it is shown that even in ambient pressure condition, the MEMS mirror has a high Q-factor, which in general depends on the oscillation amplitude.

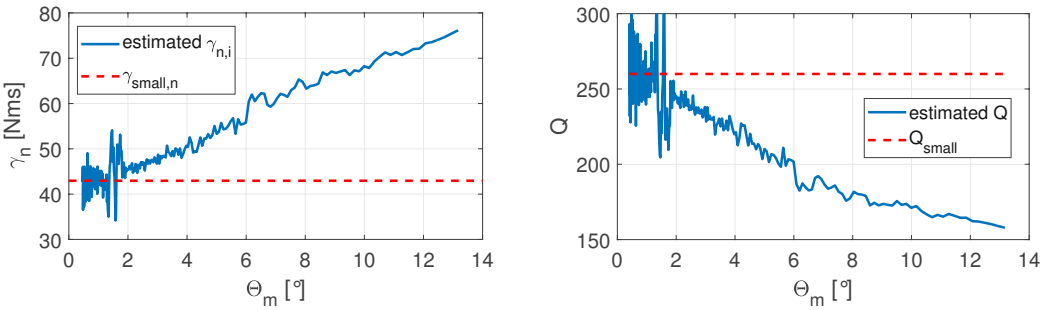

(a) (b)

Figure 3.6.: (a) Amplitude dependent normalized damping coefficient γ_{n} of the individual periods extracted from the decay measurement using Eq. (3.6). The estimation gets noisy at low amplitudes due to the limited measurement SNR. (b) Corresponding Q-factor dependency.

Realization of damping function

In order to use the identified amplitude dependent normalized damping coefficient $\gamma_{\mathrm{n}}\left(\Theta_{\mathrm{m}}\right)$ in the mirror model, the current amplitude has to be known at each simulation time step. This can be implemented by introducing an arbitrary

function, which unambiguously maps the amplitude to a value that can be calculated at each time from the current model states. In this study, a function h is used, which represents the amplitude state by the low-pass filtered angular velocity squared and is shown in Fig. 3.7a. By using the decay measurement data, the amplitude dependent normalized damping coefficient γ_{n_i} at each period can be substituted by the h-dependent function $\hat{\gamma}_{\mathrm{n}}(h)$ as shown in Fig. 3.7b.

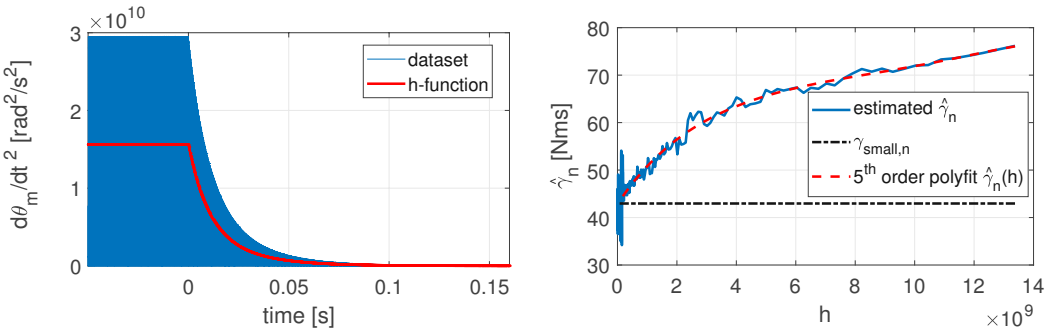

(a) (b)

Figure 3.7.: (a) Angular velocity squared of the decay measurement and ideal h-function using the $filtfilt$-function in MATLAB. (b) Corresponding h dependent normalized damping coefficient where the amplitude of each period is mapped into the function h.

The normalized mechanical MEMS mirror model is then completed as

$$\begin{aligned} \ddot{\theta}_{\mathrm{m}} + \hat{\gamma}_{\mathrm{n}}(h)\,\dot{\theta}_{\mathrm{m}} + k_{\mathrm{n}}(\theta_{\mathrm{m}})\,\theta_{\mathrm{m}} &= 0 \\ \frac{1}{\omega_{\mathrm{h}}^2}\,\ddot{h} + \frac{2\xi}{\omega_{\mathrm{h}}}\,\dot{h} + h &= \dot{\theta}_{\mathrm{m}}^2\,, \end{aligned} \tag{3.8}$$

where a second order low-pass filter ($\omega_{\mathrm{h}} = 2\pi 800\frac{1}{s}$ and $\xi = 1$) is used to obtain the corresponding h value for the damping coefficient selection. Since $\dot{\theta}_{\mathrm{m}}^2$ has doubled mirror frequency (i.e. $> 3400\,\mathrm{Hz}$), a filter bandwidth of 800 Hz is a good tradeoff between high frequency suppression and relatively fast tracking of the mirror amplitude, needed at a decay simulation.

3.2.2. Comb-drive identification

As given in Eq. (2.7) the comb-drive torque is proportional to the derivative of the comb-drive capacitance with respect to the mirror angle θ_{m}. The capacitance derivative can be calculated by measuring the current through the comb-drives and the mirror angle simultaneously. The proposed method is to perform an actuated decay, where the driving voltage is kept constant at a high value (i.e.

$V = V_\mathrm{p}$ and $\frac{\mathrm{d}V}{\mathrm{d}t} = 0$) and to integrate the measured displacement current

$$I_\mathrm{c} = V_\mathrm{p} \frac{\mathrm{d}C(\theta_\mathrm{m})}{\mathrm{d}t}\,, \tag{3.9}$$

generated by the mirror movement over a full mirror period as can be seen in Fig. 3.8a. Using the equation

$$C\left(\theta_\mathrm{m}\right) = \int_{t_\mathrm{start}}^{t_\mathrm{end}} \frac{\mathrm{d}C\left(\theta_\mathrm{m}\right)}{\mathrm{d}t}\mathrm{d}t + const. = \int_{t_\mathrm{start}}^{t_\mathrm{end}} \frac{I_\mathrm{c}}{V}\mathrm{d}t + const.\,, \tag{3.10}$$

the capacitance curve and subsequently its derivative are estimated as a function of the mirror angle and are shown in Fig. 3.8b. Since only the relative changes and not the absolute values of the capacitance are of interest, the capacitance function can be arbitrarily set to

$$C_\Delta(\theta_\mathrm{m}) = C(\theta_\mathrm{m}) - C(0^\circ)\,. \tag{3.11}$$

The almost triangular shape of $C_\Delta(\theta_\mathrm{m})$ with dedicated plateaus in its derivative of height $\bar{C}'_\Delta$ can already be expected from an overlap approximation of the rotor and stator electrodes. In contrast to the overlap approximation, the method based on an actuated decay and current measurement extracts the actual capacitance variation of the MEMS mirror, accounting for all parasitic effects such as the fringing fields with only one measurement. Alternatively, instead of the displacement current, the capacitance can be measured using other methods such as high frequency modulation or charge measurement [159].

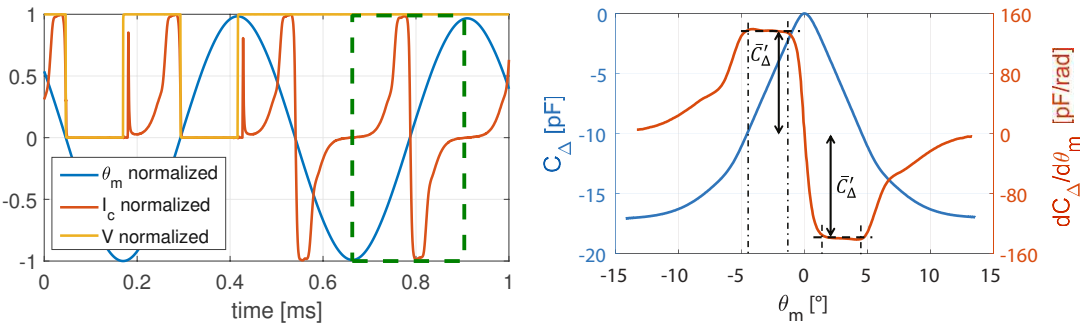

(a) (b)

Figure 3.8.: (a) Actuated decay measurement with constant voltage and data extraction window, i.e. t_{start} to t_{end}, shown by the green dashed rectangle. (b) Extracted comb-drive capacitance curve and its derivative over the mirror angle. The almost triangular shape of the capacitance leads to plateaus in the derivative between $\sim 2^\circ < |\theta_\text{m}| <\sim 4^\circ$, i.e. $\bar{C}'_\Delta$.

3.2.3. The MEMS mirror model

To derive a full model of the MEMS mirror, the normalized mechanical parameters derived in Section 3.2.1 have to be rescaled in order to match the actual physical parameters. This scaling factor, represented by the rotor inertia J, can be estimated by matching the injected energy to the dissipated energy within one period at a steady state oscillation. Assuming a synchronized excitation condition, i.e. zero phase delay where the driving voltage is switched off at the zero crossing of the mirror and switched on at the amplitude point, the injected energy per driving period is

$$E_\text{c}(\Theta_\text{m}) = \int_{\Theta_\text{m}}^{0^\circ} \frac{1}{2} V_\text{p}^2 \frac{\mathrm{d}C(\theta_\text{m})}{\mathrm{d}\theta_\text{m}} \,\mathrm{d}\theta_\text{m} = \frac{1}{2} V_\text{p}^2 \, C_\Delta(\Theta_\text{m}) \,, \tag{3.12}$$

where Θ_m is the obtained amplitude for a specific voltage V_p and C_Δ is the capacitance function.

From the decay measurement in Section 3.2.1, the dissipated energy per mirror period for each amplitude is known and given in Fig. 3.5b. Since E_c is a non-normalized energy and it is injected two times per mirror period at synchronized excitation, the inertia J can be calculated to

$$J = \frac{2\, E_\text{c}(\Theta_\text{m})}{E_\text{d,n}(\Theta_\text{m})} = 4.868 \cdot 10^{-13} \text{kg}\,\text{m}^2 \,. \tag{3.13}$$

This assumes that the actuation does not significantly change the mirror trajec-

tory and therefore the energy dissipation, which usually holds for such high Q systems driven in resonance.

The identification of the full MEMS mirror model including also the actuation terms is then completed as

$$\begin{aligned} J\,\ddot{\theta}_\mathrm{m} + \hat{\gamma}\,(h)\;\dot{\theta}_\mathrm{m} + k\,(\theta_\mathrm{m})\;\theta_\mathrm{m} &= \tau_\mathrm{c}(V,\theta_\mathrm{m}) \\ \frac{1}{\omega_\mathrm{h}^2}\,\ddot{h} + \frac{2\xi}{\omega_\mathrm{h}}\,\dot{h} + h &= \dot{\theta}_\mathrm{m}^2\,, \end{aligned} \tag{3.14}$$

with the rescaled stiffness and damping coefficients given by

$$k(\theta_\mathrm{m}) = J\,k_\mathrm{n}(\theta_\mathrm{m}) \quad \text{and} \quad \hat{\gamma}(h) = J\,\hat{\gamma}_\mathrm{n}(h)\,. \tag{3.15}$$

This allows to simulate the MEMS mirror behavior with arbitrary driving voltages in order to understand its global and local dynamics. The model is fully identified by performing trajectory and displacement current measurements during a decay and an actuated decay from an operation point with synchronized excitation.

3.2.4. External vibration coupling

In applications such as automotive lidar, severe external vibrations have to be considered during operation. Hence, knowledge of the mirror response to vibrations and its counteraction possibilities is critical to guarantee a reliable operation of the scanning system. Assuming that all undesired rigid body modes are much stiffer than the desired $\mathrm{R_X}$ mode, they are not directly actuated in resonance by the external vibrations as the typically occurring frequency spectrum is limited to low frequencies, i.e. only up to several kilohertz [166, 167]. When considering vibrations in all degrees of freedom, the obviously most influencing are the torques aligned with the rotation mode of the MEMS mirror, i.e. $\mathrm{R_X}$. However, considering the possible mounting position of a scanning system with respect to the cars body, the probability of gathering rotational vibrations to the MEMS mirror is rather low, while translational vibrations may dominate as illustrated in Fig. 3.9a. Hence, the coupling of such translational vibrations in $\mathrm{T_X}$, $\mathrm{T_Y}$ and $\mathrm{T_Z}$ directions to the mirror motion has to be analyzed. Although the use of a reinforcement structure on the backside of the mirror enables a high scanning frequency at a large mirror aperture, it also can lead to coupling of translational vibrations. The reinforcement structure shifts the center of mass by the distance L_m below the rotational axis $\mathrm{R_X}$, which causes vibration induced torques from translational Y- and Z-axis vibrations, i.e. $\mathrm{T_Y}$ and $\mathrm{T_Z}$, as illustrated in Fig. 3.9b and Fig. 3.9c. As $\mathrm{T_X}$ is orthogonal to the MEMS mirror's plane of rotation and in a direction of high mechanical stiffness by design, it may not exhibit a significant coupling to the mirror motion. Therefore, the equation of motion of the MEMS

mirror in Eq. (3.1) has to be extended by the vibration-induced torque τ_v as

$$J\,\ddot{\theta}_\mathrm{m} + \gamma\left(\Theta_\mathrm{m}\right)\,\dot{\theta}_\mathrm{m} + k\left(\theta_\mathrm{m}\right)\,\theta_\mathrm{m} = \tau_\mathrm{c}\left(V, \theta_\mathrm{m}\right) + \tau_\mathrm{v}\,, \tag{3.16}$$

where the composition of τ_v is discussed in the following.

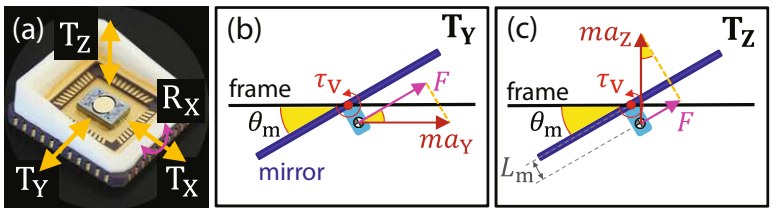

Figure 3.9.: Illustration of vibration directions (a) and coupling model for $\mathrm{T_Y}$ (b) and $\mathrm{T_Z}$ (c) vibrations. The translational accelerations a_Y and a_Z generate a torque for the main mirror rotation mode $\mathrm{R_X}$ with the mass m and the mismatch between the rotation axis and the center of mass of length L_m.

Considering translational accelerations of a_Y and a_Z along the Y- and Z-axis, the vibration-induced torque is generated as

$$\tau_\mathrm{v} = mL_\mathrm{m}F = mL_\mathrm{m}\big(a_\mathrm{Y}\cos\left(\theta_\mathrm{m}\right) + a_\mathrm{Z}\sin\left(\theta_\mathrm{m}\right)\big)\,, \tag{3.17}$$

where m and L_m denote the mass of the mirror and the distance between the rotational axis and the center of mass, respectively. The vibration-induced torque is scaled by the cosine or sine of the mirror angle θ_m due to the movement of the center of mass. For simplicity in analysis, only a single tone vibration is considered as

$$a_\mathrm{Y} = A_\mathrm{Y}\cos\left(2\pi f_{\mathrm{v_Y}}t + \varphi_{\mathrm{v_Y}}\right) \quad \text{and} \quad a_\mathrm{Z} = A_\mathrm{Z}\cos\left(2\pi f_{\mathrm{v_Z}}t + \varphi_{\mathrm{v_Z}}\right)\,, \tag{3.18}$$

where A_Y and A_Z are the acceleration amplitudes with the frequency, $f_{\mathrm{v_Y}}$ and $f_{\mathrm{v_Z}}$, and the phase to the mirror, $\varphi_{\mathrm{v_Z}}$ and $\varphi_{\mathrm{v_Y}}$, for the $\mathrm{T_Y}$ and $\mathrm{T_Z}$ vibration, respectively. Due to the nonlinear dynamics of Eq. (3.16), superposition of the vibration-induced torque does not typically hold for a large amplitude vibration. For a small vibration around a stable equilibrium point, i.e. steady state operation of the mirror, Eq. (3.16) can be linearized, leading to a generalization by the superposition of the single tone analysis. A linearization method based on a period-to-period energy conservation is described in Section 3.3, while it is used here for the analysis of the vibration coupling to the mirror motion.

Assuming the MEMS mirror is in a steady state, i.e. the energy gain and energy loss from injections by the comb-drives and damping are balanced. In

this steady state, the external torque brings a change of the energy in the mirror motion, leading to a variation of amplitude and frequency due to the nonlinear response. Assuming that the mirror trajectory is approximated by a single tone sine with a steady state mirror frequency $\bar{f}_\mathrm{m}$ and an amplitude $\bar{\Theta}_\mathrm{m}$ and the errors of the frequency and amplitude by the vibration are much smaller than the steady state frequency and amplitude, i.e. $\Delta f_\mathrm{m} \ll \bar{f}_\mathrm{m}$ and $\Delta\Theta_\mathrm{m} \ll \bar{\Theta}_\mathrm{m}$. Then the mirror angle can be approximated as

$$\theta_\mathrm{m} \approx \bar{\Theta}_\mathrm{m} \sin\left(2\pi \bar{f}_\mathrm{m} t\right) . \tag{3.19}$$

With 20° as a maximum considered mirror deflection angle, i.e. $\bar{\Theta}_\mathrm{m} < \pi/9\,\mathrm{rad}$, the single tone vibration-induced torque of Eq. (3.17) with Eq. (3.18) can be Taylor expanded as

$$\begin{aligned}\tau_\mathrm{v} \approx mL_\mathrm{m}\Bigg(& A_\mathrm{Y} \cos\left(2\pi f_{\mathrm{v_Y}} t + \varphi_{\mathrm{v_Y}}\right)\left(1 - \frac{1}{2}\,\theta_\mathrm{m}^2\right) \\ & + A_\mathrm{Z} \cos\left(2\pi f_{\mathrm{v_Z}} t + \varphi_{\mathrm{v_Z}}\right)\left(\theta_\mathrm{m} - \frac{1}{6}\,\theta_\mathrm{m}^3\right)\Bigg) ,\end{aligned} \tag{3.20}$$

Besides, the vibration-induced energy change at time t for a single nominal half period $\bar{T}_\mathrm{mh} = \left(2\bar{f}_\mathrm{m}\right)^{-1}$ of the mirror can be written by an average as

$$\Delta E_\mathrm{v}(t) = \int_t^{t+\bar{T}_\mathrm{mh}} \tau_\mathrm{v}\left(\zeta\right) \dot{\theta}_\mathrm{m}\, \mathrm{d}\zeta\,, \tag{3.21}$$

where ζ is the integration variable of time. Assuming that $f_{\mathrm{v_Y}} \neq (2n-1)\,\bar{f}_\mathrm{m}$ and $f_{\mathrm{v_Z}} \neq 2n\bar{f}_\mathrm{m}$ for $n = 1,\ 2$ and substituting Eq. (3.19) and Eq. (3.20) into Eq. (3.21) leads to

$$\begin{aligned}\Delta E_\mathrm{v}(t) \approx\ & a_\mathrm{Y}\, c_{\mathrm{Y},1}\, \bar{f}_\mathrm{m} \left.\frac{\sin\left(2\pi\left(f_{\mathrm{v_Y}} - \bar{f}_\mathrm{m}\right)\zeta + \varphi_{\mathrm{v_Y}}\right)}{2\pi\left(f_{\mathrm{v_Y}} - \bar{f}_\mathrm{m}\right)}\right|_{\zeta=t}^{\zeta=t+\bar{T}_\mathrm{mh}} \\ & + a_\mathrm{Y}\, c_{\mathrm{Y},3}\, \bar{f}_\mathrm{m} \left.\frac{\sin\left(2\pi\left(f_{\mathrm{v_Y}} - 3\bar{f}_\mathrm{m}\right)\zeta + \varphi_{\mathrm{v_Y}}\right)}{2\pi\left(f_{\mathrm{v_Y}} - 3\bar{f}_\mathrm{m}\right)}\right|_{\zeta=t}^{\zeta=t+\bar{T}_\mathrm{mh}} \\ & + a_\mathrm{Z}\, c_{\mathrm{Z},2}\, \bar{f}_\mathrm{m} \left.\frac{\cos\left(2\pi\left(f_{\mathrm{v_Z}} - 2\bar{f}_\mathrm{m}\right)\zeta + \varphi_{\mathrm{v_Z}}\right)}{2\pi\left(f_{\mathrm{v_Z}} - 2\bar{f}_\mathrm{m}\right)}\right|_{\zeta=t}^{\zeta=t+\bar{T}_\mathrm{mh}} \\ & + a_\mathrm{Z}\, c_{\mathrm{Z},4}\, \bar{f}_\mathrm{m} \left.\frac{\cos\left(2\pi\left(f_{\mathrm{v_Z}} - 4\bar{f}_\mathrm{m}\right)\zeta + \varphi_{\mathrm{v_Z}}\right)}{2\pi\left(f_{\mathrm{v_Z}} - 4\bar{f}_\mathrm{m}\right)}\right|_{\zeta=t}^{\zeta=t+\bar{T}_\mathrm{mh}} ,\end{aligned} \tag{3.22}$$

with the vibration coupling coefficients defined as

$$c_{\mathrm{Y},1} = \frac{c_0}{16}\left(8 - \Theta_\mathrm{m}\right), \quad c_{\mathrm{Y},3} = \frac{c_0}{16}\Theta_\mathrm{m}^2,$$
$$c_{\mathrm{Z},2} = \frac{c_0}{48}\left(12\Theta_\mathrm{m} - \Theta_\mathrm{m}^3\right), \quad c_{\mathrm{Z},4} = \frac{c_0}{96}\Theta_\mathrm{m}^2 \quad \text{with} \quad c_0 = 2\pi m L_\mathrm{m}\Theta_\mathrm{m}.$$

For the approximation, the terms with a higher frequency than $\bar{f}_\mathrm{m}$, e.g. $\bar{f}_\mathrm{m} + f_{\mathrm{v_Y}}$, are omitted since they are small by the averaging integral. Equation (3.22) indicates that the vibration coupling results in energy changes varying at the differences between mirror and vibration frequencies and that the orders of harmonics are different for the two directions. At the considered amplitudes of $\Theta_\mathrm{m} < \pi/9\,\mathrm{rad}$, the respective first order contributions are dominant, i.e. $c_{\mathrm{Y},1} \gg c_{\mathrm{Y},3}$ and $c_{\mathrm{Z},2} \gg c_{\mathrm{Z},4}$. $\mathrm{T_Y}$ vibration near $\bar{f}_\mathrm{m}$ and $\mathrm{T_Z}$ vibration near $2\bar{f}_\mathrm{m}$ are mainly considered, i.e. $|\bar{f}_\mathrm{m} - f_{\mathrm{v_Y}}| \ll \bar{f}_\mathrm{m}$ and $|2\bar{f}_\mathrm{m} - f_{\mathrm{v_Z}}| \ll \bar{f}_\mathrm{m}$ since the local dynamics of amplitude and frequency at an equilibrium typically has a much lower bandwidth than the mirror frequency. This allows further approximation of Eq. (3.22) as

$$\begin{aligned}\Delta E_\mathrm{v}(t) \approx\ & \frac{1}{2} a_\mathrm{Y} c_{\mathrm{Y},1} \cos\left(2\pi\left(f_{\mathrm{v_Y}} - \bar{f}_\mathrm{m}\right)t + \varphi_{\mathrm{v_Y}}\right) \\ & - \frac{1}{2} a_\mathrm{Z} c_{\mathrm{Z},2} \sin\left(2\pi\left(f_{\mathrm{v_Z}} - 2\bar{f}_\mathrm{m}\right)t + \varphi_{\mathrm{v_Z}}\right). \end{aligned} \tag{3.23}$$

This result implies four aspects of vibration coupling to the scanning motion of the MEMS mirror in operation.

- The injected energy per half period by vibrations can be approximated by a sinusoidal function with the frequency difference between the vibration frequency and the mirror frequency or the mirror actuation frequency.
- Only vibrations near the mirror frequency or the mirror actuation frequency are coupled to the mirror dynamics, hence representing band-limited local dynamics at an equilibrium.
- Vibration sensitivity with respect to vibration frequencies depends on the direction of the vibration, e.g. high sensitivity for $\mathrm{T_Y}$ vibration with frequencies near the mirror frequency and high sensitivity for $\mathrm{T_Z}$ vibration with frequencies near the mirror actuation frequency, i.e. twice the mirror frequency.
- Coupling of $\mathrm{T_Y}$ vibrations to the mirror dynamics is expected to be stronger than coupling of $\mathrm{T_Z}$ vibrations, considering a maximum mirror amplitude of 20°.

Fig. 3.10 shows a simulation result of $\mathrm{T_Y}$ vibrations, where the variations of the mirror amplitude $\Delta\Theta_\mathrm{m}$, phase delay Δt_ϕ and duration ΔT_mh of each half

period are recorded for different vibration frequencies at a constant acceleration amplitude. The values are obtained by extracting the frequency component $|f_{\mathrm{v_Y}} - \bar{f}_{\mathrm{m}}|$ from the recorded data and the corresponding phases are relative to the injected energy ΔE_{v} per half period. As expected the half period variations are mainly shifted by 180° regarding the amplitude according to the progressive spring behavior and the phase delay is lagging by 90° and shifted by 180° as for a constant driving period the phase delay is the negative sum of the half period variations, i.e.

$$\Delta t_{\phi_i} = -\sum_{j=0}^{j=i} \Delta T_{\mathrm{mh}_j} + \Delta t_{\phi_0} \,, \tag{3.24}$$

with the half period index i. From the steady state frequency response of the mirror in Fig. 3.3 at high amplitudes, it can be observed that for a constant driving voltage and duty cycle the phase delay represents the necessary comb-drive energy injection, i.e. the amplitude increases with decreasing phase delay as more energy is required. Hence, an energy injected by vibrations causes the amplitude and consequently the period to change, leading to variations in the phase delay, which in turn leads to changes in the injected comb-drive energy. This behavior can lead to resonances as shown in Fig. 3.10 when the phase delay has a 90° phase lag. However, the response to negative frequency offsets is different from the positive frequency offsets, e.g. the errors are higher for $f_{\mathrm{v_Y}} > \bar{f}_{\mathrm{m}}$, which cannot be explained by the vibration induced energy injection in Eq. (3.23). Furthermore, the phase between amplitude and period variations can be different from 180°, i.e both get in phase for small and large negative offset frequencies. This leads to zeros in the response of either the amplitude or the period and phase delay at the transitions between in phase and out of phase conditions as shown in the figure insets. Hence, the progressive springs are not the only cause for period variations. Also the electrostatic stiffness caused by the phase delay variations cannot be the reason as it would lead to the same response for both positive and negative vibration offset frequencies.

A qualitative explanation can be found by noticing that each external torque component in phase with the mirror oscillation θ_{m} changes the effective stiffness. For example the time between two consecutive zero crossings, i.e. the half period, increases if a positive external force is applied during a positive half-swing and decreases in case of a negative force. It has to be noted, that according to Eq. (3.21) such a force does not contribute net energy to the system on a half period average. Hence, assuming small perturbations an external vibration can contribute energy or stiffness, whenever it has a component in phase with the mirror velocity or mirror angle, respectively. As an approximation, the variation

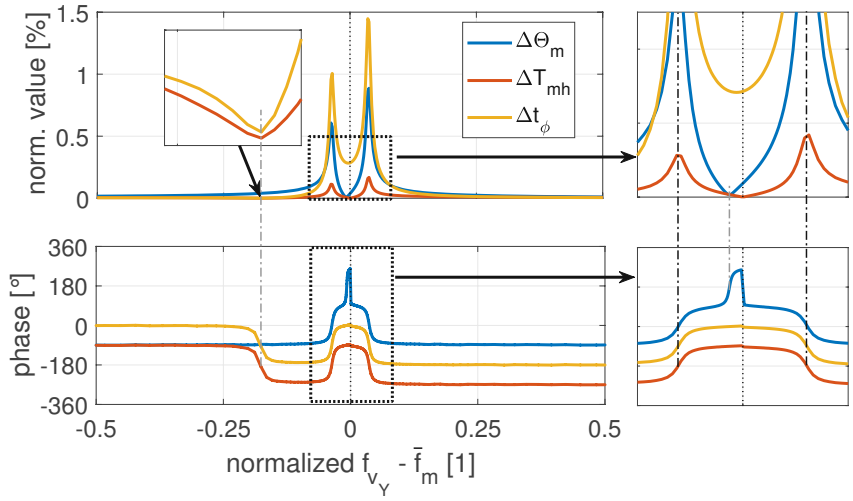

Figure 3.10.: Simulated response of mirror amplitude, half period and phase delay variations to T_Y vibration of $1\,g_{RMS}$ at a nominal mirror amplitude $\bar{\Theta}_m = 13^\circ$ and constant driving frequency. The phase is relative to the induced vibration energy per half period and obtained by extracting the frequency component $|f_{vY} - \bar{f}_m|$. Insets show close-ups for better visibility of the occurring zeros in the response. The values are normalized by the nominal mirror half period and nominal amplitude for time and angle values, respectively.

of the mirror half period induced by vibrations can be expressed as

$$\Delta T_{\mathrm{mh,v}}(t) \propto \int_{t}^{t+\bar{T}_{\mathrm{mh}}} \tau_{\mathrm{v}}\left(\zeta\right) \theta_{\mathrm{m}} \, \mathrm{d}\zeta \,, \tag{3.25}$$

whose solution is -90° shifted regarding the vibration-induced energy in Eq. (3.23), i.e.

$$\begin{aligned} \Delta T_{\mathrm{mh,v}}(t) \propto & -\frac{1}{2} a_{\mathrm{Y}} c_{\mathrm{Y},1} \sin\left(2\pi \left(f_{\mathrm{v_Y}} - \bar{f}_{\mathrm{m}}\right) t + \varphi_{\mathrm{v_Y}}\right) \\ & -\frac{1}{2} a_{\mathrm{Z}} c_{\mathrm{Z},2} \cos\left(2\pi \left(f_{\mathrm{v_Z}} - 2\bar{f}_{\mathrm{m}}\right) t + \varphi_{\mathrm{v_Z}}\right) \,. \end{aligned} \tag{3.26}$$

As acording to Eq. (3.24) the phase delay is the negative sum of the half period variations, it is given as

$$\begin{aligned} \Delta t_{\phi,\mathrm{v}}(t) \propto & -\frac{a_{\mathrm{Y}} c_{\mathrm{Y},1} \bar{f}_{\mathrm{m}}}{2\pi \left(f_{\mathrm{v_Y}} - \bar{f}_{\mathrm{m}}\right)} \cos\left(2\pi \left(f_{\mathrm{v_Y}} - \bar{f}_{\mathrm{m}}\right) t + \varphi_{\mathrm{v_Y}}\right) \\ & + \frac{a_{\mathrm{Z}} c_{\mathrm{Z},2} \bar{f}_{\mathrm{m}}}{2\pi \left(f_{\mathrm{v_Z}} - 2\bar{f}_{\mathrm{m}}\right)} \sin\left(2\pi \left(f_{\mathrm{v_Z}} - 2\bar{f}_{\mathrm{m}}\right) t + \varphi_{\mathrm{v_Z}}\right) \,, \end{aligned} \tag{3.27}$$

and represents the energy injection by the comb-drives, i.e. a positive phase delay causes a negative energy injection. Hence, the comb-drive energy injection caused by stiffness variation in Eq. (3.27) shows a dependency on the sign of the vibration frequency offset and increases the total vibration-induced energy for positive offsets and decreases it for negative offsets. This provides a qualitative understanding why the response to vibrations shows lower amplitudes at negative frequency offsets and a different phase behavior. Hence, this mechanism reduces the errors for the frequency band lower than the mirror frequency, which can be beneficial for automotive applications as the dominant vibrations are at lower frequencies.

3.2.5. Model verification

In this section the identified MEMS mirror model is simulated in MATLAB Simulink and compared to the measured data for two cases, normal operation and under external vibration.

Operation under normal condition

Fig. 3.11a shows a comparison of the simulated and the measured decay response of the mirror. For model validation of linear systems in time domain, the modified index of agreement d_1 [168–170] can be used, which allows a phase and amplitude error sensitive comparison of trajectories [171]. However, in contrast to linear

systems, the frequency varies along the decay and a small frequency error would accumulate to a large phase error as the time passes, resulting in a low agreement value and misleading the performance of the identified model. Therefore, a period-based modified index of agreement is proposed as

$$d_1(i) = 1 - \frac{\sum_k^{N(i)} |\theta_i(k) - \hat{\theta}_i(k)|}{\sum_k^{N(i)} |\theta_i(k) - \bar{\theta}_i| + |\hat{\theta}_i(k) - \bar{\theta}_i|}, \tag{3.28}$$

where θ_i and $\hat{\theta}_i$ denote measurement and simulation of the mirror angles during the i-th period from the start of decay, respectively. $\bar{\theta}_i$ is the average value of the measured mechanical mirror angle at i-th period and typically close to zero. The evaluation size $N(i)$ consists of the zero-crossings at start and end of the i-th period as well as all measured sample points in between. The simulation data of the i-th period is shifted in time to match the corresponding start zero-crossing of the measurement and is interpolated at the times corresponding to the measured sample points to obtain $\hat{\theta}_i(k)$. Fig. 3.11b illustrates the period-based modified index of agreement along the decay measurement showing that the derived model fits the measured data with a modified index of agreement of at least 0.995 at each period in this case study.

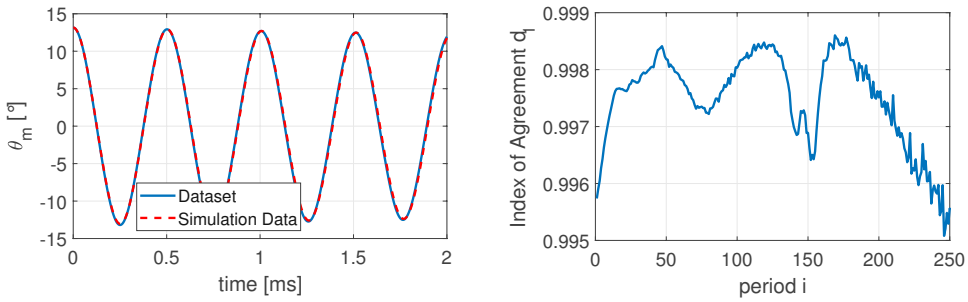

Figure 3.11.: (a) Decay trajectory comparison of simulation and measured data. Only first four periods are shown for clarity of the trajectories. (b) Period-based modified index of agreement calculated for each individual period. The accumulated phase error is compensated by shifting the trajectory of each period in time such that the first zero crossings match.

Fig. 3.12 shows the simulation of the steady state frequency response and a comparison to the measurements. The mismatch at low amplitudes and high frequency may stem from model insufficiency such as possible asymmetries caused by the manufacturing or a too coarse estimation of the comb-drive capacitance. Especially the capacitance curvature around the rest position of the mirror deter-

mines the stability regions, i.e. where the mirror is able to start to oscillate [124]. Apart from this, the simulation results closely match the measured amplitude over frequency behavior of the MEMS mirror. The derived model also shows bifurcations, which accurately match to the measurements even though the model parameters are identified solely from a decay and an actuated decay measurement data.

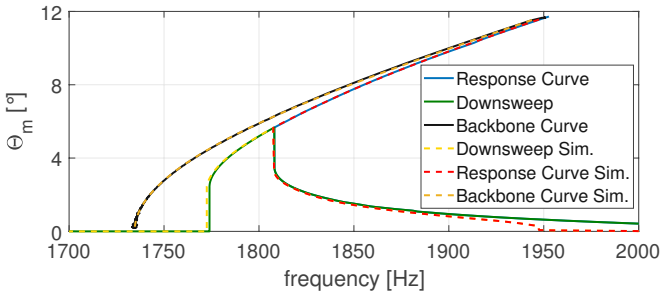

Figure 3.12.: Measured and simulated frequency response of the MEMS mirror. The derived model closely matches the measured response and shows the same characteristics, such as bifurcations and stiffening.

Operation under external vibration

Fig. 3.13 illustrates a vibration test setup for evaluation of vibration influences on a MEMS scanning system. A shaker (TV 51110-M, Tira GmbH, Schalkau, Germany) generates a single directional vibration to a PCB adapter cube. The PCB adapter cube delivers the vibration to the two mirror PCB locations, allowing for T_Y and T_Z vibration test. The mirror PCB is tightly attached to one of the faces of the cube without a gap so that unwanted modes induced by the PCB are suppressed. While the vibration is applied to the MEMS mirror, the mirror trajectory is measured with a PSD, using a collimated fiber laser. The cross-coupling between vibrations and the PSD angle measurement is negligible compared to the vibration influence on the mirror angle trajectory. For the control of the vibration and the data acquisition of the measured PSD signal, an FPGA module in a PXIe system (NI PXIe 7856-R, Austin, TX, USA) is used. The velocity of the vibration is measured by a laser Doppler vibrometer (OFV 534 with OFV 5000, Polytec GmbH, Waldbronn, Germany) and controlled to keep a constant target acceleration of 2 g_{RMS} over various vibration frequencies. The strong single tone acceleration is chosen to attain a reasonable SNR to characterize the vibration influence, while it is much harsher than expected in automotive applications [167]. For T_Z vibration, the vibrometer measures directly the frame

of the MEMS mirror, while the socket is measured instead for T_Y vibration since direct measurement of the MEMS mirror is not applicable. A model based distance calibration is used to calculate the mirror angle from the position of laser beam on the PSD. Hence, the mirror parameters are identified in advance and the operational distance between the MEMS mirror and the PSD is calculated by matching the measurement with the simulated amplitude.

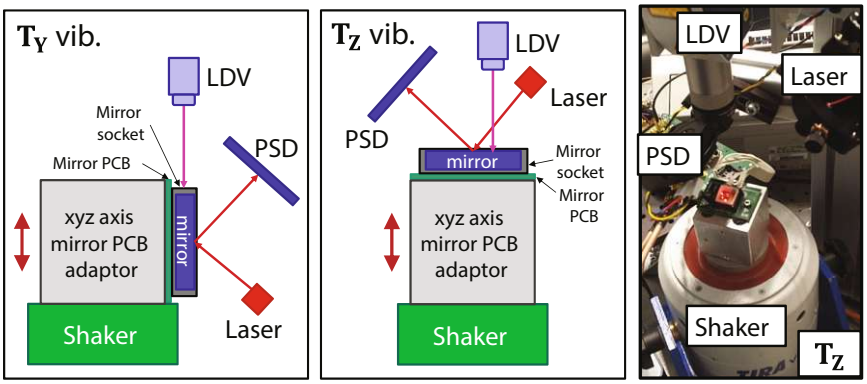

(a) (b) (c)

Figure 3.13.: Vibration test setup schematics for T_Y (a) and T_Z (b) directions and an example picture (c). A PCB adapter cube allows the installation of the mirror PCB for T_Y and T_Z vibrations. The acceleration of the MEMS mirror is measured by a laser Doppler vibrometer (LDV) while the mirror scanning trajectory is recorded by a PSD.

For the vibration influence evaluation the MEMS mirror is operated at a nominal operation point on the upper branch of the response curve with constant driving conditions, i.e. constant frequency, duty cycle and high voltage. Fig. 3.14 shows a comparison of the measured and the simulated response of the mirror amplitude and frequency to T_Y or T_Z vibrations, respectively. The vibration frequencies are slowly swept and the recorded PSD data at each frequency is analyzed. The mean of amplitude and frequency tends to stay constant for all vibration frequencies, while the maximum and the minimum amplitudes and frequencies vary symmetrically with respect to the mean. For the comparison the vibration coupling parameter mL_m, i.e. the product of rotor mass and center of mass displacement from the rotation axis, is estimated by scaling the simulated response to match the measurements with the known acceleration amplitude. As can be seen, the simulation accurately reproduces the measurement data as both show the same resonance peaks and zeros as well as the asymmetry of negative and positive vibration frequency offsets. A comparison of the vibration results shows that the influence in T_Y direction is as expected about a factor 10 higher and therefore has to be considered more in the scanning system design.

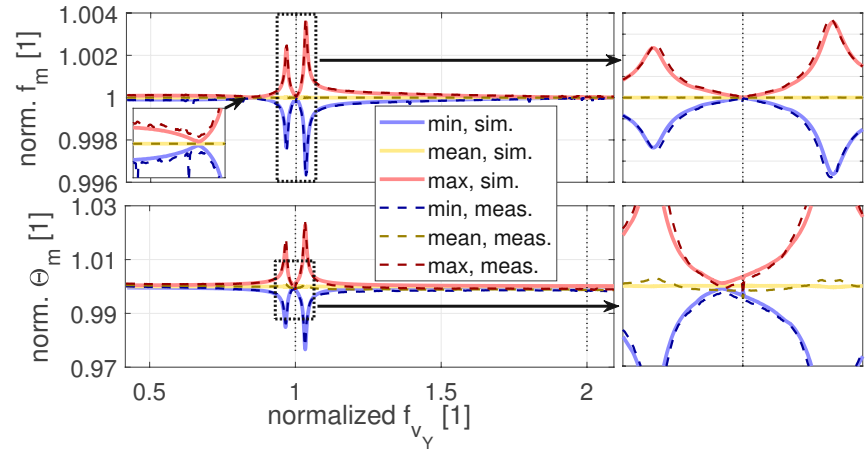

(a) T_Y vibration influence

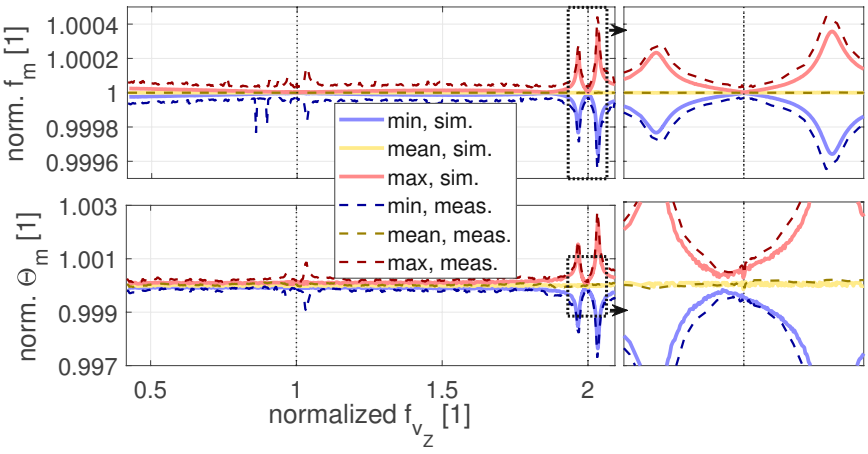

(b) T_Z vibration influence

Figure 3.14.: Influence of T_Y (a) and T_Z (b) vibration on the mirror amplitude and frequency versus the vibration frequencies at the nominal operation point. The values are normalized by the nominal mirror frequency and amplitude. Shown are simulation (solid) and measurement (dashed) results. The influence is represented by the maximum, mean, and minimum of the mirror amplitude and frequency during the vibration. Details are shown by insets. A potential alignment error of the vibration direction may be the cause of coupling to T_Y in (b) leading to the observed small amplitudes around the mirror frequency.

3.3. Linearized period-to-period MEMS mirror model

Simulations of the dynamic response of a MEMS mirror based on the nonlinear model derived in the previous section can deal with arbitrary input functions or operation points but are typically time consuming. Analytical solutions can only be found by applying simplifications on the dynamics and the input function [125, 126]. Furthermore, all nonlinearities have to be properly modeled in order to predict the behavior accurately, which requires much effort on the model parameter identification. However, in applications such as lidar, the global MEMS mirror behavior may not be important, but only the local dynamics at the nominal operation point. Therefore, an accurate model of the MEMS mirror, valid around the nominal operation point is sufficient for the necessary analysis. In this section, an accurate small perturbation model of a MEMS mirror actuated by a square wave driving voltage is derived, which is based on a period-to-period energy conservation. It is shown that for certain operation conditions, the local dynamics of the MEMS mirror become linear in a wide range and therefore can easily be analyzed by conventional linear system theory.

3.3.1. Linearized model derivation

Since the MEMS mirror is a high Q system and the trajectory is mainly given by the mechanical spring and the inertia, the dynamic behavior can be analyzed in a period-to-period basis. One period refers here to a driving signal period T_{dr} and therefore corresponds to a half mirror period T_{mh} as only first-order parametric resonance is considered. At the nominal operation point with a fixed driving signal, the obtained values for the mirror half period T_{mh}, the amplitude Θ_{m} and the phase delay t_ϕ are the nominal values $\bar{T}_{\mathrm{mh}}$, $\bar{\Theta}_{\mathrm{m}}$ and $\bar{t}_\phi$. As this operation point is stationary, the dissipated energy matches the injected comb-drive energy. The local dynamics can then be analyzed by assuming small perturbations of the injected energy, leading to deviations from the nominal operation point, which are indicated by a Δ in the prefix of the variables.

The total system energy change from the start of the i-th to the $(i+1)$-th mirror half period can be expressed as

$$E_{\mathrm{tot}_{i+1}} - E_{\mathrm{tot}_i} = E_{\mathrm{c}_i} + E_{\mathrm{ext}_i} - E_{\mathrm{d}_i}\,, \tag{3.29}$$

where E_{c_i} is the injected comb-drive energy, E_{ext_i} is an external disturbance energy and E_{d_i} is the dissipated energy within the i-th period. E_{tot_i} can be seen as the kinetic energy available at the start of the i-th mirror half period, which results in an amplitude Θ_{m_i}. Therefore, the total energy change results in a

change of the maximum potential energy E_p and the dissipated energy E_d in the following mirror half period, i.e.

$$E_{\mathrm{tot}_{i+1}} - E_{\mathrm{tot}_i} = E_{\mathrm{p}_{i+1}} + E_{\mathrm{d}_{i+1}} - E_{\mathrm{p}_i} - E_{\mathrm{d}_i}\,, \tag{3.30}$$

which defines the change in mirror amplitude. Considering only small perturbations, Eq. (3.29) and the nonlinear frequency response can be linearized at a nominal operation point with mirror amplitude $\bar{\Theta}_\mathrm{m}$ and mirror half period $\bar{T}_\mathrm{mh}$. Therefore, Eq. (3.29) and Eq. (3.30) can be rewritten to

$$\begin{aligned}&\left(\frac{\mathrm{d}E_\mathrm{p}(\bar{\Theta}_\mathrm{m})}{\mathrm{d}\Theta_\mathrm{m}} + \frac{\mathrm{d}E_\mathrm{d}(\bar{\Theta}_\mathrm{m})}{\mathrm{d}\Theta_\mathrm{m}}\right)\left(\Delta\Theta_{\mathrm{m}_{i+1}} - \Delta\Theta_{\mathrm{m}_i}\right)\\ &= \Delta E_{\mathrm{c}_i} + E_{\mathrm{ext}_i} - \frac{\mathrm{d}E_\mathrm{d}(\bar{\Theta}_\mathrm{m})}{\mathrm{d}\Theta_\mathrm{m}}\Delta\Theta_{\mathrm{m}_i}\,,\end{aligned} \tag{3.31}$$

where $\Delta\Theta_{m_i} = \Theta_{m_i} - \bar{\Theta}_m$ and $\Delta E_{\mathrm{c}_i} = E_{\mathrm{c}_i} - \bar{E}_\mathrm{c}$ are the deviations from their nominal value in the *i-th* period. The nominal injected comb-drive energy $\bar{E}_\mathrm{c}$ is the energy needed to sustain the nominal operation point in steady state and has to match $E_\mathrm{d}(\bar{\Theta}_\mathrm{m})$.

The nonlinear potential and dissipated energy functions can be expressed similar to Eq. (3.4) and Eq. (3.6) as

$$\begin{aligned}E_\mathrm{p}(\Theta_\mathrm{m}) &= \int_0^{\Theta_\mathrm{m}} k(\theta_\mathrm{m})\,\theta_\mathrm{m}\,\mathrm{d}\theta_\mathrm{m} \quad \text{and}\\ E_\mathrm{d}(\Theta_\mathrm{m}) &= \gamma(\Theta_\mathrm{m}) \int_{\theta_\mathrm{m}(0)}^{\theta_m(T_\mathrm{m})} \dot{\theta}_\mathrm{m}\,(t)\;\mathrm{d}\theta_\mathrm{m}\,,\end{aligned} \tag{3.32}$$

with the nonlinear spring stiffness k and the amplitude dependent damping coefficient γ. As discussed in the previous section, the modeling by an amplitude dependent damping coefficient is sufficient to cope with its nonlinearities due to the high Q factor.

Finally the injected comb-drive energy has to be analyzed regarding an amplitude change. If only square wave driving with fixed voltage and duty cycle is considered, the injected comb-drive energy per driving period is

$$E_{\mathrm{c}_i} = \frac{1}{2}V^2\big(C_\Delta\left(\theta_\mathrm{m}\left(t_{\mathrm{off}_i}\right)\right) - C_\Delta\left(\theta_\mathrm{m}\left(t_{\mathrm{on}_i}\right)\right)\big)\,, \tag{3.33}$$

which only depends on the switching times, i.e. t_on and t_off. If the MEMS mirror is operated at high amplitudes, i.e. $\bar{\Theta}_\mathrm{m} > 10^\circ$ for the used variant, the comb-drive energy depends only marginally on the small amplitude variations, since the comb-drive torque is concentrated at low angles, as can be seen in Fig. 3.8.

However, due to the nonlinear frequency response, the mirror half period T_{mh} changes with the oscillation amplitude, which leads to a changed phase delay in the following period. Therefore, Eq. (3.33) has to be analyzed regarding the local time derivatives. Using a Taylor approximation of up to the second order, the comb-drive energy change can be expressed as

$$\Delta E_{\mathrm{c}_i} \approx \frac{1}{2}V^2\left(\frac{\mathrm{d}C_\Delta\left(\theta_{\mathrm{m}}\left(\bar{t}_{\mathrm{off}}\right)\right)}{\mathrm{d}t}\Delta t_{\mathrm{off}_i} + \frac{1}{2}\frac{\mathrm{d}^2C_\Delta\left(\theta_{\mathrm{m}}\left(\bar{t}_{\mathrm{off}}\right)\right)}{\mathrm{d}t^2}\Delta t_{\mathrm{off}_i}^2 - \frac{\mathrm{d}C_\Delta\left(\theta_{\mathrm{m}}\left(\bar{t}_{\mathrm{on}}\right)\right)}{\mathrm{d}t}\Delta t_{\mathrm{on}_i} - \frac{1}{2}\frac{\mathrm{d}^2C_\Delta\left(\theta_{\mathrm{m}}\left(\bar{t}_{\mathrm{on}}\right)\right)}{\mathrm{d}t^2}\Delta t_{\mathrm{on}_i}^2\right), \tag{3.34}$$

where Δt_{off} and Δt_{on} are the deviation from their nominal value $\bar{t}_{\mathrm{off}}$ and $\bar{t}_{\mathrm{on}}$, respectively.

By using the chain rule,

$$\frac{\mathrm{d}C_\Delta\left(\theta_{\mathrm{m}}\right)}{\mathrm{d}t} = \frac{\mathrm{d}C_\Delta\left(\theta_{\mathrm{m}}\right)}{\mathrm{d}\theta_{\mathrm{m}}}\frac{\mathrm{d}\theta_{\mathrm{m}}}{\mathrm{d}t} \qquad \text{and}$$
$$\frac{\mathrm{d}^2C_\Delta\left(\theta_{\mathrm{m}}\right)}{\mathrm{d}t^2} = \frac{\mathrm{d}^2C_\Delta\left(\theta_{\mathrm{m}}\right)}{\mathrm{d}\theta_{\mathrm{m}}^2}\left(\frac{\mathrm{d}\theta_{\mathrm{m}}}{\mathrm{d}t}\right)^2 + \frac{\mathrm{d}C_\Delta\left(\theta_{\mathrm{m}}\right)}{\mathrm{d}\theta_{\mathrm{m}}}\frac{\mathrm{d}^2\theta_{\mathrm{m}}}{\mathrm{d}t^2}, \tag{3.35}$$

a linear relationship from switching time error to comb-drive energy change can be obtained if the nominal switching points are on the capacitance gradient plateau, e.g. $\sim 2^\circ < |\theta_m\left(\bar{t}\right)| <\sim 4^\circ$ for the used MEMS mirror variant (see Fig. 3.8), i.e.

$$\Delta E_{\mathrm{c}_i} \approx \frac{1}{2}V^2\left(\frac{\mathrm{d}C_\Delta\left(\theta_{\mathrm{m}}\left(\bar{t}_{\mathrm{off}}\right)\right)}{\mathrm{d}\theta_{\mathrm{m}}}\frac{\mathrm{d}\theta_{\mathrm{m}}\left(\bar{t}_{\mathrm{off}}\right)}{\mathrm{d}t}\Delta t_{\mathrm{off}_i} - \frac{\mathrm{d}C_\Delta\left(\theta_{\mathrm{m}}\left(\bar{t}_{\mathrm{on}}\right)\right)}{\mathrm{d}\theta_{\mathrm{m}}}\frac{\mathrm{d}\theta_{\mathrm{m}}\left(\bar{t}_{\mathrm{on}}\right)}{\mathrm{d}t}\Delta t_{\mathrm{on}_i}\right). \tag{3.36}$$

This is because at high oscillation amplitudes, the magnitude of the comb-drive capacitance derivative $\frac{\mathrm{d}C_\Delta(\theta_{\mathrm{m}})}{\mathrm{d}\theta_{\mathrm{m}}}$ and of the mirror angular velocity $\frac{\mathrm{d}\theta_{\mathrm{m}}}{\mathrm{d}t}$ are high and rather constant at the switching points, while that of the comb-drive capacitance curvature $\frac{\mathrm{d}^2C_\Delta(\theta_{\mathrm{m}})}{\mathrm{d}\theta_{\mathrm{m}}^2}$ and of the angular acceleration $\frac{\mathrm{d}^2\theta_{\mathrm{m}}}{\mathrm{d}t^2}$ are low.

The switching times $\bar{t}_{\mathrm{off}}$ and $\bar{t}_{\mathrm{on}}$ cannot be independently chosen, since the injected comb-drive energy has to match the dissipation in order to maintain the nominal amplitude in steady state and is given by Eq. (3.33). As the used MEMS mirror reaches high amplitudes only with positive phase delay, $\bar{t}_{\mathrm{off}}$ has to be after the zero crossing. Furthermore, phase margin should be secured not to cause a fallback bifurcation, where the mirror amplitude rapidly drops. In order to reduce the necessary driving voltage, $\bar{t}_{\mathrm{on}}$ is set such that the capacitance is minimum at the switching point, i.e. $C_\Delta\left(\theta_{\mathrm{m}}\left(\bar{t}_{\mathrm{on}}\right)\right) \approx C_\Delta\left(\bar{\Theta}_{\mathrm{m}}\right)$, which maximizes the injected energy. This has the effect that at high oscillation amplitudes, Δt_{on} in Eq. (3.34) has almost no influence since the associated derivatives of the capacitance are

small. As a result, a rather typical operation condition with 57% duty cycle at a nominal amplitude of 14° is obtained as shown in Fig. 3.15, where the driving voltage is switched off at the current plateau $\bar{I}_\mathrm{c}$. Therefore, Eq. (3.36) can be rewritten to

$$\Delta E_{\mathrm{c}_i} \approx \frac{1}{2} V^2 \frac{\mathrm{d}C_\Delta\left(\theta_\mathrm{m}\left(\bar{t}_\mathrm{off}\right)\right)}{\mathrm{d}\theta_\mathrm{m}} \frac{\mathrm{d}\theta_\mathrm{m}\left(\bar{t}_\mathrm{off}\right)}{\mathrm{d}t} \Delta t_{\mathrm{off}_i} = \epsilon_\mathrm{c}\, \Delta t_{\mathrm{off}_i} \tag{3.37}$$

which is a linear relationship with the comb-drive power constant ϵ_c. The comb-drive power constant can be easily measured by the comb-drive current, i.e.

$$\epsilon_\mathrm{c} = \frac{1}{2} V\, \bar{I}_\mathrm{c}\,. \tag{3.38}$$

Therefore, Eq. (3.37) is valid as long as the driving signal is switched off at the plateau of the current signal, where I_c is almost constant. Fig. 3.15 shows the measured signals around the nominal operation point with negative phase error Δt_ϕ in order to depict the definitions of the used variables. In the case of a constant 57% duty cycle driving signal, a driving period variation $\Delta T_{\mathrm{dr}_i} = T_{\mathrm{dr}_i} - \bar{T}_\mathrm{mh}$ effects the switching off time as

$$\Delta t_{\mathrm{off}_i} = \Delta t_{\phi_i} + 0.07\, \Delta T_{\mathrm{dr}_i} \approx \Delta t_{\phi_i}\,, \tag{3.39}$$

as the nominal phase delay corresponds to 7% of the nominal driving period. However, the contribution of ΔT_{dr_i} in Eq. (3.39) is rather small and is therefore neglected.

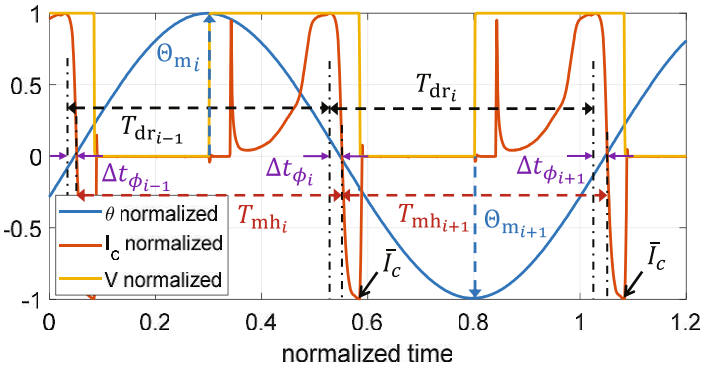

Figure 3.15.: Signals and definitions around the nominal operation point featuring a large linear range of the system dynamics at a negative phase error Δt_ϕ for illustration purpose. The driving signal is switched on at maximum deflection and switched off at the plateau of the displacement current $\bar{I}_\mathrm{c}$. The peak in the current signal I_c after the switching on, is an artifact of the measurement circuitry (see [172]).

In order to analyze the dynamic relation between amplitude and period changes of the MEMS mirror, the driving period is varied around the operation point. The response of the mirror is measured optically by a position sensitive detector and given in Fig. 3.16. Due to the elliptic shape of the measured response, it is evident that the mirror amplitude cannot solely depend on the mirror period. By realizing that not only the mechanical springs are influencing the stiffness of the mirror but also the comb-drives, the phase error at the beginning of the corresponding period has to be taken into account. Therefore, the suggested model for the measured response in Fig. 3.16 is

$$\Delta\Theta_{\mathrm{m}_i} \approx \kappa_\Theta \left(\Delta T_{\mathrm{mh}_i} + \kappa_\mathrm{c}\, \Delta t_{\phi_{i-1}}\right) = \kappa_\Theta\, \Delta T_{\Theta_i}\,, \tag{3.40}$$

where the amplitude scaling factor $\kappa_\Theta = -2.73 \cdot 10^5\,^\circ/s$ and the comb-drive stiffening parameter $\kappa_\mathrm{c} = 8 \cdot 10^{-3}$ are the fitted constants. The sign of κ_c shows that for positive phase errors, the mirror half period gets lower at the same amplitude, i.e. increasing the effective stiffness. As shown in Fig. 3.16, the model shows a good match to the measured data even at rather large deviations from the nominal operation point of about $\pm 0.4^\circ$ in amplitude. The timing error ΔT_Θ is introduced, as it provides a direct equivalent to the errors of the oscillation amplitude.

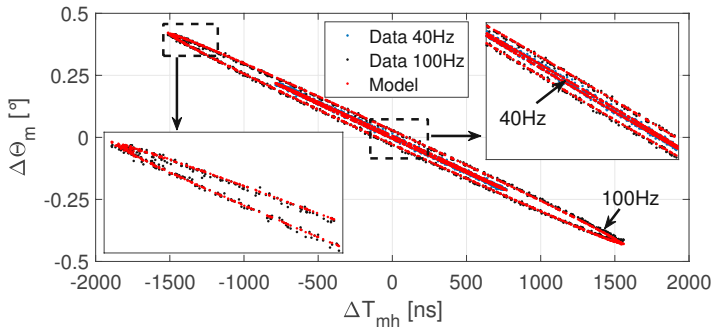

Figure 3.16.: Mirror amplitude over half period deviation at cyclic open loop driving period variation and linear model approximation. The open loop period is varied with 40 Hz or 100 Hz and 600 ns amplitude, which results in an elliptical amplitude over period behavior, measured by the optical setup (blue and black dots). The measured response can be fitted by the linear model Eq. (3.40) (red).

By using Eq. (3.37), (3.39) and (3.40), Eq. (3.31) can be rewritten as

$$\begin{aligned}&(\kappa_\mathrm{sp} + \kappa_\mathrm{d}) \left(\Delta T_{\mathrm{mh}_{i+1}} - \Delta T_{\mathrm{mh}_i} + \kappa_\mathrm{c} \left(\Delta t_{\phi_i} - \Delta t_{\phi_{i-1}}\right)\right) \\ &= (\kappa_\mathrm{sp} + \kappa_\mathrm{d}) \left(\Delta T_{\Theta_{i+1}} - \Delta T_{\Theta_i}\right) = \Delta t_{\phi_i} + \frac{1}{\epsilon_\mathrm{c}} E_{\mathrm{ext}_i} - \kappa_\mathrm{d}\, \Delta T_{\Theta_i}\,,\end{aligned} \tag{3.41}$$

where

$$\kappa_{\mathrm{sp}} = \frac{\kappa_\Theta}{\epsilon_\mathrm{c}}\, k(\bar{\Theta}_\mathrm{m})\, \bar{\Theta}_\mathrm{m} \quad \text{and}$$
$$\kappa_\mathrm{d} = \frac{\kappa_\Theta}{\epsilon_\mathrm{c}} \frac{\mathrm{d}E_\mathrm{d}(\bar{\Theta}_\mathrm{m})}{\mathrm{d}\Theta_\mathrm{m}} \tag{3.42}$$

are normalized spring and damping parameters.

Finally, with the evolution of the phase error defined by

$$\begin{aligned}\Delta t_{\phi_{i+1}} &= \Delta t_{\phi_i} + T_{\mathrm{dr}_i} - T_{\mathrm{mh}_{i+1}} \\ &= \Delta t_{\phi_i} + \Delta T_{\mathrm{dr}_i} - \Delta T_{\mathrm{mh}_{i+1}}\,,\end{aligned} \tag{3.43}$$

and Eq. (3.41), the linear small perturbation model can be written in an explicit discrete time-invariant state space form as

$$\begin{aligned}\begin{bmatrix}\Delta t_{\phi_{i+1}} \\ \Delta T_{\Theta_{i+1}}\end{bmatrix} &= \frac{1}{\kappa_{\mathrm{sp}} + \kappa_\mathrm{d}} \begin{bmatrix}(\kappa_{\mathrm{sp}} + \kappa_\mathrm{d})\,(\kappa_\mathrm{c}+1) - 1 & -\kappa_{\mathrm{sp}} \\ 1 & \kappa_{\mathrm{sp}}\end{bmatrix} \cdot \begin{bmatrix}\Delta t_{\phi_i} \\ \Delta T_{\Theta_i}\end{bmatrix} \\ &\quad + \begin{bmatrix}1 \\ 0\end{bmatrix} \Delta T_{\mathrm{dr}_i} + \frac{1}{\epsilon_\mathrm{c}\,(\kappa_{\mathrm{sp}} + \kappa_\mathrm{d})} \begin{bmatrix}-1 \\ 1\end{bmatrix} E_{\mathrm{ext}_i}\,, \\ \begin{bmatrix}\Delta t_{\phi_i} \\ \Delta \Theta_{\mathrm{m}_i}\end{bmatrix} &= \begin{bmatrix}1 & 0 \\ 0 & \kappa_\Theta\end{bmatrix} \begin{bmatrix}\Delta t_{\phi_i} \\ \Delta T_{\Theta_i}\end{bmatrix}\,.\end{aligned} \tag{3.44}$$

This model represents the MEMS mirror dynamic behavior under small disturbances, when it is driven with a fixed voltage and duty cycle around the nominal operation point defined by $\bar{\Theta}_\mathrm{m}$ and $\bar{T}_\mathrm{mh}$.

Summarizing, the local system dynamics can be linearized in a wide range if two conditions are met. First, the oscillation amplitude is high enough such that the comb-drive capacitance at maximum deflection is hardly changing by small amplitude variations, i.e. the combs are fully disengaging. Second, the driving voltage is switched on at the maximum deflection and off at the plateau of the displacement current. As the driving voltage and duty cycle can be adjusted such that the switching off is in the center of the current plateau, i.e. $\theta_\mathrm{m}(\bar{t}_\mathrm{off}) \approx 3^\circ$, a large linear range for the comb-drive energy injection can be provided. It has to be noted that the proposed model does not explicitly assume a hardening behavior of the MEMS mirror. Therefore, Eq. (3.44) can in general be also applied for softening mirrors [124–126], where a stable oscillation can be achieved by a duty cycle $< 50\%$, i.e. the switching off happens at the current plateau bevor the zero crossing of the mirror.

3.3.2. Linearized model parameter estimation

The linearized small perturbation model Eq. (3.44) has only three independent parameters that describe the dynamic behavior, which are κ_{sp}, κ_{d} and κ_{c}, as well as the input and output scaling factors ϵ_{c} and κ_{Θ}, respectively. The normalized parameters κ_{sp} and κ_{d} can be obtained by multiplying the individually identified parameters as given in Eq. (3.42). Also the comb-drive stiffening parameter κ_{c} can be estimated from measurements as shown in the previous section. An easier and more accurate method is to estimate the parameters from the measured dynamic response on an open loop driving period step, as shown in the following.

Three equations are needed in order to fully identify the state equation in Eq. (3.44). The first equation can be found by measuring the change in dissipated energy before and after the period step. An equivalent for the dissipated energy is the difference of the steady state phase errors before and after the step Δt_{ϕ_∞} as shown in Fig. 3.17. If the MEMS mirror is operated at the nominal operation point with $\Delta T_{\mathrm{mh}_0} = \Delta t_{\phi_0} = 0$ and jumps to a period $\Delta T_{mh_\infty} \neq 0$ and $\Delta t_{\phi_\infty} \neq 0$, then Eq. (3.41) with Eq. (3.40) yields

$$0 = \Delta t_{\phi_\infty} \left(1 - \kappa_{\mathrm{d}}\, \kappa_{\mathrm{c}}\right) - \kappa_{\mathrm{d}}\, \Delta T_{\mathrm{mh}_\infty} \,. \tag{3.45}$$

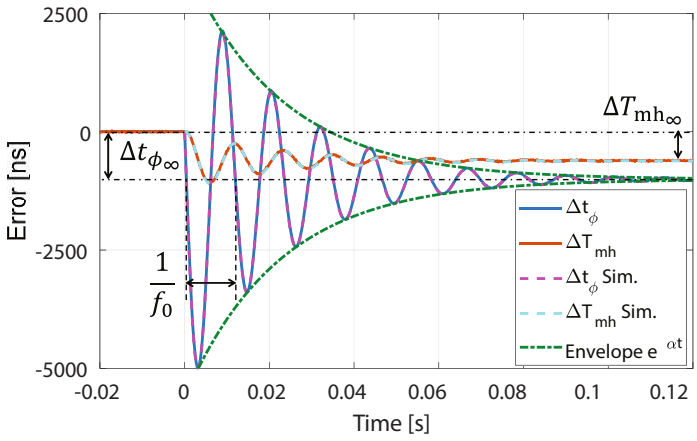

Figure 3.17.: Dynamic response on a 10 Hz open loop driving frequency step at the nominal operation point. The steady state offset Δt_{ϕ_∞}, the envelope $e^{\alpha t}$ and the oscillation frequency f_0 of the phase error are used for the model parameter estimation. The identified model (dashed lines) closely matches the measured response.

The two other equations are found by analyzing the dynamic response in Fig. 3.17. If λ is the complex conjugate eigenvalue of the model in Eq. (3.44) and an exponential function $e^{\alpha t}$ is fitted to the response envelope, it can be found

that

$$e^{\alpha \bar{T}_{\mathrm{mh}}} = |\lambda| = \sqrt{\frac{(1+\kappa_{\mathrm{c}})\ \kappa_{\mathrm{sp}}}{\kappa_{\mathrm{sp}}+\kappa_{\mathrm{d}}}}\,, \tag{3.46}$$

which represents the second equation. Furthermore, by measuring the oscillation frequency f_0 of the response, a third equation can be found as

$$\mathrm{Re}\left(e^{\alpha \bar{T}_{\mathrm{mh}} + j\,2\pi f_0 \bar{T}_{\mathrm{mh}}}\right) = \mathrm{Re}\,(\lambda) = \frac{\kappa_{\mathrm{c}}\,(\kappa_{\mathrm{sp}}+\kappa_{\mathrm{d}}) + \kappa_{\mathrm{d}} + 2\kappa_{\mathrm{sp}} - 1}{2\,(\kappa_{\mathrm{sp}}+\kappa_{\mathrm{d}})}\,. \tag{3.47}$$

The dynamic model parameters can be identified by combining Eq. (3.45), (3.46) and (3.47). The estimated parameters for the MEMS mirror used in this study are $\kappa_{\mathrm{sp}} = 52.91$, $\kappa_{\mathrm{d}} = 1.60$ and $\kappa_{\mathrm{c}} = 7.74 \cdot 10^{-3}$ and shows, that the dynamics are mainly influenced by κ_{sp}, which represents the ratio of potential energy gradient at maximum deflection and the comb-drive power constant. The reason why κ_{c} differs slightly from the previously identified value is because the measurements in Fig. 3.16 are more noisy and less accurate. The proposed method can be used to identify the MEMS mirror small perturbation dynamics by only measuring the phase error. However, to also fully identify the external disturbance input matrix as well as the output matrix in Eq. (3.44), the displacement current plateau and an oscillation amplitude measurement is needed according to Eq. (3.38) and (3.40).

3.3.3. Linearized external vibration coupling

The external vibration coupling analysis in Section 3.2.4 reveals that the vibration can be considered in a linearized model by a vibration-induced energy per half period, i.e. $E_{\mathrm{ext}} = \Delta E_{\mathrm{v}}$ according to Eq. (3.23). As a period-to-period model cannot distinguish negative from positive vibration frequency offsets, the amplitude of ΔE_{v} is assumed independent of the vibration frequency. This does not allow to account for the asymmetry regarding the sign of the vibration frequency offsets, e.g. the zero at large negative frequency offsets in Fig. 3.10, but covers the regions of high vibration influence accurately. Fig. 3.18 shows the frequency response comparison of $\mathrm{T_Y}$ vibration using the linearized model and the nonlinear model reprinted from Fig. 3.10 with absolute frequency offset. The linearized model correctly represents the phase behavior of one branch of the nonlinear model corresponding to positive frequency offsets, while the other shows some mismatches due to not considered zeros in the response. However, those mismatches are in regions with a low response and therefore do not cause much errors. Hence, both the response of the phase delay Δt_ϕ and the amplitude representative timing error ΔT_Θ using Eq. (3.44) agree with the nonlinear simulation using Eq. (3.14) in the frequency band of high influence, i.e. around the resonance. The amplitude representative timing error for the nonlinear simulation is calcu-

lated using the amplitude errors and the phase delays according to Eq. (3.40). At regions with low amplitude errors, i.e. at low and high frequencies, the phase of the amplitude representative timing error is more governed by the phase of the phase delay and bends up or down as Eq. (3.40) contains the phase delay of the previous period. Since the response to T_Z vibrations around twice the mirror frequency has similar local dynamics but a lower amplitude, it is not separately shown here. Hence, the most sensitive regions for T_Y or potential R_X vibrations around the mirror frequency as well as for T_Z vibrations around twice the mirror frequency can be represented by the same linearized dynamic model.

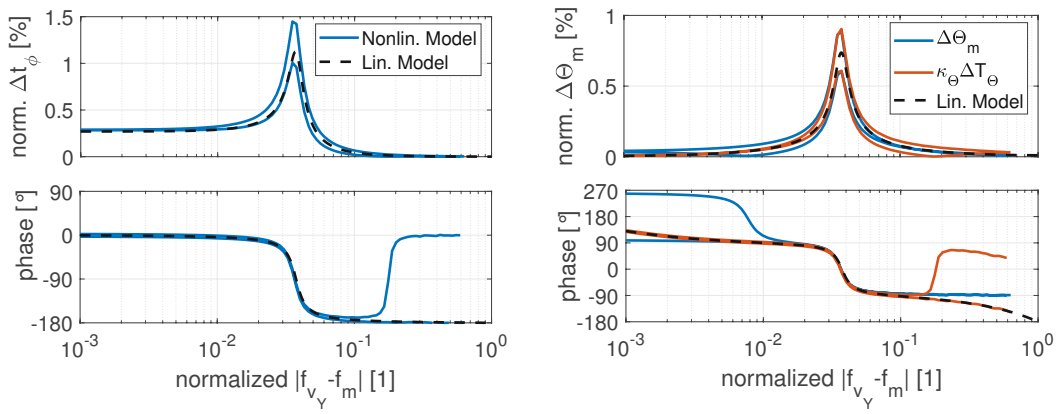

(a) (b)

Figure 3.18.: Vibration frequency response comparison of nonlinear and linearized MEMS mirror model. The values are normalized by the nominal mirror half period and nominal amplitude for time and angle values, respectively.

3.3.4. Linearized model verification

In this subsection the obtained linearized model of the MEMS mirror given by Eq. (3.44) is verified by measurements and the variation of the model parameters by the operation points are discussed.

Linearity and model accuracy

The validity of the linear small perturbation model Eq. (3.44) can be checked by measuring a bode plot from the driving period input to the corresponding outputs. However, this does not prove the proposed linearity as the superposition theorem is not verified. Therefore, the driving period is not swept, but randomly varied. Fig. 3.19 shows that the measured transfer functions agree with the derived model. The increase of the measured high frequency amplitudes of ΔT_{mh} is because it is

calculated by the subtraction of two adjacent phase errors and the corresponding driving period according to Eq. (3.43) and therefore originates from measurement noise. In order to validate also the output equation in Eq. (3.44), the mirror amplitude spectrum is measured via a position sensitive detector and shown in Fig. 3.20. Since all three outputs show the dynamic behavior of the proposed model for small perturbations, the model correctly represents the MEMS mirror at the nominal operation point.

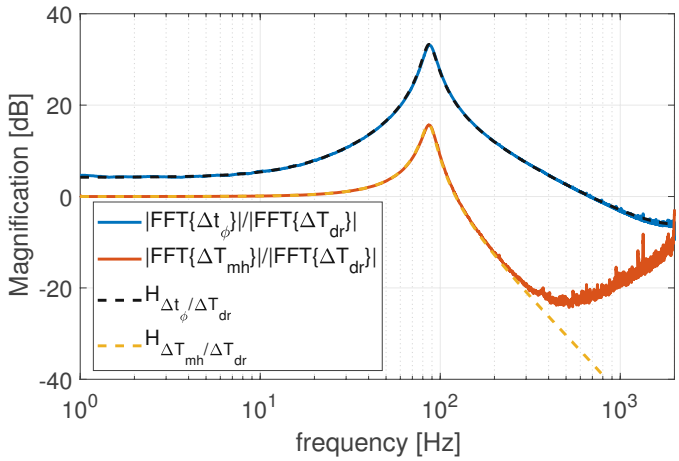

Figure 3.19.: Transfer functions of phase error and mirror half period at open loop random driving period variation. The applied driving period and the measured phase error are logged at each period for 180 s. The obtained spectrum is smoothed for better readability (MATLAB function *smooth* with a 2 Hz span). The transfer functions $H_{\Delta t_\phi/\Delta T_{\mathrm{dr}}}$ and $H_{\Delta T_{\mathrm{mh}}/\Delta T_{\mathrm{dr}}}$ of the model closely match the measurements. The increase of the red curve at high frequencies is due to measurement noise as ΔT_{mh} is calculated by the subtraction of two adjacent phase errors.

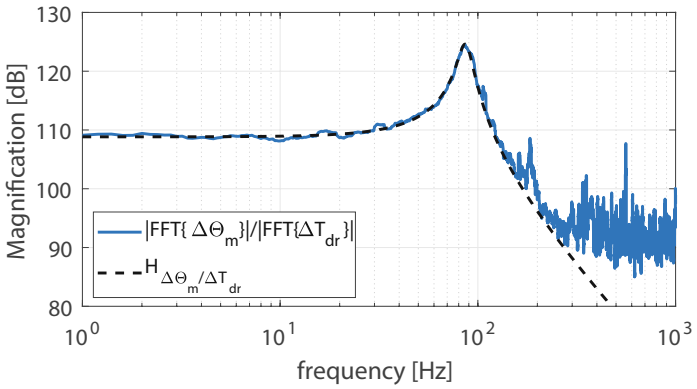

Figure 3.20.: Transfer function of mirror amplitude error at random driving period variation. The driving and the optical sensing signals are logged via the data acquisition card with 200 kHz for 5 s. The obtained spectrum is smoothed with a 2 Hz span for better readability. The measurement noise is rather high but the trend closely matches the transfer function $H_{\Delta\Theta_m/\Delta T_{\mathrm{dr}}}$ obtained by the model Eq. (3.44). The peaks above 100 Hz are measurement artifacts as they change by different sampling frequencies.

Operation point dependencies

As advanced control concepts are designed based on the proposed linear model, it should be analyzed how the local system dynamics change by the operation point. Therefore, the model parameters are estimated at different operation points, and compared to the nominal case. Two approaches are chosen as the extreme cases. In the first case the driving signal voltage V_{p} is kept constant and the duty cycle $D \in [0, 1]$ is adjusted such that the phase delay fulfills the condition

$$t_\phi = (D - 0.5)\, T_{\mathrm{dr}} \tag{3.48}$$

at each frequency point. Hence, the driving signal is always switched on at maximum deflection, while the switching off depends on the duty cycle, i.e. the operation point. In the second case, the duty cycle is kept constant and the driving signal voltage is adjusted such that the same condition is met. Fig. 3.21 shows the resulting relative variations of the three model parameters for both cases. It reveals that a constant driving voltage changes the system parameters less compared to a constant duty cycle. Even if the operation point frequency changes by -4%, which corresponds to an amplitude change of about -20%, the parameters κ_{sp} and κ_{d} vary in the first case only by about 4% and 8%, respectively. However, for larger deviations from the nominal operation point the model parameters rapidly change. The rather large variation of κ_{c} is hardly influencing the system dynamics as can be seen in Fig. 3.22, where the change

of the system pole characteristics are shown. The magnitude of the eigenvalue stays almost constant, while the characteristic frequency given by $f_0\,T_{\mathrm{mh}}$ varies similarly to κ_{sp} and κ_{d}. Hence, it can be concluded that the duty cycle control influences the system dynamics less than driving voltage control and therefore allows a robust control design considering parameter variations.

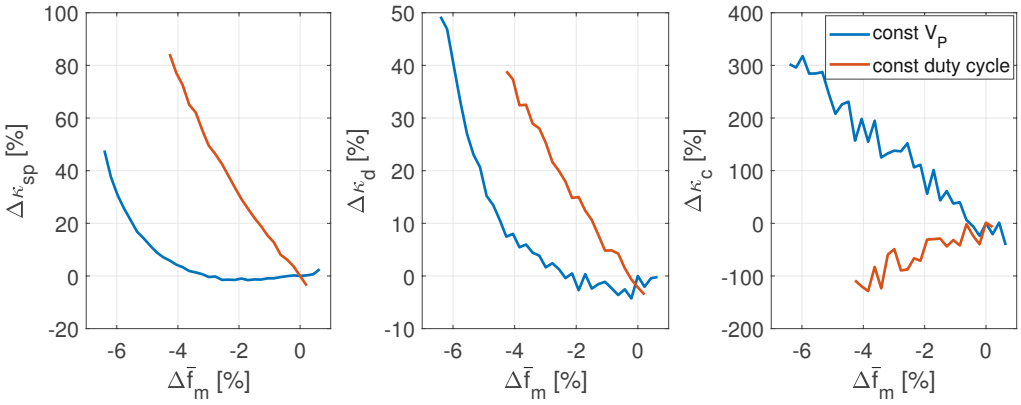

Figure 3.21.: Variation of the identified model parameters with the operation point. To fulfill Eq. (3.48) at every operation point two extreme cases are shown, i.e. constant driving voltage with adjusted duty cycle (blue) and constant duty cycle with adjusted driving voltage (red).

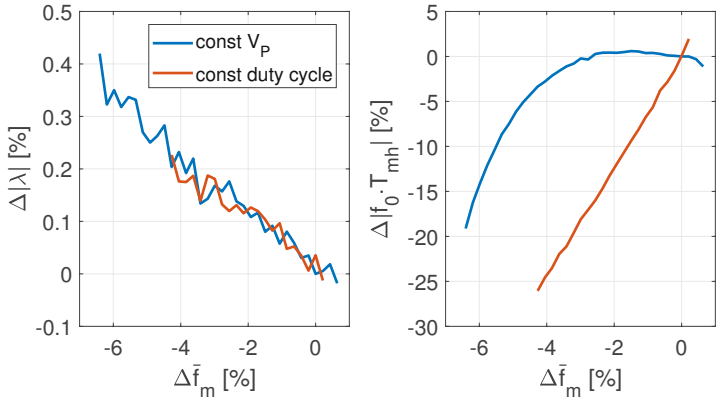

Figure 3.22.: Variation of the measured model dynamics with the operation point.

3.4. Mode coupling of MEMS mirrors

A rigid MEMS mirror rotor has in general 6 DoFs as shown in Fig. 3.23. Since it is intended to oscillate only at its desired rotational axis $\mathrm{R_X}$, all other DoFs

have to be suppressed by design. Hence, modes which cause the rotor to move in an undesired DoF should not be excited and their corresponding resonance frequencies have to be fairly above the R_X mode. However, in [90] a nonlinear and temperature dependent coupling between the R_X and the R_Z mode is observed for their MEMS mirror design. Furthermore, the MEMS mirror typically exhibits structural modes at higher frequencies, which deform the rotor. In general a full decoupling of all modes is hardly possible, especially if the mirror shall be tuned to its maximum performance, e.g. high frequency and tuning range, dynamical flatness and strong actuation including nonlinearities in the design. In this section two observed parasitic modes of the used MEMS mirror are discussed, the translational mode in Y direction T_Y and the comb-drive arm mode, which both occur during normal operation. While the first can be regarded as a rigid body mode of the rotor, the second is a structural deformation mode within the rotor, i.e. the comb-drive arms. Other modes, can be prevented by design using dedicated suspensions or can only be excited by applying a driving voltage at the corresponding resonance frequency, such that unwanted modes, e.g. T_Z and R_Z, should not be excited during normal operation.

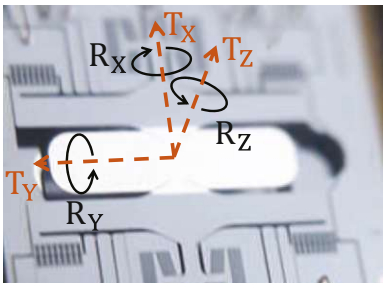

Figure 3.23.: Illustration of the 6 principal DoFs of a MEMS mirror rotor.

3.4.1. R_X-T_Y mode coupling

Besides direct actuation of a parasitic mode by the comb-drives, also a mode coupling can occur, where energy of the first mode is drained to the second. Fig. 3.24 shows a frequency up-sweep through the top response curve of a MEMS mirror, where kinks and jumps are observed in both the amplitude and the phase delay at locations depending on the driving voltage. A similar phenomenon is observed by sweeping through the bottom response curve, while it is not shown in the figure for visibility. As shown in Fig. 3.25a the response passes a hysteresis if the driving frequency is swept down after the kink. Fig. 3.25b depicts the measured trajectories just before and after passing the kink, where the difference of both trajectories reveals a relatively strong fifth harmonic oscillation. As the measured trajectory distortion is the biggest at the point ▲ and vanishes just after passing

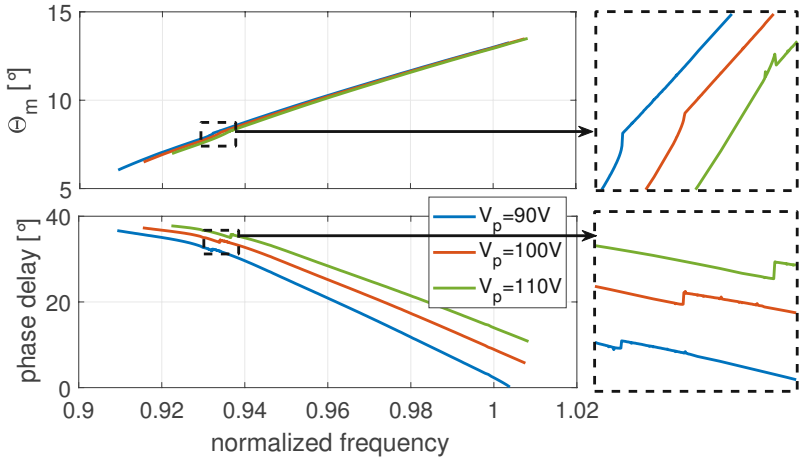

Figure 3.24.: Up-sweep through the top response curve using different voltages of the square wave driving signal. Kinks and jumps in amplitude and phase delay can be observed at different locations depending on the driving voltage. The frequency is normalized by a typical operation point.

it, i.e. at ▼, we associate the first as a resonance point and the second as a fallback bifurcation.

Herein the mirror amplitude Θ_m is the peak deflection during one oscillation cycle and the frequency is defined by every other zero crossing. Due to the nonlinear stiffness and the comb-drive torque, Θ_m is in general not equal to the first harmonic amplitude, as also higher harmonics exist. Hence, for the following analysis the variable $\Theta_{m,j}$ represents the j-th harmonic amplitude, which are derived by a harmonic decomposition of the trajectory. Fig. 3.26 shows the first and the fifth harmonic amplitude when sweeping through the R_X-T_Y hysteresis using different driving voltages. As shown, the response of $\Theta_{m,1}$ is different from Θ_m and the hysteresis curve can be clearly observed. Furthermore the fifth harmonic exhibits a strong stiffening behavior as it shows the characteristic bifurcation jumps in phase and amplitude. The phase of the fifth harmonic ϕ_5 is its relative phase shift regarding the first harmonic, where $5 \cdot 360^\circ$ correspond to one period of the first harmonic.

R_X-T_Y model derivation

The observed coupling phenomena originates from the lightweight design of the MEMS mirror. A thicker reinforcement structure on the backside of the mirror shifts the center of mass away from the rotation axis, whose out-of-plane position

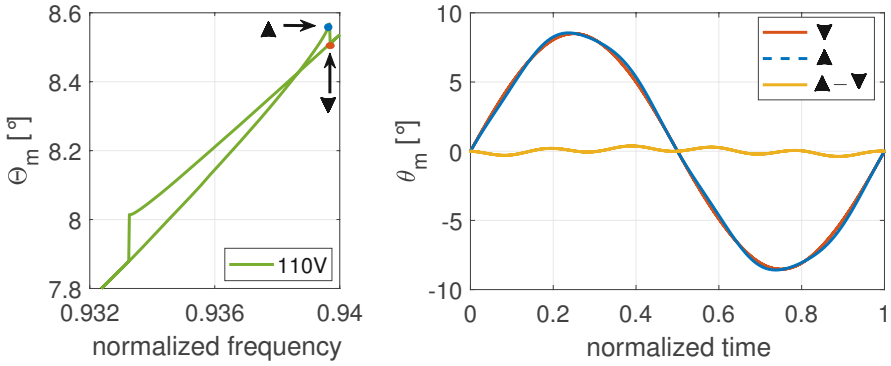

(a) (b)

Figure 3.25.: Measured hysteresis of the frequency response (a) and trajectory distortion (b) due to the R_X-T_Y mode coupling. After passing the kink, the frequency is swept down to obtain the hysteresis. At the resonance point ▲, the trajectory shows a strong fifth harmonic distortion compared to the trajectory at the fallback ▼.

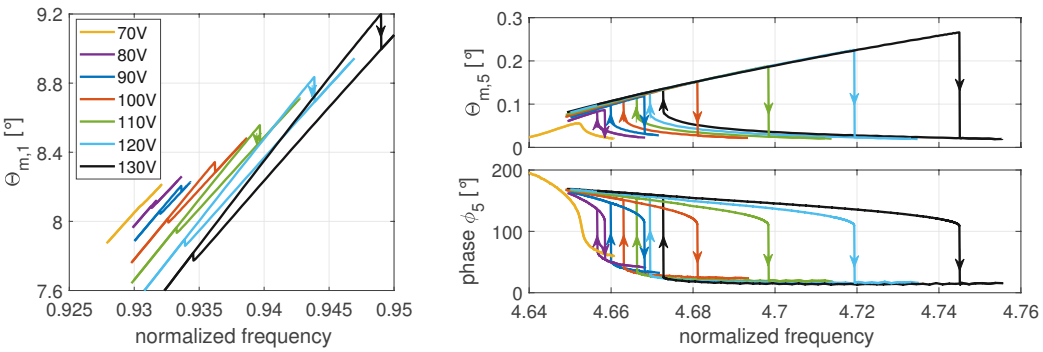

(a) (b)

Figure 3.26.: Measured first (a) and fifth (b) trajectory harmonic when sweeping through the R_X-T_Y hysteresis. The amplitudes are derived by harmonic decomposition of the trajectory. The phase of the fifth harmonic shows its relative phase shift regarding the first harmonic. Arrows indicate the direction of the bifurcation jumps.

is mainly determined by the thinner suspensions. Fig. 3.27a shows a schematic cross-section of the MEMS mirror, illustrating the shifted center of mass by L_m. This means that the MEMS mirror acquires a rotating unbalance, which is usually not affecting the proper mirror operation. A simplified mechanical model of the $\mathrm{R_X}$-$\mathrm{T_Y}$ coupling phenomena is shown in Fig. 3.27b. The rotational mode is modeled as a 1 DoF pendulum with the state θ_m and oscillates within a coordinate system frame $\mathcal{F}$ that can move in $\mathrm{T_Y}$ direction with the state y relative to the global coordinate system. The actual coupling happens due to the inertial forces, that the acceleration of the mass within the frame $\mathcal{F}$ causes in the global coordinate system and vice versa.

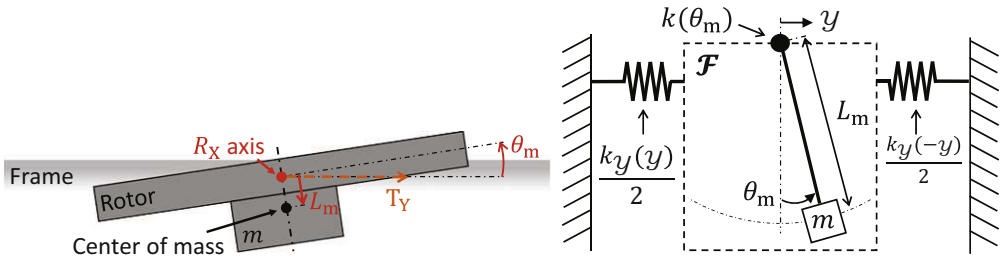

(a) (b)

Figure 3.27.: Illustration of the shifted center of mass from the rotation axis (a) and a schematic of the $\mathrm{R_X}$-$\mathrm{T_Y}$ coupling model (b). The thick reinforcement structure on the backside of the mirror shifts the center of mass away from the rotation axis. The $\mathrm{R_X}$-$\mathrm{T_Y}$ coupling model comprises a pendulum fixed inside a coordinate system frame $\mathcal{F}$, which can move in $\mathrm{T_Y}$ regarding the global coordinate system.

Another coupling mechanism can be caused by the comb-drives, as the capacitance and therefore its derivative may depend on both θ_m and y. However, due to the symmetric comb-drive design as shown in Fig. 3.28 it only has a marginal dependency on y. This is because the capacitance change on the left side of the rotation axis is compensated by the right side as illustrated by the changed overlaps between stator and rotor combs. Only fringe effects at the edges of the combs can cause a total capacitance change due to a y movement, which add only small additional actuation forces for the $\mathrm{T_Y}$ and can be neglected. While the total capacitance change is subtle, a difference in left and right side capacitance is observed. Fig. 3.29a shows two exemplary current difference signals I_cLR obtained by subtracting the right side comb-drive currents from the left side at an operation point with a high and a low fifth harmonic amplitude. A considerable high frequency oscillation can be observed, which is in general not of a single harmonic due to the nonlinear capacitance dependency. It also shows that even if the fifth harmonic is low or absent, a small peak in the current difference is

measured, whose sign depends on the mirror scanning direction. As the exact capacitance dependency on both θ_m and y is not known, the current difference is hard to analyze. But the time derivative of the capacitance difference $C_{\Delta\mathrm{LR}}$ obtained by

$$\frac{\mathrm{d}C_{\Delta\mathrm{LR}}}{\mathrm{d}t} = \frac{I_{\mathrm{cLR}}}{V_\mathrm{p}}\,, \tag{3.49}$$

provides an insight, as its peak-to-peak value over a mirror period shows a quadratic relationship to the fifth harmonic amplitude as shown in Fig. 3.29b. The increase of the current difference by the fifth harmonic amplitude supports the proposed coupling model.

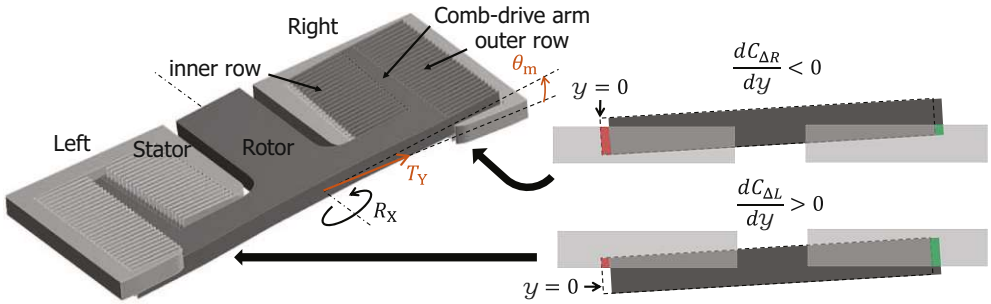

Figure 3.28.: Illustration of the comb-drive capacitance dependency regarding a $\mathrm{T_Y}$ movement. The capacitance decrease for $y > 0$ of the right side comb-drive arm is balanced by the increase of the left side arm.

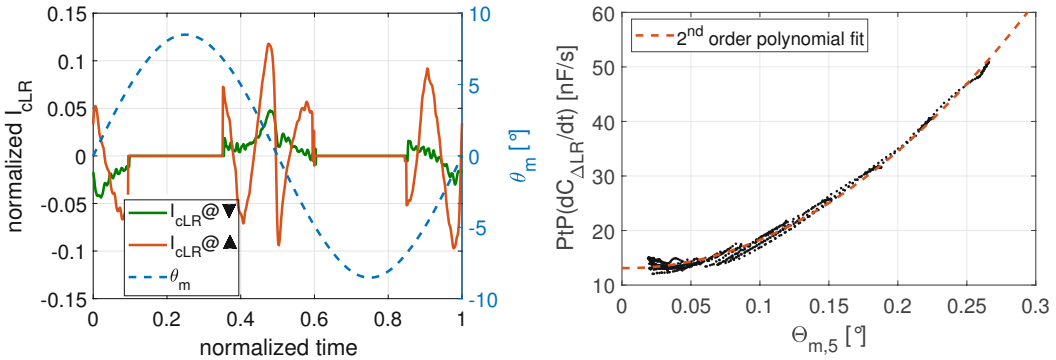

(a) (b)

Figure 3.29.: (a) Difference of left and right side current signals for an operation point with high ▲ and low ▼ fifth harmonic amplitude. The current signals are normalized by the corresponding maximum total current. (b) Peak-to-peak value of the left-right capacitance time-derivative calculated by Eq. (3.49) for all measurement points in Fig. 3.26 with a second order polynomial fit.

Finally, the R_X-T_Y coupling model can be expressed as

$$\begin{aligned} J\,\ddot{\theta}_\mathrm{m} + \hat{\gamma}(h)\,\dot{\theta}_\mathrm{m} + k\big(\theta_\mathrm{m}\big)\,\theta_\mathrm{m} + mL_\mathrm{m}\ddot{y} &= \tau_\mathrm{c}\big(V, \theta_\mathrm{m}\big) \\ m\ddot{y} + \gamma_y\,\dot{y} + k_y(y)\,y + mL_\mathrm{m}\ddot{\theta}_\mathrm{m} &= 0\,, \end{aligned} \tag{3.50}$$

where the rotational mode parameters are derived in Section 3.2 while the damping realization function h is the same as in Fig. 3.14. As the MEMS mirror is usually operated at amplitudes $< 20^\circ$, the direction dependency of the inertial forces are omitted due to $\cos(\theta_\mathrm{m}) \approx 1$ for all θ_m. The consequences of the inertial coupling in Eq. (3.50) can be qualitatively understood by a modal analysis, excluding damping, actuation and nonlinearities. Rewritten in a matrix form, the simplified model yields

$$\underbrace{\begin{bmatrix} J & mL_\mathrm{m} \\ mL_\mathrm{m} & m \end{bmatrix}}_{\mathbf{M}} \begin{bmatrix} \ddot{\theta}_\mathrm{m} \\ \ddot{y} \end{bmatrix} + \underbrace{\begin{bmatrix} k(0) & 0 \\ 0 & k_y(0) \end{bmatrix}}_{\mathbf{K_0}} \begin{bmatrix} \theta_\mathrm{m} \\ y \end{bmatrix} = 0\,, \tag{3.51}$$

where $k(0)$ and $k_y(0)$ are the corresponding linear stiffness values. The eigenvectors of the matrix $\mathbf{M}^{-1}\mathbf{K_0}$ then represent the new orthogonal modes, which are in general a composition of θ_m and y caused by the coupling. To calculate those modes, the effective mass m for the T_Y movement and the center of mass displacement L_m are obtained by FEM. The stiffness $k_y(0)$ can be roughly approximated by assuming that the uncoupled resonance frequency is five times higher than the R_X resonance, i.e.

$$k_y(0) \approx 5^2\,k(0)\,\frac{m}{J}\,, \tag{3.52}$$

as the measurements suggest. Using these values, the eigenvectors result to

$$\mathbf{v}_\theta = \begin{bmatrix} 1 \\ 5 \cdot 10^{-6} \end{bmatrix} \quad \text{and} \quad \mathbf{v}_y = \begin{bmatrix} 1 \\ -0.002 \end{bmatrix}\,, \tag{3.53}$$

which reveals that the low frequency mode corresponding to $\mathbf{v}_\theta$ is almost pure rotational, while the high frequency mode has a significant admixture of rotation and translation. This explains the observed strong fifth harmonic of the mirror trajectory, as the mirror rotates with an amplitude according to the coupling ratio $\kappa_y = -\frac{1}{0.002} = -0.029\,^\circ/\mu\mathrm{m}$. Furthermore, the mode coupling can be destructive for the comb fingers if they crash into the stator due to a too high y movement amplitude.

R_X-T_Y model identification

As the rotational mode is already identified, only the parameters of the translational mode are necessary to be estimated. FEM simulations predict the effective mass and dimensions such as the center of mass displacement rather accurately,

while it can be also estimated by a vibration test measurement as described in Section 3.2. The damping and nonlinear stiffness parameters suffer from manufacturing tolerances and have to be identified by measurements. First the nonlinear stiffness is estimated by matching the peak amplitude over frequency behavior for the different driving voltages, assuming a constant coupling ratio of the fifth harmonic κ_y at resonance. Due to the expected low damping and the rather weak non-linearities, this assumption does not limit the proposed method. The coupling ratio obtained by the eigenvector decomposition in Eq. (3.53) shows that for the fifth harmonic, the rotation and the translation movement have negative sign. Furthermore, it can be assumed that the stiffness has to be symmetric by design and can be approximated by a polynomial of up to second order, as for a Duffing oscillator. Hence, the equation of motion at the resonance peak can be simplified to

$$(m + mL_\mathrm{m}\,\kappa_y)\,\ddot{y} + k_{y0}\left(1 + \beta\,y^2\right)\,y = 0\,, \tag{3.54}$$

where the coupling ratio acts as an effective mass change. The resonance peak amplitude $\Theta_{\mathrm{m},5}\big|_{\blacktriangle}$ over frequency behavior can be approximated by

$$\omega_y\big|_{\blacktriangle} \approx \sqrt{\frac{k_{y0}}{m + mL_\mathrm{m}\,\kappa_y}}\sqrt{1 + \beta\,\frac{3}{4}\left(\frac{\Theta_{\mathrm{m},5}\big|_{\blacktriangle}}{\kappa_y}\right)^2}\,. \tag{3.55}$$

The derivation of this formula is provided in Appendix A. Using a least squares approach, k_{y0} and β can be calculated such that the measured and the estimated response match. However, the coupling ratio κ_y depends on the zero displacement stiffness $k_y(0) = k_{y0}$, while κ_y effects the estimation of k_{y0} and β. As this relationship is rather complex, the chosen identification algorithm performs an iterative refinement of the estimation, which quickly converges in the third iteration.

A simple method to identify the damping coefficient γ_y is by analyzing the total current through the comb-drives I_c during the driving voltage is on, as its time-integral relates to the total injected energy, i.e.

$$E_\mathrm{c}(t) = \int_0^t \frac{1}{2} V_\mathrm{p}\, I_\mathrm{c}(t)\mathrm{d}t\,. \tag{3.56}$$

Fig. 3.30a shows the current signal at the resonance peak and after the breakdown of the high frequency mode oscillation as well as their difference. It is clearly observed that the high fifth harmonic oscillation is also influencing the total current signal shape. The integration of the current difference over one period of the first harmonic yields the necessary additional injected energy ΔE_c to maintain the high amplitude of the fifth harmonic. By the different driving voltages, which result in different resonance amplitudes, Fig. 3.30b can be drawn. For compari-

son the dissipated energy at the corresponding first harmonic amplitude $E_{\mathrm{d},1}$ and its change due to the observed small first harmonic amplitude jump $\Delta E_{\mathrm{d},1}$ are shown, which are both calculated by the decay measurement from Section 3.2. Interestingly, the additional dissipated energy due to the coupling, i.e. ΔE_{c}, almost doubles the total energy loss at high fifth harmonic amplitudes, i.e. gets similar to $E_{\mathrm{d},1}$.

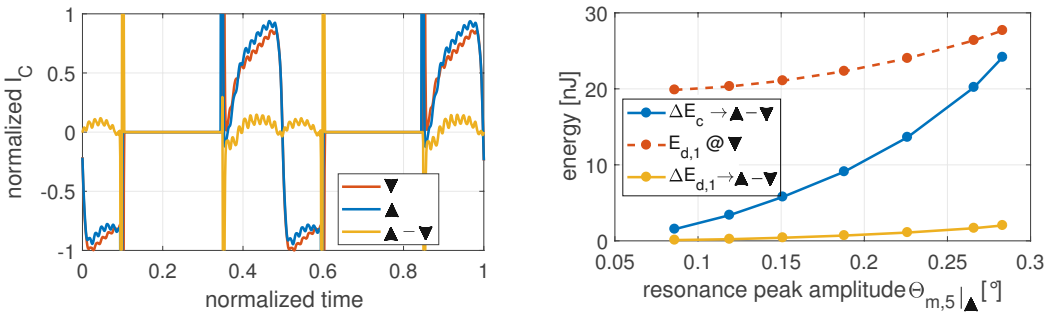

(a) (b)

Figure 3.30.: (a) Comb-drive current signals just before ▲ and after ▼ passing the $\mathrm{R_X}$-$\mathrm{T_Y}$ resonance peak. (b) Additionally dissipated energy per mirror period over the resulting peak fifth harmonic amplitude for different driving voltages. For comparison the dissipated energy $E_{\mathrm{d},1}$ for the pure rotational mode is shown.

By using the derivation in Appendix A for the dissipated energy per oscillation period for a Duffing oscillator, the damping coefficient γ_y can be estimated from

$$\frac{1}{5}\left(\Delta E_{\mathrm{c}} - \Delta E_{\mathrm{d},1}\right) = \pi \, \frac{1}{\kappa_y^2} \, \omega_y\big|_{▲} \gamma_y \left(\Theta_{\mathrm{m},5}^2\big|_{▲} - \Theta_{\mathrm{m},5}^2\big|_{▼}\right) , \tag{3.57}$$

where $\omega_y\big|_{▲}$ is the corresponding circular resonance frequency and $\Theta_{\mathrm{m},5}\big|_{▼}$ is the steady state amplitude after passing the resonance peak. However, the evaluation of Eq. (3.57) shows, that only for small amplitudes the damping coefficient is constant, as can be seen in Fig. 3.31a. The amplitude dependent behavior of the damping coefficient can then be estimated by the knowledge of its small amplitude value, i.e. $\gamma_{y,\mathrm{small}}$, as

$$\gamma_y = \frac{1}{\Theta_{\mathrm{m},5}^2\big|_{▲}} \left(\frac{\kappa_y^2 \left(\Delta E_{\mathrm{c}} - \Delta E_{\mathrm{d},1}\right)}{5 \, \pi \, \omega_y\big|_{▲}} + \gamma_{y,\mathrm{small}} \, \Theta_{\mathrm{m},5}^2\big|_{▼} \right) . \tag{3.58}$$

Since the results show only a moderate increase of about 10% in the measured range, the small angle damping coefficient is sufficient for the proper reproduction of the measured behavior in the simulation. The corresponding Q-factor

of about 470 corroborates the assumption of low damping. Fig. 3.31b shows the comparison of simulated and measured response of the fifth harmonic for different driving voltages. Discrepancies between the desired resonance peaks calculated by Eq. (3.55) and the simulation are mainly due to the simplified calculation of κ_y, which turned out to be about 1.5% higher by the nonlinearities in the model. Overall the derived model, which is identified without the need of time consuming a priori simulations, closely matches the measured response in phase and amplitude.

Finally the results reveal that the lightweight design of the MEMS mirror is the root cause of the coupling mechanism and the prominent stiffening behavior of the R_X mode increases the likelihood that the modes couple in resonance during the start-up of the mirror. This information helps MEMS designers to prevent undesired or even destructive operation modes by avoiding the corresponding frequency region. Furthermore, the undesired mode can be detected by the difference of left and right side comb-drive current and measures can be taken to avoid high amplitudes of such modes.

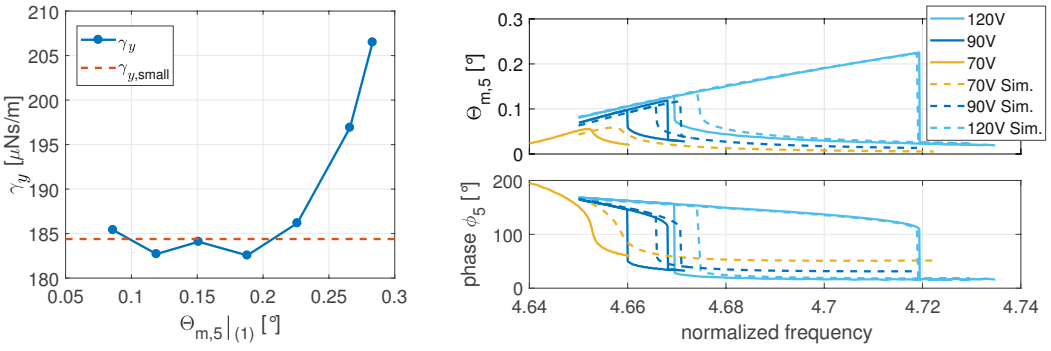

(a) (b)

Figure 3.31.: (a) Estimated damping coefficient of the T_Y mode. (b) Comparison of simulated and measured response of the fifth harmonic for different driving voltages.

3.4.2. Comb-drive arm mode

A strong electrostatic actuation requires a large overlap area of the comb-drives to maximize the capacitance variation. Therefore, the used MEMS mirror variants feature comb-drive arms, which have two rows of fingers as shown in Fig. 3.32. This introduces a deformation mode of the rotor as illustrated in the figure, which can be excited by the high frequency components of the electrostatic forces. Due to the high eigenfrequency of the mode, only relatively low movement amplitudes

and therefore no destructive behavior is expected. However, the current through the comb-drives during a constant driving voltage is used for several analysis as well as for feedback control, which is very sensitive to high frequency movements.

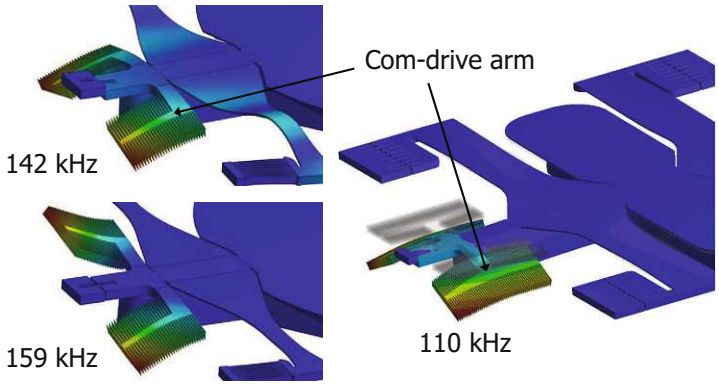

Figure 3.32.: Exemplary mode shapes and eigenfrequencies of comb-drive arm modes for two different designs. (courtesy of Stephan Albert, Infineon Technologies AG)

Assuming that the small arm movement does not effect the capacitance and can be modeled as an equivalent average angular movement θ_A of the comb fingers added to the rotational mode, the current signal for one of the four arms can be written as

$$I_\mathrm{c1} = \frac{1}{4} V_\mathrm{p} \frac{\mathrm{d}C_\Delta\left(\theta_\mathrm{m}\right)}{\mathrm{d}\theta_\mathrm{m}} \left(\dot{\theta}_\mathrm{m} + \dot{\theta}_\mathrm{A}\right) . \tag{3.59}$$

This reveals that the current signal is undistorted at mirror angles where the capacitance gradient is low, i.e. at zero and high angles according to Fig. 3.8b. Furthermore, the plateau of the capacitance gradient allows a simple estimation of the comb-drive arm movement amplitude, because it is wide enough to cover several oscillations of the mode. Because the mirror velocity has negligible spectral content higher than 100 kHz, the equivalent angular amplitude of the arm mode can be estimated by

$$\Theta_\mathrm{A} \approx \hat{I}_\mathrm{c1,A} \frac{4}{\omega_\mathrm{A} V_\mathrm{p} \bar{C}'_\Delta} , \tag{3.60}$$

where $\hat{I}_\mathrm{c1,A}$ and ω_A are the amplitude and circular frequency of the current signal associated with the comb-drive arm mode on the capacitance derivative plateau $\bar{C}'_\Delta$. Fig. 3.33 exemplary shows three operation points of the MEMS mirror with and without an excited comb-drive arm mode for a single arm. The obtained maximum equivalent amplitude of 14 mdeg is rather low and results in a ratio of average comb finger movement to its thickness of only about 0.05%. The individual currents generated by the four comb-drive arms can add up in phase

or out of phase in the summed current, hence they can increase by up to a factor of four or even cancel out. Due to manufacturing tolerances that shift the actual mode frequencies and the nonlinear actuation that lead to large and operation point dependent spectral content of the electrostatic forces, the excitation of a comb-drive arm mode can hardly be prevented by design. It can be reduced by avoiding the corresponding frequency content using an appropriate driving voltage or by filtering the measured current signal. Another possible solution is a reduced damping by lowering the pressure in the MEMS mirror package such that less actuation forces are needed and the comb-drive arms can be designed smaller.

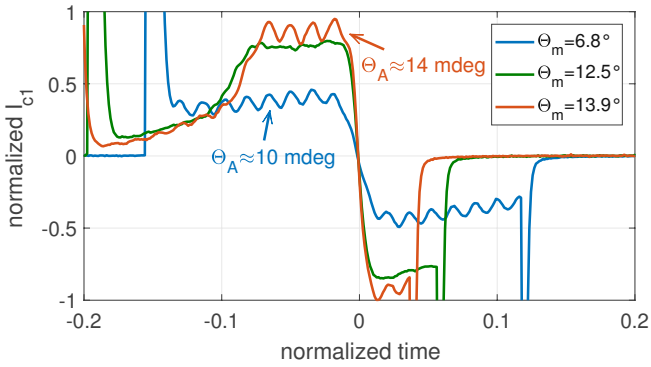

Figure 3.33.: Measured current signal at different operation points for comb-drive arm mode estimation. The high frequency oscillation can be clearly observed on the plateau of the capacitance gradient. The equivalent angular amplitude is estimated by Eq. (3.60) using the measured amplitude and frequency of the observed oscillations.

3.5. Summary

In order to obtain detailed knowledge of the behavior of resonant electrostatic MEMS mirrors and to design control concepts, modeling and identification methods are discussed in this chapter. First, an identification method for a generalized nonlinear SDoF model is proposed to characterize a single axis electrostatic resonant MEMS mirror without the need of prior knowledge on the used modeling parameters but solely measurement data. The high Q factor of resonant MEMS mirrors allows to estimate the nonlinear stiffness by matching the amplitude over frequency behavior along a decay measurement, assuming the system to be energy conservative. Subsequently the nonlinear damping is approximated by averaged damping coefficients for each period, which are assumed to be amplitude dependent. As a realization of the identified damping behavior a function h is introduced, representing the amplitude state during simulation. The comb-drive

capacitance and torque are estimated by a simultaneous measurement of the angle and the current through the comb-drives by an actuated decay. By a synchronized driving of the mirror and matching of injected and dissipated energy, the rotor inertia is calculated, enabling a full response simulation of the mirror. The derived nonlinear model is verified in time domain by introducing a period-based modified index of agreement, which results in values of over 0.995 at each period. The frequency response also shows a close match especially at the bifurcations, which have never been considered in the identification and highly depend on the system parameters. An external vibration coupling analysis reveals that not only torques aligned with the rotational mode R_X influence the MEMS mirror dynamics, but also translational vibrations in the plane of rotation, i.e. T_Y and T_Z. The translational vibration coupling happens as a reinforcement structure is used to improve the MEMS mirror performance. It causes a mismatch of the center of mass and the axis of rotation, allowing a tangential force to generate a torque. An energy injection analysis and measurements reveal that the most translational vibration influence is in T_Y direction close to the mirror scanning frequency. The second most influence is in T_Z direction close to twice the mirror scanning frequency, but with 10 times lower magnitude.

Second, a linear small perturbation model of the MEMS mirror at a nominal operation point is derived based on the law of energy conservation and is verified by measurements. It is found that the change of the injected comb-drive energy has a linear relation to the phase error, if the driving signal is switched off at the plateau of the comb-drive current and switched on at maximum deflection. Furthermore, the dynamic amplitude over frequency behavior of the MEMS mirror as well as external vibration coupling is linearly modeled, allowing conventional linear system theory analysis. The dynamic behavior of the MEMS mirror given by the system equation of the derived model can be fully identified by analyzing the obtained phase error at an open loop period step. Therefore, a controller that drives the MEMS mirror can identify the dynamic model by the proposed procedure and adjust the control gains to meet the desired specifications.

Finally, mode coupling phenomena of the MEMS mirror are analyzed, which reveals that two modes can occur during normal operation, i.e. a R_X-T_Y mode coupling and a comb-drive arm mode. The R_X-T_Y mode coupling is also a consequence of the shifted center of mass regarding the rotation axis and happens when the mirror trajectory includes a harmonic at the T_Y resonance. While the R_X mode is operated in parametric resonance due to the electrostatic actuation, the T_Y mode shows a typical Duffing oscillator response. An inertial coupling model is derived and identified by measurements, which correctly reproduces the observed nonlinear behavior. A modal analysis reveals that the resulting orthogonal modes are an admixture of angular and translational movement due to the inertial coupling. Hence, when the higher mode is excited it is observed in the

mirror trajectory with a coupling ratio of $-0.029\,^{\circ}/\mu$m, causing errors in application. The comb-drive arm mode is a rotor deformation mode caused by the bending of the rather large comb-drive arms designed for maximum capacitance variation. As the ratio of maximum movement of an average comb finger to its thickness is only about 0.05% there is no dynamic effect on the mirror motion nor a destruction of the combs. However, it causes a distortion of the measured current signal by its high frequency of $> 100\,$kHz, which has to be considered by design of the MEMS mirror or the sensing circuitry.

CHAPTER 4

Precision Sensing of Resonant MEMS Mirrors[1]

Precise and accurate sensing of the MEMS mirror movement is crucial for reliable operation in harsh environmental conditions. As only high frequency and high Q resonant operation of the MEMS mirror is considered, the trajectory shape is hardly influenced by the actuation forces nor by external vibration and is mainly determined by the suspensions [73, 175]. Hence, the trajectory can be reconstructed by measuring frequency and amplitude of the oscillation. Considering production cost and system integration complexity, optical read-out or dedicated sensing structures such as piezoresistive sensors on the MEMS should be avoided and self-sensing methods are preferred. Self-sensing uses the same structures for sensing and for actuation and provides the minimum system complexity at the cost of flexibility as driving and sensing are not independent. The proposed sensing concept utilizes the variation of the comb-drive capacitance to estimate the MEMS mirror movement. Specifically, the methods are based on measuring the current collected by the stator comb-drive electrodes, i.e.

$$I = V \frac{\mathrm{d}C\left(\theta_\mathrm{m}\right)}{\mathrm{d}\theta_\mathrm{m}} \dot{\theta}_\mathrm{m} + C\left(\theta_\mathrm{m}\right) \dot{V}\,, \tag{4.1}$$

which consists of the displacement current generated by the mirror movement and the measurement noise originating from driving voltage changes. Due to the capacitance symmetry of out-of-plane moving comb-drives, the displacement

[1] Parts of this chapter are also published in
[173] D. Brunner, H. W. Yoo and G. Schitter. "Precise phase control of resonant MOEMS mirrors by comb-drive current feedback". Mechatronics, 71:102420, 2020.
[174] D. Brunner, S. Albert, M. Hennecke, F. Darrer and G. Schitter. "Self-sensing control of resonant MEMS scanner by comb-drive current feedback". Mechatronics, 78:102631, 2021.

current is the same for negative and positive angles, which necessitates an intrinsic asymmetry for the scanning direction detection. In the following section, the sensing methods for phase, amplitude and direction detection are described for two different comb-drive designs, a single-layer (SL) and a double-layer (DL) design as illustrated in Fig. 4.1. The former has comb-drives consisting of a single layer with no asymmetry in the capacitance, while the latter has a thin layer stacked on a thick layer to provide capacitance asymmetry. Such a double-layer design is used for the development of a MEMS driver ASIC in [175] and is herein analyzed regarding the achievable performance. As all stator comb-drive electrodes and layers are isolated, either four or eight sensing electrodes are available, which are distinguished by top or bottom, left or right and front or back. Due to the time differentiation of the capacitance in Eq. (4.1), the displacement current also allows to detect higher order modes of the MEMS mirror as discussed in Section 3.4.

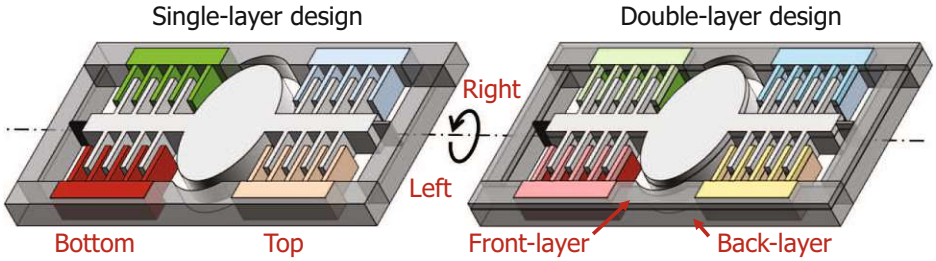

Figure 4.1.: Single- and double-layer comb-drive design illustration. The single-layer design provides four stator comb-drive electrodes separated into bottom or top and left or right. In the double-layer design a thin isolated layer is stacked to introduce asymmetry in the design. In total eight stator comb-drive electrodes are provided as front and back layer can be individually accessed.

4.1. Single-layer comb-drive design

The circuitry used for driving and sensing the MEMS mirror with single-layer comb-drives is shown in Fig. 4.2, where the comb-drives are modeled as variable capacitors. A single bit digital signal D_{HVact} controls the rotor potential via a MOSFET half-bridge generating an unipolar square wave driving voltage. The individually accessible stator combs are separated into left and right side and connected to transimpedance amplifiers (TIA) to measure the comb-drive current. The TIA outputs are both summed and subtracted in order to allow the detection of phase, amplitude and scanning direction. Fig. 4.3 shows measured sensing signals and illustrates the used variables for the following discussion.

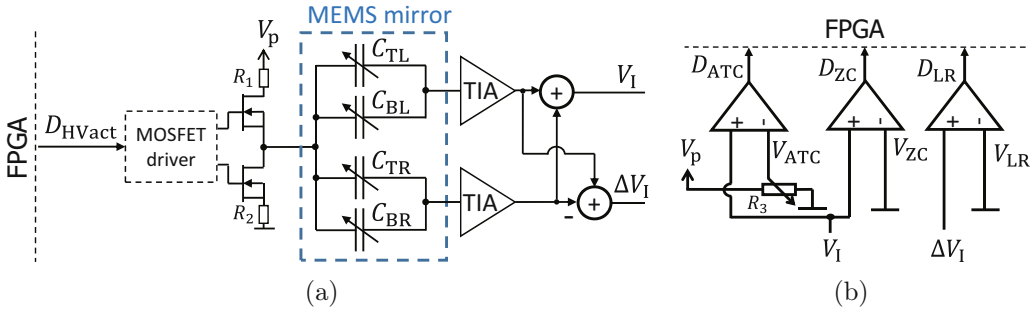

Figure 4.2.: Driving and sensing circuitry for a single-layer comb-drive design. (a) The rotor potential can be switched by D_{HVact}. The stator combs are separated into left and right side and connected to TIAs to measure the generated displacement current. (b) Circuitry for phase, amplitude and direction detection consisting of three comparators. The digital output signals of the comparators are directly connected to the FPGA pins where the controllers are implemented. The signal D_{ZC} is used for phase detection, D_{ATC} and D_{ZC} for amplitude detection and D_{LR} for direction detection.

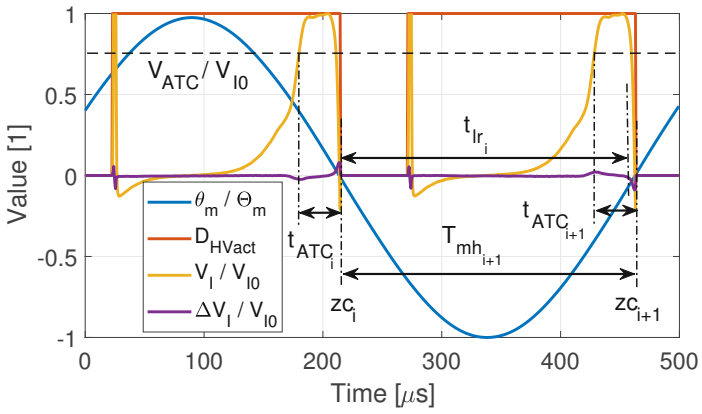

Figure 4.3.: Measured sensing signals for phase, amplitude and direction detection for a single-layer comb-drive design ($\Theta_{\mathrm{m}} = 13.75°$, $V_{\mathrm{I0}} = 1.377\,\mathrm{V}$, TIAs gain $G_{\mathrm{TIA}} = 45.16\,\frac{V}{mA}$). The summed comb-drive current signal V_{I} provides a precise zero crossing (zc) and amplitude timing value measurement (t_{ATC}). The difference current signal ΔV_{I} allows a direction detection due to a non-resonant $\mathrm{R_X}$-$\mathrm{T_Y}$ mode coupling. The sharp peaks in the summed current signal V_{I} are due to the fast driving voltage switching.

4.1.1. SL phase detection

Accurate phase detection is required to keep the pixel synchronization jitter low and to allow proper control. The proposed phase detector uses the sharp zero crossing of the measured displacement current when the mirror passes the zero angle position. The total capacitance between the rotor and stator comb-drive electrodes can be generally expressed as

$$C(\theta_\mathrm{m}) = C(0^\circ) + C_\Delta(\theta_\mathrm{m})\,, \tag{4.2}$$

where θ_m is the mirror rotation angle, $C(0^\circ)$ is the comb-drive capacitance at zero angle and $C_\Delta(\theta_\mathrm{m})$ is the variable capacitance with $C_\Delta(0^\circ) = 0\,\mathrm{F}$.
Besides the transient behavior at the switching of the square wave driving signal, the applied voltage $V \in [0, V_\mathrm{p}]$ between the comb-drive electrodes is constant, and the measured current can be expressed as

$$I_\mathrm{c} = V\,\dot{C}(\theta_\mathrm{m}) = V\,\frac{\mathrm{d}C_\Delta(\theta_\mathrm{m})}{\mathrm{d}\theta_\mathrm{m}}\,\dot{\theta}_\mathrm{m}\,, \tag{4.3}$$

where $\frac{dC_\Delta(\theta_\mathrm{m})}{d\theta_\mathrm{m}}$ is a pure geometrical parameter and $\dot{\theta}_\mathrm{m}$ is the angular velocity. Hence, a measurement signal is only obtained if the driving voltage is switched on. The variable comb-drive capacitance and its angular derivative are exemplary shown in Fig. 3.8b. The capacitance curve is an almost triangular function due to the change in overlap area of stator and rotor combs by the rotation.

It follows that the displacement current provides a zero crossing when the mirror crosses the position with the maximum capacitance, i.e. the zero angle position. Using this property, the simplest implementation of a phase detector is a comparator with a threshold corresponding to zero current, i.e. $V_\mathrm{ZC} = 0\,\mathrm{V}$, providing a digital signal D_ZC to the FPGA. As the MEMS mirror has two zero crossings per period, this method provides one precise phase measurement in each mirror half period. The phase detection jitter is then defined by the steepness of the current at the zero crossing, which can be calculated by

$$\dot{I}_\mathrm{c} = V_\mathrm{p}\left[\frac{\mathrm{d}^2C_\Delta(\theta_\mathrm{m})}{\mathrm{d}\theta_\mathrm{m}^2}\,\dot{\theta}_\mathrm{m}^2 + \frac{\mathrm{d}C_\Delta(\theta_\mathrm{m})}{\mathrm{d}\theta_\mathrm{m}}\,\ddot{\theta}_\mathrm{m}\right]. \tag{4.4}$$

The second term in the square brackets is negligible at $\theta_\mathrm{m} = 0^\circ$ since the capacitance gradient is zero and the inertial force is close to zero. The low inertial force can be shown by using the nonlinear parametric oscillator model derived in Section 3.2 as the spring, the damping and the actuation torque are low at the zero crossing. Due to the symmetric design, the angular velocity is maximum at the zero crossing and is equal to the velocity amplitude $\dot{\theta}_\mathrm{m}\big|_{\theta_\mathrm{m}=0^\circ}$. Therefore, the steepness of the current at the zero crossing scales with the product of the

applied voltage, the curvature of the comb-drive capacitance at zero angle and the squared angular velocity amplitude, i.e.

$$\dot{I}_\mathrm{c}\Big|_{\theta_\mathrm{m}=0^\circ} = V_\mathrm{p}\,\frac{\mathrm{d}^2 C_\Delta(\theta_\mathrm{m})}{\mathrm{d}\theta_\mathrm{m}^2}\Big|_{\theta_\mathrm{m}=0^\circ}\left(\dot{\theta}_\mathrm{m}\big|_{\theta_\mathrm{m}=0^\circ}\right)^2 . \tag{4.5}$$

Eq. (4.5) can be used to analyze how the noise on the current signal affects the phase detection uncertainty, i.e. the timing error between the actual zero crossing and the switching of the phase detection comparator. Assuming a constant additive Gaussian noise with a standard deviation σ_I on the current signal, the standard deviation of the phase error detection can be expressed as

$$\sigma_{\Delta \mathrm{t}_\phi} = \left(\dot{I}_\mathrm{c}\Big|_{\theta_\mathrm{m}=0^\circ}\right)^{-1}\sigma_\mathrm{I} = \left(V_\mathrm{p}\,\frac{\mathrm{d}^2 C_\Delta(\theta_\mathrm{m})}{\mathrm{d}\theta_\mathrm{m}^2}\Big|_{\theta_\mathrm{m}=0^\circ}\left(\dot{\theta}_\mathrm{m}\big|_{\theta_\mathrm{m}=0^\circ}\right)^2\right)^{-1}\sigma_\mathrm{I}\,. \tag{4.6}$$

Hence, the standard deviation scales inverse-proportionally with the squared mirror velocity.
For faster mirrors the same pixel synchronization uncertainty $\sigma_{\mathrm{t_{px}}}$ in general results in an increased optical pointing error, as

$$\sigma_{\theta_\mathrm{opt}} = 2\,\dot{\theta}_\mathrm{m}\,\sigma_{\mathrm{t_{px}}}\,, \tag{4.7}$$

where the factor 2 comes from the optical leverage and $\dot{\theta}_\mathrm{m}$ is the angular velocity at the corresponding pixel angle. In a PLL application, the pixel synchronization error depends on both the phase detection error as well as the PLL implementation, e.g. phase tracking errors and clock speed.

In the following, the theoretical achievable resolution of a scanning system with the proposed phase detection method is analyzed. It is assumed that the laser shooting is not limited by any clock speed and the driving signal jitter has no considerable effect on the MEMS mirror oscillation. Additionally, the PLL does not perform any filtering of the phase detection error, which is the worst case. According to Eq. (4.7) the maximum optical pointing error is where the angular velocity is the highest, i.e. $\dot{\theta}_\mathrm{m}\big|_{\theta_\mathrm{m}=0^\circ}$ at the zero crossing. There, the laser shot is triggered directly with the phase detection comparator switching and therefore the pixel synchronization error equals the phase detection error, i.e. $\sigma_{\mathrm{t_{px}}} = \sigma_{\Delta \mathrm{t}_\phi}$. Hence, the worst optical pointing uncertainty is given as

$$\sigma_{\theta_\mathrm{opt}} = 2\,\dot{\theta}_\mathrm{m}\big|_{\theta_\mathrm{m}=0^\circ}\,\sigma_{\Delta \mathrm{t}_\phi} = 2\left(V_\mathrm{p}\,\frac{\mathrm{d}^2 C_\Delta(\theta_\mathrm{m})}{\mathrm{d}\theta_\mathrm{m}^2}\Big|_{\theta_\mathrm{m}=0^\circ}\dot{\theta}_\mathrm{m}\big|_{\theta_\mathrm{m}=0^\circ}\right)^{-1}\sigma_\mathrm{I}\,. \tag{4.8}$$

Eq. (4.8) shows how the minimum pixel size of the scanning system depends on the MEMS mirror design parameters and the operation condition.

The pixel size d_{px} is given by the FoV divided by the number of pixels N_{px}, i.e.

$$d_{\mathrm{px}} = \frac{4\,\Theta_{\mathrm{m}}}{N_{\mathrm{px}}}\,. \tag{4.9}$$

Assuming a Gaussian distribution of the pointing error of a pixel defined by $\sigma_{\theta_{\mathrm{opt}}}$, the probability that the pixel error is not within $\pm d_{\mathrm{px}}/2$ can be calculated by

$$P_{\mathrm{out}} = \mathrm{erfc}\left(\frac{d_{\mathrm{px}}}{2\sqrt{2}\,\sigma_{\theta_{\mathrm{opt}}}}\right) = \mathrm{erfc}\left(\frac{4\,\Theta_{\mathrm{m}}}{N_{\mathrm{px}}\,2\sqrt{2}\,\sigma_{\theta_{\mathrm{opt}}}}\right)\,. \tag{4.10}$$

For high quality imaging, the pixel size should be much bigger than the worst optical uncertainty to keep the outlier probability low. In this investigation, the pixel size is chosen to be $10\,\sigma_{\theta_{\mathrm{opt}}}$. Hence, Eq. (4.10) calculates to

$$P_{\mathrm{out}} = \mathrm{erfc}\left(\frac{5}{\sqrt{2}}\right) = 5.73\cdot 10^{-7}\,, \tag{4.11}$$

where the optical pointing error of the worst pixel results in 0.1 outliers per operation hour, assuming a 50 Hz frame rate. The number of pixels is then

$$N_{\mathrm{px}} = \frac{4\,\Theta_{\mathrm{m}}}{10\,\sigma_{\theta_{\mathrm{opt}}}}\,. \tag{4.12}$$

Considering a phase detection method by using photo diodes, the laser crosses the diodes with higher speed for faster mirrors, leading probably to sharper edges of the sensing signal. Hence, the phase detection standard deviation $\sigma_{\Delta \mathrm{t}_\phi}$ scales inverse-proportionally with the mirror velocity. This theoretically results in a linear increase of the pixel number by the scanner amplitude but does not change with the scanning frequency as $\sigma_{\theta_{\mathrm{opt}}}$ is constant according to Eq. (4.7). However, with the proposed current sensing based phase detection, the number of pixels is obtained by combining Eq. (4.8) and Eq. (4.12), as

$$N_{\mathrm{px}} = \frac{1}{5}V_{\mathrm{p}}\left.\frac{\mathrm{d}^2 C_\Delta(\theta_{\mathrm{m}})}{\mathrm{d}\theta_{\mathrm{m}}^2}\right|_{\theta_{\mathrm{m}}=0^\circ}\left.\dot{\theta}_{\mathrm{m}}\right|_{\theta_{\mathrm{m}}=0^\circ}\Theta_{\mathrm{m}}\frac{1}{\sigma_{\mathrm{I}}}\,. \tag{4.13}$$

This shows that the scanning system resolution can be improved by increasing the product of the driving voltage, the curvature of the comb-drive capacitance, the mirror amplitude and angular velocity, i.e. the frequency. Furthermore, as the mirror velocity is proportional to the mirror amplitude, the number of pixels increases quadratically with the amplitude Θ_{m}. Therefore, the current sensing based phase detection provides higher efficiency for wide angle scanning compared to optical methods.

4.1.2. SL timing based amplitude error detection

Amplitude error detection and control is crucial as a fixed FoV has to be guaranteed during operation. The amplitude detection method is based on the time difference between two comparator threshold crossings, i.e. V_{ATC} and V_{ZC}, of the summed current signal V_{I}. This concept is named amplitude timing control (ATC) because a time difference , i.e. the amplitude timing value t_{ATC} is used in a feedback loop instead of a direct amplitude measurement. Assuming that the driving voltage is switched on and the mirror zero crossing happens at $t = 0\,\mathrm{s}$, the condition for the crossing of V_{ATC} with a TIA gain G_{TIA} can be expressed as

$$\frac{V_{\mathrm{ATC}}}{G_{\mathrm{TIA}}} \stackrel{!}{=} V_{\mathrm{p}} \frac{\mathrm{d}C_{\Delta}\left(\theta_{\mathrm{m}}|_{t=-t_{\mathrm{ATC}}}\right)}{\mathrm{d}\theta_{\mathrm{m}}} \dot{\theta}_{\mathrm{m}}|_{t=-t_{\mathrm{ATC}}}\,, \tag{4.14}$$

which represents a highly nonlinear relation with the comb-drive capacitance curve in Fig. 3.8b. The operator "$\stackrel{!}{=}$" is used herein to define a condition, i.e. both sides are only equal at specific parameter values. In order to judge the usability of a specific threshold voltage, the sensitivity of the amplitude timing value regarding amplitude changes, i.e.

$$S = \frac{\mathrm{d}\,t_{\mathrm{ATC}}}{\mathrm{d}\,\Theta_{\mathrm{m}}}\,, \tag{4.15}$$

Eq. (4.14) has to be analyzed. However, not only the sensitivity but also the uncertainty of the amplitude detection is of interest, as fast controllers need a high precision sensing. The precision of the detection signal depends on the local current gradient in Eq. (4.4) evaluated at both threshold crossings. Due to the high steepness of the current at the zero crossing of the mirror, the uncertainty is mainly determined by the less steep crossing of V_{ATC}. Therefore, the uncertainty scaling of the amplitude detection originating from noise on the current signal is

$$U = |\frac{\mathrm{d}\,\Theta_{\mathrm{m}}}{\mathrm{d}\,t_{\mathrm{ATC}}}|\,|\dot{I}_{\mathrm{c}}|^{-1}\Big|_{t=-t_{\mathrm{ATC}}} = |S\,\dot{I}_{\mathrm{c}}|^{-1}\Big|_{t=-t_{\mathrm{ATC}}}\,. \tag{4.16}$$

In order to calculate Eq. (4.15) and Eq. (4.16) for different thresholds and operation points, the mirror angle, velocity and acceleration at the crossing of V_{ATC} are necessary. For simplicity the MEMS mirror model is approximated by a conservative system with the equation of motion

$$\ddot{\theta}_{\mathrm{m}} + k_{\mathrm{n}}\left(\theta_{\mathrm{m}}\right)\,\theta_{\mathrm{m}} = 0\,, \tag{4.17}$$

where $k_{\mathrm{n}}\left(\theta_{\mathrm{m}}\right)$ is the normalized nonlinear spring stiffness obtained in Section 3.2. This approximation is valid as the quality factor of such MEMS mirrors is usually high, e.g. larger than 160 for this specific design. The velocity can then

be calculated by the energy conservation law since the sum of the kinetic and the potential energy have to be constant and equal to the total system energy, i.e.

$$\overbrace{\frac{1}{2}\dot{\theta}_\mathrm{m}^2}^{\text{norm. kinetic energy}} + \overbrace{\int_0^{\theta_\mathrm{m}} k_n\left(\theta_\mathrm{m}\right)\theta_\mathrm{m}\,\mathrm{d}\theta_\mathrm{m}}^{\text{norm. potential energy}} = \overbrace{\int_0^{\Theta_\mathrm{m}} k_n\left(\theta_\mathrm{m}\right)\theta_\mathrm{m}\,\mathrm{d}\theta_\mathrm{m}}^{\text{norm. total energy}} . \tag{4.18}$$

Therefore, the mirror velocity can be expressed as

$$\dot{\theta}_\mathrm{m} = \sqrt{2}\sqrt{\int_{\theta_\mathrm{m}}^{\Theta_\mathrm{m}} k_\mathrm{n}\left(\theta_\mathrm{m}\right)\theta_\mathrm{m}\,\mathrm{d}\theta_\mathrm{m}}\,, \tag{4.19}$$

which only depends on the mirror angle and amplitude. Subsequently, t_ATC can be calculated by simple integration of the inverse mirror velocity $\dot{\theta}_\mathrm{m}$ until the condition Eq. (4.14) is fulfilled. The sensitivity can then be obtained by slightly varying the amplitude Θ_m. The uncertainty can be calculated by evaluating Eq. (4.16) using Eq. (4.4), Eq. (4.17) and Eq. (4.19) and the corresponding sensitivity. By this the trade-offs between sensitivity and uncertainty can be analyzed.

Experimental validation

First, the threshold voltage V_ATC is varied at a typical operation point to obtain the amplitude timing values t_ATC, as shown in Fig. 4.4, which are in good agreement with the proposed model. The deviations at low threshold voltages are due to model errors, but also due to the low gradient and finite curvature of the current signal at the threshold crossing, which leads to a shift of the average value by noise. Therefore, the shift depends on the noise level, which is not desirable if the system is intended to operate in unknown environments with varying noise influences.

The sensitivity can be estimated by measuring the amplitude change, which causes the amplitude timing value t_ATC to change a fixed value, while the threshold voltage is constant. Fig. 4.5a shows the sensitivity over the threshold voltage, which again agrees well with the predicted behavior. It reveals that for threshold voltages smaller than 0.35 V the amplitude detection sensitivity increases up to -5.5 ns/mdeg, while higher voltages achieve only about -2 ns/mdeg.
Assuming a Gaussian additive noise on the current signal with a standard deviation σ_I, the uncertainty of the amplitude detection can be estimated by the standard deviation of the measured amplitude timing value σ_{t_ATC} and the corresponding sensitivity, according to Eq. (4.16). However, as the obtained amplitude timing noise is in the range of an FPGA tick (i.e. 10 ns), quantization effects have to be taken into account. Assuming that the quantization is uncorrelated with

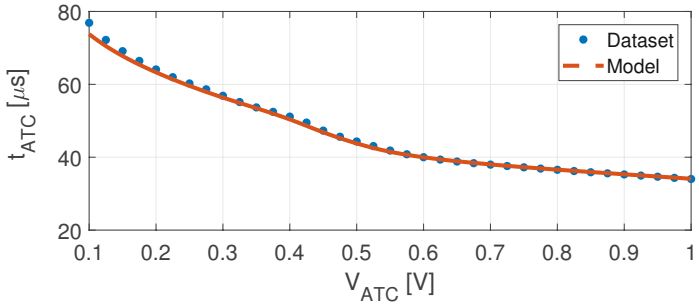

Figure 4.4.: Measured t_{ATC} and theoretical model over threshold voltage at a typical operation point of constant amplitude. Only at low threshold voltages a slight deviation from the model is observed.

the signal, the uncertainty model $\hat{U}$ and the measured uncertainty $\tilde{U}$ can be calculated by

$$\hat{U} = \sqrt{U^2 + \left(\frac{1}{S}\frac{\sigma_{\mathrm{qu}}}{\sigma_{\mathrm{I}}}\right)^2} \quad \text{and} \quad \tilde{U} = \frac{1}{|S|}\frac{\sigma_{t_{\mathrm{ATC}}}}{\sigma_{\mathrm{I}}}, \tag{4.20}$$

where S and U represent the original model while σ_{qu} and σ_{I} are fitting constants. Fig. 4.5b shows that the updated model matches the data with good agreement while deviations occur as the assumption of uncorrelated quantization may not always be true, especially at such low errors. This shows that the timing quantization of the measured amplitude timing value due to the FPGA clock is directly influencing the achievable accuracy and precision of the amplitude measurement. To overcome this a time-to-digital converter (TDC) can be used especially for faster mirrors, allowing timing resolutions in the pico-second range.

Finally, the results suggest to use a low threshold voltage as it provides a high sensitivity while the measurement uncertainty is kept low. However, in noisy environments the current signal curvature around the threshold crossing may cause a shift of the mean amplitude timing value, resulting in an amplitude change. If this cannot be compensated or avoided, a threshold between 0.6 V and 1 V should be chosen corresponding to approximately $45 - 70\%$ of the maximum current signal value at the plateau V_{I0} for the used operation point, resulting in a sensitivity of about -2 ns/mdeg.
It has to be noted that in general the optimal threshold voltage depends on the driving voltage and the operation point as V_{I0} changes. However, the threshold voltage can be made independent of the driving voltage by using a simple voltage divider as shown in Fig. 4.2. Hence, V_{ATC} scales the same as V_{I0} for every change in the driving voltage.

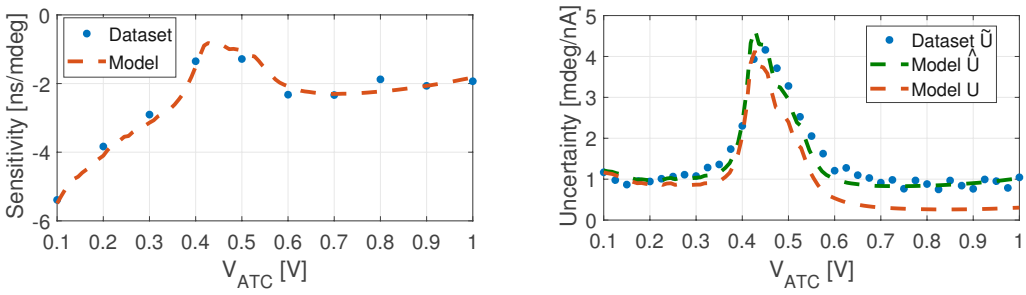

(a) (b)

Figure 4.5.: Measured and estimated sensitivity and uncertainty of the amplitude detection over comparator threshold voltage. (a) Sensitivity obtained by measuring the amplitude change for a 50 ns amplitude timing value step and the proposed model. (b) Uncertainty obtained by evaluating the measured amplitude timing noise and a comparison to the proposed model. As the FPGA clock is limited, an uncertainty model is fitted that takes the timing quantization into account ($\sigma_{\mathrm{qu}} = 11\,\mathrm{ns}$, $\sigma_{\mathrm{I}} = 6.2\,\mathrm{nA}$).

Robustness analysis

The amplitude detection threshold has to be well controlled as variations, e.g. due to thermal drifts, immediately relate to an amplitude error. With the uncertainty calculation in Eq. (4.16), a threshold variation of ΔV_{ATC} corresponds to an amplitude detection error of

$$\Delta\hat{\Theta}_{\mathrm{m}} = \frac{U}{G_{\mathrm{TIA}}}\,\Delta V_{\mathrm{ATC}}\,, \tag{4.21}$$

with $U/G_{\mathrm{TIA}} = 5.8\,\mathrm{mdeg/mV}$ at the used operation point and nominal threshold voltage $V_{\mathrm{ATC}} = 0.8\,V$. Hence, a drift by 1% of the nominal threshold corresponds to an amplitude change of 50 mdeg, which already violates the targeted resolution criterion of 0.1° optically. Similarly, a drift of the TIA gain results in amplitude errors. However, this can be avoided by either proper control of the corresponding parameters or by using a temperature sensor and a dedicated calibration scheme.

As many system parameters such as stiffness, inertia and capacitance curve of the MEMS mirror as well as the driving voltage and the TIA gain influence the relation between amplitude and amplitude timing value, an initial calibration may be necessary as those parameters vary by manufacturing tolerances. For example the actual scanning frequency at the same amplitude may not be constant for different mirrors due to a slightly different stiffness or inertia. Besides the variations of the mirror parameters by manufacturing also the dynamic changes

due to environmental influences such as temperature has to be considered [156]. Considering a variation of the normalized linear spring stiffness $k_{\text{small,n}}$ by $\pm 1\%$ with a fixed reference amplitude timing value $\bar{t}_{\text{ATC}}$ and threshold voltage, the amplitude detection error at the nominal amplitude can be estimated by

$$\Delta\hat{\Theta}_{\text{m}} = \frac{\bar{t}_{\text{ATC}} - t_{\text{ATC}}(k_{\text{small,n}})}{S}\,, \tag{4.22}$$

where $t_{\text{ATC}}(k_{\text{small,n}})$ is the obtained amplitude timing value. For the given variation and $V_{\text{ATC}} = 0.8\,V$ this results in a peak-to-peak error of 94 mdeg. When considering the effect of the scanning frequency to the threshold crossing condition given in Eq. (4.14), it can be guessed that a normalization of the amplitude timing value by the mirror half period reduces the influence of frequency changes. Hence, the reference value for nominal operation is then $\bar{r}_{\text{ATC}} = \bar{t}_{\text{ATC}}/\bar{T}_{\text{mh}}$ and the resulting amplitude detection error is expressed as

$$\Delta\hat{\Theta}_{\text{m}} = \frac{\bar{r}_{\text{ATC}} - \frac{t_{\text{ATC}}(k_{\text{small,n}})}{T_{\text{mh}}(k_{\text{small,n}})}}{S}\,, \tag{4.23}$$

which reduces the error to 29 mdeg peak-to-peak. This time normalization lowers the calibration effort considering production tolerances and the errors due to parameter drifts caused by environmental changes or degradation.

4.1.3. SL direction detection

Capacitive sensing methods with single-layer out-of-plane moving comb-drives usually have difficulties to determine the scanning direction as the capacitance variation is the same for positive and negative angles. In this section we propose a direction detection exploiting the coupling to a parasitic translational mode for lightweight MEMS mirrors with reinforcement structures as illustrated in Fig. 4.6a. Fig. 4.6b shows zoomed graphs at the mirror zero crossings of Fig. 4.3. As described in Section 3.4.1 the R_X-T_Y mode coupling generates an asymmetry, which results in a difference of the right and the left side comb-drive currents. The measured difference current signal ΔV_{I} shows distinct peaks at the zero crossings of the mirror with positive or negative voltage depending on the mirror movement direction. These peaks happen as the T_Y mode is actuated by a frequency well below its resonance, where the coupling model in Eq. (3.50) reveals that the y displacement is in phase with the rotation angle according to the eigenvector $\mathbf{v}_\theta$. This causes an increase in the left side comb-drive capacitance and a decrease in the right side, when the mirror changes from positive to negative angles, leading to a positive peak in the current difference. Therefore, a simple method to detect the scanning direction is to use a comparator with a threshold voltage V_{LR} at zero volt to evaluate the sign of the peaks. A robust concept for a PLL implementation in FPGA is to count a register up or down whenever the comparator output D_{LR}

is high or low, respectively and to read the register at the end of the evaluation window. As the evaluation window should be limited to a reasonable time span close to the zero crossing, its starting time can be arbitrarily defined as

$$t_{\mathrm{lr}_i} = \left(1 - 2^{-6}\right) T_{\mathrm{mh}_i} \,, \tag{4.24}$$

with the measured mirror half period T_{mh_i} and it ends at the next detected zero crossing, i.e. zc_{i+1}. For the proposed method even a quite weak coupling is sufficient. Thus a strong parasitic mode suppression by design is compatible with the method such that the scanner's operational robustness is not compromised.

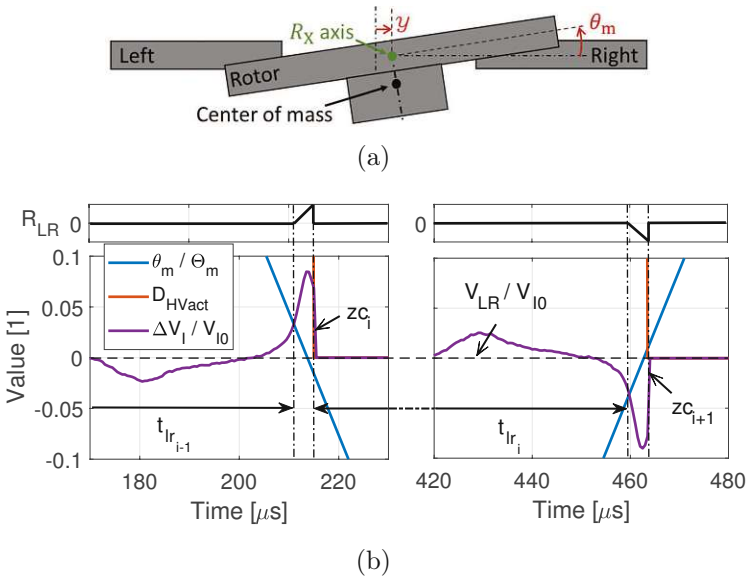

Figure 4.6.: (a) Principle illustration of MEMS mirror coordinate definitions. (b) Signals and definitions used for direction detection zoomed from Fig. 4.3. The subtraction of the left and the right current signals provides distinct peaks whose sign depend on the zero crossing direction. During the evaluation window defined by t_{lr} and the following zero crossing, the FPGA register $\mathrm{R_{LR}}$ counts up or down whenever the comparator output D_{LR} is high or low respectively.

4.2. Double-layer comb-drive design

The double-layer design provides several benefits in the detection of amplitude and direction. The circuitry used for driving and sensing the MEMS mirror with double-layer comb-drives is shown in Fig. 4.7. Despite the rotor combs also have two layers, both are connected to allow a single bit digital signal D_{HVact} to control the rotor potential for simplicity. The eight individual accessible stator combs are separated in front and back layer, where the front layer is further separated into left and right side. The TIA outputs are all summed to allow a precise phase detection, while the left and right side front layer signals are used for amplitude and scanning direction detection by the methods presented in this section. In Fig. 4.8a the obtained capacitance derivatives are depicted for the proposed configuration, where C_Δ is the sum of all capacitances to generate the signal V_{I} and $C_{\mathrm{LF}} = C_{\mathrm{TLF}} + C_{\mathrm{BLF}}$ and $C_{\mathrm{RF}} = C_{\mathrm{TRF}} + C_{\mathrm{BRF}}$. Fig. 4.8b shows a typical operation point with the corresponding sensing signals and illustrates the used variables for the following discussion.

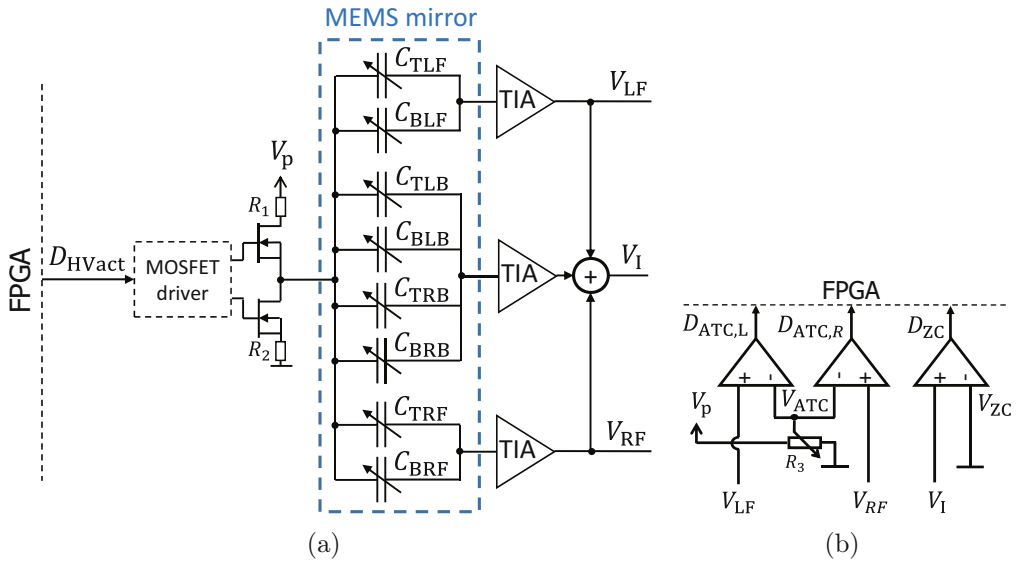

Figure 4.7.: Driving and sensing circuitry for a double-layer comb-drive design. (a) Both rotor layers are connected and controlled by D_{HVact}. The stator combs are grouped as depicted and connected to TIAs, where for example C_{TLF} means the top-left-front comb-drive capacitance. (b) Circuitry for phase, amplitude and direction detection consisting of three comparators directly connected to FPGA pins. The signal D_{ZC} is used for phase detection and with $D_{\mathrm{ATC,L}}$ and $D_{\mathrm{ATC,R}}$ for amplitude and direction detection.

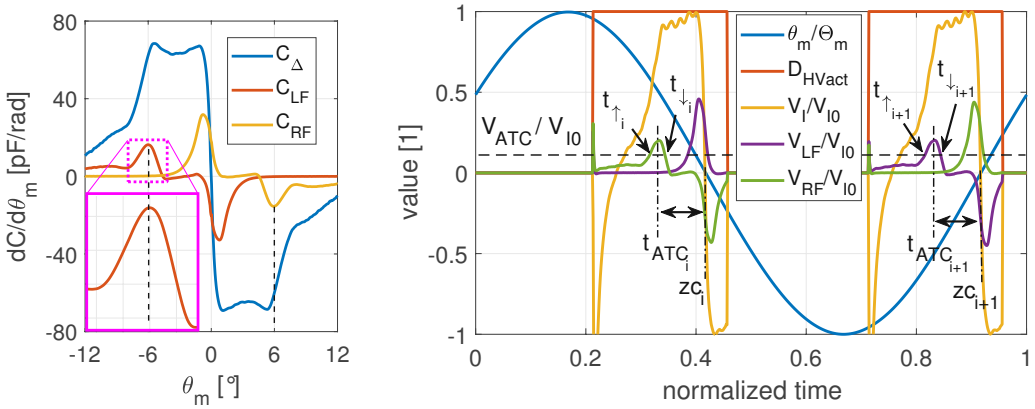

Figure 4.8.: Capacitance derivative and typical operation point signals for a double-layer comb-drive design. (a) Capacitance derivative of combs used for sensing. C_Δ is the sum of all combs and C_{LF} or C_{RF} are the sum of left or right side front-layer combs. C_{LF} and C_{RF} show distinct peaks in their derivatives at -6° and 6°, respectively. (b) Typical operation point and corresponding sensing signals. The asymmetry of C_{LF} and C_{RF} is used for direction detection, while for amplitude detection the peaks in the current signal at $\pm 6^\circ$ are used.

4.2.1. DL phase detection

The phase detection method is the same as for the single-layer design in Section 4.1.1 because all generated displacement currents are summed. Hence, all derivations and conclusions are the same.

4.2.2. DL timing based amplitude error detection

The double-layer design provides distinct peaks in the left and right side front layer capacitance derivatives at $\pm 6^\circ$ leading to peaks in the corresponding current signals as shown in Fig 4.8. Hence, a similar concept as the optical encoding using photo diodes can be used, where the amplitude is derived from the time between passing a fixed nonzero angle and the zero crossing of the mirror, i.e. the double-layer amplitude timing value t_{ATC}. This provides a clear advantage to the single-layer design as the amplitude detection is solely based on geometrically defined parameters. Assuming an almost sinusoidal trajectory of the mirror, a simple calculation of the mechanical amplitude can be obtained by

$$\Theta_{\mathrm{m}} = \frac{6^\circ}{\sin\left(2\pi f_{\mathrm{m}} t_{ATC}\right)} \,. \tag{4.25}$$

MEMS mirrors with a nonlinear spring torque slightly deviate from a pure sinusoidal trajectory, leading to a more complicated calculation. For example by using the energy conservation in Eq. (3.4) and Eq. (3.5) the amplitude for a certain frequency f_m and time t_{ATC} can be calculated but does not lead to an explicit form. However, above equation still provides a good approximation as the stiffness nonlinearities are typically relatively low.

The detection of a current signal peak, i.e. at $\pm 6^\circ$, in time necessitates an ADC with a high sampling rate and resolution or a differentiator, which is complex and susceptible to noise. Therefore, a detection based on a simple comparator with a threshold at the edges of the current signal peaks is used as shown in Fig. 4.8b. This provides two time instances $t_\uparrow$ and $t_\downarrow$, where the comparator output shows a rising and a falling edge, which can be used for peak time estimation. As shown in the inset of Fig. 4.8a the capacitance derivative peak has slightly asymmetric rising and falling slopes, which means that the peak time cannot be assumed to lie exactly between $t_\uparrow$ and $t_\downarrow$. Hence, the amplitude timing value for the double-layer design is expressed as

$$t_\mathrm{ATC} = G_\mathrm{Asym}\, t_\downarrow + (1 - G_\mathrm{Asym})\; t_\uparrow\,, \tag{4.26}$$

where $0 \leq G_\mathrm{Asym} \leq 1$ is the peak asymmetry gain and is optimally set to $G_\mathrm{Asym} = 0.65$ for the used MEMS mirror. Fig. 4.9a shows the obtained timing values using the model derived in the previous section. As can be observed, the amplitude timing value is almost independent of the chosen threshold voltage. The corresponding sensitivity plot obtained by Eq. (4.15) is shown in Fig. 4.9b. For the uncertainty estimation, Eq. (4.16) has to be modified as the ATC threshold is crossed two times, i.e. at $t_\uparrow$ and $t_\downarrow$. Assuming uncorrelated current signal noise at both crossings, the uncertainty can be expressed as

$$U = |S|^{-1} \frac{1}{\sqrt{\left(G_\mathrm{Asym}\, \dot{I}_\mathrm{c}\big|_{t=t_\downarrow}\right)^2 + \left((1 - G_\mathrm{Asym})\, \dot{I}_\mathrm{c}\big|_{t=t_\uparrow}\right)^2}}\,. \tag{4.27}$$

The results in Fig. 4.9b reveal that the sensitivity is almost the same as in the single-layer case with the chosen threshold voltage, while the uncertainty is at least 50 times lower. This is due to the insensibility to threshold changes and shows the benefit of this method.

Robustness analysis

As the amplitude timing value t_ATC changes only marginally by the threshold voltage (see Fig. 4.9a), the amplitude detection method for the double-layer design is rather insensitive to threshold or TIA gain drifts. Besides the peak asymmetry gain the amplitude detection method does not depend on the actual capacitance

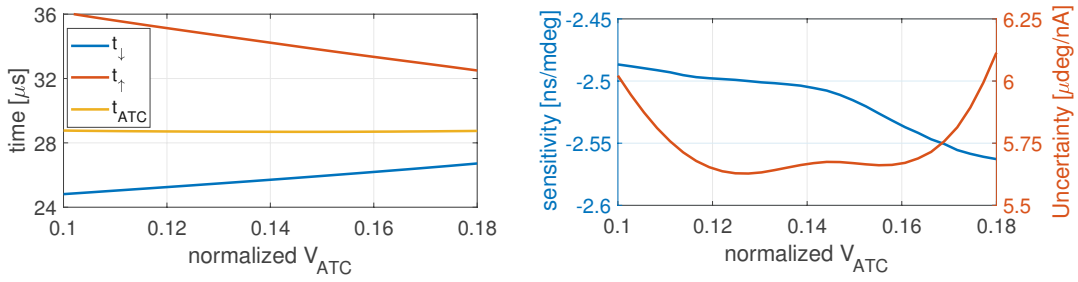

(a) (b)

Figure 4.9.: Simulated amplitude timing value with sensitivity and uncertainty of the amplitude detection over comparator threshold voltage. V_{ATC} is normalized by the maximum summed current signal plateau value V_{I0} (a) Timing of comparator rising and falling edge as well as amplitude timing value obtained by Eq. (4.26). (b) Sensitivity and uncertainty of the double-layer amplitude detection method.

curve and the amplitude timing value is solely defined by the mirror trajectory. Furthermore, the influence of amplitude detection errors due to scanning frequency changes are reduced. With the amplitude timing value normalization by the mirror half period as in Eq. (4.23), a normalized linear spring stiffness variation of $\pm 1\%$ results in only 6 mdeg peak-to-peak amplitude detection error, which is 5 times less than in the single-layer case.

4.2.3. DL direction detection

The detection of the scanning direction is simple as an asymmetry is introduced by the additional thin layer. One possible method is to evaluate whether V_{LF} or V_{RF} showed an amplitude detection peak as this reveals the sign of the trajectory. Similarly, $D_{\mathrm{ATC,L}}$ and $D_{\mathrm{ATC,R}}$ can be evaluated just before the zero crossing since large asymmetric peaks are observed in the current signals as shown in Fig. 4.8b.

4.3. Summary

Constraints as complexity, integrability, cost as well as robustness limit the choice of sensing methods for the targeted application. This chapter discusses a robust self-sensing method to detect the phase, amplitude and scanning direction of the mirror oscillation using the displacement current generated by the moving comb-drives, which are also used for actuation. The concepts are shown for two comb-drive designs, i.e. a single- and a double-layer design with the same total MEMS mirror size. In the single-layer design the stator and rotor combs consists of the same layer with high symmetry, while the double-layer design stacks

a thin front-layer onto a thick back-layer to introduce asymmetry. The phase detection method for both designs is based on detecting the sharp zero crossing of the summed current signal when the mirror crosses 0° and is independent of the chosen design. An analysis of the method reveals that the achievable optical resolution scales by the product of the driving voltage, the curvature of the comb-drive capacitance at 0°, the mirror amplitude and its maximum velocity.
The amplitude detection for the single-layer design is based on the time between the summed current signal reaching a comparator threshold and the subsequent zero crossing of the mirror. The sensitivity and uncertainty are analyzed with respect to the chosen threshold level, revealing that a level between 45% and 70% of the maximum current signal plateau value is preferable as it provides a good trade-off, resulting in a high sensitivity of about -2 ns/mdeg. The double-layer design utilizes a geometric feature, i.e. a capacitance gradient peak at $\pm 6^{\circ}$ of the front layer combs, to detect the amplitude by the time between the peak and the subsequent zero crossing of the mirror. The peaks are detected by the crossing of a comparator threshold showing a 50 times lower uncertainty regarding threshold variations compared to the single-layer design, while the sensitivity is similar. A robustness analysis reveals that the normalization of the measured time by the mirror period decreases the effect of parameter variations, e.g. stiffness variations due to manufacturing tolerances or temperature drifts, where the geometric detection method of the double-layer design also shows a 5 times better robustness than the single-layer design.
Phase and amplitude are measured in each half period of the MEMS mirror oscillation, while there is no information whether the half-swing is positive or negative. The intrinsic asymmetry of the double-layer design allows a simple direction detection, whereas the single-layer design has a high geometric symmetry of the capacitance. However, this symmetry can be broken by utilizing the mode coupling phenomenon that is implied by the lightweight MEMS mirror design using reinforcement structures and allows the scanning direction detection. Hence, the double-layer design adds cost and may allow less maximum stress due to the stacked layers, while it enables a more robust amplitude detection and direction detection for MEMS mirrors with no reinforcement structure or insufficient coupling.
The self-sensing concepts discussed in this chapter provide precise and robust feedback better than the targeted resolution of 0.1°, do not require any additional component at the MEMS mirror and use only simple circuitry. The analysis of the detection concepts is also applicable for other electrostatic resonant MEMS mirror designs and allows the performance estimation during the design phase of the mirror. Furthermore, it provides quantitative values for the hardware selection, such as required timing resolution, TIA gain settings and filters even before a manufactured and operational MEMS mirror is available.

CHAPTER 5

Closed Loop Control Design[1]

In precision scanning applications, such as automotive lidar providing safety relevant features, a correct and reliable operation during the whole lifetime is crucial. It has to be considered, that the MEMS mirror behavior varies due to manufacturing tolerances and dynamic influences caused by environmental changes. The former can be avoided by a calibration of the scanning system, while the latter necessitates proper control in the application. Environmental influences can be separated into slow drifts, such as temperature and pressure, and dynamic disturbances, such as vibrations or electromagnetic interferences.

In this chapter two approaches are discussed to enable a desired operation of the controlled MEMS mirror despite disturbances and nonlinearities. First, the digital-asynchronous PLL (DAsPLL) is proposed, which performs immediate phase compensation instead of frequency adjustments and therefore represents an unusual PLL design. The DAsPLL allows fast start-up and tracking of the MEMS mirror oscillation enabling also stabilization of open loop unstable operation points. Furthermore, it is used to demonstrate high precision scanning and to verify the derived sensing concept scaling laws in Chapter 4. Second, a time normalized digital PLL and an optimal loop filter design based on the linearized

[1]Parts of this chapter are also published in
[173] D. Brunner, H. W. Yoo and G. Schitter. "Precise phase control of resonant MOEMS mirrors by comb-drive current feedback". Mechatronics, 71:102420, 2020.
[174] D. Brunner, S. Albert, M. Hennecke, F. Darrer and G. Schitter. "Self-sensing control of resonant MEMS scanner by comb-drive current feedback". Mechatronics, 78:102631, 2021.
[157] D. Brunner, H. W. Yoo and G. Schitter. "Linear modeling and control of comb-actuated resonant MEMS mirror with nonlinear dynamics". IEEE Trans. Ind. Electron., 68(4):3315-3323, 2021.

period-to-period model derived in Section 3.3 are discussed for robust operation in harsh environments. The time normalization allows minimum programming effort for varying MEMS mirror parameters, such as scanning frequency.

5.1. Digital-asynchronous PLL

To motivate the digital-asynchronous PLL design, an analysis of the MEMS mirror energy injection using a square wave driving signal is discussed first. The injected comb-drive energy per driving signal period can be expressed as

$$E_\mathrm{c} = \frac{V_\mathrm{p}^2}{2}\left[C_\Delta\big(\theta_\mathrm{m}(t_\mathrm{off})\big) - C_\Delta\big(\theta_\mathrm{m}(t_\mathrm{on})\big)\right], \tag{5.1}$$

where t_off and t_on are the switching off and on time of the voltage V_p, respectively. Therefore, the injected energy for an oscillating mirror is only defined by these two time instances. In steady state, the dissipated energy is compensated by E_c and the corresponding switching times are the nominal values $\bar{t}_\mathrm{off}$ and $\bar{t}_\mathrm{on}$. Assuming the mirror is at a high amplitude such that the combs are fully disengaged at maximum angle, where the comb-drive capacitance depends only marginally on small amplitude variations as only fringe fields contribute to the capacitance. Then the influence of the driving signal jitter can be analyzed by the local time derivatives of Eq. (5.1). Using a Taylor approximation of up to the second order, the injected energy variation from the nominal case can be expressed as

$$\begin{aligned}\Delta E_\mathrm{c} \approx \frac{V_\mathrm{p}^2}{2}\Bigg[&\dot{C}_\Delta\left(\theta_\mathrm{m}\left(\bar{t}_\mathrm{off}\right)\right)\,\Delta t_\mathrm{off} + \ddot{C}_\Delta\left(\theta_\mathrm{m}\left(\bar{t}_\mathrm{off}\right)\right)\,\frac{\Delta t_\mathrm{off}^2}{2}\\ &- \dot{C}_\Delta\left(\theta_\mathrm{m}\left(\bar{t}_\mathrm{on}\right)\right)\,\Delta t_\mathrm{on} - \ddot{C}_\Delta\left(\theta_\mathrm{m}\left(\bar{t}_\mathrm{on}\right)\right)\,\frac{\Delta t_\mathrm{on}^2}{2}\Bigg],\end{aligned} \tag{5.2}$$

where Δt_off and Δt_on are the corresponding driving signal jitter. Using Eq. (4.3), Eq. (5.2) can be rewritten to

$$\Delta E_\mathrm{c} \approx \frac{V_\mathrm{p}}{2}\left[I_\mathrm{c}\left(\bar{t}_\mathrm{off}\right)\,\Delta t_\mathrm{off} + \dot{I}_\mathrm{c}\left(\bar{t}_\mathrm{off}\right)\,\frac{\Delta t_\mathrm{off}^2}{2} - I_\mathrm{c}\left(\bar{t}_\mathrm{on}\right)\,\Delta t_\mathrm{on} - \dot{I}_\mathrm{c}\left(\bar{t}_\mathrm{on}\right)\,\frac{\Delta t_\mathrm{on}^2}{2}\right]. \tag{5.3}$$

This shows the benefit of synchronized excitation, where the driving signal is switched on at maximum deflection and switched off at the zero crossing of the mirror. The current at both switching times as well as the current gradient at the switching on time are then almost zero, as can be seen by the current signal V_I in Fig. 5.1, leading to a low disturbance of the mirror motion by a driving jitter. However, the driving voltage should be accurately switched off at the zero crossing due to the high current gradient $\dot{I}_\mathrm{c}\left(\bar{t}_\mathrm{off}\right)$. The switching on time is more relaxed due to the low angular velocity around the amplitude point and the

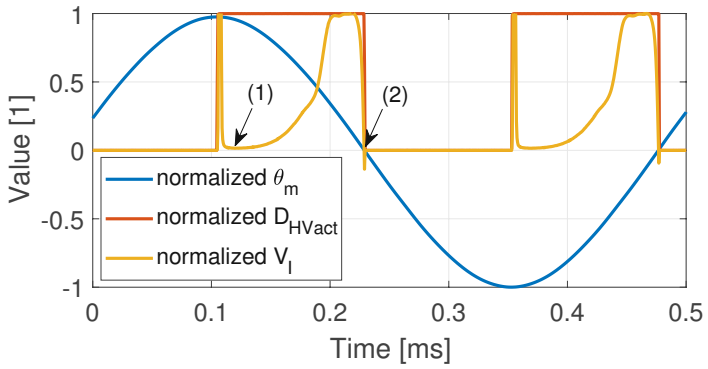

Figure 5.1.: Illustration of synchronized excitation. The negative edge of the digital driving signal D_{HVact} coincides with the zero crossing of the current signal V_{I} and with the zero crossing of the mirror exhibiting zero phase delay. As indicated by (2) the switching off current is low but with a high gradient. The current at the switching on is shown by (1) which is almost zero with a low gradient. The sharp peak before (1) is due to switching on the driving voltage and does not represent a comb-drive capacitance change.

resulting low currents.

5.1.1. Phase control

The principle implementation of the DAsPLL phase control is shown in Fig. 5.2. Two comparator signals D_{ZC} and D_{C1} are the inputs to the DAsPLL, which have negative edges at and slightly before the zero crossing of the mirror, respectively. The clock synchronized logic block measures the mirror period by adjacent zero crossing detections, using the comparator signals and provides a driving signal D_{HV} and a multiplexer control signal D_{MUX}. At a detected zero crossing, a counter is triggered that holds D_{HV} low for a quarter mirror period, which is derived from prior zero crossing detections. Subsequently, D_{HV} gets high again, waiting for the next zero crossing of the mirror. Hence, an internal clock based square wave signal is generated on the output D_{HV}, which keeps synchronized excitation.
To switch the driving voltage off accurately at the zero crossing of the mirror without internal clock dependency, an asynchronous multiplexer MUX is implemented. The negative edge of the first comparator signal D_{C1} is used to switch the asynchronous multiplexer such that it connects the zero crossing comparator signal D_{ZC} directly to the driving output D_{HVact} of the DAsPLL. Therefore, if the current signal hits the zero crossing comparator threshold, i.e. the mirror crosses 0°, the comparator signal is passed to the driving circuitry and switches

the voltage at the mirror off. After at least one clock cycle the multiplexer is switched back again and connects the synchronized driving signal D_{HV} to the driving output. Hence, for the asynchronous switching an additional comparator is necessary in the detection circuits for the single- and the double-layer designs, i.e. Fig. 4.2b and Fig. 4.7b, to provide the signal D_{C1} by a threshold crossing of the summed current signal V_{I}.

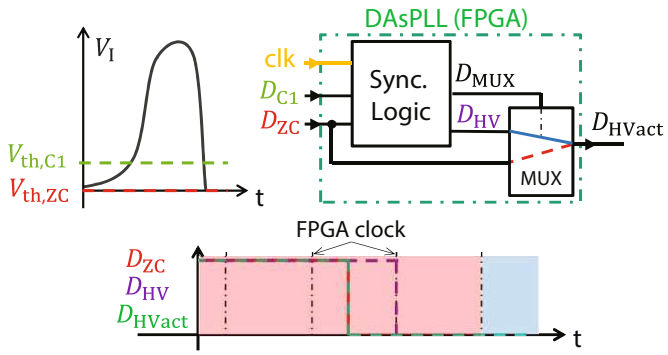

Figure 5.2.: Operation principle of the DAsPLL. (top-left) Illustration of a current signal V_{I} with comparator threshold values given by dashed lines. (top-right) DAsPLL scheme comprising a clock synchronized logic and an asynchronous multiplexer (MUX). The multiplexer is controlled by the synchronized logic and connects the driving output D_{HVact} directly to the zero crossing comparator signal D_{ZC} if a negative edge is detected on D_{C1}. (bottom) Asynchronous switching of the driving signal D_{HVact} without internal clock dependency.

The DAsPLL immediately compensates the phase error with a high precision and stabilizes the MEMS mirror with nonlinear dynamics. This is fundamentally different from conventional PLLs, which usually only adapt their frequency regarding the measured phase error [130]. The DAsPLL generates a driving signal directly linked to the MEMS mirror movement, which allows fast tracking of the mirror oscillation and spontaneously establishes synchronized excitation.

5.1.2. Fast start-up

A comb-drive actuated resonant MEMS mirror is only able to start at specific driving conditions, given by the so called stability regions [124, 125]. In general it reveals that the frequency region where the MEMS mirror can be started is limited and increases with the driving voltage and also depends on the duty cycle. An open loop start at constant driving frequency leads to a transient beating of the mirror amplitude and frequency until it converges to a steady state oscillation

with low amplitude as shown in Fig. 3.2. In order to achieve a fast and reliable start-up of the MEMS mirror to high amplitudes, the mirror behavior has to be either predictable, i.e. known in advance, or the control loop has to be closed as soon as possible. Due to the uncertain start of the oscillation as well as process variations and environmental influences, the mirror may be hardly predictable during the initial transient beating phase.

In case of current sensing based phase detection, the zero crossing is required to happen during the driving voltage is on, corresponding to a positive phase delay in Fig. 3.3. However, the stable point after an open loop start of the used MEMS mirror has typically a negative phase delay, meaning that the zero crossing is not detectable. Therefore, the driving frequency is usually slowly swept down in order to reach the bifurcation jump and to obtain a positive phase delay. The method in [176] achieves the bifurcation jump very fast by first applying a driving frequency where the mirror is able to start and after a specific time switching directly to the bifurcation frequency. As this is still an open loop method and the bifurcation frequency has to be known in advance, this method may not be reliable enough as environmental conditions can influence the bifurcation point. Furthermore, a subsequent slow frequency up-sweep is required to bring the mirror to high amplitudes, leading to rather long start-up times.

A faster and more reliable approach is to close the control loop already during the transient beating of an open loop start and to run the mirror to the maximum amplitude. The proposed method is shown in Fig. 5.3. Once a valid zero crossing of the current signal is detected, i.e. both comparator thresholds are crossed in the correct order and successively in time, the learning mode is started. During the learning mode the voltage is constantly on and the DAsPLL measures the mirror period by successive zero crossings of the current signal. After sufficient valid detections, the DAsPLL switches to the closed loop mode and runs the mirror to the maximum amplitude, by keeping zero phase delay. Except for the initial open loop start and the learning mode, this method represents the fastest possible start-up for a given maximum driving voltage as the energy injection per period is maximum. Furthermore, the proposed method does not require any knowledge about the MEMS mirror but only a rough frequency band where the mirror can be started. The square wave signal of the open loop start does not have to be a single frequency but can be mixed frequencies or a chirp in order to minimize the required prior knowledge about the MEMS mirror.
The learning mode is also applicable to minimize the re-lock time after loosing lock due to environmental influences to the MEMS mirror or its sensing, such as mechanical shocks or strong EMI. If an unusual behavior is observed, e.g. sudden changes of amplitude or phase, the DAsPLL returns to the learning mode and tries to synchronize on the mirror movement again.

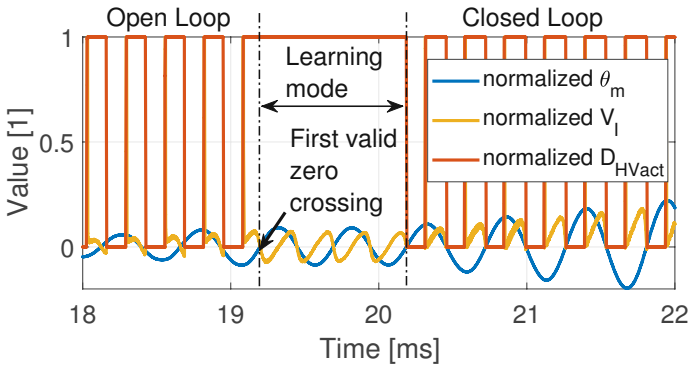

Figure 5.3.: Fast start-up method of the MEMS mirror using current sensing based phase detection. The MEMS mirror is started in open loop manner until a first valid zero crossing is detected in the current signal. After the learning mode, where the mirror frequency is measured, the loop is closed and the MEMS mirror is run to maximum amplitude.

The threshold of the comparator C1, $V_{\mathrm{th,C1}}$ in Fig. 5.2 has to be properly chosen based on the obtained current signal, the measurement noise and the internal clock of the DAsPLL. A higher threshold requires a higher current signal since it has to cross the threshold. A too low threshold, however, may increase the risk of false detections due to sensing noise, which may result in malfunctioning. Furthermore, the time between the crossing of the first comparator and the zero crossing comparator has to be at least one clock cycle to allow proper control of the multiplexer.

5.1.3. Amplitude control

As the DAsPLL phase control keeps zero phase with a fixed duty cycle, the mirror amplitude can vary by changes of environmental conditions [95], which necessitates an amplitude control. There are two possibilities for controlling the amplitude, i.e. either adjusting the supply voltage V_{p} [95] or the duty cycle [125] of the driving signal. As fast control requires a large bandwidth, the supply voltage control would increase the detection noise due to the differentiating behavior of the driving voltage to the comb-drive current (see Eq. (4.1)), which is not desirable. Therefore, the time when the driving voltage is switched on again after a detected zero crossing t_{on} is used to control the mirror amplitude. This concept is similar to the duty cycle control, while zero phase is kept, i.e. switching off of the driving voltage coincides with the mirror zero crossing. Control margin can be secured by using a duty cycle smaller or larger than 50%. However, an increased

duty cycle provides more measurement time, i.e. a longer time period where the driving voltage is on. Fig. 5.4a shows an operation point with 77% duty cycle, providing a reasonable control margin. Considering the effects of driving signal jitter on the energy injection given in Eq. (5.3), this operation point is still favorable as the current and the current gradient at the switching-on are rather low.

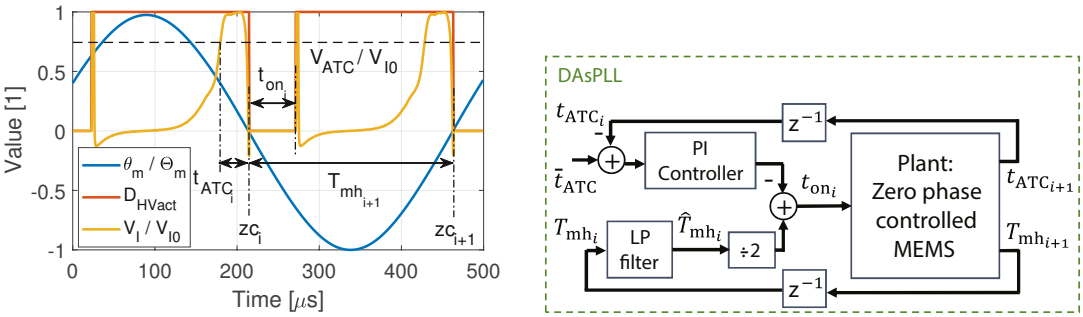

(a) (b)

Figure 5.4.: (a) Definitions and measured signals at a typical operation point ($\Theta_\mathrm{m} = 13.75^\circ$, 77% duty cycle). At a detected zero crossing (zc) the mirror half period T_mh is measured and the delay t_on is calculated for amplitude control. The amplitude timing value is exemplarily shown for the single-layer design case. (b) Block diagram of the amplitude control loop, executed at each detected zero crossing. The plant represents the MEMS mirror operated in zero phase. The measured periods are low pass filtered, divided by 2 and added to the PI controlled amplitude errors to obtain the switching on delay.

A block diagram of the amplitude control loop is shown in Fig. 5.4b, which is executed at each detected zero crossing, where new amplitude and period measurements are available. In this study, a simple PI feedback approach is used to control the mirror amplitude by the measured amplitude timing error. The control law is therefore given by

$$t_{\mathrm{on}_i} = \frac{1}{2}\hat{T}_{\mathrm{mh}_i} - G_\mathrm{P}\left(\bar{t}_\mathrm{ATC} - t_{\mathrm{ATC}_\mathrm{i}}\right) - G_\mathrm{I}\sum_{j=-\infty}^{i}\left(\bar{t}_\mathrm{ATC} - t_{\mathrm{ATC}_\mathrm{j}}\right)\,, \tag{5.4}$$

where $\bar{t}_\mathrm{ATC}$ is the reference amplitude timing value corresponding to the desired amplitude and G_P and G_I are the P and I gains, respectively. In order to cope with measurement noise the mirror half period T_mh is filtered using a first order low-pass, i.e.

$$\hat{T}_{\mathrm{mh}_i} = \hat{T}_{\mathrm{mh}_{i-1}} + G_\mathrm{LP}\left(T_{\mathrm{mh}_i} - \hat{T}_{\mathrm{mh}_{i-1}}\right)\,, \tag{5.5}$$

where G_{LP} is the filter gain. A low filter gain is preferred for noise suppression, while a too low gain may cause dynamic effects on the amplitude control loop as the mirror period is not sufficiently tracked.

It has to be noted that for the used MEMS mirror the operation points with zero phase and duty cycles larger than 50%, as in Fig. 5.4a, are unstable in open loop operation, but can be maintained by the immediate phase compensation of the DAsPLL. Therefore, the DAsPLL can properly operate MEMS mirrors exhibiting both softening or hardening behavior in open loop stable or unstable regions, while their implementation is simple. This comes with the drawback that excessive noise on the mirror zero crossing detection directly influences the jitter of the driving signal, which necessitates additional filtering methods to obtain a stable laser synchronization in harsh environments.

5.1.4. Experimental verification

In this section, experimental results of the proposed fast start-up method and the achieved residual pointing uncertainty are discussed. The scaling laws of the phase detection method in Section 4.1.1 and the amplitude control using the detection method in Section 4.1.2 are verified. The DAsPLL is implemented in an FPGA (Zedboard, Avnet, Phoenix, US), operated at 100 MHz internal clock. The MEMS mirror angle is measured using a position sensitive detector and a continuous laser source [34]. A CCD camera and a pulsed laser source, triggered by the FPGA, provide precise measurements of the optical pointing errors.

Verification of reliable fast start-up

Fig. 5.5a shows the proposed fast start-up procedure, where the phase control loop is closed already about 20 ms after the begin of actuation. In closed loop operation, the mirror oscillation is precisely tracked for maximum energy injection such that the mirror is run to the high amplitude as fast as possible. The MEMS mirror amplitude over frequency behavior is shown in Fig. 5.5b for three different initial open loop driving frequencies f_{dr}. At the first two datasets, the initial driving frequency is twice the mirror frequency corresponding to the first-order parametric resonance. The third dataset shows the proposed method at an initial start at the second-order parametric resonance, where the driving frequency is equal to the mirror frequency. After the learning mode, the response is almost the same for all initial start frequencies and the MEMS mirror is run to maximum amplitude in the first-order parametric resonance by keeping zero phase delay. The sudden jumps to higher frequencies and back are due to the additional electrostatic stiffness caused by the comb-drives during the learning mode. By the proposed start-up method the mirror can be run to 99.9% of the final amplitude within less than 100 ms depending on the chosen initial driving condition.

A start-up experiment of a similar MEMS mirror using an open loop frequency sweep in [176] results in already about 400 ms to reach the bifurcation jump, i.e. only a fraction of the desired high amplitude. The results in this section show that each comb-drive actuated resonant MEMS mirror can be automatically run to its maximum amplitude by using the proposed fast start-up method, once it reaches a sufficient high current signal for a valid zero crossing detection.

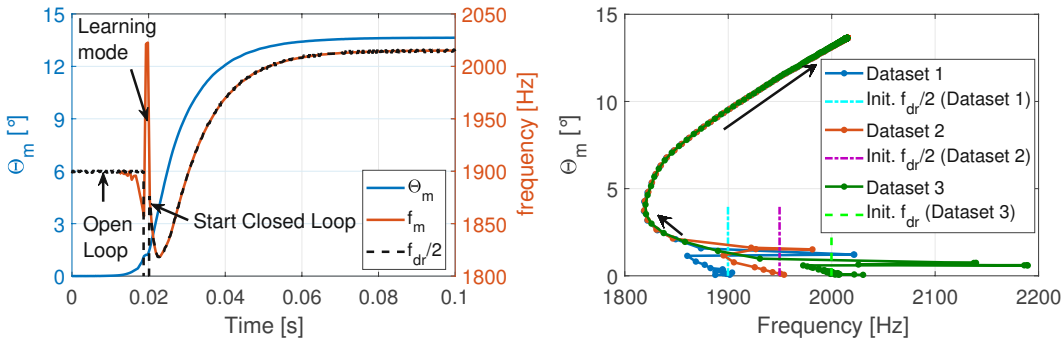

(a) (b)

Figure 5.5.: (a) Measured fast start-up using the proposed method. The phase control loop is closed already ∼ 20 ms after the begin of actuation and 99.9% of the final amplitude is reached at 88.9 ms. (b) MEMS mirror amplitude over frequency behavior at the proposed fast start-up method. Datasets one and two initially start in first-order parametric resonance whereas the third dataset starts in second-order parametric resonance.

Verification of amplitude control

Fig. 5.6 shows the dynamic response on an ATC set-point step of -100 ns, resulting in 50 mdeg amplitude increase and a duty cycle reduction of 0.7%. The used mirror period filter gain $G_{\mathrm{LP}} = 0.125$ provides accurate tracking of the mirror period while the noise is reduced as shown in the inset of the figure. The amplitude timing control gains $G_{\mathrm{P}} = 4$ and $G_{\mathrm{I}} = 0.25$, are set to achieve an overdamped behavior with a settling time of less than 50 ms for sudden external disturbance compensation.

Pointing uncertainty measurement

As MEMS mirrors are intended to be used in high precision scanning and projection systems, both the trajectory stability and the precision of the pixel synchronization are of importance. Hence, the optical pointing uncertainties are

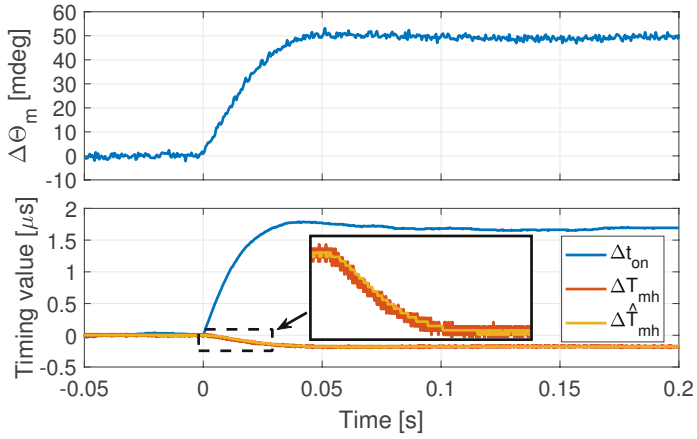

Figure 5.6.: Mirror amplitude response on a -100 ns set-point step of the ATC control loop ($\Theta_m = 13.75^\circ$, $V_{ATC} = 0.8\,V$). With the gains $G_{LP} = 0.125$, $G_P = 4$ and $G_I = 0.25$, the response shows an overdamped behavior and a fast settling time of $< 50\,ms$. The variables with a Δ prefix only contain the deviation from the nominal operation point values.

evaluated at the center and the edges of the FoV. The first is effected by the precision of the zero crossing detection while the second is mainly influenced by mirror amplitude errors.

Center pixel evaluation

In order to analyze the achieved optical resolution by the proposed phase detection method and control structure, a pulsed laser is triggered directly with the zero crossing signal asynchronously to the internal FPGA clock. By this, the pointing uncertainty of the DAsPLL at the zero crossing of the mirror, i.e. at the center of the FoV, can be measured by a CCD. The experimental setup for the center uncertainty evaluation is illustrated in Fig. 5.7a. The closed loop system comprises the DAsPLL implemented on an FPGA, the driving and sensing circuits and the MEMS mirror. For precise evaluation, the exposure time of the CCD is set to less than the mirror period to obtain only a single shot in each frame. A video is captured for each evaluation point and analyzed regarding the standard deviation and the center displacement of the captured spots. For highly reliable detection of the spot movement on the CCD, the first captured frame in a video serves as a reference and is cross-correlated with the other frames. Assuming a 90° incidence angle of the laser on the CCD, the optical pointing error

can be calculated by

$$\Delta\theta_{\text{opt}} = \tan^{-1}\left(\frac{\Delta l}{D}\right), \tag{5.6}$$

where Δl is the relative spot movement on the CCD regarding the reference frame, in meter. A large distance D between the MEMS mirror and the CCD allows an angular resolution of 0.68 mdeg optically per pixel on the CCD. In order to achieve sub-pixel resolution, a Gaussian function is fitted to the result of the cross-correlation around the maximum point as can be seen in Fig. 5.7b. As the used MEMS mirror has only one oscillation axis, fitting is necessary only along the X axis of the CCD.

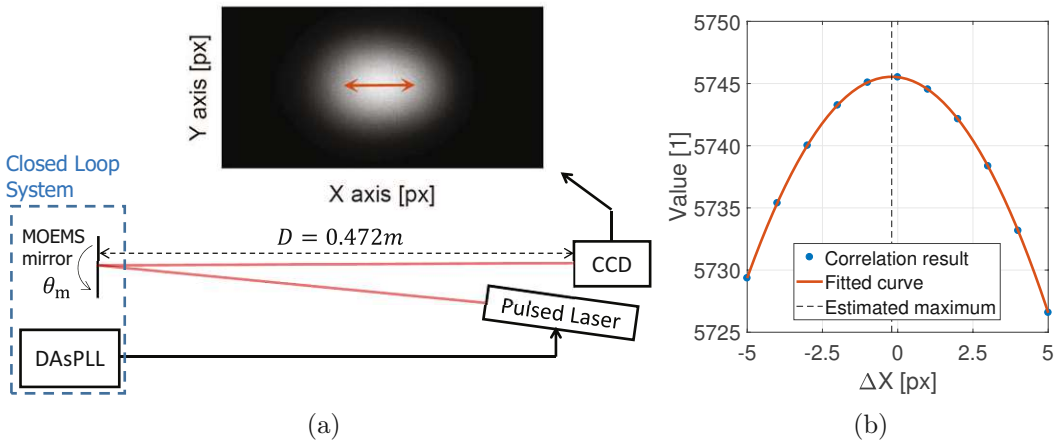

Figure 5.7.: (a) Evaluation setup scheme with a CCD frame example. The DAsPLL triggers the pulsed laser source with the phase detection signal, i.e. at the zero crossing of the mirror. The reflected beam directly hits the CCD chip and the optical uncertainty can be measured by analyzing the frames containing single shots. The direction of the spot movement due to pointing errors is indicated by a red arrow. (b) Cross-correlation result of a CCD frame with the reference frame and a Gaussian fit. The fitting provides sub-pixel resolution with an estimated relative maximum shift of −0.2 px in this example.

If no amplitude control is applied, the DAsPLL establishes synchronized excitation with 50% duty-cycle and the reached mirror amplitude is defined by the driving voltage V_p. Fig. 5.8a shows the obtained steady state amplitude over driving voltage behavior. As the sensing circuitry has a large impact on the system performance, two different settings are discussed in the following. A low gain setting using a TIA gain G_{TIA} of 45.16 V/mA with a cut-off frequency at 270 kHz and an increased gain setting with a TIA gain of 93.28 V/mA resulting in a cut-off frequency at 148 kHz. Fig. 5.8b shows the obtained amplitude dependent center

displacement, i.e. the mean spot shift on the CCD in optical angle relative to the lowest amplitude case. This may be caused by three effects, the finite but constant time delay of the pulsed laser, possible parasitic modes of the mirror and the bandwidth limitation of the current sensing circuitry, which delays the detected zero crossing by the increasing frequency content with amplitude. The kinks in the center displacement might be due to the comb-drive arm mode excitation at some operation points, leading to a small shift of the detected zero crossing. However, in an application, this effect can be calibrated and therefore represents no restriction.

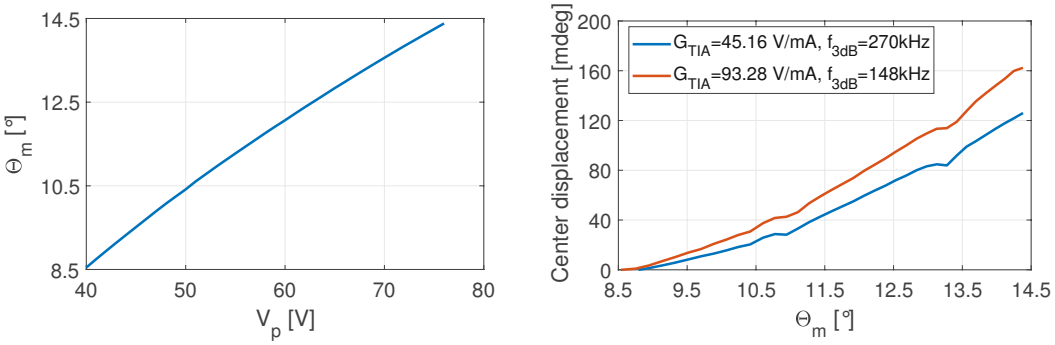

(a) (b)

Figure 5.8.: (a) Amplitude of the MEMS mirror over applied driving voltage, when it is operated by the DAsPLL without amplitude control. (b) Amplitude dependent center displacement measured by the CCD. The measurements are made with a high and a low gain setting of the current sensing circuitry. The zero reference at 8.5° amplitude are not the same for both measurements, since the corresponding beam positions are different.

The asynchronous laser triggering results in a Gaussian shaped histogram of the optical pointing error as shown in Fig. 5.9. This jitter originates from a white noise source given by the current sensing circuitry and therefore directly reflects the phase detection error without dependency on the FPGA clock. The achievable optical resolution by the FPGA clock of 10 ns would be ~ 2 mdeg at the lowest and ~ 3.5 mdeg at the highest amplitude and would therefore show a distorted histogram. In Fig. 5.10a the obtained standard deviation of the pointing error is shown for the two different gain settings of the current sensing circuitry. In order to compare the results to the theoretical model given by Eq. (4.8), the model

$$\hat{\sigma}_{\theta_{\mathrm{opt}}} = K_0 \left(V_\mathrm{p}\, \dot{\theta}_\mathrm{m}\big|_{\theta_\mathrm{m}=0^\circ} \right)^{-1} , \tag{5.7}$$

is fitted to the data where K_0 is the fitting constant and $\dot{\theta}_\mathrm{m}\big|_{\theta_\mathrm{m}=0^\circ}$ is measured

by the position sensitive detector for each amplitude. Hence, the parameter K_0 represents twice the ratio of the standard deviation of the current signal noise to the comb-drive capacitance curvature at zero angle, which are hard to measure accurately. The theoretical model and the measurements show good agreement in general. The small discrepancies can have several reasons as the obtained standard deviations are rather small. First, the MEMS mirror is only phase controlled, so environmental fluctuations or the jitter of the driving voltage switching may cause errors due to the amplitude dependent center displacement. Furthermore, the mirror has also parasitic modes that may cause a distortion of the current signal at the zero crossing. The bandwidth of the sensing circuitry also influences the results. If the gain is increased, the bandwidth is reduced and therefore also the current signal noise given by σ_I is decreased as well. Following this, the pointing uncertainty in Fig. 5.10a at the same operation amplitudes should be at least improved by a factor of ~ 2 as given by the ratio of the used TIA gains, but actually only achieves 1.46. This shows that the bandwidth may not be sufficient to accurately represent the actual current signal and distorts the current gradient at the zero crossing. Therefore, a further increase of the TIA gain may not improve the system performance significantly as the current gradient gets flattened due to a decreased bandwidth. Furthermore, it has to be considered that a low bandwidth causes a delay between the actual and the detected zero crossing, leading to a late switching off of the driving voltage by the DAsPLL. The minimum achieved optical standard deviation is 0.3 mdeg at a mirror amplitude of 14.38° and a scanning frequency of 2032 Hz corresponding to a phase detection standard deviation of only 0.84 ns.

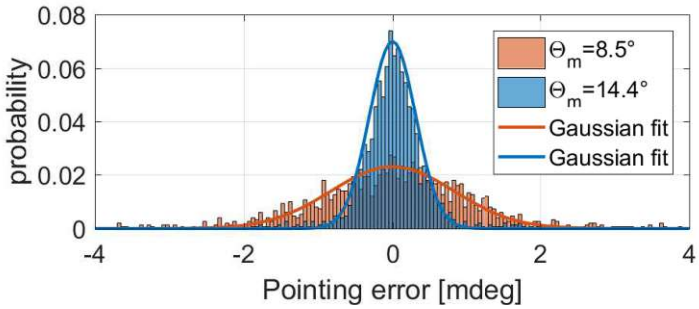

Figure 5.9.: Histogram of the measured optical pointing error at lowest and highest amplitude and their Gaussian fits. Each dataset includes 1500 measured single shot frames.

Finally Fig. 5.10b shows the obtained possible number of pixels calculated by Eq. (4.12) with a precision of 10 sigma. The theoretical model Eq. (4.13) is fitted to the data and shows the expected disproportional increase of resolution. The

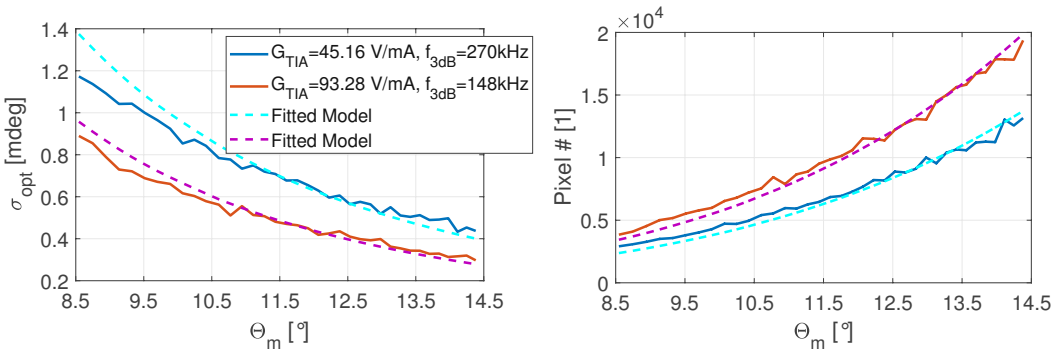

(a) (b)

Figure 5.10.: (a) Standard deviation of optical pointing error over mirror amplitude and theoretical fits using Eq. (5.7). The results show that for such small errors, the used bandwidth, drifts and also parasitic modes of the MEMS mirror may affect the current gradient at the zero crossing. (b) Number of possible pixels using Eq. (4.12) and the fitted theoretical model given by Eq. (4.13). The data shows the expected disproportional increase of resolution by amplitude. The maximum achieved resolution is $\sim$ 19000 pixels with a precision of 10 sigma.

maximum resolution achieved has about 19000 pixels at a FoV of 57.52°. The phase detection method based on photo diodes presented in [95] for a MEMS mirror with about eleven times higher scanning frequency and a similar FoV of 40° would only achieve about 230 pixels with a precision of 10 sigma. Thus the phase detection errors have to be averaged to obtain a higher resolution, which makes the PLL more complex and slow. Furthermore, the model in Eq. (4.13) reveals that the current sensing based phase detection method would achieve even better performance if the scanning frequency is increased.

Edge pixel evaluation

For evaluation of the pixel at the edge of the FoV, the setup in Fig. 5.7a is rearranged such that the CCD covers the edge pixel. The pulsed laser is triggered, when the mirror is expected to be at maximum deflection, i.e. at Θ_m, which is a quarter mirror period after a detected zero crossing. To avoid bandwidth problems of the sensing signal, the low TIA gain setting is used.

Fig. 5.11 shows the mirror amplitude deviation from 13.75°, when the amplitude timing control is turned off at time zero and turned on again after about 2.7 hours. The setup is placed in a lab without ambient conditioning. The result

shows that the amplitude drifts due to environmental variations such as temperature and pressure, as also shown in [95]. However, the proposed ATC concept compensates the drift of −13 mdeg and keeps the MEMS mirror at the desired amplitude with a standard deviation of 0.26 mdeg. This corresponds to an optical pointing uncertainty of only 0.52 mdeg at the edges of a 55° FoV, while at the center 0.39 mdeg are achieved in measurements. Furthermore, the DAsPLL correctly identified the scanning direction during all measurements by the proposed direction detection method.

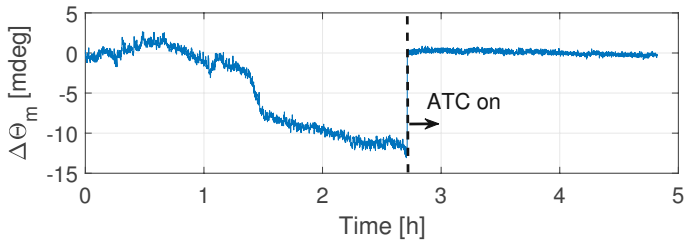

Figure 5.11.: Edge pixel errors with and without amplitude control in an uncontrolled environment ($\Theta_m = 13.75^\circ$, $V_{ATC} = 0.8$ V). Every 3 seconds one CCD frame is captured for the analysis. The mirror amplitude drifts due to environmental influences which is compensated when the ATC is turned on ($G_{LP} = 0.125$, $G_P = 4$, $G_I = 0.25$).

5.2. Optimal PLL design

In this section an optimal PLL design based on the linearized MEMS mirror model and time-normalization is discussed. The 1D, i.e. single axis, scanning is described first and then extended by a second axis to perform 2D Lissajous scanning using a dedicated synchronization approach for a fixed frequency ratio. Two control design approaches are considered for either case, i.e. a conventional single-input-single-output (SISO) and a multiple-input-multiple-output (MIMO) controller design, which are compared regarding their vibration and EMI robustness.

5.2.1. Time-normalized PLL

The concept of time normalization allows to operate different MEMS mirrors or to cope with manufacturing tolerances with minimized programming effort, as events such as a laser shot timing do not have to be known in absolute time but only relative to the oscillation period, i.e. representing the phase of an oscillation,

and is proposed in [77]. A time-normalized PLL design is illustrated in Fig. 5.12. The PLL phase detector calculates the PLL phase error Δt_ϕ, which is the time between the zero crossing of the mirror, provided by a negative edge of D_{ZC}, and the overflow of the digital controlled oscillator (DCO) output, i.e. the expected zero crossing defined by $s = 0$. The PLL controller P adjusts a L-bit register representing the PLL period T_{PLL} according to the measured errors. The first stage of the DCO generates a clock signal, whose average period is 2^{-N} times the PLL period and consists of two counters. The upper counter counts the FPGA clock cycles (f_{clk}) until the value given by the $L - N$ MSBs of the PLL period register is reached, which resets the counter and sets the output to high for one clock cycle. The lower counter has N bits and adds the N LSBs of the PLL period up if the upper counter is high at the output. An overflow of the lower counter causes the upper counter to ignore one FPGA clock cycle. The second stage of the DCO uses the frequency generated by the first stage to count up the phase slices s.

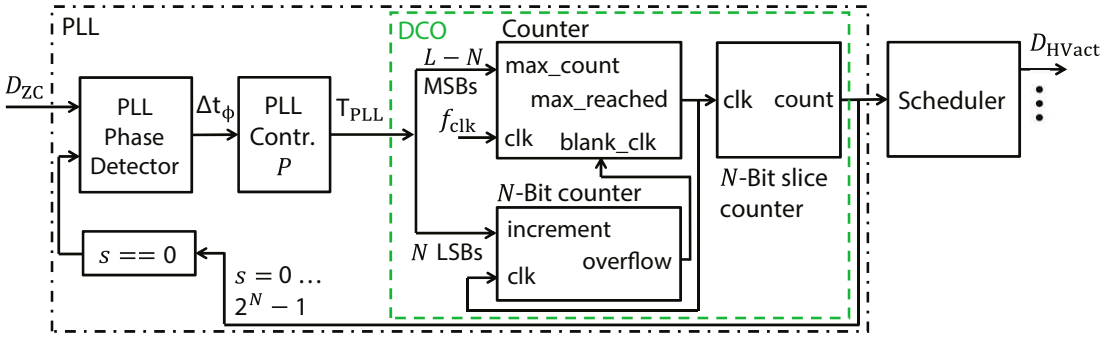

Figure 5.12.: Simplified block diagram of the time-normalized PLL implementation. The DCO generates 2^N phase slices s, corresponding to one PLL period. The PLL phase detector measures the error between the zero crossing of the mirror, detected by D_{ZC}, and the slice counter overflow, which gets compensated by the PLL controller. The scheduler provides the necessary signals for the closed loop operation based on the phase slices.

With the given structure and in steady state, the output of the DCO is a sawtooth signal that counts from 0 to $2^N - 1$ and jumps back to 0 between two adjacent zero crossings of the mirror as illustrated in Fig. 5.13. The scheduler generates the driving, sensing and synchronization signals based on the phase slices, e.g. the driving signal D_{HVact} is turned on and off at phase slice s_{on} and s_{off}, respectively. Furthermore, in steady state the reference amplitude timing ratio $\bar{r}_{\mathrm{ATC}}$ used for amplitude detection in Chapter 4 corresponds to a constant

phase slice

$$s_{\mathrm{ATC}} = 2^N \left(1 - \frac{\bar{t}_{\mathrm{ATC}}}{T_{\mathrm{PLL}}}\right) = 2^N \left(1 - \frac{\bar{t}_{\mathrm{ATC}}}{\bar{T}_{\mathrm{mh}}}\right) = 2^N \left(1 - \bar{r}_{\mathrm{ATC}}\right) . \tag{5.8}$$

This means that in steady state the amplitude timing value corresponds to the time between phase slice s_{ATC} and $s = 0$ as depicted in the Fig. 5.13. In the case of amplitude and phase errors, the amplitude timing error can be expressed as

$$\Delta t_{\mathrm{ATC}} = t_{\mathrm{ATC}} - \bar{t}_{\mathrm{ATC}} = \bar{r}_{\mathrm{ATC}}\, T_{\mathrm{PLL}} + \Delta t_{\mathrm{s_{ATC}}} - \Delta t_{\phi} - \bar{t}_{\mathrm{ATC}} \approx \Delta t_{\mathrm{s_{ATC}}} - \Delta t_{\phi} \,, \tag{5.9}$$

where $\Delta t_{\mathrm{s_{ATC}}}$ is the timing error between the phase slice s_{ATC} and the event initiating the ATC timing measurement, e.g. the crossing of V_{ATC} for the single-layer comb-drive design. Hence, the proposed implementation allows to set the reference amplitude timing value as a ratio of the nominal mirror period and a simple measurement of the amplitude timing error Δt_{ATC} by $\Delta t_{\mathrm{s_{ATC}}}$ and the phase error Δt_{ϕ}.

The PLL adapts its period T_{PLL} to keep the mirror zero crossings synchronized with the phase slice $s = 0$. The driving signal voltage as well as the switching slices, i.e. s_{on} and s_{off}, influence the resulting operation point, which can be used for amplitude control or synchronization purpose [125,151]. A similar implementation of this time-normalized PLL concept is proposed in [175], where a driver ASIC for MEMS-based lidar is developed.

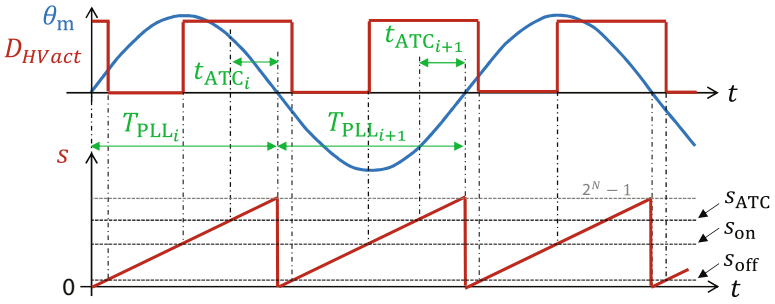

Figure 5.13.: Mirror trajectory and phase slices generated by the PLL. The phase slice s results in a sawtooth signal with a period corresponding to the mirror half period in steady state, i.e. zero phase error. The driving signal D_{HVact} is defined by the switching slices s_{on} and s_{off} and exemplary shown. At nominal operation the reference amplitude timing value corresponds to the time between phase slice s_{ATC} and slice zero.

5.2.2. 1D scanning control concept

The steady state operation point of a PLL controlled resonant MEMS mirror can be influenced by both the driving voltage and the duty cycle. As a variable driving voltage V_p requires a more complex driving circuitry, duty cycle control is preferred since the switching of the voltage can be easily varied. In the proposed system, the driving voltage is turned on at the phase slice 2^{N-1}, corresponding to the time instance of maximum mirror deflection, while the duty cycle is adjusted by the turning off phase slice s_off, which in the nominal case happens on the current plateau. This choice allows to approximate the local MEMS mirror dynamics by a linear period-to-period model, which is discussed in detail in Section 3.3. However, in the derived model the duty cycle is assumed constant, which is not valid anymore and the model needs to be extended. As illustrated in Fig. 5.14 the switching off delay deviation is given by

$$\Delta t_{\mathrm{off}_i} = \Delta t_{\phi_i} + \frac{T_{\mathrm{PLL}_i}}{2^N}\, s_{\mathrm{off}_i} - \bar{t}_\mathrm{off}\,, \tag{5.10}$$

which shows a nonlinearity as s_{off_i} and T_{PLL_i} are multiplied and are both control inputs. Since only small perturbations are assumed and s_off is rather small, e.g. 7% of 2^N slices according to a nominal duty cycle of 57%, the PLL period in Eq. (5.10) can be approximated by the nominal mirror half-period $\bar{T}_\mathrm{mh}$, i.e.

$$\Delta t_{\mathrm{off}_i} \approx \Delta t_{\phi_i} + \frac{\bar{T}_\mathrm{mh}}{2^N}\, s_{\mathrm{off}_i} - \bar{t}_\mathrm{off} = \Delta t_{\phi_i} + \frac{\bar{T}_\mathrm{mh}}{2^N}\, \Delta s_{\mathrm{off}_i} = \Delta t_{\phi_i} + \kappa_\mathrm{t/s}\, \Delta s_{\mathrm{off}_i}\,, \tag{5.11}$$

with the nominal time per phase slice $\kappa_\mathrm{t/s} = \bar{T}_\mathrm{mh}/2^N$, the nominal switching off delay $\bar{t}_\mathrm{off} = \kappa_\mathrm{t/s}\, \bar{s}_\mathrm{off}$ and $\Delta s_{\mathrm{off}_i} = s_{\mathrm{off}_i} - \bar{s}_\mathrm{off}$.

By using the derivations in Section 3.3, the state equation of the linear small perturbation model in Eq. (3.44) can be extended by the duty cycle control input Δs_off as

$$\overbrace{\begin{bmatrix}\Delta t_{\phi_{i+1}}\\ \Delta T_{\Theta_{i+1}}\end{bmatrix}}^{\mathbf{x}_{i+1}} = \overbrace{\frac{1}{\kappa_\mathrm{sp}+\kappa_\mathrm{d}}\begin{bmatrix}(\kappa_\mathrm{sp}+\kappa_\mathrm{d})\,(\kappa_\mathrm{c}+1)-1 & -\kappa_\mathrm{sp}\\ 1 & \kappa_\mathrm{sp}\end{bmatrix}}^{\mathbf{A}} \cdot \overbrace{\begin{bmatrix}\Delta t_{\phi_i}\\ \Delta T_{\Theta_i}\end{bmatrix}}^{\mathbf{x}_i} + \underbrace{\begin{bmatrix}\kappa_\mathrm{t/s}\left(\kappa_\mathrm{c}-\frac{1}{\kappa_\mathrm{sp}+\kappa_\mathrm{d}}\right) & 1\\ \kappa_\mathrm{t/s}\frac{1}{\kappa_\mathrm{sp}+\kappa_\mathrm{d}} & 0\end{bmatrix}}_{\mathbf{B}} \cdot \underbrace{\begin{bmatrix}\Delta s_{\mathrm{off}_i}\\ \Delta T_{\mathrm{PLL}_i}\end{bmatrix}}_{\mathbf{u}_i} + \underbrace{\frac{1}{\epsilon_\mathrm{c}\,(\kappa_\mathrm{sp}+\kappa_\mathrm{d})}\begin{bmatrix}-1\\ 1\end{bmatrix}}_{\mathbf{G}} E_{\mathrm{ext}_i}\,, \tag{5.12}$$

where E_ext is the external disturbance input, e.g. due to vibrations. The corre-

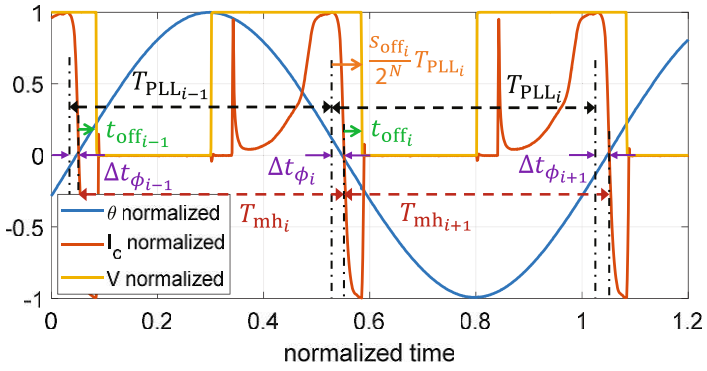

Figure 5.14.: Signals and definitions around the nominal operation point for PLL and duty cycle control at negative phase error Δt_ϕ for illustration purpose. The driving signal is switched on at maximum deflection and switched off at the plateau of the displacement current $\bar{I}_\mathrm{c}$ for linear local dynamics.

sponding output equation is

$$\begin{bmatrix} \Delta t_{\phi_i} \\ \Delta \Theta_{\mathrm{m}_i} \end{bmatrix} = \begin{bmatrix} 1 & 0 \\ 0 & \kappa_\Theta \end{bmatrix} \begin{bmatrix} \Delta t_{\phi_i} \\ \Delta T_{\Theta_i} \end{bmatrix} . \tag{5.13}$$

As the MEMS mirror amplitude is actually measured by the amplitude timing value, the self-sensing measurement equation is given as

$$\underbrace{\begin{bmatrix} \Delta \tilde{t}_{\phi_i} \\ \Delta \tilde{t}_{\mathrm{ATC}_i} \end{bmatrix}}_{\mathbf{y}_i} = \underbrace{\begin{bmatrix} 1 & 0 \\ 0 & S\,\kappa_\Theta \end{bmatrix}}_{\mathbf{C}} \underbrace{\begin{bmatrix} \Delta t_{\phi_i} \\ \Delta T_{\Theta_i} \end{bmatrix}}_{\mathbf{x}_i} + \underbrace{\begin{bmatrix} v_{\phi_i} \\ v_{\mathrm{s}_{\mathrm{ATC}i}} - v_{\phi_i} \end{bmatrix}}_{\mathbf{v}_i} , \tag{5.14}$$

where v_{ϕ_i} and $v_{\mathrm{s}_{\mathrm{ATC}i}}$ are the phase detection and ATC measurement noise, respectively and S is the corresponding ATC sensitivity, resulting in $S\,\kappa_\Theta \approx 0.85$ for the used operation point. The input vector $\mathbf{u}$ allows control of both amplitude and phase delay in order to stabilize the system and to counteract dynamic disturbances given by E_ext. As the driving period and the switching off slice are inputs to the DCO or scheduler, respectively, with a phase and an amplitude measurement in each PLL period, the controller perceives the MEMS mirror as a MIMO system represented by the model in Eq. (5.12) and (5.14). For such a system two methods can be used for control design. The first method is to separate the time constants of amplitude and phase control, which allows simple SISO controllers. This method is the typical approach for resonant MEMS mirrors, where a fast PLL compensates the phase errors for stable operation and a slow amplitude controller adjusts either the driving voltage [95] or the duty cycle [125]. The second

method is a MIMO controller, which considers the cross-coupling of the system to optimally drive the MEMS mirror, while it is typically more complex. Both approaches are discussed in the following.

SISO controller design

Fig. 5.15a illustrates the SISO control scheme with separated time constants as the amplitude controller Ψ is slow while the PLL controller P is fast. The amplitude controller slowly adjusts s_{off} to reach the desired amplitude $\bar{\Theta}_{\text{m}}$ by the integral law

$$\begin{aligned} \Delta s_{\text{off}_i} &= \Gamma_{\Psi_i} + G_{\Psi\text{I}}\, \Delta t_{\text{ATC}_i} \\ \Gamma_{\Psi_{i+1}} &= \Gamma_{\Psi_i} + G_{\Psi\text{I}}\, \Delta t_{\text{ATC}_i}\,, \end{aligned} \tag{5.15}$$

with the controller state Γ_Ψ and the integral gain $G_{\Psi\text{I}}$, which is chosen small enough for a sufficiently high time constant. Since the amplitude is controlled much slower than the phase, the phase control loop can be assumed independent of the amplitude control, i.e. only the phase control with a constant s_{off} has to be considered for dynamic analysis as illustrated by the block diagram in Fig. 5.15b. The nonlinear MEMS mirror is represented by the linear model in Eq. (5.12) and influenced by disturbances E_{ext} and phase measurement noise v_ϕ as shown in the figure. In the following the closed loop system stability is analyzed for I and PI control laws, which are usually applied in a PLL.

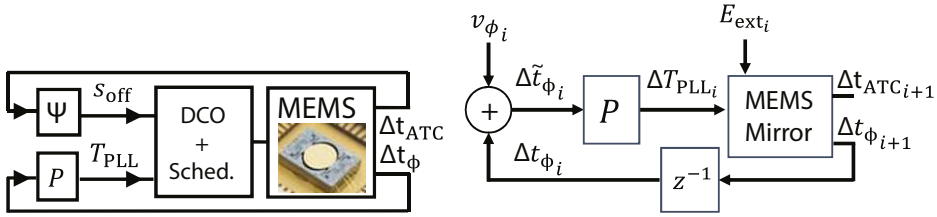

Figure 5.15.: (a) SISO control scheme with a slow amplitude controller Ψ and a fast PLL controller P. (b) Dynamic model of the closed loop system. The MEMS mirror is represented by the derived linear small perturbation model and affected by the measurement noise v_ϕ of the phase detector and random external disturbances E_{ext}.

I-control

One of the most simple controller is an integrator with the feedback law

$$\begin{aligned} \Delta T_{\mathrm{PLL}_i} &= \Gamma_{P_i} + G_\mathrm{I}\, \Delta\tilde{t}_{\phi_i} \\ \Gamma_{P_{i+1}} &= \Gamma_{P_i} + G_\mathrm{I}\, \Delta\tilde{t}_{\phi_i}\,, \end{aligned} \tag{5.16}$$

where Γ_P is the PLL integrator state and G_I is the integral gain which has to be negative due to the definition of the phase delay Δt_ϕ. In Fig. 5.16a the root locus of the closed loop system with three nonzero poles is shown for different control gains G_I. It is found that the faster the controller, the less robust the system gets. The frequency of the conjugate complex poles increases by the gain magnitude, while their damping ratio decreases as can be seen by the grid lines of constant natural frequency and constant damping ratio in the root locus obtained by the MATLAB command *zgrid*. Already at an integral gain of $G_\mathrm{I} = -0.053$ the stability boundary is reached. This result shows that a pure integral controller is not desirable at least for resonant electrostatic MEMS mirrors with progressive mechanical springs.

PI-control

Another commonly used control law is a proportional gain G_P added to an integrator and can be expressed as

$$\begin{aligned} \Delta T_{\mathrm{PLL}_i} &= \Gamma_{P_i} + (G_\mathrm{I} + G_\mathrm{P})\, \Delta\tilde{t}_{\phi_i} \\ \Gamma_{P_{i+1}} &= \Gamma_{P_i} + G_\mathrm{I}\, \Delta\tilde{t}_{\phi_i}\,. \end{aligned} \tag{5.17}$$

Fig. 5.16b shows the root locus for various proportional and integral gains. The proportional gain stabilizes the complex conjugate poles, which would be otherwise outside of the unit circle for pure integral control with the same gain. The pole movement by the proportional gain shows that it strongly increases damping at a moderate pole frequency increase, revealing its stabilizing behavior. Hence, the use of a proportional gain reduces overshoots and oscillations in the closed loop response. The effect of a proportional gain gets recognized if the control law in Eq. (5.17) is rewritten by using Eq. (3.43), i.e.

$$\begin{aligned} \Delta T_{\mathrm{PLL}_i} &= \Delta T_{\mathrm{PLL}_{i-1}} + G_\mathrm{I}\, \Delta\tilde{t}_{\phi_i} + G_\mathrm{P}\left(\Delta\tilde{t}_{\phi_i} - \Delta\tilde{t}_{\phi_{i-1}}\right) \\ &= \Delta T_{\mathrm{PLL}_{i-1}} + G_\mathrm{I}\, \Delta\tilde{t}_{\phi_i} + G_\mathrm{P}\left(v_{\phi_i} - v_{\phi_{i-1}}\right) - G_\mathrm{P}\left(\Delta T_{\mathrm{mh}_i} - \Delta T_{\mathrm{PLL}_{i-1}}\right)\,. \end{aligned} \tag{5.18}$$

It shows that the proportional control law serves as a first order low pass filter for the mirror half period with the filter gain $-G_\mathrm{P}$. By increasing both the integral and the proportional gain a low settling time can be achieved, while it also

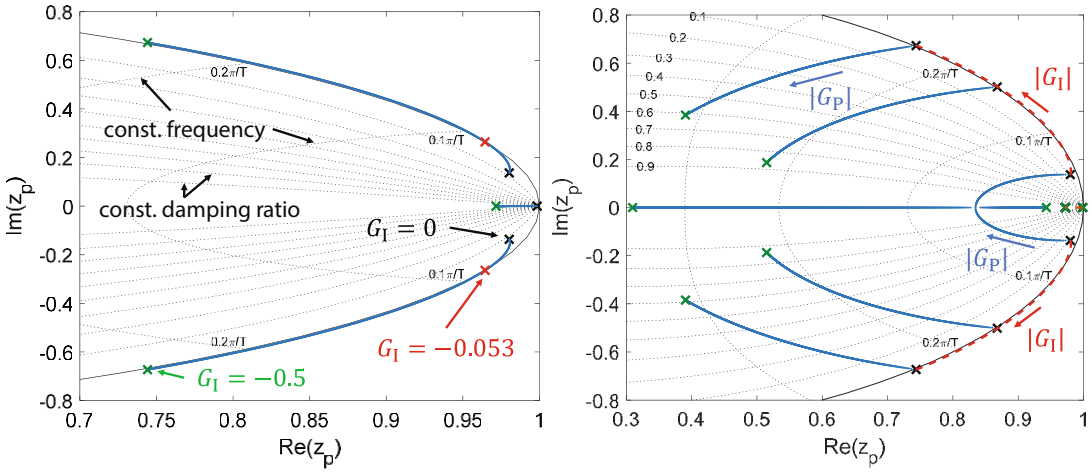

(a) (b)

Figure 5.16.: (a) Root locus of the closed loop system with I control law at different gain settings. Starting from the open loop poles (black cross) the system gets less robust for increasing control gains. The grid lines depict pole locations of constant natural frequency and constant damping ratio. (b) Root locus of the closed loop system with PI control law at different gain settings. The pole movement by $G_P \in [-0.5, 0]$ (blue lines) is exemplary shown for three different integral gains $G_I \in \{-0.001, -0.25, -0.5\}$. For comparison the poles at pure integral control are also shown (red dashed lines). Already low proportional gains stabilize the system at high integral gains. The real valued pole is only slightly influenced by G_P.

increases noise influence.

Experimental verification

In this paragraph the SISO control analysis based on the linearized MEMS mirror model is verified by measurements. First the stabilization of high integral gains with a proportional control law is shown by a step response from the noise input v_ϕ to the phase and amplitude error. Fig. 5.17a shows the step response with two different gain settings, which are accurately represented by the Linearized model. Large oscillations are obtained if only integral control is used and furthermore they are easily excited by measurement noise as shown in the inset. If the integral controller is made faster, these oscillations get worse as in agreement with the analysis above. However, if a proportional gain is added, much higher integral gains can be also applied as shown by the case $G_\mathrm{I} = G_\mathrm{P} = -0.5$, achieving low settling times.
Second, to fully verify the closed loop system representation by the proposed linear model, a random disturbance is applied on the noise input v_ϕ and the output spectrum of phase Δt_ϕ, mirror half-period ΔT_mh and amplitude errors $\Delta\Theta_\mathrm{m}$ are measured. Fig. 5.17b shows the corresponding estimated and simulated transfer functions $\mathrm{H}_{\Delta \mathrm{t}_\phi/\mathrm{v}_\phi}$, $\mathrm{H}_{\Delta \mathrm{T}_\mathrm{mh}/\mathrm{v}_\phi}$ and $\mathrm{H}_{\Delta\Theta_\mathrm{m}/\mathrm{v}_\phi}$ of the MEMS mirror with PI control at a high gain setting. The proposed model again predicts the measured MEMS mirror behavior with good agreement, allowing model based closed loop control design. The high frequency content of ΔT_mh deviates from the model as it is derived by Eq. (3.43), i.e. by the difference of two adjacent phase error measurements and the corresponding PLL period, and therefore is influenced by measurement noise. From the obtained transfer functions it is found that a high gain setting allows low settling times but leads to magnification of measurement noise to the phase error at around 500 Hz. Hence, this results and analysis reveal that the integral gain should be chosen rather low to achieve a desired maximum settling time and sufficient time constant separation from the amplitude control. The proportional gain should be chosen rather high to achieve a high damping ratio of the conjugate poles, while noise influence has to be considered.

Finally, Fig. 5.18 shows the spectral influence of external broadband vibration in T_Y direction to the measured phase and amplitude timing errors for open loop and PI controlled cases. The used vibration profile has a constant power spectrum density at the frequencies of the most vibration influence, i.e. around the mirror scanning frequency, such that the derived linearized model can be fitted to the response by a single scaling factor and shows good agreement. For proper comparison to the measured amplitude timing errors an estimated noise floor is added to the simulations by geometrically adding a constant noise spectrum. For both phase and amplitude errors the response to vibrations shows large peaks in

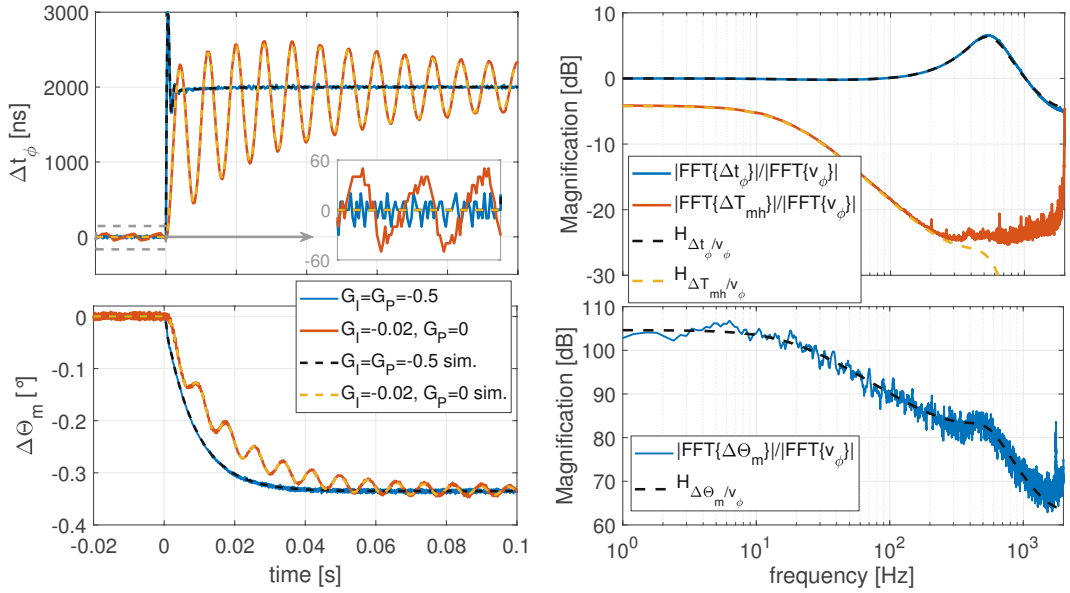

(a) (b)

Figure 5.17.: (a) Measured and simulated step response from phase noise input v_ϕ to phase error (top) and amplitude error (bottom) for I and PI control. Pure integral control results in large oscillations already at low gains which are also easily excited by measurement noise as shown in the inset. The addition of a proportional gain stabilizes the system even at high integral gains. (b) Transfer function of the closed loop system with high PI control gains ($G_\mathrm{I} = G_\mathrm{P} = -0.5$) under random phase noise. The transfer functions obtained by the proposed linear model accurately describe the measured behavior. A 2 Hz span smoothing filter is applied for better readability.

case of open loop operation, which are unacceptable in application. It is shown that with higher control gains the vibration influence can be reduced especially for the phase errors, while the amplitude errors increase at low frequencies. This is because the PLL follows the MEMS mirror oscillation regardless of its amplitude as the amplitude control is too slow. As higher control gains also show higher noise influence a trade-off has to be made between vibration compensation and sensitivity to EMI. Considering this, the gains $G_\mathrm{I} = -0.0088$ and $G_\mathrm{P} = -0.44$ are identified as a good compromise, achieving a well damped behavior with moderate noise and vibration influence.

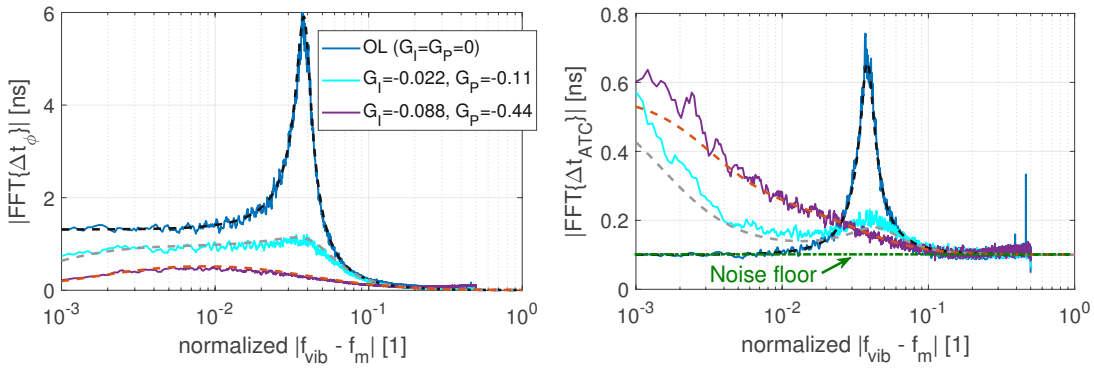

(a) (b)

Figure 5.18.: Spectral content of measured phase (a) and amplitude timing errors (b) at a broadband vibration profile from 500 Hz to 2500 Hz in $\mathrm{T_Y}$ direction for open loop and closed loop operation. The comparison to the linearized model (dashed lines) shows good agreement.

MIMO controller design

In order to account for the cross-coupling of inputs and outputs of the system a model based MIMO controller, as shown in Fig. 5.19 is designed in the following. The used controller is a linear-quadratic-gaussian (LQG) regulator, comprising an linear-quadratic regulator (LQR) and a Kalman estimator, as it allows direct control of the system states and inputs by the definition of cost functions [131]. Due to the separation of estimation and control theorem [177] the LQR can be designed independently of the Kalman estimator and vice versa.

LQR design

For the LQR design the system states are assumed to be known and the optimal feedback gain for a specific cost function of states $\mathbf{x}$ and inputs $\mathbf{u}$ can be calculated based on the stationary Riccati equation, which yields the optimal feedback

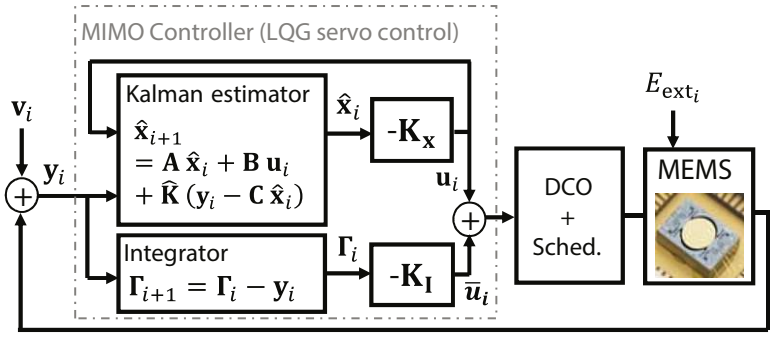

Figure 5.19.: MIMO control scheme using LQG servo control to compensate external vibration influence E_{ext} and to suppress the measurement noise $\mathbf{v}$. The controller comprises a Kalman estimator with the gain $\hat{\mathbf{K}}$, optimal state feedback gains $\mathbf{K}_\mathrm{x}$ and $\mathbf{K}_\mathrm{I}$ as well as an integrator for nominal operation point convergence.

controller $\mathbf{u} = -\mathbf{K}_\mathrm{x}\,\mathbf{x}$, where $\mathbf{K}_\mathrm{x}$ denotes the state feedback gain. However, as the MEMS mirror is actually a nonlinear system an integrator with the states $\mathbf{\Gamma}$ has to be added to guarantee convergence to the nominal operation point where the derived linear model is valid and the proposed optimality is true. Hence, the driving input signal obtained by the slow integrator path in Fig. 5.19 at infinite time is $\bar{\mathbf{u}}_\infty = \begin{bmatrix}\bar{s}_\mathrm{off} & \bar{T}_\mathrm{mh}\end{bmatrix}^\mathrm{T}$, i.e. the nominal switching off slice and mirror half period. With the positive semi-definite weighting matrices $\mathbf{Q}$, $\mathbf{R}$ and $\mathbf{N}$ the cost function for the LQR problem is then defined as

$$J(\mathbf{u}) = \sum_{i=0}^{\infty} \begin{bmatrix}\mathbf{x}_i \\ \mathbf{\Gamma}_i\end{bmatrix}^\mathrm{T} \mathbf{Q} \begin{bmatrix}\mathbf{x}_i \\ \mathbf{\Gamma}_i\end{bmatrix} + \mathbf{u}_i^\mathrm{T}\mathbf{R}\,\mathbf{u}_i + 2\begin{bmatrix}\mathbf{x}_i \\ \mathbf{\Gamma}_i\end{bmatrix}^\mathrm{T} \mathbf{N}\,\mathbf{u}_i\,, \tag{5.19}$$

subject to the linearized model in Eq. (5.12) and Eq. (5.14) as constraints. Hence, the optimal state feedback gains with an integrator can be calculated using the MATLAB function *lqi*, which minimizes the cost function under the dynamic model constraints. The choice of the weighting matrices is in general not trivial, but allows control of the individual states and inputs. Due to symmetry reasons $\mathbf{Q}$ and $\mathbf{R}$ have to be symmetric and are typically chosen to have only diagonal entries while all others are zero, i.e.

$$\mathbf{Q} = diag\left(W_{\mathrm{t}_\phi}, W_{\mathrm{T}_\Theta}, W_{\mathrm{t}_{\phi\mathrm{I}}}, W_{\mathrm{T}_{\Theta\mathrm{I}}}\right) \quad \text{and} \quad \mathbf{R} = diag\left(W_{\mathrm{s}_\mathrm{off}}, W_{\mathrm{T}_\mathrm{PLL}}\right)\,. \tag{5.20}$$

This allows to penalize each state and input individually by its corresponding weighting value. The matrix $\mathbf{N}$ can be used to explicitly penalize coupling between the states and the inputs, which is assumed not relevant for the single axis MEMS mirror control and therefore set to zero.

Finally, the weighting values in Eq. (5.20) have to be set in context to each other for proper controller design. Hence, we arbitrarily set $W_{\mathrm{t}_\phi} = 1$, which penalizes the phase error and calculate the desired relative effect of the other states and the inputs. Considering a scanning application the weighting of the states should be done such that amplitude and phase errors cause equal effects on the optical pointing error $\sigma_{\theta_{\mathrm{opt}}}$ resulting in rather uniform distributed errors along the total scan line. By the optimization the variance of ΔT_Θ, i.e. $\sigma^2_{\mathrm{T}_\Theta}$, can be assumed scaled down relative to the phase error $\sigma^2_{\mathrm{t}_\phi}$ with the weighting value W_{T_Θ}. Therefore, the desired equal pointing uncertainty effect for amplitude and phase errors can be expressed as

$$\sigma^2_{\theta_{\mathrm{opt}}} = 4 \left(\dot{\theta}_{\mathrm{m}} \big|_{\theta_{\mathrm{m}}=0^\circ} \right)^2 \sigma^2_{\mathrm{t}_\phi} \stackrel{!}{=} 4\,\Delta\Theta^2_{\mathrm{m}} = 4\,\kappa^2_\Theta\,\sigma^2_{\mathrm{T}_\Theta} = 4\,\kappa^2_\Theta \frac{\sigma^2_{\mathrm{t}_\phi}}{W_{\mathrm{T}_\Theta}}\,, \tag{5.21}$$

where $\dot{\theta}_{\mathrm{m}}\big|_{\theta_{\mathrm{m}}=0^\circ}$ is the angular velocity amplitude of the mirror at the nominal operation point, and the factor 4 results from the optical leverage. The weighting value W_{T_Θ} then results in

$$W_{\mathrm{T}_\Theta} = \frac{\kappa^2_\Theta}{\left(\dot{\theta}_{\mathrm{m}} \big|_{\theta_{\mathrm{m}}=0^\circ} \right)^2}\,, \tag{5.22}$$

with $W_{\mathrm{T}_\Theta} = 1.9$ for the used MEMS mirror. The integrator has to only compensate slow drifts due to variations of environmental conditions such as temperature or pressure, which are of time scales in the order of minutes or hours and should not cause considerable dynamic effects. Hence, the integrator gain weightings are chosen as $W_{\mathrm{t}_{\phi\mathrm{I}}} = 10^{-5}\,W_{\mathrm{t}_\phi}$ and $W_{\mathrm{T}_{\Theta\mathrm{I}}} = 10^{-5}\,W_{\mathrm{T}_\Theta}$.
For designing the weighting values for the inputs, their effect on the scanning system has to be considered. As all relevant signals such as the laser shooting are based on the phase slices generated by the DCO, it is not desirable to use the PLL period for fast dynamic error compensation. Rather, it is better to use fast duty cycle changes to push the mirror oscillation back to synchronize with the PLL, whose period is slowly changing. Hence, in case of an external disturbance of the mirror, the controller does not immediately follow the mirror oscillation but compensates for the oscillation variation by adapting the duty cycle, i.e. s_{off}. Therefore, the input weighting values are chosen as $W_{\mathrm{s_{off}}} = 6 \cdot 10^{-4} \kappa^2_{\mathrm{t/s}}$ and $W_{\mathrm{T_{PLL}}} = 3$, where the factor $\kappa_{\mathrm{t/s}}$ accounts for the scaling between DCO phase slices and time (i.e. time per slice) for a proper comparison. This results in the optimal feedback gains as

$$\mathbf{K} = \begin{bmatrix} \mathbf{K}_{\mathrm{x}} & \mathbf{K}_{\mathrm{I}} \end{bmatrix} = \begin{bmatrix} -10\,\kappa^{-1}_{\mathrm{t/s}} & 46\,\kappa^{-1}_{\mathrm{t/s}} & 0.035\,\kappa^{-1}_{\mathrm{t/s}} & -0.1\,\kappa^{-1}_{\mathrm{t/s}} \\ 0.34 & -0.27 & -0.0011 & -0.0014 \end{bmatrix}\,, \tag{5.23}$$

with the MEMS mirror parameters $\kappa_{\mathrm{sp}} = 67.6$, $\kappa_{\mathrm{d}} = 2.18$ and $\kappa_{\mathrm{c}} = 0.0054$. As

can be seen, the entries of the integrator gain $\mathbf{K}_\mathrm{I}$ are much lower than those of the state feedback gains $\mathbf{K}_\mathrm{x}$ and the duty cycle control is much faster than that of the PLL period. The system matrix $\mathbf{A}$ with the eigenvalues $\lambda_{1,2} = 0.987\angle\pm 6.83^\circ$ is replaced by the effective system matrix $\mathbf{A} - \mathbf{B}\cdot\mathbf{K}_\mathrm{x}$ with the eigenvalues $\lambda_{1,2} = 0.465\angle\pm 21.2^\circ$ due to the state feedback controller.

Kalman estimator design

The system states $\mathbf{x}$ are typically not known in application and have to be estimated from the measured outputs $\mathbf{y}$. Assuming a stochastic nature of the disturbance and the measurement noise with a zero mean value, the learning gain matrix $\hat{\mathbf{K}}$ for the optimal observer, i.e. a Kalman estimator, can be calculated from the linear system model and the corresponding covariance matrices, provided that the disturbance and the noise are not correlated. The covariance matrix of a sampled vector $\mathbf{v}_i$ with the sample index $i \in \mathbb{N}_0$ is defined as $\mathrm{E}\big(\mathbf{v}_i^\mathrm{T}\mathbf{v}_i\big)$, where $\mathrm{E}(\cdot)$ denotes the expectation value of the argument. For the external disturbance E_ext the covariance matrix corresponds to the variance $\sigma^2_{\mathrm{E}_\mathrm{ext}}$ of the expected vibration energy that couples into the mirror per period. The covariance matrix for the measurement noise can be obtained by measurements. As the amplitude timing error $\Delta t_{\mathrm{ATC}_i}$ is calculated from two measurements, i.e. $\Delta t_{\mathrm{s}_{\mathrm{ATC}i}}$ and the phase error Δt_{ϕ_i}, as defined in Eq. (5.9), the noise covariance matrix has also non-diagonal entries. Hence, for the MEMS mirror the covariance matrices are given as

$$\mathrm{E}\left(E^2_{\mathrm{ext}_i}\right) = \sigma^2_{\mathrm{E}_\mathrm{ext}} \qquad \text{and} \qquad \mathrm{E}\left(\mathbf{v}_i^\mathrm{T}\mathbf{v}_i\right) = \begin{bmatrix} \sigma^2_{v_\phi} & -\sigma^2_{v_\phi} \\ -\sigma^2_{v_\phi} & \sigma^2_{v_{\mathrm{s}_\mathrm{ATC}}} + \sigma^2_{v_\phi} \end{bmatrix}. \tag{5.24}$$

Considering EMI influence the standard deviation of the phase detection is set to $\sigma_{v_\phi} = 15\,\mathrm{ns}$ and based on measurements it can be assumed that $\sigma_{v_{\mathrm{s}_\mathrm{ATC}}} \approx 2.25\,\sigma_{v_\phi}$. In order to provide high vibration robustness the expected standard deviation of the vibration energy is chosen to $\sigma_{\mathrm{E}_\mathrm{ext}} = 1.25\,\epsilon_\mathrm{c}\,(\kappa_\mathrm{sp} + \kappa_\mathrm{d})\,\sigma_{v_\phi}$, which is also motivated by measurements. By using the MATLAB function *kalman* the corresponding Kalman gain matrix results in

$$\hat{\mathbf{K}} = \begin{bmatrix} 1.4 & 0.033\,\frac{1}{S\,\kappa_\Theta} \\ -0.54 & 0.019\,\frac{1}{S\,\kappa_\Theta} \end{bmatrix}. \tag{5.25}$$

With the feedback gain matrix in Eq. (5.23), the Kalman gain matrix in Eq. (5.25) and the linearized MEMS mirror model in Eq. (5.12) and Eq. (5.14) the LQG controller comprising four internal states is fully designed. Fig. 5.20 depicts the resulting transfer functions of the designed MIMO LQG controller. It can be observed that the optimal control design approach introduces tamped differential gains to provide phase lead at frequencies around 500 Hz in order to achieve a

high closed loop bandwidth. As designed, the driving voltage turning off phase slice, i.e. the duty cycle, variations are fast due to the high gains in Fig. 5.20a, while the PLL period reacts rather slow on errors.

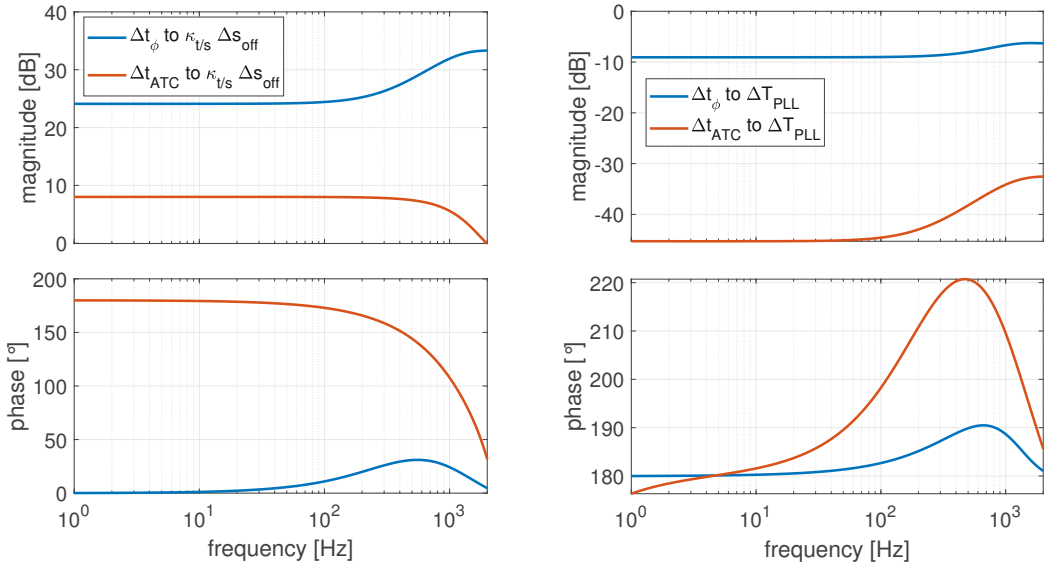

(a) (b)

Figure 5.20.: Bode plots of the designed MIMO LQG controller. (a) Transfer functions from measured errors to the driving voltage turning off phase slice variation. (b) Transfer functions from measured errors to the PLL period, i.e. driving voltage period.

Experimental verification

Considering an efficient implementation of the MIMO LQG controller, the number of necessary multipliers in the FPGA, which typically require a large chip area, can be reduced by not explicitly calculating the internal states of the LQG controller, i.e. $\hat{\mathbf{x}}$ and $\mathbf{\Gamma}$, but using a single state space representation of the LQG (see MATLAB command *lqgreg* or *lqgtrack*). Furthermore, the LQG does not have to be executed at each clock cycle but only once in each PLL period, which allows to use a state machine for sequential calculation of all multiplications even with only one multiplier actually present in the hardware design. Fig. 5.21 shows the performance of the implemented LQG controller under a broadband vibration profile compared to the SISO PI control. Both amplitude and phase errors are effectively suppressed, resulting in a flat spectral content of the measured errors.

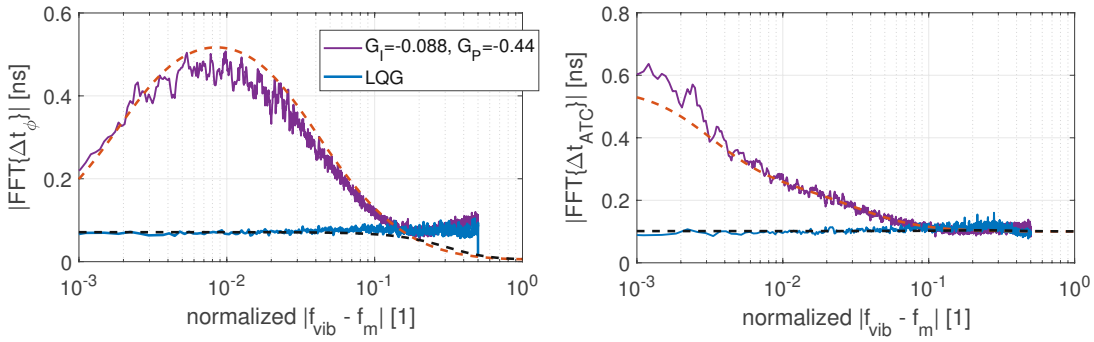

(a) (b)

Figure 5.21.: Spectral content of measured phase (a) and amplitude timing errors (b) at a broadband vibration profile from 500Hz to 2500Hz in T_Y for LQG and PI control. The comparison to the linearized model with added noise floor (dashed lines) shows good agreement.

The measured phase and amplitude timing values also contain noise, which do not correspond to an actual error in the application and degrades the actual performance. Hence, the controllers have to be evaluated regarding the resulting optical pointing uncertainty of the shot pixels as this reveals the performance in the targeted application. For a comparative evaluation to automotive standards a custom made piezo-shaker shown in Fig. 5.22a, is developed to provide strong and broadband vibrations to the MEMS mirror in the most influencing direction and frequency band, i.e. in T_Y around the mirror scanning frequency. The shaker consists of a massive outer frame, a piezo-stack actuator and a mover connected by four flexures, providing sufficient high stiffness in all undesired degrees of freedom. The MEMS mirror package is clamped into the PCB socket, which is clamped and glued onto the mover for a stiff connection. Fig. 5.22b shows two power spectrum density profiles calibrated by iterative refinement of the piezo-stack input signal using the obtained accelerations derived from laser-Doppler-vibrometer measurements at the mover. The vibration profile 1 corresponds to the highest frequency content of a specification profile in the automotive industry LV124 [167], where all devices have to operate in their specifications during and after the exposure to the vibration. The LV124 standard is defined for vibration frequencies less than 2 kHz, while the mirror frequency is above 2 kHz and therefore no significant influence to the mirror is observed. However, to evaluate a worst case scenario also higher frequencies are tested as well, including low frequency offsets from the mirror frequency. The vibration profile 2 applies frequencies ranging from 2 kHz to 3 kHz where the scanning frequency typically lies in and the vibration influence to the mirror is the worst. Fig. 5.23a shows the four evaluated pixel positions on the scanning trajectory obtained by shooting a pulsed laser at the corresponding phase slices. By placing a CCD in the direction of the reflected

beam a pointing uncertainty measurement is made for each pixel position, which are shown in Fig. 5.23b for LQG and PI control exposed to the vibration profile 2. As can be seen, even at such a worst case vibration scenario the LQG controller can provide precise pixel synchronization that rarely exceeds the targeted optical resolution criterion of 0.1° defined for automotive lidar. Hence, the model based MIMO LQG controller with fast duty cycle and slow PLL period control outperforms state of the art methods of SISO PI controllers, reducing the optical pointing uncertainty by about 66% to less than 15 mdeg.

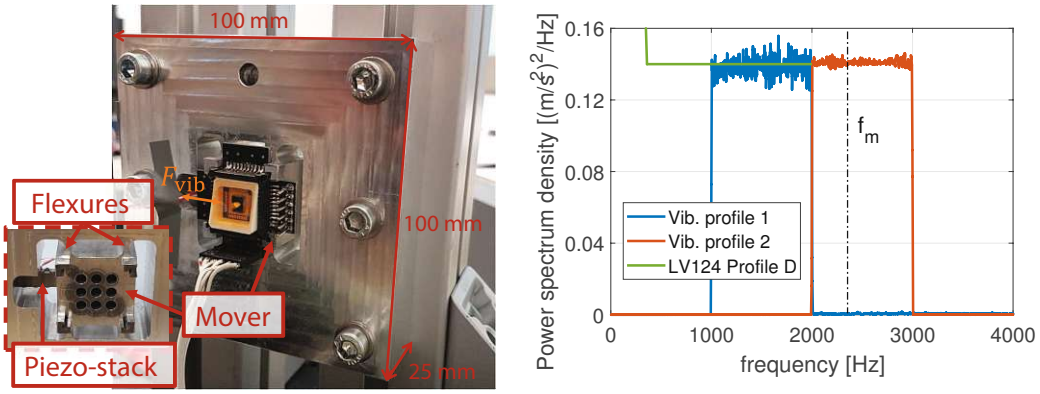

(a) (b)

Figure 5.22.: (a) Experimental setup for vibration robustness evaluation. The piezo-shaker is capable of providing broadband vibration in T_Y direction of the attached MEMS mirror as illustrated by F_{vib}. (b) Calibrated vibration power spectrum density profiles applied on the MEMS mirror compared to the specification profile LV124 of the automotive industry [167]. The profile 2 extends the profile of LV124 towards higher frequencies to cover also the regions of most influence close to typical mirror frequencies f_m.

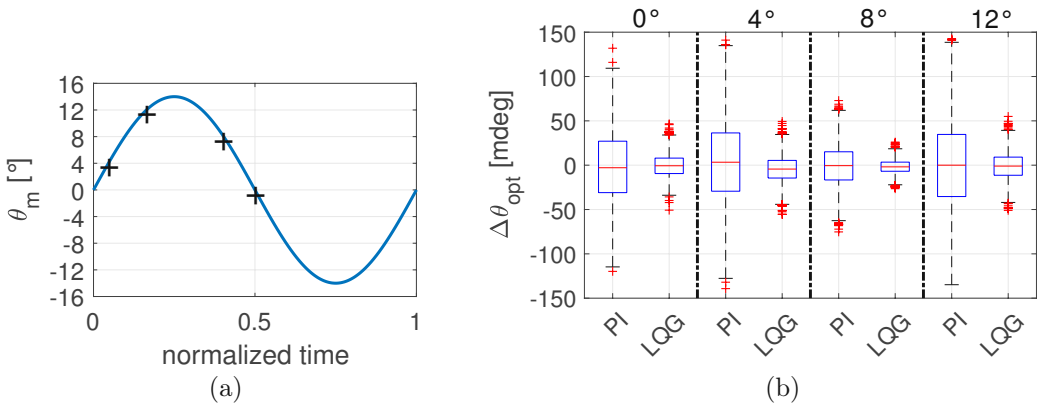

Figure 5.23.: Multi-pixel pointing uncertainty evaluation under broadband vibration using LQG or PI control. (a) Mirror trajectory and pixels (black crosses) at which the pointing uncertainty is evaluated. (b) Box-plot of the obtained pointing errors by analyzing 3000 single-shot CCD frames for each pixel position during exposure of vibration profile 2.

5.3. Summary

The reliable operation of a scanning system in harsh automotive applications with various and varying environments can only be ensured by a properly designed closed loop control, keeping the MEMS mirror trajectory as desired and aligned with the pixel shooting. Typically, a PLL is used to track the MEMS mirror phase by rather fast PLL period adjustments, while the oscillation amplitude is controlled by relatively slow driving voltage or duty cycle variations. This is called SISO control concept as two SISO controllers are used with separated time constants. In this chapter, two approaches of control design are discussed, the DAsPLL and an optimal PLL design with time-normalization and improved vibration suppression.

The DAsPLL represents an unusual PLL design as it generates a driving signal directly linked to the MEMS mirror oscillation, where the driving signal is switched off precisely with the detected zero crossing of the mirror, while the switching on time is determined based on previously detected zero crossings and is used to control the mirror amplitude. The fast tracking capability of the DAsPLL allows a fast and reliable start-up of the MEMS mirror from rest to maximum amplitude within less than 100 ms, i.e. <200 oscillations at a Q-factor of about 200, as well as the stabilization of open loop unstable operation points. The used asynchronous logic provides laser triggering aligned with the zero crossings of the mirror, achieving a minimum standard deviation of 11 times less than the used FPGA clock and resulting in an optical pointing uncertainty of down to 0.3 mdeg at the center of a 57.52° FoV. A long term evaluation of the amplitude

control reveals that the amplitude drifts by temperature and pressure variations are successfully compensated, leading to an optical uncertainty of 0.52 mdeg at the edges of the FoV.
The optimal PLL design exploits time normalization by dividing the PLL period into a fixed number of phase slices using a dedicated DCO counter structure, to easily manage the timing of driving, sensing and pixel shooting by a scheduler. Based on the linearized MEMS mirror model it is shown that the SISO control concept is only marginally stable for pure integral control and necessitates a proportional gain to allow fast phase tracking without causing instability. The integral gain mainly increases the natural frequency of the closed loop system complex conjugate poles, while the proportional gain increases damping as it acts as a mirror period filter. A combination of a rather low integral gain and a high proportional gain is found that allows a good vibration suppression, while the noise influence is moderate. Experiments verify the accuracy of the linearized model, correctly predicting the influence of noise and broadband vibration for various control gain settings. For improved vibration suppression a MIMO control concept is developed using a model-based LQG servo controller, which is designed to compensate for the effects of vibration by fast duty cycle changes keeping the mirror oscillation stable. Besides considering the cross-coupling of the inputs and outputs, the used MIMO controller design approach adds tamped differential gains to achieve large closed loop control bandwidth for vibration suppression. A custom made piezo-shaker provides strong vibrations to the MEMS mirror in T_Y direction with calibrated vibration profiles extending the LV124 standard towards higher frequencies to evaluate a worst case scenario. The MIMO control concept shows superior performance reducing the pixel shooting errors to a 3 times better optical pointing uncertainty of 15 mdeg and stay within the targeted 0.1° resolution limit.

CHAPTER 6

2D Lissajous scanning control concept

Lissajous scanning allows the use of two resonant axes, which are orthogonally aligned to each other in order to perform a 2D scan. The incremental relative phase move between both axes generates the typical scanning pattern. Despite the advantages of using resonant axes compared to other non-resonant scanning methods, such as simple and robust MEMS design and single axis control, both axes have to be precisely synchronized in a fixed frequency ratio. Hence, the synchronization and control approach needs to ensure that the relative phase between both axes is as desired even during operation in automotive environments.

In this chapter a robust and high precision synchronization method is discussed and demonstrated by Lissajous scanning using two single axis MEMS mirrors. The time-normalized DCO structure discussed in the previous chapter allows a simple synchronization approach of multiple MEMS mirrors or MEMS mirror axes in a fixed frequency ratio. The synchronization method exploits a master-slave principle, where one MEMS mirror controller provides synchronization signals to the slave MEMS mirror, while also a method using a dedicated master DCO and two slave MEMS mirrors is discussed. Based on the linearized MEMS mirror model, SISO and MIMO controllers are designed and evaluated regarding their performance in harsh environments. Alternative example applications for synchronization control can be an enlarged receiver aperture by synchronous operation of multiple mirrors as in [151, 152].

6.1. The Lissajous scanning system

The used Lissajous scanning system comprises two single axis MEMS mirrors of the same type, which are orthogonally oriented to each other in order to perform 2D scanning. In Fig. 6.1 the Lissajous scanning setup is depicted, where both mirrors are controlled by one FPGA and have identical but independent driving and sensing circuits. To project the Lissajous scanning pattern on a screen, a laser beam is first deflected in Y-axis by the MEMS mirror M1, redirected to the second MEMS mirror M2 by a lens system and deflected in X-axis. A CCD camera monitors the projection for optical evaluation. An on-board CPU is used to configure the FPGA and to provide an Ethernet data stream of the internal registers for analysis. Both MEMS mirrors are controlled using individual time-normalized PLLs. A proper Lissajous scan grid generation requires a fixed frequency ratio between both scanning axes with a precise phase synchronization method, which imposes difficulties in control design due to the nonlinear behavior of the parametric excitation. Hence, in the following a master-slave synchronization concept with a model-based control design is discussed.

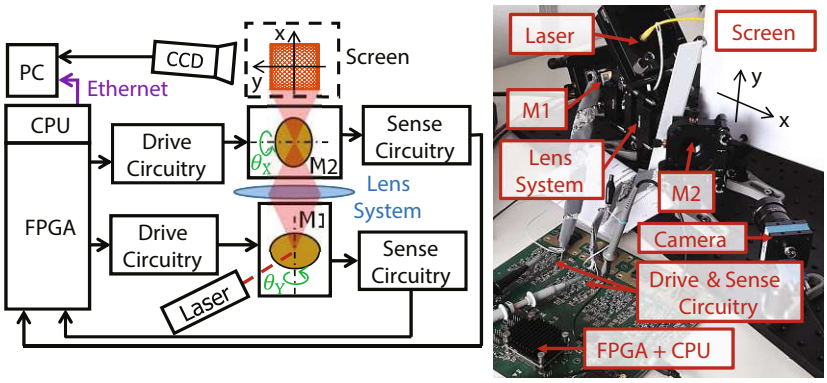

Figure 6.1.: Block diagram (left) and picture (right) of the Lissajous scanning system with two individually controlled single axis MEMS mirrors. The controllers are implemented in an FPGA, which is configured and monitored by an on-board CPU. For optical evaluation, the generated Lissajous pattern is projected on a screen and monitored by a CCD camera.

6.2. Master-slave synchronization concept

In this concept one MEMS mirror, e.g. M2 (X-axis), serves as the master and provides synchronization signals to the other mirror M1 (Y-axis), which is the slave.

Fig. 6.2 shows the synchronization concept for a fixed frequency ratio between both MEMS mirrors over one Lissajous frame. Two single bit synchronization signals are used, h_{fr} indicating the start of the Lissajous frame and h_δ indicating necessary zero crossings of the slave mirror for synchronized operation. The phase slicing of the DCO provides a simple approach to obtain a fixed frequency ratio $\bar{r} = f_{\mathrm{X}}/f_{\mathrm{Y}}$. As 2^N phase slices correspond to a relative phase shift of π between both mirror oscillations, the necessary master slice shift per slave PLL period $T_{\mathrm{PLL_Y}}$ is

$$s_\Delta = 2^N \frac{T_{\mathrm{PLL_Y}} - T_{\mathrm{PLL_X}}}{T_{\mathrm{PLL_X}}} = 2^N \left(\bar{r} - 1\right) , \tag{6.1}$$

where $T_{\mathrm{PLL_X}}$ is the master PLL period. Equation (6.1) shows that a fixed frequency ratio results in a constant slice shift s_Δ. The master controller generates synchronization pulses every $2^N + s_\Delta$ phase slices, which indicate the necessary zero crossings of the slave mirror for a synchronized operation with a fixed frequency ratio. Hence, the condition for a repetitive Lissajous pattern can be expressed as

$$\frac{s_\Delta}{2^N} T_{\mathrm{PLL_X}} \, 2N_{\mathrm{Y0}} = 2\, T_{\mathrm{PLL_X}} \, K \, , \tag{6.2}$$

where $2N_{\mathrm{Y0}}$ is the number of synchronization pulses, i.e. slave half periods, until the start of the next Lissajous frame and K is the smallest number of relative period shifts between the mirrors, where K and N_{Y0} have to be co-prime integers. With Eq. (6.1), Eq. (6.2) can be rewritten to

$$\frac{K}{N_{\mathrm{Y0}}} = \left(\bar{r} - 1\right) , \tag{6.3}$$

where K and N_{Y0} are guaranteed to be integers since $\bar{r}$ is an integer ratio in Lissajous scanning. As a consequence, the system generates the same Lissajous pattern independently of the actual master frequency, i.e. no integer frequency is required, which solely determines the resulting frame rate acording to Eq. (2.5).

6.2.1. Linearized model extension for slave mirror

For proper control design the linearized MEMS mirror model in Eq. (5.12) and Eq. (5.14) needs to be extended for the slave mirror, considering the synchronization error, while the master is unchanged. Assuming the master mirror is in steady state and sends synchronization pulses every nominal mirror half period of the slave, i.e. $\bar{T}_{\mathrm{mh}}$, the evolution of the synchronization error Δt_δ is given as

$$\Delta t_{\delta_{i+1}} = \Delta t_{\delta_i} + \bar{T}_{\mathrm{mh}} - T_{\mathrm{mh}_{i+1}} = \Delta t_{\delta_i} - \Delta T_{\mathrm{mh}_{i+1}} \, , \tag{6.4}$$

where ΔT_{mh} denotes the mirror half period deviation. The slave measures those synchronization errors by sampling the current phase slice of the DCO at a re-

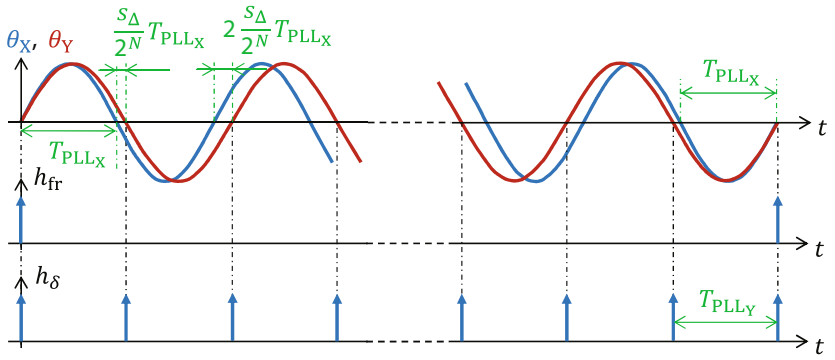

Figure 6.2.: Mirror trajectories and signaling for the master-slave synchronization concept over one Lissajous frame to achieve a fixed frequency ratio. The master controller generates synchronization pulses every frame start, i.e. h_{fr}, and at every $2^N + s_\Delta$ phase slices, i.e. h_δ, corresponding to the necessary zero crossings of the slave mirror for synchronized operation.

ceived synchronization pulse, i.e. s_{h_i}, and the phase error Δt_{ϕ_i} to obtain the synchronization error slices as

$$\Delta s_{\delta_i} = \frac{2^N}{T_{\mathrm{PLL}_{i-1}}} \Delta t_{\delta_i} = s_{\delta_i} + \frac{2^N}{T_{\mathrm{PLL}_{i-1}}} \Delta t_{\phi_i} \,. \tag{6.5}$$

Since only small perturbations are assumed the PLL period in Eq. (6.5) can be approximated by the nominal period $\bar{T}_{\mathrm{mh}}$, i.e.

$$\Delta s_{\delta_i} \approx s_{\delta_i} + \frac{2^N}{\bar{T}_{\mathrm{mh}}} \Delta t_{\phi_i} = s_{\delta_i} + \kappa_{\mathrm{t/s}}^{-1} \Delta t_{\phi_i} \,. \tag{6.6}$$

Furthermore, an additional disturbance input d_{δ_i} has to be added, as the master mirror may deviate from its nominal frequency during operation, which necessitates also a deviation of the slave mirror for correct synchronization. Summariz-

ing, the linearized model for the slave mirror can be expressed as

$$\overbrace{\begin{bmatrix}\Delta t_{\phi_{i+1}}\\ \Delta T_{\Theta_{i+1}}\\ \Delta t_{\delta_{i+1}}\end{bmatrix}}^{\mathbf{x}_{\mathrm{S}_{i+1}}} = \overbrace{\frac{1}{\kappa_{\mathrm{sp}}+\kappa_{\mathrm{d}}}\begin{bmatrix}(\kappa_{\mathrm{sp}}+\kappa_{\mathrm{d}})(\kappa_{\mathrm{c}}+1)-1 & -\kappa_{\mathrm{sp}} & 0\\ 1 & \kappa_{\mathrm{sp}} & 0\\ (\kappa_{\mathrm{sp}}+\kappa_{\mathrm{d}})\kappa_{\mathrm{c}}-1 & -\kappa_{\mathrm{sp}} & 1\end{bmatrix}}^{\mathbf{A}_{\mathrm{S}}} \cdot \overbrace{\begin{bmatrix}\Delta t_{\phi_i}\\ \Delta T_{\Theta_i}\\ \Delta t_{\delta_i}\end{bmatrix}}^{\mathbf{x}_{\mathrm{S}_i}}$$
$$+ \underbrace{\begin{bmatrix}\kappa_{\mathrm{t/s}}\left(\kappa_{\mathrm{c}}-\frac{1}{\kappa_{\mathrm{sp}}+\kappa_{\mathrm{d}}}\right) & 1\\ \kappa_{\mathrm{t/s}}\frac{1}{\kappa_{\mathrm{sp}}+\kappa_{\mathrm{d}}} & 0\\ \kappa_{\mathrm{t/s}}\left(\kappa_{\mathrm{c}}-\frac{1}{\kappa_{\mathrm{sp}}+\kappa_{\mathrm{d}}}\right) & 0\end{bmatrix}}_{\mathbf{B}_{\mathrm{S}}} \cdot \underbrace{\begin{bmatrix}\Delta s_{\mathrm{off}_i}\\ \Delta T_{\mathrm{PLL}_i}\end{bmatrix}}_{\mathbf{u}_{\mathrm{S}_i}} + \underbrace{\begin{bmatrix}\frac{-1}{\epsilon_{\mathrm{c}}(\kappa_{\mathrm{sp}}+\kappa_{\mathrm{d}})} & 0\\ \frac{1}{\epsilon_{\mathrm{c}}(\kappa_{\mathrm{sp}}+\kappa_{\mathrm{d}})} & 0\\ \frac{-1}{\epsilon_{\mathrm{c}}(\kappa_{\mathrm{sp}}+\kappa_{\mathrm{d}})} & 1\end{bmatrix}}_{\mathbf{G}_{\mathrm{S}}} \cdot \underbrace{\begin{bmatrix}E_{\mathrm{ext}_i}\\ d_{\delta_i}\end{bmatrix}}_{\mathbf{w}_{\mathrm{S}_i}}, \quad (6.7)$$

with the measurement equation as

$$\underbrace{\begin{bmatrix}\Delta\tilde{t}_{\phi_i}\\ \Delta\tilde{t}_{\mathrm{ATC}_i}\\ \Delta\tilde{s}_{\delta_i}\end{bmatrix}}_{\mathbf{y}_{\mathrm{S}_{i+1}}} = \underbrace{\begin{bmatrix}1 & 0 & 0\\ 0 & S\,\kappa_{\Theta} & 0\\ 0 & 0 & \kappa_{\mathrm{t/s}}^{-1}\end{bmatrix}}_{\mathbf{C}_{\mathrm{S}}} \cdot \underbrace{\begin{bmatrix}\Delta t_{\phi_i}\\ \Delta T_{\Theta_i}\\ \Delta t_{\delta_i}\end{bmatrix}}_{\mathbf{x}_{\mathrm{S}_i}} + \underbrace{\begin{bmatrix}v_{\phi_i}\\ v_{\mathrm{s}_{\mathrm{ATC}i}}-v_{\phi_i}\\ \kappa_{\mathrm{t/s}}^{-1}(v_{\delta_i}+v_{\phi_i})\end{bmatrix}}_{\mathbf{v}_{\mathrm{S}_i}}, \quad (6.8)$$

where v_{δ_i} considers the synchronization signal timing noise caused by the master due to errors between its DCO and the actual mirror oscillation.

6.2.2. SISO controller design

Fig. 6.3 shows a block diagram of the proposed SISO control concept consisting of a master control block (MCB) and a slave control block (SCB). The master mirror is controlled in amplitude, while the slave has to be controlled in relative phase to the master, to achieve synchronized operation. Both mirrors are controlled by independent PLLs, which compensate for the PLL phase errors Δt_{ϕ} between the mirror zero crossings and the corresponding DCO. The PLL controllers P_{X} and P_{Y} calculate the i-th PLL period as in the 1D scanning control case by utilizing a PI control law, i.e.

$$\begin{aligned} T_{\mathrm{PLL}_i} &= (G_{\mathrm{I}}+G_{\mathrm{P}})\;\Delta t_{\phi_i}+\Gamma_{P_i}\\ \Gamma_{P_{i+1}} &= \Gamma_{P_i}+G_{\mathrm{I}}\,\Delta t_{\phi_i}\,, \end{aligned} \quad (6.9)$$

with the integrator state Γ_P and the gains G_{I} and G_{P}. The MCB in Fig. 6.3 additionally comprises an amplitude controller Ψ consisting of an integrator, to reach the desired amplitude $\bar{\Theta}_{\mathrm{m}}$, and the synchronization pulse generator to provide synchronization signals derived from the corresponding DCO phase slices. The phase detector of the SCB measures the synchronization error slices Δs_{δ}, i.e. the slice difference between the received synchronization pulses and the measured

mirror zero crossings, as described in the previous paragraph. The synchronization controller Υ compensates the obtained synchronization errors by adjusting the driving signal duty cycle as

$$\begin{aligned} s_{\mathrm{off}_{\Upsilon_i}} &= (G_{\Upsilon\mathrm{I}} + G_{\Upsilon\mathrm{P}})\ \Delta s_{\delta_i} + \Gamma_{\Upsilon_i} \\ \Gamma_{\Upsilon_{i+1}} &= \Gamma_{\Upsilon_i} + G_{\Upsilon\mathrm{I}}\,\Delta s_{\delta_i}\,, \end{aligned} \tag{6.10}$$

with the integrator state Γ_Υ and the gains $G_{\Upsilon\mathrm{I}}$ and $G_{\Upsilon\mathrm{P}}$. The slave mirror amplitude at synchronized operation has to be the nominal amplitude as no control input is available to compensate for amplitude errors regardless of the frequency. Hence, the resulting amplitude is given solely by the master mirror frequency and the chosen frequency ratio. A possible solution is to adjust the driving voltage V_p, which allows to compensate for small amplitude variations and is discussed in a separated paragraph at the end of this section.

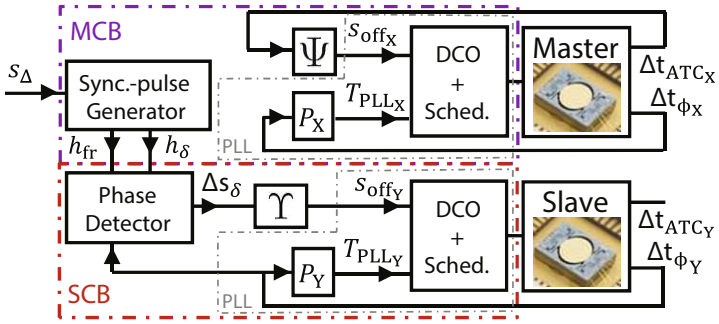

Figure 6.3.: Block diagram of the SISO synchronization control concept for 2D Lissajous scanning. Both mirrors are phase controlled by individual PLLs. The MCB additionally controls the amplitude of the master mirror by duty cycle adjustment and provides synchronization pulses for the SCB. The SCB phase detector measures the synchronization error slices, which the synchronization controller Υ compensates by duty cycle variation.

While the controllers for the MCB can be designed as in the 1D scanning case, i.e. with separated time constants, this is not possible for the SCB as phase errors between the mirror oscillation and the DCO as well as the synchronization errors to the master have to be compensated similarly fast. Hence, the four control gains of the SCB have to be designed based on the derived linearized slave mirror model to provide stable and precise operation. The zero crossing detection noise of both mirrors is considered as the main noise source, affecting the corresponding PLL phase error measurements. A noisy PLL phase error of the master causes the synchronization signals to shift back and forth, leading to a distorted synchronization error measurement by the SCB phase detector. The control gains used

in the following analysis are manually set as a trade-off between noise influence and settling time of the system. Hence, a low noise influence while a settling time of less than a Lissajous scan period is required. For the identified model parameters of the used MEMS mirror and a frequency ratio of $\bar{r} = 92/91$, control gains fulfilling the above conditions are found to be $G_{\mathrm{I}} = -2^{-9}$, $G_{\mathrm{P}} = -2^{-3}$, $G_{\Upsilon\mathrm{I}} = 2^{-12}$ and $G_{\Upsilon\mathrm{P}} = 2^{-1} + 2^{-3}$.

Experimental verification

First, the derived linear model of the synchronized slave mirror is verified in frequency and time domain using artificially generated noise inputs. For noise emulation, the on-board CPU is used, which applies random values to the FPGA in each PLL period. By logging the Ethernet data stream, frequency responses from the disturbance inputs to the synchronization phase error can be derived using FFT. Fig. 6.4a shows the measured frequency responses, which are scaled by the nominal time per phase slice to match the units. The comparison to the corresponding simulated transfer functions $H_{\Delta \mathrm{s}_\delta / v_\delta}$ and $H_{\Delta \mathrm{s}_\delta / v_\phi}$ proves the validity of the proposed model.
For time domain analysis a sudden synchronization error is simulated by a step response at the disturbance input d_δ. Fig. 6.4b shows the measured response over time, which matches with the simulation and also proves that the settling time is less than a Lissajous scan period. Therefore, the dynamics of the slave MEMS mirror, controlled in relative phase to the master, is accurately represented by the derived linearized model.
Second, the proposed synchronization control concept is verified by measurements. An optical evaluation of the projected scan lines is made by the CCD image given in Fig. 6.5a, which shows the obtained Lissajous scanning pattern. The properly projected center grid is clearly visible in the inset at the bottom right. The bright line in the image is caused by a direct reflection of the first mirror scan line on the second mirror cover class. In application, this can be removed by glass coating or other mirror packaging [56]. The proposed fixed frequency ratio between master and slave mirror using the constant slice shift method is verified by varying the master amplitude and consequently its frequency. The obtained RMS values of the PLL frequency ratio error, which is defined by

$$\Delta r_i = \frac{T_{\mathrm{PLL}_{\mathrm{Y}_i}}}{T_{\mathrm{PLL}_{\mathrm{X}_i}}} - \bar{r}\,, \tag{6.11}$$

are shown in Fig. 6.5b for each operation point as a percentage of $\bar{r}$. The average RMS error over all operation points is 0.0029% of $\bar{r}$ and is mainly due to the limited FPGA clock.

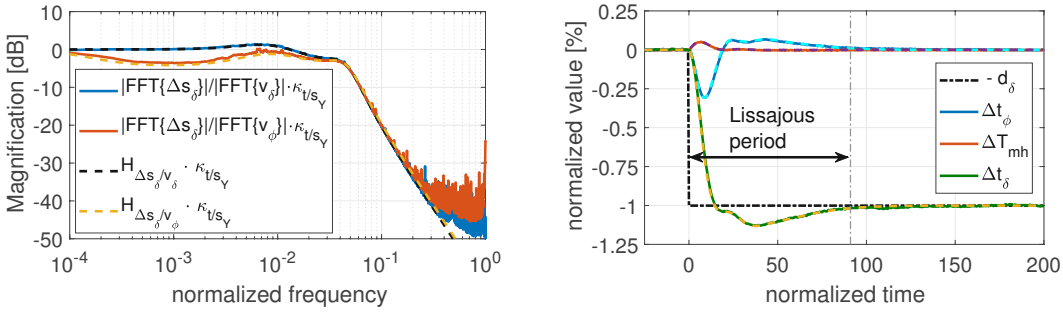

(a) (b)

Figure 6.4.: (a) Comparison of measured and simulated frequency response of the synchronization error on random noise at the inputs v_δ and v_ϕ in closed loop operation. The applied noise values and the measured phase errors are logged at each period for 90 s. A 2 Hz span smoothing filter is applied for better readability and the frequencies are normalized by the nominal slave mirror frequency. (b) Comparison of measured (solid) and simulated (dashed) step response at the synchronization disturbance input d_δ. The linearized model correctly represents the dynamic behavior. The values are normalized by the nominal mirror period $2\,\bar{T}_{\mathrm{mh_Y}}$.

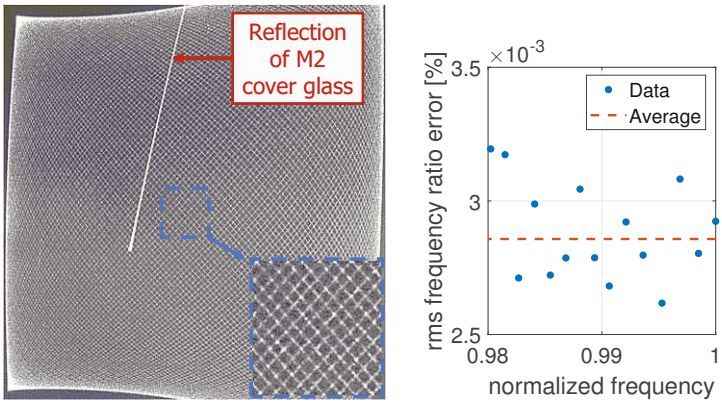

(a) (b)

Figure 6.5.: (a) CCD Image of the projected Lissajous pattern generated by the proposed system using a frequency ratio of 92/91. The visible line is a reflection on the cover glass of the second MEMS mirror M2. (b) RMS value of the frequency ratio error defined by Eq. (6.11) obtained by variation of the master frequency.

The necessity of the continuous synchronization control is shown in Fig. 6.6, where the synchronization controller Υ is turned off and the phase error starts to drift due to random frequency variations. Insets show the obtained Lissajous pattern at the center, which results in a distorted grid if no synchronization control is applied. In closed loop operation, however, the proposed system achieves precise synchronization, as the RMS value of the measured synchronization error is 0.003 %, corresponding to 0.19 mrad (1.34 mrad peak-to-peak). Furthermore, the actual synchronization error is even lower, since the sensing signals are affected by noise and quantization errors, while the MEMS mirror serves as a natural lowpass filter due to its dynamics as shown in Fig. 6.4a.

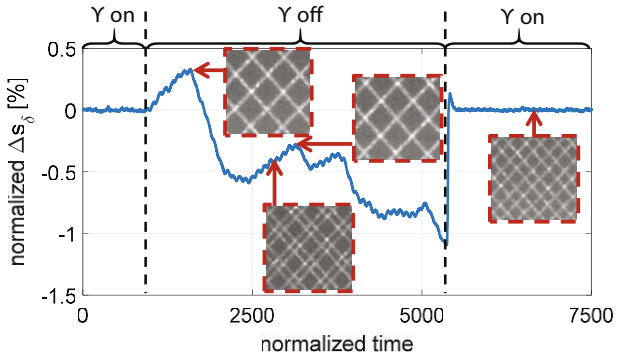

Figure 6.6.: Measured synchronization error slices and Lissajous grid at the image center, when the synchronization controller Υ is on or off. If the control is turned off, the phase starts to drift due to random frequency variations. The phase error slices are normalized by $2^{(N+1)}$ corresponding to a full mirror period.

For precise evaluation of the pixel synchronization errors, the DC laser in Fig. 6.1 is replaced by a pulsed laser and triggered by the frame start signal h_{fr}. Hence, the laser is shot when both mirrors are expected to have zero angle, where their angular velocity is the highest, and hits a CCD after reflection at both mirrors in order to evaluate the optical pointing uncertainty. The corresponding mechanical angle errors are then obtained by

$$\Delta\theta_{\mathrm{X}} = \frac{1}{2}\tan^{-1}\left(\frac{\Delta l_{\mathrm{X}}}{D}\right) \qquad \text{and} \qquad \Delta\theta_{\mathrm{Y}} = \frac{1}{2}\tan^{-1}\left(\frac{\Delta l_{\mathrm{Y}}}{D}\right), \tag{6.12}$$

where Δl_{X} and Δl_{Y} are the relative spot movements on the CCD in the X-axis or Y-axis direction, respectively. Fig. 6.7a shows a CCD image example and a box-plot of the obtained normalized angle errors at the center of the Lissajous grid. The slave errors are higher since the laser triggering signal are derived from the master mirror oscillation. Assuming a sine wave trajectory of the mirrors,

the normalized angle errors correspond to the center pixel synchronization errors, i.e.

$$\frac{\Delta\theta_{\mathrm{X}}}{\bar{\Theta}_{\mathrm{X}}} = \sin\left(\Delta\varphi_{\mathrm{X}}\right) \approx \Delta\varphi_{\mathrm{X}} \qquad \text{and} \qquad \frac{\Delta\theta_{\mathrm{Y}}}{\bar{\Theta}_{\mathrm{Y}}} = \sin\left(\Delta\varphi_{\mathrm{Y}}\right) \approx \Delta\varphi_{\mathrm{X}}\,, \tag{6.13}$$

which are 0.09 mrad RMS (0.57 mrad peak-to-peak) for the X-axis (master) and 0.13 mrad RMS (0.91 mrad peak-to-peak) for the Y-axis (slave).

The achieved precise synchronization allows high resolution Lissajous scanning as shown in Fig. 6.7b, where a frequency ratio $\bar{r}$ of 2350/2349 is used to project a dense grid. The horizontal and vertical distance between the corners of a unit cell at the center of the Lissajous grid, as illustrated in the figure, correspond to a relative phase given by

$$\Delta\varphi_{\mathrm{XU}} = \frac{\pi}{K}\left(\bar{r} - 1\right) \approx \frac{\Delta\theta_{\mathrm{XU}}}{\bar{\Theta}_{\mathrm{X}}} \quad \text{and} \quad \Delta\varphi_{\mathrm{YU}} = \frac{\pi}{K}\left(\frac{1}{\bar{r}} - 1\right) \approx \frac{\Delta\theta_{\mathrm{YU}}}{\bar{\Theta}_{\mathrm{Y}}}\,. \tag{6.14}$$

As the frequency ratio is approximately one, $|\Delta\varphi_{\mathrm{YU}}| \approx |\Delta\varphi_{\mathrm{XU}}| = 1.3\,\mathrm{mrad}$ and are higher than the obtained peak-to-peak errors. As the unit cell is the largest at the image center, the achieved resolution corresponds to at least 1500×1500 constant unit cells of largest size. Hence, with the attained pixel synchronization accuracies above, the high resolution Lissajous scanning is demonstrated by a uniform and symmetric scan grid at the center.

Finally, the external vibration robustness is evaluated using the experimental setup shown in Fig. 6.8a. As the slave mirror relies on the accuracy of the received synchronization pulses sent by the master, errors in both scanning directions are expected if the master mirror is disturbed by vibrations. Hence, as a worst case scenario the holder of the MEMS mirror M2 (master) in the Lissajous scanning setup in Fig. 6.1 is replaced by the piezo-shaker to apply the two calibrated vibration profiles in Fig. 5.22 to the master. Fig. 6.8b shows an evaluation image where the pixels are shot based on the phase slices of the master mirror DCO and its pixel distortion due to the applied vibrations in close-ups. As can be seen, the image has sharp pixels even under exposure of the vibration profile 1, while for the profile 2 the pixels blur into each other, which may lead to critical errors in applications such as automotive lidar. A pointing uncertainty measurement of the pixel at the image center is shown in Fig. 6.8c, where also large errors of up to 0.8° peak-to-peak are observed at the exposure of the vibration profile 2. Furthermore, it reveals that even though the vibration is only applied to the master, the slave shows 60% larger errors due to the inaccurate synchronization signals. For vibration profiles lower than 2 kHz as defined in automotive standards, the proposed Lissajous scanning system achieves the targeted optical resolution of 0.1° for lidar applications. However, to also provide robustness against higher

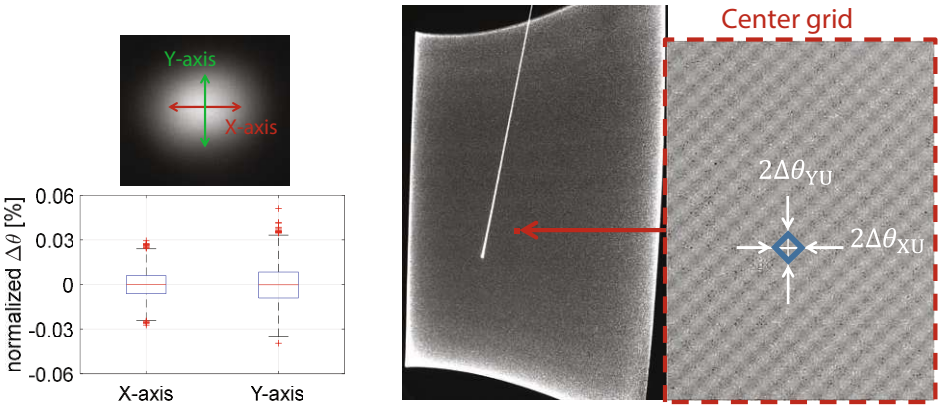

(a) (b)

Figure 6.7.: (a) Image example of a single laser shot hitting the CCD chip and box-plot of the obtained center grid angle errors along both axes calculated by Eq. (6.12) using 3000 captured CCD frames and normalized by their individual nominal amplitudes, i.e. $\bar{\Theta}_{\mathrm{X}}$ and $\bar{\Theta}_{\mathrm{Y}}$. (b) Image of the projected high resolution Lissajous pattern using a frequency ratio of 2350/2349. A close-up of the center grid shows the proper projection by the proposed system. The resolution $\Delta\theta_{\mathrm{XU}}$ and $\Delta\theta_{\mathrm{YU}}$ defined by the corner distance of a unit cell (blue rectangle) are depicted.

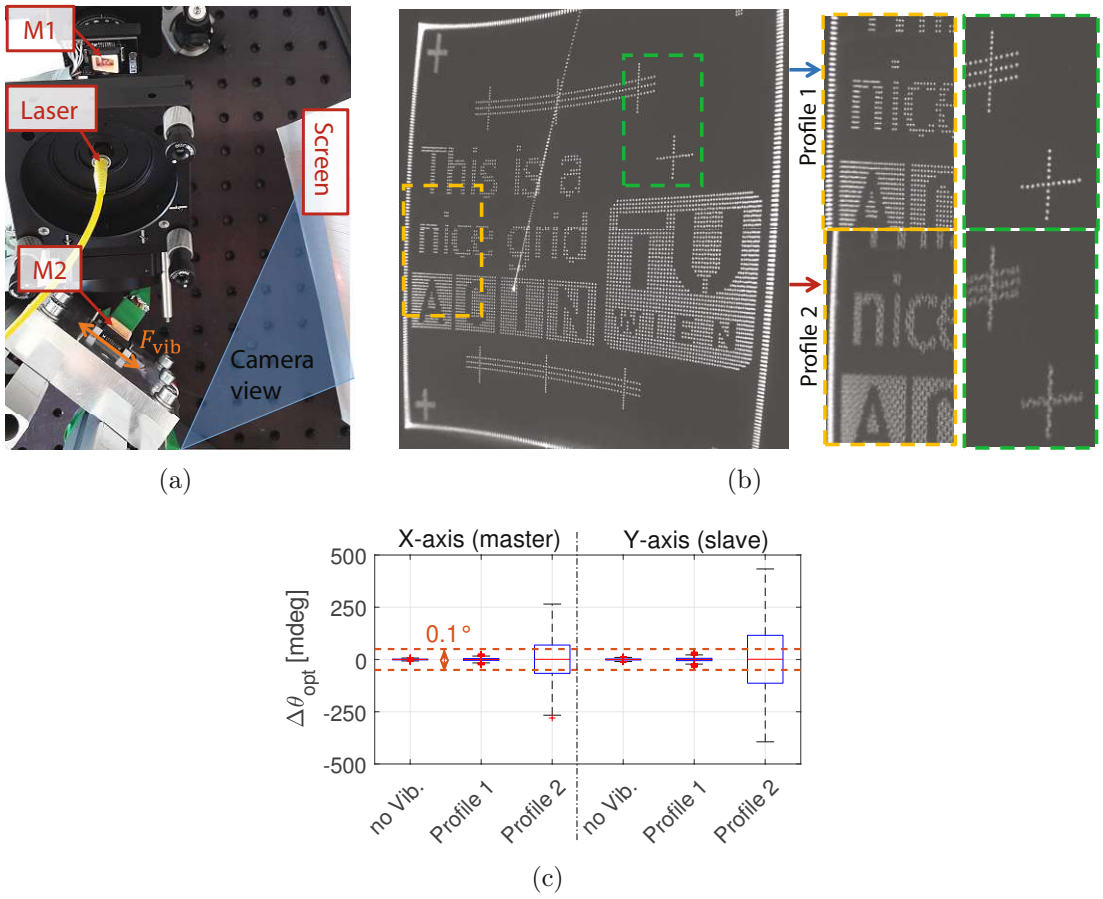

Figure 6.8.: (a) Experimental setup for vibration robustness evaluation of the Lissajous scanning system. The holder of the master mirror (M2) in the Lissajous scanning setup is replaced by a piezo-shaker capable of providing broadband vibration in T_Y direction of the attached MEMS mirror illustrated by F_{vib}. (b) Projected evaluation image with close-ups showing the influence of the vibration profiles on the pixels. (c) Box-plot of the center pixel pointing errors in both scanning directions compared to the targeted resolution criterion of 0.1° for automotive lidar.

frequency vibrations an advanced control concept may be required. Hence, the following paragraph discusses a MIMO control design for vibration suppression.

6.2.3. MIMO controller design

Similar to the 1D scanning system the MIMO control concept can provide superior performance as also the interdependencies of the individual in- and outputs are taken into account and the feedback control can be optimally designed. The

use of a single MIMO controller for both MEMS mirrors is difficult as in general the MEMS mirror half periods and thus the sampling frequencies are different. Furthermore, the approach should be modular such that additional MEMS mirrors can be added and synchronized with low effort. Hence, the proposed control concept is shown in Fig. 6.9 where both axes use individual MIMO LQG servo controllers. For the master, the control design does not differ from the 1D scanning case, while that of the slave needs to be adapted for synchronization control. Hence, the controller of the slave, i.e. $\mathrm{LQG_S}$, is designed based on the control loop in Fig. 6.10 and the linearized slave mirror model.

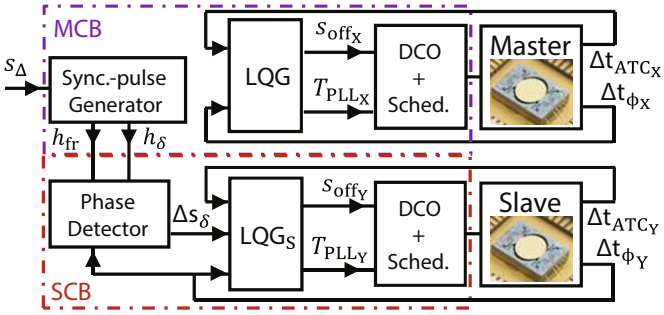

Figure 6.9.: Block diagram of the advanced synchronization control concept for 2D Lissajous scanning. Both mirrors are controlled by individual LQG servo controllers of slightly different design.

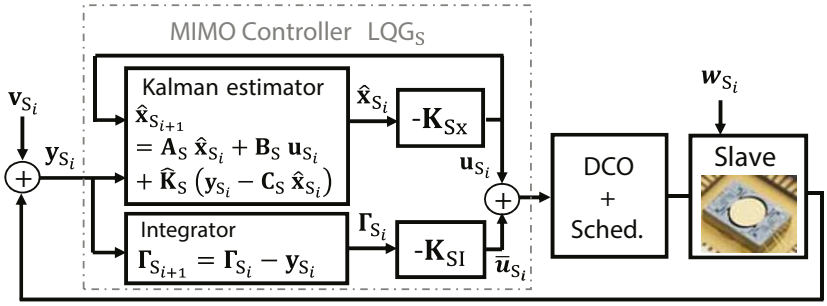

Figure 6.10.: MIMO control scheme for the slave mirror using LQG servo control to compensate disturbances $\mathbf{w}_S$ and to suppress the measurement noise $\mathbf{v}_S$. The controller comprises a Kalman estimator with the gain $\hat{\mathbf{K}}_S$, optimal state feedback gains $\mathbf{K}_{Sx}$ and $\mathbf{K}_{SI}$ as well as an integrator for nominal operation point convergence.

Slave LQR design

With the positive semi-definite weighting matrices $\mathbf{Q}_\mathrm{S}$, $\mathbf{R}_\mathrm{S}$ and $\mathbf{N}_\mathrm{S}$ the cost function for the LQR problem for the SCB is defined as

$$J(\mathbf{u}_\mathrm{S}) = \sum_{i=0}^{\infty} \begin{bmatrix} \mathbf{x}_{\mathrm{S}_i} \\ \mathbf{\Gamma}_{\mathrm{S}_i} \end{bmatrix}^\mathrm{T} \mathbf{Q}_\mathrm{S} \begin{bmatrix} \mathbf{x}_{\mathrm{S}_i} \\ \mathbf{\Gamma}_{\mathrm{S}_i} \end{bmatrix} + \mathbf{u}_{\mathrm{S}_i}^\mathrm{T} \mathbf{R}_\mathrm{S}\, \mathbf{u}_{\mathrm{S}_i} + 2 \begin{bmatrix} \mathbf{x}_{\mathrm{S}_i} \\ \mathbf{\Gamma}_{\mathrm{S}_i} \end{bmatrix}^\mathrm{T} \mathbf{N}_\mathrm{S}\, \mathbf{u}_{\mathrm{S}_i} \,, \tag{6.15}$$

subject to the linearized model in Eq. (6.7) and Eq. (6.8) as constraints. For individual state penalization the weighting matrices are again set to diagonal matrices as

$$\begin{aligned} \mathbf{Q}_\mathrm{S} &= diag\left(W_{\mathrm{t}_\phi}, W_{\mathrm{T}_\Theta}, W_{\mathrm{t}_\delta}, W_{\mathrm{t}_{\phi\mathrm{I}}}, W_{\mathrm{T}_{\Theta\mathrm{I}}}, W_{\mathrm{t}_{\delta\mathrm{I}}}\right) \,, \\ \mathbf{R}_\mathrm{S} &= diag\left(W_{\mathrm{s}_\mathrm{off}}, W_{\mathrm{T}_\mathrm{PLL}}\right) \,, \end{aligned} \tag{6.16}$$

and the coupling matrix $\mathbf{N}_\mathrm{S}$ is set to zero. The difference to the LQR design for the 1D case is that the phase error Δt_ϕ between the DCO and the mirror oscillation are of less importance compared to the synchronization error Δt_δ. This means that to some extend the errors of the DCO are less important as long as the relative phase of the mirror oscillation is correct, i.e. its zero crossings coincide with the received synchronization pulses. Hence, we set $W_{\mathrm{t}_\delta} = 1$ and weight the PLL phase errors much lower, i.e. $W_{\mathrm{t}_\phi} = 10^{-3}$. The weighting value W_{T_Θ} can then be calculated similarly to the 1D case as shown in Eq. (5.22) using the slave mirror parameters.
The integrators only compensate for slow drifts of the environmental conditions to maintain the nominal operation point and are chosen as $W_{\mathrm{t}_{\phi\mathrm{I}}} = 10^{-3}\, W_{\mathrm{t}_\phi}$, $W_{\mathrm{T}_{\Theta\mathrm{I}}} = 10^{-3}\, W_{\mathrm{T}_\Theta}$ and $W_{\mathrm{t}_{\delta\mathrm{I}}} = 10^{-3}\, W_{\mathrm{t}_\delta}$. Variations in the PLL period of the SCB and consequently the timing of its DCO phase slices are of less concern as no signals relevant for a scanning application such as the laser shooting are derived from them, but only from the DCO phase slices of the MCB. Nevertheless, duty cycle control should be still preferred to avoid too large misalignment of the DCO and the mirror oscillation. Hence, the input weighting values are chosen as $W_{\mathrm{s}_\mathrm{off}} = 6 \cdot 10^{-4}\, \kappa_{\mathrm{t/s}}^2$ and $W_{\mathrm{T}_\mathrm{PLL}} = 0.1$, which results in the optimal feedback gains as

$$\mathbf{K}_\mathrm{S} = \begin{bmatrix} \mathbf{K}_\mathrm{Sx} & \mathbf{K}_\mathrm{SI} \end{bmatrix} = \begin{bmatrix} 0.96\,\kappa_{\mathrm{t/s}}^{-1} & 60\,\kappa_{\mathrm{t/s}}^{-1} & -22\,\kappa_{\mathrm{t/s}}^{-1} & 0.001\,\kappa_{\mathrm{t/s}}^{-1} & 0 & 0.7\,\kappa_{\mathrm{t/s}}^{-1} \\ 0.12 & 0.1 & -0.021 & -0.0030 & 0 & 0.0006 \end{bmatrix} . \tag{6.17}$$

As can be seen, with the state vector $\mathbf{x}_\mathrm{S} = [\Delta t_\phi,\ \Delta T_\Theta,\ \Delta t_\delta]^\mathrm{T}$ the duty cycle control mainly compensates for amplitude and synchronization errors, while the PLL period control considers amplitude and PLL phase errors more. Even though amplitude errors influence both inputs according to the state feedback controller, they are ignored by the integrator. This is due to the link of amplitude and

frequency by the nonlinear stiffness, which does not allow to achieve both the compensation of amplitude and synchronization errors at the same time by only the two inputs.

Slave Kalman estimator design

In addition to PLL and amplitude errors the SCB also receives synchronization errors, which can cause a disturbance d_δ due to a true variation of the master mirror frequency and noise v_δ due to a misalignment of the MCB DCO and the master mirror oscillation. Hence, the disturbance and noise covariance matrices for the slave mirror are given as

$$\mathrm{E}\left(\mathbf{w}_{\mathrm{S}_i}^{\mathrm{T}}\mathbf{w}_{\mathrm{S}_i}\right) = \begin{bmatrix} \sigma_{\mathrm{E_{ext}}}^2 & 0 \\ 0 & \sigma_{\mathrm{d}_\delta}^2 \end{bmatrix} \quad \text{and}$$

$$\mathrm{E}\left(\mathbf{v}_{\mathrm{S}_i}^{\mathrm{T}}\mathbf{v}_{\mathrm{S}_i}\right) = \begin{bmatrix} \sigma_{v_\phi}^2 & -\sigma_{v_\phi}^2 & \sigma_{v_\phi}^2\,\kappa_{\mathrm{t/s}}^{-1} \\ -\sigma_{v_\phi}^2 & \sigma_{v_{\mathrm{s_{ATC}}}}^2 + \sigma_{v_\phi}^2 & -\sigma_{v_\phi}^2\,\kappa_{\mathrm{t/s}}^{-1} \\ \sigma_{v_\phi}^2\,\kappa_{\mathrm{t/s}}^{-1} & -\sigma_{v_\phi}^2\,\kappa_{\mathrm{t/s}}^{-1} & \left(\sigma_{v_\delta}^2 + \sigma_{v_\phi}^2\right)\kappa_{\mathrm{t/s}}^{-2} \end{bmatrix}. \tag{6.18}$$

With the same setting as in the 1D case, i.e. $\sigma_{v_\phi} = 15\,\mathrm{ns}$, $\sigma_{v_{\mathrm{s_{ATC}}}} \approx 2.25\,\sigma_{v_\phi}$ and $\sigma_{\mathrm{E_{ext}}} = 1.25\,\epsilon_{\mathrm{c}}\,(\kappa_{\mathrm{sp}} + \kappa_{\mathrm{d}})\,\sigma_{v_\phi}$, the disturbance is considered by $\sigma_{\mathrm{d}_\delta} = 2\,\sigma_{v_\phi}$ corresponding to rather strong environmental influences to the master, while the MCB DCO is assumed to have low errors due to the LQG control, i.e. $\sigma_{v_\delta} = 0.2\,\sigma_{v_\phi}$. The corresponding Kalman estimator design is then given as

$$\hat{\mathbf{K}}_{\mathrm{S}} = \begin{bmatrix} 1.3 & 0.041\,\frac{1}{S\,\kappa_\Theta} & 0 \\ -0.49 & 0.012\,\frac{1}{S\,\kappa_\Theta} & 0 \\ 0.34 & 0.041\,\frac{1}{S\,\kappa_\Theta} & 0.99\,\kappa_{\mathrm{t/s}} \end{bmatrix}. \tag{6.19}$$

The chosen values for $\sigma_{\mathrm{d}_\delta}$ and σ_{v_δ} let the Kalman estimator to trust the measured synchronization signals as can be seen by the Kalman gain of 0.99.

Experimental verification

To evaluate the SISO and the MIMO control performance under external vibration, two pixels are shot based on the master DCO phase slices, one at the center and the other at the corner of the scanning pattern. Both pixels are monitored by CCD cameras as shown in Fig. 6.11a to perform pointing uncertainty measurements. This allows to evaluate phase errors mainly causing pixel errors at the center of the FoV and amplitude errors, which effect the pixel at the corners. Hence, by analyzing the pixel movement in both directions corresponding to the MEMS mirror axes, the results in Fig. 6.11b are obtained, where both vibration profiles are applied to the master mirror. As can be seen, the MIMO LQG control

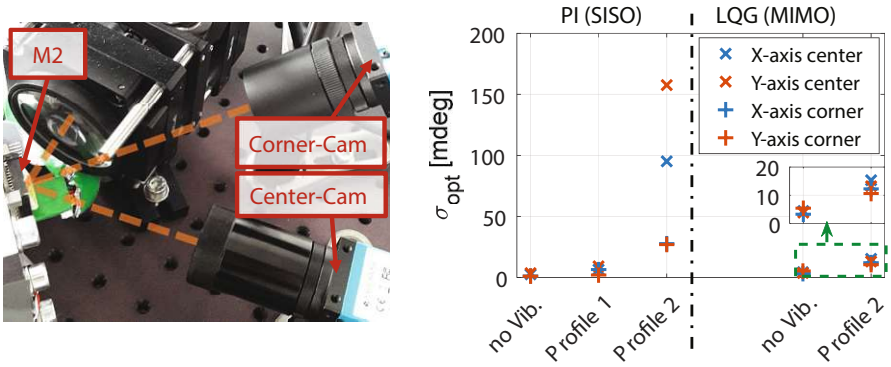

Figure 6.11.: Pointing uncertainty evaluation of center and corner pixel for 2D Lissajous scanning. (left) Setup with two CCD cameras to monitor the center and the corner pixel. (right) Evaluation results with optical standard deviations in both corresponding scanning axes for the two pixel positions. The vibration profiles are applied by the piezo-shaker in T_Y direction of the master mirror.

for both axes shows superior vibration robustness even at vibration frequencies close to the MEMS mirror scanning frequency, reducing the worst optical pointing uncertainty by 90% to about 15 mdeg.

Fig. 6.12 shows averaged images containing multiple pixels at the center of the FoV during vibration exposure for SISO and MIMO control. As can be seen, for SISO control the vibration profile 1 (b) does not cause a significant blur of the pixels, while at profile 2 (c) the pixels almost disappear due to the large errors. An increased image brightness in Fig. 6.12c reveals that the pixels mainly blur along the corresponding scan line, which are either in right or left diagonal direction, resulting in a zigzag shaped pixel distribution. This shows that the PLL phase error of the master and the synchronization error of the slave are correlated for the main vibration influence. Fig. 6.12d shows the MIMO control concept under exposure of vibration profile 2, where the most errors are compensated. The remaining errors also show a slight blur of the pixels along the corresponding scan line direction.

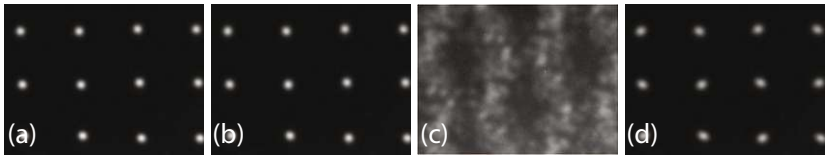

Figure 6.12.: Averaged CCD image of multiple pixels at the center of the FoV with vibration exposure to the master mirror. The images show 125 accumulated CCD frames using SISO control with (a) no vibration, (b) vibration profile 1 and (c) vibration profile 2 (image brightness increased for visibility). The image (d) shows MIMO control during exposure of vibration profile 2.

6.3. Master-slave-slave synchronization concept

The proposed master-slave (MS) synchronization approach has the inherent issue that errors of the master consequently propagate to the slave due to fast variations of the master DCO causing errors in both scanning directions. Another possible synchronization approach is to generate fixed reference signals for both MEMS mirrors with the appropriate frequency ratio and to operate both MEMS mirrors as slavesv (M-SS). However, this approach may result in amplitude errors for both MEMS mirrors as each device has a slightly different amplitude at the same frequency due to manufacturing tolerances. The M-SS synchronization approach shown in Fig. 6.13 combines both methods by introducing an additional time-normalized master DCO (M-DCO) and controlling both MEMS mirrors with SCBs. Both SCBs receive synchronization pulses from the M-DCO and are of the same design except the gain setting of the MIMO controller, which is based on the corresponding MEMS mirror model and the operation point. To operate the X-axis mirror at its nominal operation point, i.e. at nominal amplitude, the controller Ψ is used, which applies a simple integral law to adjust the M-DCO frequency with a low gain to cause no dynamic effects. Hence, in steady state the M-DCO sends the synchronization signal h_{δ_X}, whose period correspond to the X-axis mirror half period $\bar{T}_{\mathrm{mh_X}}$ at nominal operation, while the period of h_{δ_Y} is given by the chosen frequency ratio. This provides a decoupling of both axes as the Y-axis SCB receives synchronization signals, which do not depend on the dynamic errors of the X-axis and its DCO. The MIMO controllers can be designed as previously based on the slave mirror model and the corresponding mirror parameters, except that the synchronization disturbance d_δ and noise v_δ can be considered low or even not present due to the decoupling. All signals relevant for a scanning application such as pixel shooting are based on the M-DCO phase slices.

Fig. 6.14a shows pointing uncertainty measurements at the center and the

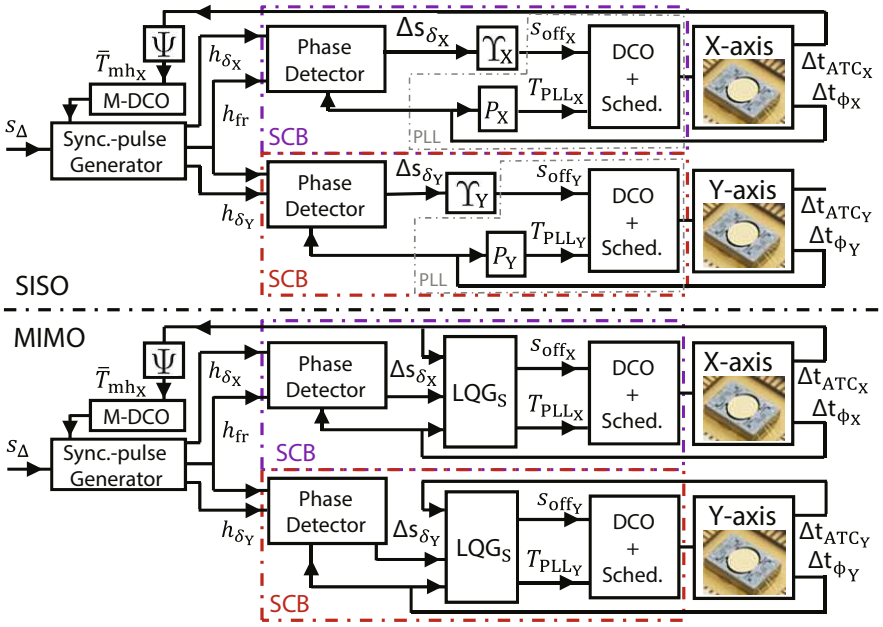

Figure 6.13.: Blockdiagram of the M-SS synchronization control concept with decoupled scanning axes using SISO (top) or MIMO (bottom) control. The additional M-DCO provides synchronization signals for both axes based on its phase slices and adjusts its frequency based on the master mirror amplitude errors with the controller Ψ. Both MEMS mirrors are controlled by the same SCBs with individually configured controllers.

corner pixel for both proposed synchronization concepts with SISO and MIMO control. As can be seen, the Y-axis mirror shows almost no influence by the exposure of the vibration profiles to the X-axis in the M-SS case. On the other hand, the errors of the X-axis are higher compared to the MS case, because the X-axis has to additionally synchronize to the M-DCO to which the laser shot timing is related. The insets reveal that for the MIMO LQG control the errors are either almost equally distributed on both axes for the MS case or only on one axis but higher for the M-SS case. Specifically, the worst optical pointing uncertainty during vibration exposure to the X-axis increase by about 33% to 20 mdeg for the M-SS concept, while the Y-axis is not influenced at all. Fig. 6.14b shows the pixel blur if 3000 single shot CCD frames are accumulated during exposure of vibration profile 2 using SISO PI control. In the MS case the errors are along both axes, which again show a significant correlation. In contrast to the MS synchronization approach the M-SS concept effectively decouples both axes as the pixels blur only along the X-axis. Considering simultaneous disturbances in both scanning axes solely the Y-axis errors increase for both synchronization concepts, while the X-axis keeps the same. Hence, the MS synchronization concept results in precise X-axis scanning with increased Y-axis errors, while the M-SS concept provides similar errors in both axes.

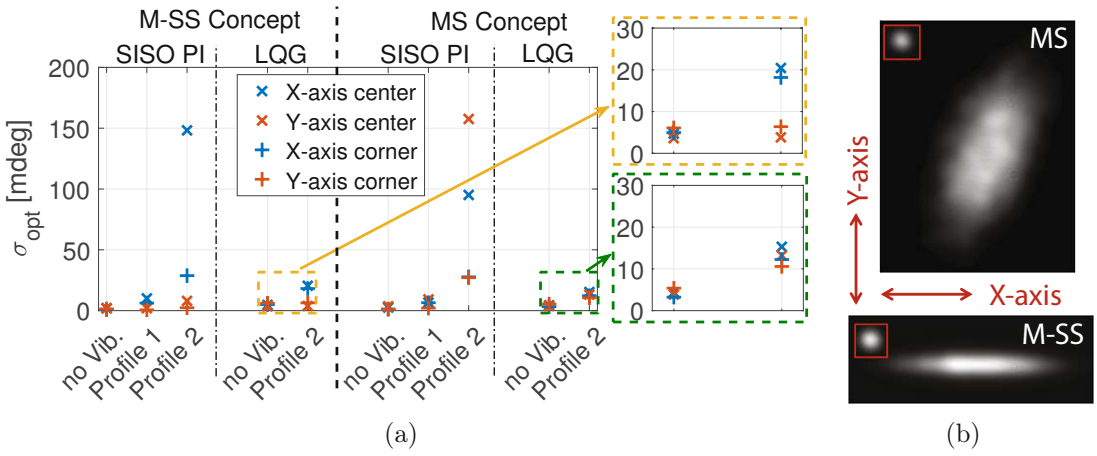

Figure 6.14.: (a) Pointing uncertainty evaluation of center and corner pixel for 2D Lissajous scanning using two different synchronization approaches. At vibration exposure to the X-axis mirror the M-SS concept shows almost no errors in Y-axis but higher errors in X-axis. Insets show the different error distribution on both axes for LQG control depending on the synchronization concept. (b) Blur of the center pixel with 3000 accumulated frames for both synchronization methods using SISO PI control. The insets show the pixel size captured by one frame.

6.4. Slave amplitude adjustment

The simultaneous compensation of amplitude and synchronization errors of the slave mirror using driving period and duty cycle control is only possible if the resulting amplitude at synchronized operation is equal to the nominal amplitude. However, in the application small amplitude errors may occur due to manufacturing tolerances or environmental changes, which can be compensated by adjusting the driving voltage V_p. A simple concept is to add an integrator to the SCB, which slowly adjusts the driving voltage based on the measured amplitude errors. A simulation using the nonlinear SDoF model in Section 3.2 reveals that the possibility of amplitude adjustment strongly depends on the nominal mirror amplitude as also shown in [151]. For example, at the nominal amplitude of 11° a variation of the driving voltage from 75 V to 140 V reduces the amplitude by about 0.6° while at a nominal amplitude of 9° the corresponding amplitude reduction is almost double. This is due to the higher electrostatic stiffness generated by the comb-drives compared to the stiffness of the suspension at lower amplitudes. Hence, to allow an amplitude compensation at high nominal amplitudes the comb-drives have to be designed strong enough and large driving voltage changes may be necessary. In Fig. 6.15a the compensation of a slave mirror amplitude error is demonstrated, which corresponds to an amplitude change of about 0.3°. During the compensation the frequency ratio between both axes is not influenced as can be seen in Fig. 6.15b, resulting in a correct projection of the Lissajous grid. Similarly, also the driving voltage of the master mirror can be adjusted to vary its frequency at the nominal amplitude and to possibly reduce the tuning effort of the slave.

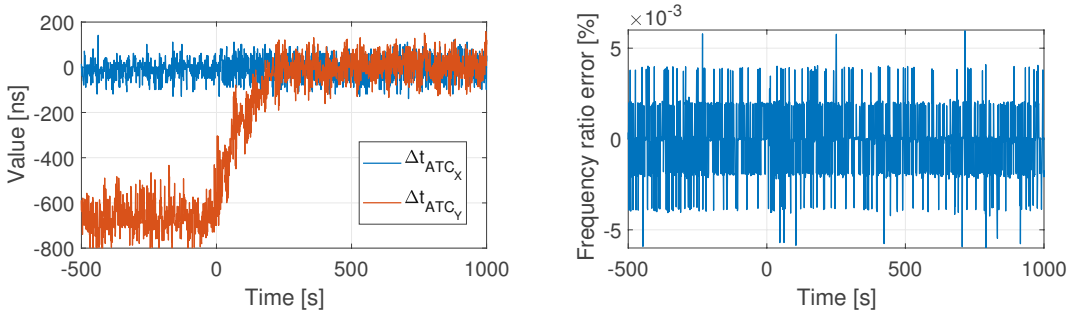

(a) (b)

Figure 6.15.: Compensation of slave mirror amplitude errors (a) by driving voltage control and resulting frequency ratio errors (b). The initial slave mirror amplitude error is compensated by turning on the driving voltage integrator at t=0. The frequency ratio is not influenced by the slow driving voltage adjustment.

6.5. Summary

Lissajous scanning requires a precisely synchronized fixed frequency ratio between both scanning axes, which has to be ensured even in harsh environments such as automotive applications. The time-normalized DCO allows a simple method to synchronize multiple scanners with a fixed frequency ratio, where a master sends synchronization pulses to the slaves as demonstrated by a Lissajous scanning system using two single-axis MEMS mirrors achieving an average RMS frequency ratio error of 0.0029%. The linearized MEMS mirror model of the slave is extended by the synchronization method and used to design simple SISO controllers from phase delay to PLL period and from synchronization error to duty cycle, respectively. Experimental results verify the model validity resulting in a settling time of less than a Lissajous period and a center pixel synchronization error of less than 0.13 mrad RMS, enabling high resolution Lissajous scanning. Due to the master-slave structure a vibration exposure solely to the master mirror consequently results in errors of both axes, where the slave shows even 60% larger errors with a significant correlation. For improved vibration suppression both the master and the slave are controlled by dedicated MIMO LQG servo controllers, improving the worst optical pointing uncertainty during vibration exposure to the master by 90% to about 15 mdeg.

To allow an effective decoupling of both scanning axes, another DCO is added to provide synchronization signals to both axes and to manage the pixel scheduling by its phase slices. Experimental results verify the decoupling, showing errors only in the axis exposed to vibrations, while the worst optical pointing uncertainty increases by 33% to 20 mdeg due to the additional burden of the synchronization control.

As the slaves use the driving signal period and duty cycle for phase delay and synchronization control, the resulting amplitude can only be influenced by the driving voltage. Simulations reveal that an increase in driving voltage lowers the amplitude at the same scanning frequency due to the increases electrostatic stiffness, achieving an amplitude error adjustment of 0.3° in experiments, while the fixed frequency ratio is kept.

CHAPTER 7

Advanced Scanning System Concepts[1]

In this chapter two concepts are proposed enhancing the performance of conventional systems, the laser shot correction (LSC) and the adaptive Lissajous scanning. In contrast to a dedicated controller aiming to minimize the dynamic errors of the scanner, e.g. induced by external vibrations, the LSC corrects the pixel errors for 1D or raster scanning by the laser scheduling without influence to the system dynamics. The adaptive Lissajous scanning allows to overcome the shortcoming of inflexible scan patterns in conventional Lissajous scanning by a dedicated phase modulation of at least one axis, generating for example a region of interest (ROI) in the FoV with dense pixels.

7.1. Laser shot correction

Dynamic variations of the mirror frequency and amplitude caused by environmental influences such as EMI or vibrations, leading to wrong pixel timings and therefore errors in the application accuracy. Advanced control methods as the MIMO control show effective suppression of the dynamic errors, but require a rather high variation of the control inputs such as the duty cycle of the driving signal, possibly reaching limits in the implementation. For too high variations the linearized model might not be valid anymore due to the inherent nonlinear behavior of the electrostatic stiffness and energy injection, resulting in inaccurate estimations of the states by the Kalman estimator and a non-optimal state feedback controller or even cause instability. However, for 1D line scanning systems

[1]Parts of this chapter are also published in
[178] D. Brunner, H. W. Yoo, R. Schroedter and G. Schitter. "Adaptive Lissajous scanning pattern design by phase modulation". Opt. Express, 29(18):27989–28004, 2021.

or the fast axis of raster scanning systems where despite dynamic errors the correct pixel position is still passed by the trajectory in the desired resolution limit, the pixel errors can be compensated by a simple shift in the laser shot timing. Such a LSC method is illustrated in Fig. 7.1, where three example pixels are corrected by shifts in the DCO phase slices using the measured phase and amplitude errors. The expected trajectory is defined by the nominal amplitude and the phase corresponding to the DCO phase slices. Hence, at nominal operation a constant phase slice s_{LS_j} corresponds to a constant mirror angle, i.e. the pixel j. However, it has to be considered that the mirror trajectory has half the frequency of the DCO, which means that the DCO shows two phase slice overflows during one mirror period corresponding to 2^{N+1} slices and has to be considered to distinguish positive and negative angles. Due to dynamic errors in period i the actual mirror trajectory deviates from the expected trajectory, whose effect on the pixel j is compensated by the phase slice shifts $\Delta s_{\mathrm{LS}_{j,i}}$ minimizing errors in the application. The necessary phase slice shifts for a pixel depends on its location on the mirror trajectory and the measured phase and amplitude errors as shown in the following Subsection.

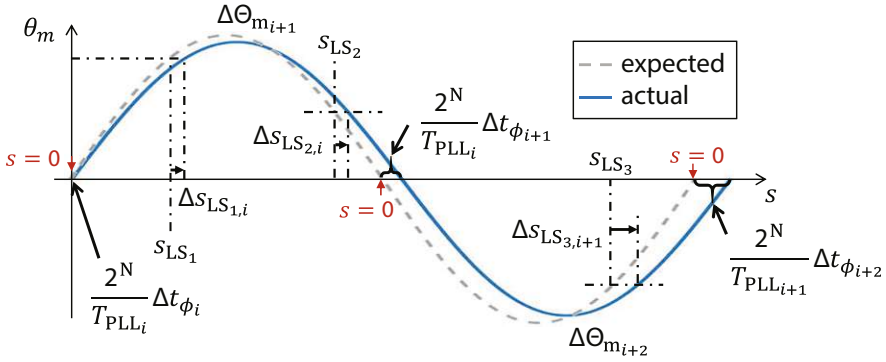

Figure 7.1.: Illustration of the laser shot correction principle. The pixels shot at the phase slices s_{LS_j} are erroneous due to the deviation of the actual trajectory from the expected trajectory. The timing of the pixels is shifted by the corresponding phase slice shifts $\Delta s_{\mathrm{LS}_{j,i}}$ to compensate for the errors.

7.1.1. Correction algorithm

The proposed correction algorithm is based on a first order approximation of the phase, frequency and amplitude error influences on the pixel position. For simplicity it is assumed that the mirror trajectory can be approximated by a sine wave, i.e. at nominal operation the angular position of a pixel shot during one

DCO period at phase slice $s_{\mathrm{LS}_j} \in [0, 2^N - 1]$ is given by

$$\theta_{\mathrm{m}_j} = \bar{\Theta}_{\mathrm{m}} \sin\left(\pi \frac{s_{\mathrm{LS}_j}}{2^N}\right) , \tag{7.1}$$

where the sign of θ_{m_j} can be either positive or negative according to the current mirror half swing. In accordance with a first order approximation, the effects of phase or frequency errors on the resulting pixel position are analyzed separately from those of amplitude errors. Hence, the obtained phase slice shifts consist of terms solely related to phase errors $\Delta s_{\mathrm{LS}\phi_{j,i}}$ or to amplitude errors $\Delta s_{\mathrm{LS}\Theta_{j,i}}$ as

$$\Delta s_{\mathrm{LS}_{j,i}} = \Delta s_{\mathrm{LS}\phi_{j,i}} + \Delta s_{\mathrm{LS}\Theta_{j,i}} . \tag{7.2}$$

Correction of phase and frequency errors

For the analysis of phase and frequency errors, the mirror is assumed to operate at nominal amplitude. In this context frequency errors do not mean deviations from the nominal frequency but rather differences between the mirror and the PLL frequency, causing incorrect phase slices. Hence, the condition to compensate the pixel errors by the phase slice shifts $\Delta s_{\mathrm{LS}\phi_{j,i}}$ can be expressed as

$$\bar{\Theta}_{\mathrm{m}} \sin\left(\pi \frac{s_{\mathrm{LS}_j}}{2^N}\right) \stackrel{!}{=} \bar{\Theta}_{\mathrm{m}} \sin\left(\pi \frac{1}{T_{\mathrm{mh}_{i+1}}} \left(\underbrace{T_{\mathrm{PLL}_i} \frac{s_{\mathrm{LS}_j} + \Delta s_{\mathrm{LS}\phi_{j,i}}}{2^N}}_{\text{time since } s=0} + \Delta t_{\phi_i} \right)\right) . \tag{7.3}$$

As the phase slice shifts are typically small, i.e. $\Delta s_{\mathrm{LS}\phi_{j,i}} \ll 2^N$, the above condition can be rewritten by only using the arguments of the sine functions as

$$\frac{s_{\mathrm{LS}_j}}{2^N} \stackrel{!}{=} \frac{1}{T_{\mathrm{mh}_{i+1}}} \left(T_{\mathrm{PLL}_i} \frac{s_{\mathrm{LS}_j} + \Delta s_{\mathrm{LS}\phi_{j,i}}}{2^N} + \Delta t_{\phi_i} \right) . \tag{7.4}$$

Using the expression of the mirror half period $T_{\mathrm{mh}_{i+1}} = T_{\mathrm{PLL}_i} + \Delta t_{\phi_i} - \Delta t_{\phi_{i+1}}$, the above condition can be solved after the phase slice shifts and approximated as

$$\begin{aligned} \Delta s_{\mathrm{LS}\phi_{j,i}} &= \frac{s_{\mathrm{LS}_j} - 2^N}{T_{\mathrm{PLL}_i}} \Delta t_{\phi_i} - \frac{s_{\mathrm{LS}_j}}{T_{\mathrm{PLL}_i}} \Delta t_{\phi_{i+1}} \\ &\approx \underbrace{\frac{s_{\mathrm{LS}_j} - 2^N}{\bar{T}_{\mathrm{mh}}}}_{\beta_{\phi_j}} \Delta t_{\phi_i} + \underbrace{\frac{-s_{\mathrm{LS}_j}}{\bar{T}_{\mathrm{mh}}}}_{-\beta_{\phi_j} - \frac{2^N}{\bar{T}_{\mathrm{mh}}}} \Delta t_{\phi_{i+1}} , \end{aligned} \tag{7.5}$$

with the approximation $T_{\mathrm{PLL}_i}^{-1} \approx \bar{T}_{\mathrm{mh}}^{-1}$. Hence, the phase and frequency correction needs the previous and the future phase error and weights them according to β_{ϕ_j},

which is linearly dependent on the nominal pixel phase slice s_{LS_j}.

Correction of amplitude errors

For the correction of pixel errors due to amplitude deviations, the mirror trajectory is linearized at the corresponding pixel position, while errors between mirror and PLL frequency are ignored or assumed to be small. Hence, the necessary phase slice shift to compensate for an amplitude error can be expressed as

$$\Delta s_{\mathrm{LS}\Theta_{j,i}} \approx \frac{\mathrm{d}s_{\mathrm{LS}_j}}{\mathrm{d}\bar{\Theta}_{\mathrm{m}}} \Delta\Theta_{\mathrm{m}_{i+1}} \,, \tag{7.6}$$

which already reveals that the future amplitude error is needed to properly correct the pixel. With the definition of the mirror trajectory in Eq. (7.1), the derivative is given as

$$\begin{aligned} \frac{\mathrm{d}s_{\mathrm{LS}_j}}{\mathrm{d}\bar{\Theta}_{\mathrm{m}}} = \frac{2^N}{\pi} \frac{\mathrm{d}}{\mathrm{d}\bar{\Theta}_{\mathrm{m}}} \sin^{-1}\left(\frac{\theta_{\mathrm{m}_j}}{\bar{\Theta}_{\mathrm{m}}}\right) &= \frac{2^N}{\pi} \frac{-\theta_{\mathrm{m}_j}}{\bar{\Theta}_{\mathrm{m}}\sqrt{\bar{\Theta}_{\mathrm{m}}^2 - \theta_{\mathrm{m}_j}^2}} \\ &= \frac{-2^N}{\pi\,\bar{\Theta}_{\mathrm{m}}} \tan\left(\pi\frac{s_{\mathrm{LS}_j}}{2^N}\right) \,, \end{aligned} \tag{7.7}$$

where the tangent is obtained by utilizing trigonometric identities. By combining Eq. (7.6),(7.7) and (3.40), the corresponding phase slice shift of a pixel j results in

$$\begin{aligned} \Delta s_{\mathrm{LS}\Theta_{j,i}} &= \frac{-2^N}{\pi\,\bar{\Theta}_{\mathrm{m}}} \tan\left(\pi\frac{s_{\mathrm{LS}_j}}{2^N}\right) \Delta\Theta_{\mathrm{m}_{i+1}} \\ &= \underbrace{\frac{-2^N}{\pi\,\bar{\Theta}_{\mathrm{m}}} \tan\left(\pi\frac{s_{\mathrm{LS}_j}}{2^N}\right) \kappa_\Theta}_{\beta_{\Theta_j}} \Delta T_{\Theta_{i+1}} \,, \end{aligned} \tag{7.8}$$

where β_{Θ_j} is pixel position dependent and diverges for angles close to the mirror amplitude as shown in Fig. 7.2a for a nominal amplitude of $\bar{\Theta}_{\mathrm{m}} = 15^\circ$. This is due to the used linearization, which cannot deal with the relatively large curvature around the amplitude point. Fig. 7.2b shows the theoretical minimum pixel position errors defined as

$$\Delta\theta_{\mathrm{m}_{j,i}} = \bar{\Theta}_{\mathrm{m}} \sin\left(\pi\frac{s_{\mathrm{LS}_j}}{2^N}\right) - \left(\bar{\Theta}_{\mathrm{m}} + \Delta\Theta_{\mathrm{m}_i}\right) \sin\left(\pi\frac{s_{\mathrm{LS}_j} + \Delta s_{\mathrm{LS}\Theta_{j,i}}}{2^N}\right) \,, \tag{7.9}$$

assuming an amplitude variation of $\Delta\Theta_{\mathrm{m}_i} = \pm 0.1^\circ$, which can be expected as maximum error in a worst case vibration scenario using SISO control (see Fig. 5.23b). Hence, any pixel position error caused by amplitude variations in application is

expected to be between these two extreme cases represented by the solid and the dashed curves in the figure with and without the LSC. The figure reveals that the targeted resolution of $\Delta\theta_\mathrm{m} = 0.05^\circ$ is only achieved in the range of $-4^\circ \leq \theta_\mathrm{m} \leq 4^\circ$ by the given amplitude error without LSC. The proposed LSC reduces the pixel position errors independent of the sign of the amplitude variation, which is because the main residual approximation errors are of second order, i.e. depend on $\Delta\Theta^2_{\mathrm{m}_i}$. Hence, the targeted resolution can be still achieved in the range of $-14.95^\circ \leq \theta_\mathrm{m} \leq 14.95^\circ$ at a nominal amplitude of 15°. This defines the theoretically guaranteed FoV of slightly less than the nominal FoV considering the maximum expected amplitude variations due to environmental influences. However, such limitation can be overcome by advanced pixel shooting algorithms, which may schedule the pixels close to the amplitude point at periods where the amplitude errors are positive, i.e. the amplitude is $\geq 15^\circ$ to ensure that the pixels are reached. Furthermore, considering an automotive long range forward looking lidar application the most outer pixels are typically less critical as the car moves along the center direction.

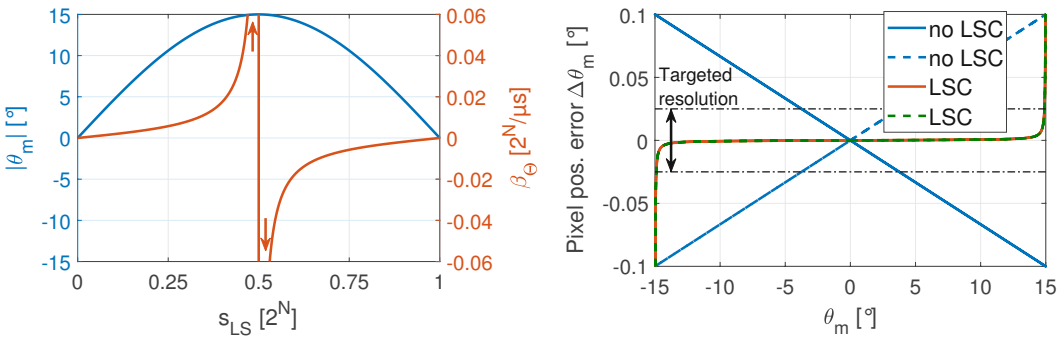

(a) (b)

Figure 7.2.: (a) Pixel position and corresponding amplitude correction factor. The amplitude correction factor diverges for angles close to the mirror amplitude due to the linearization. (b) Pixel position error for amplitude variations of 0.1° (solid) and -0.1° (dashed) with and without the laser shot correction.

7.1.2. Error prediction

The LSC correction algorithm is summarized as

$$\Delta s_{\mathrm{LS}_{j,i}} = \beta_{\phi_j}\,\Delta t_{\phi_i} + \left(-\beta_{\phi_j} - \kappa_{\mathrm{t/s}}^{-1}\right)\,\Delta t_{\phi_{i+1}} + \beta_{\Theta_j}\,\Delta T_{\Theta_{i+1}}\,, \tag{7.10}$$

which only needs the two pixel position dependent parameters, i.e. β_{ϕ_j} and β_{Θ_j} as well as the phase error of the current period i and the phase and amplitude

errors of the following period $i+1$. However, as measurements of phase and amplitude are only available until the period i, a predictor is necessary to allow the LSC implementation. Hence, the Kalman estimator used for the MIMO control in Section 5.2.2 is adapted to also provide a state prediction output as shown in Fig. 7.3. For clarity we introduce the subscript nomenclature that $\hat{\mathbf{x}}_{i|i}$ is an estimate of $\mathbf{x}_i$ based on i measurements, while $\hat{\mathbf{x}}_{i+1|i}$ is a prediction of $\mathbf{x}_{i+1}$ also based on i measurements. The Kalman estimator state equation with the Kalman gain in Eq. (5.25) then yields

$$\hat{\mathbf{x}}_{i+1|i} = \mathbf{A}\,\hat{\mathbf{x}}_{i|i-1} + \mathbf{B}\,\mathbf{u}_i + \hat{\mathbf{K}}\left(\mathbf{y}_i - \mathbf{C}\,\hat{\mathbf{x}}_{i|i-1}\right) , \tag{7.11}$$

providing the predicted value. The update equation is then given as

$$\hat{\mathbf{x}}_{i|i} = \hat{\mathbf{x}}_{i|i-1} + \mathbf{L}\left(\mathbf{y}_i - \mathbf{C}\,\hat{\mathbf{x}}_{i|i-1}\right) , \tag{7.12}$$

with the innovation gain $\mathbf{L}$ also obtained by the MATLAB function *kalman*. The controller in the block diagram can be either the proposed SISO PI control concept or the MIMO LQR state feedback controller with the integrator as the Kalman estimator is already implemented.

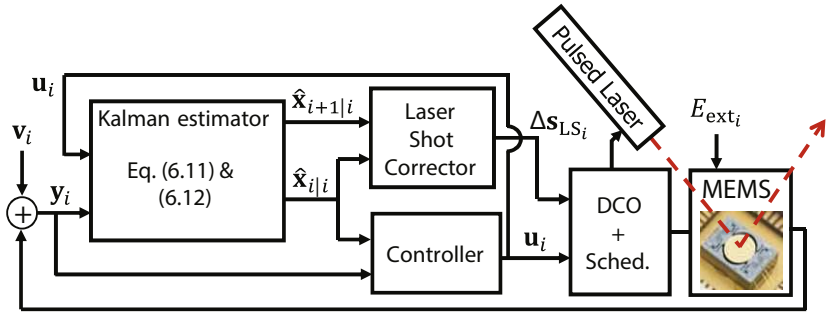

Figure 7.3.: Block diagram of the 1D MEMS scanning system with LSC. The laser shot corrector receives the estimated and predicted errors from the Kalman estimator and adapts the laser shot timing according to Eq. (7.10). The phase slice shifts of the scheduled pixels in period i are merged into the vector $\Delta\mathbf{s}_{\mathrm{LS}_i}$. The controller can be either of SISO or MIMO type.

7.1.3. Experimental verification

Fig. 7.4 shows the setup used for LSC evaluation. The MEMS mirror is mounted on the piezo-shaker to provide dynamic disturbances. A DC and a pulsed laser are combined, deflected by the MEMS mirror and hit a ruler with an angular grid. Both lasers are slightly tilted to each other such that both hit the MEMS

mirror at its center, but are shifted vertically on the ruler as can be seen in the bottom of the figure. Hence, the scan line variation and the pixel position errors at several angular positions can be observed simultaneously. The bottom picture of Fig. 7.4 shows two SISO PI controlled cases with and without LSC at the exposure to strong single frequency vibration with a low offset frequency for visibility. Two snapshots are taken for each case with maximum and minimum scan line amplitude. As can be seen, the seven pixel positions stay almost the same if the LSC is used, while relatively large errors occur in the case of no LSC, especially close to the maximum angles. This is because the low vibration frequency offset results in a slow beating of the errors, allowing the relatively fast PLL to track the phase while the amplitude errors are high.

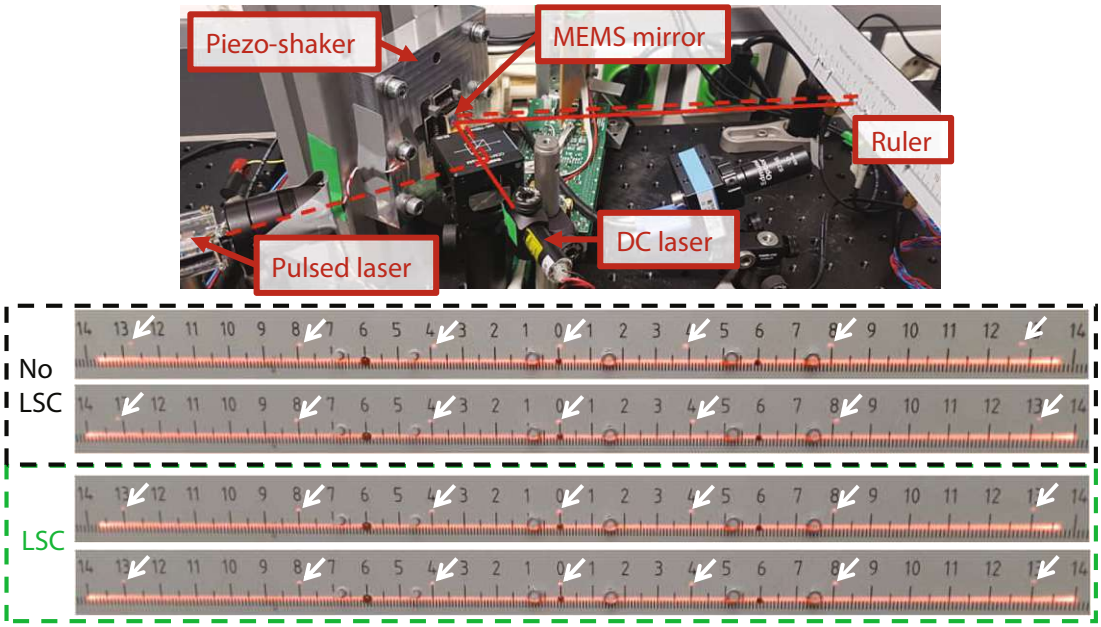

Figure 7.4.: (top) LSC evaluation setup with the MEMS mirror mounted on the piezo-shaker. A DC and a pulsed laser provide optical evaluation on an angular gridded ruler. (bottom) Snapshots of the ruler at the exposure of a $2\,g_{RMS}$ single frequency vibration using SISO control with and without LSC. Shown are the DC laser scan lines at the time instances of minimum and maximum scan line width and the corresponding shot pixels (arrows).

First the tracking performance of the Kalman estimator is evaluated by measurements. Fig. 7.5a shows a comparison of the measured, estimated and predicted phase errors under exposure to harsh vibrations (profile 2 in Fig. 5.22b) using SISO PI controllers. As can be seen, the Kalman estimator provides accu-

rate tracking of the dynamic errors with low deviation from the measurements. However, the measured phase error also contains noise, which does not allow a precise evaluation of the tracking performance. Hence, an optical pointing uncertainty measurement of multiple pixels is made and shown in Fig. 7.5b. The reduced error for the SISO PI control at 8° indicates that for some pixels a correlation of the dynamic phase and amplitude errors can partly compensate their effects on the pointing uncertainty, while this is not possible for all pixels. The comparison to the performance of the MIMO LQG controller reveals that the SISO PI control with the proposed LSC concept provides a similar vibration robustness. Hence, dynamic pixel errors can be compensated using low performance SISO control and simple laser shot correction, causing no influence on the stability of the system. The LSC method can be also combined with a dedicated MIMO LQG control, e.g. to reduce amplitude errors by control, while the LSC compensates for phase and frequency or vice versa.

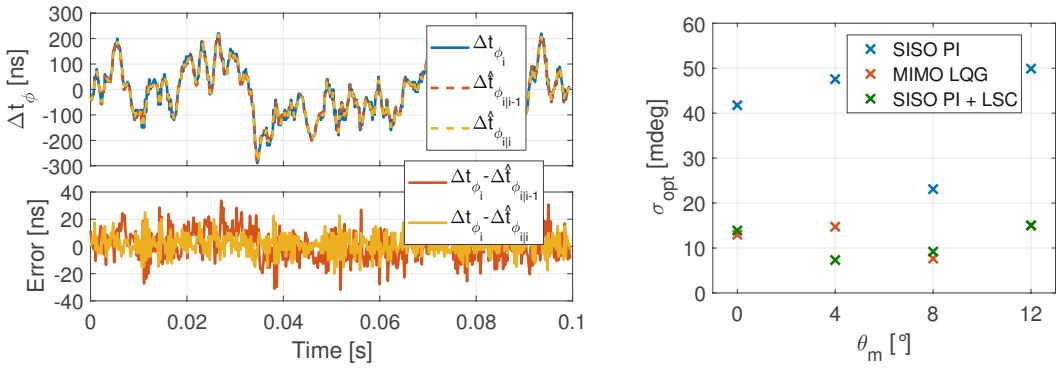

(a) (b)

Figure 7.5.: (a) Phase error tracking and prediction performance of the Kalman estimator. The measured Δt_{ϕ_i}, estimated $\Delta\hat{t}_{\phi_{i|i}}$ and predicted phase errors $\Delta\hat{t}_{\phi_{i+1|i}}$ are recorded during exposure to vibration profile 2. The predicted value is shifted back by one period to compare with the appropriate phase errors. (b) Comparison of the achieved optical pointing uncertainty at multiple pixel positions defined in Fig. 5.23a during exposure to vibration profile 2. The results are compared to those of the SISO PI and MIMO LQG control concepts without LSC.

7.2. Adaptive Lissajous scanning

In environmental perception applications such as lidar for autonomous vehicles a fast reaction on sudden appearing obstacles is safety critical [34, 179]. Capturing the whole scene with high resolution might result in a not manageable amount of data and only partly contains useful information. Hence, it can be beneficial to define ROIs, which are scanned with a high resolution, while the resolution at the rest of the FoV is reduced [180]. This potentially allows a faster frame rate and a lower reaction time as less data overhead is produced. The method can be also used in the manufacturing inspection, where a first overall scan of the inspected device defines regions which shall be imaged with higher resolution in a subsequent scan [46, 181]. Random access scanning systems can provide such ROI scans as the pixels can be individually addressed, while mechanical scanning systems are in general limited by their inertia, i.e. cannot change the scanning speed abruptly. Furthermore, the operation principle of high Q resonant scanners such as MEMS mirrors does not allow to permanently point to specific positions in the FoV as it has to oscillate at resonance.
A novel method for adaptive Lissajous scanning based on phase modulation is proposed in this section, allowing to shape the scan pattern, e.g. to obtain a ROI without changing the frame rate or FoV. The Lissajous trajectory definitions in Eq. (2.1) are modified by the phase modulation function $\eta(t)$ as

$$x(t) = \sin(2\pi f_{\mathrm{X}}\, t) \quad \text{and} \quad y(t) = \sin\left(2\pi \bar{f}_{\mathrm{Y}}\, t + \eta(t)\right) , \tag{7.13}$$

where $\bar{f}_{\mathrm{Y}}$ is the mean Y-axis frequency and defines the Lissajous scan parameters N_{X0}, N_{Y0}, K and f_0 as given in Section 2.1.2. For simplicity, in the following analysis either N_{X0} or N_{Y0} is considered to be even, while the case of two odd total period numbers can be analyzed with the same methods. Similarly, the modulation can be applied on the X-axis or on both axes.
In the following, design criteria for the phase modulation function and pixel timings are derived based on a rigorous analysis of the Lissajous scanning method. An accurate and simple calculation of the obtained resolution in the full FoV is proposed based on the area spanned by neighboring pixels and subsequently used for scan pattern optimization. The method is demonstrated by two orthogonally oriented single axis resonant MEMS mirrors with enhanced frequency tuning capabilities.

7.2.1. Modulation design constraints

By definition, the first constraints of the phase modulation function $\eta(t)$ are

$$\eta(0) = \eta(T_0) = 0\,, \tag{7.14}$$

as otherwise the Lissajous trajectory does not repeat after T_0, resulting in a change of the frame rate or a non-repeating scan. Furthermore, if $K > 1$ the modulation function has to repeat in each preview period T_0/K, which results in the general repetition constraints

$$\eta\left(m\,\frac{T_0}{K}\right) = 0 \quad \text{and} \quad \eta\left(t\right) = \eta\left(m\,\frac{T_0}{K} + t\right)\,, \tag{7.15}$$

with any number $m \in \mathbb{Z}$. Without loss of generality the analysis herein assumes the modulation to be fixed for infinite time while in practice the modulation can be changed in subsequent periods. Another constraint can be found by analyzing the anti-symmetry of the first and the second half of a preview period as shown in Fig. 7.6. For any preview period, the scan line at the first half period starts along the right diagonal and ends along the left diagonal, while the second half period does this vice versa. Hence, to obtain a smooth Lissajous grid the modulation has to be anti-symmetric regarding each preview period, i.e.

$$\eta\left(t\right) = -\eta\left(m\,\frac{T_0}{K} - t\right)\,. \tag{7.16}$$

This also implies that the modulation function has to be zero at each half of the preview periods. Therefore the necessary constraints, which a phase modulation function has to fulfill can be summarizes as

$$\eta\left(m\,\frac{T_0}{2K}\right) = 0 \quad \text{and} \quad \eta\left(t\right) = \eta\left(m\,\frac{T_0}{K} + t\right) = -\eta\left(m\,\frac{T_0}{K} - t\right)\,, \tag{7.17}$$

for any number $m \in \mathbb{Z}$.

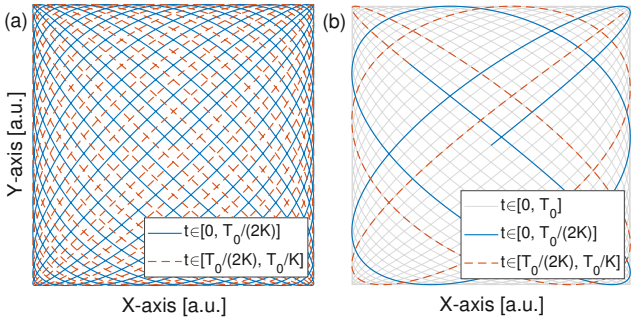

Figure 7.6.: Examples of Lissajous scan patterns. (a) No preview scanning ($N_{\mathrm{X0}} = 26$, $N_{\mathrm{Y0}} = 25$, $K = 1$, $f_0 = 90\,\mathrm{Hz}$). (b) Fast preview scanning due to $K > 1$ ($N_{\mathrm{X0}} = 26$, $N_{\mathrm{Y0}} = 21$, $K = 5$, $f_0 = 90\,\mathrm{Hz}$).

The derived constraints in Eq. (7.17) are automatically fulfilled if the phase modulation function is composed by sine waves with multiple harmonics of the

preview frame rate, i.e.

$$\eta\left(t\right) = \sum_{q=1}^{\infty} a_q \, \sin\left(2\pi \, q \, \frac{K}{T_0} \, t\right) = \sum_{q=1}^{\infty} a_q \, \sin\left(2\pi \, q \, \left(f_{\mathrm{X}} - \bar{f}_{\mathrm{Y}}\right) \, t\right), \tag{7.18}$$

where q is regarded as the modulation order and a_q are the design parameters. The maximum achievable modulation order is practically limited by the scanner dynamics as the frequency of the scanner has to be changed according to the second derivative, i.e. the curvature, of the phase modulation function. Furthermore, to obtain a non-overlapping Lissajous pattern the gradient of the relative phase between both axes has to be positive at any time, resulting in

$$f_{\mathrm{X}} > \bar{f}_{\mathrm{Y}} + \frac{1}{2\pi} \, \dot{\eta}\left(t\right) \, . \tag{7.19}$$

Fig. 7.7b-d shows three examples of single order modulation functions, which shape the Lissajous scanning grid differently. Hence, the grid can be designed to obtain higher resolution with dense grid lines at desired positions in the FoV, i.e. at regions of interest, without sacrificing the frame rate. As also shown in the figure, the increased resolution at one position is sacrificed with a lower resolution at another position. Furthermore, the scanning grid features defined in one quadrant, e.g. Q1, also appear in the other quadrants due to the symmetry of the Lissajous scanning method.

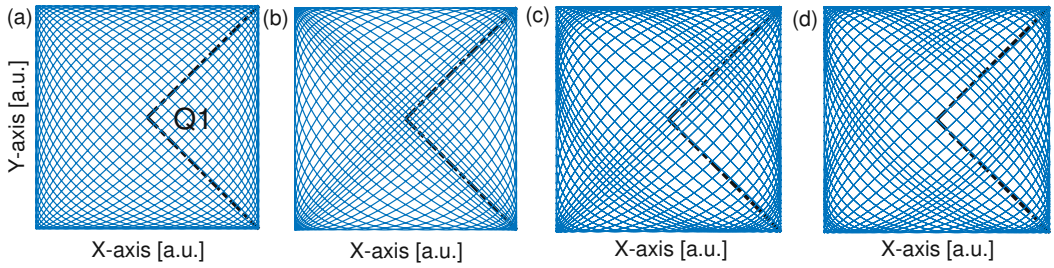

Figure 7.7.: Examples of adaptive Lissajous scan patterns using single frequency modulation functions Eq. (7.18): (a) no modulation, (b) only second order $a_2 = 0.25\,\mathrm{rad}$, (c) only third order $a_3 = 0.15\,\mathrm{rad}$ and (d) only fourth order $a_4 = -0.1\,\mathrm{rad}$. The Lissajous parameters $N_{\mathrm{X0}} = 26$, $N_{\mathrm{Y0}} = 25$ and the frame rate are unchanged. Also the similarity quadrant Q1 is shown where the grid features are repeated in the other quadrants.

7.2.2. Pixel distribution and resolution criterion

For a phase modulation function, design criteria have to be defined to evaluate the resulting scan grid. In this study the resolution is defined by the distance of neighboring pixels, which are derived from scan line intersection points, as this reveals the uncovered area. For simplicity, the intersection points of a Lissajous scan grid without phase modulation is discussed first. With the identity of $\sin(\varphi) = \sin(n\pi + (-1)^n \varphi)$ for any integer number n, the conditions such that two scan lines intersect can be expressed as

$$\begin{aligned} \sin(2\pi f_\mathrm{X} t_j) &\overset{!}{=} \sin\left(n_{\mathrm{X}j}\pi + (-1)^{n_{\mathrm{X}j}}\, 2\pi f_\mathrm{X} t_j\right) , \\ \sin(2\pi f_\mathrm{Y} t_j) &\overset{!}{=} \sin\left(n_{\mathrm{X}j}\pi \frac{N_\mathrm{Y0}}{N_\mathrm{X0}} + (-1)^{n_{\mathrm{X}j}}\, 2\pi f_\mathrm{Y} t_j\right) , \end{aligned} \tag{7.20}$$

where $n_{\mathrm{X}j}$ is the necessary X-axis half periods shift in between and t_j is the intersection time, which both have to be found for each intersection j. The first condition in Eq. (7.20) is automatically fulfilled for all times t_j if $n_{\mathrm{X}j} \in \mathbb{Z}$, while only at a certain time also the Y-axis equation is fulfilled. By sampling the trajectory with the constant sampling time [62]

$$\Delta t_\mathrm{S} = \frac{1}{4\, f_\mathrm{X} N_\mathrm{Y0}} , \tag{7.21}$$

a high resolution rectilinear pixel grid can be obtained if an initial shift of half a sampling time is applied. It can be found that a subset of the total samples at $t_j = j\,\Delta t_\mathrm{S}$ with the sample number j contains the intersection points, where each is sampled twice along two different scan lines. The subset, which does not belong to intersection points are at the edges of the FoV and correspond to the points where either the X-axis or the Y-axis reaches its amplitude point as shown in Fig. 7.8. Hence, the total set of samples in one Lissajous period is $S = \{j \in \mathbb{N}_0 \mid 0 \le j \le 4 N_\mathrm{Y0} N_\mathrm{X0} - 1\}$ and the subset $S_\mathrm{I} \subset S$ corresponding to intersection points is

$$S_\mathrm{I} = \left\{ j \in S \;\middle|\; \begin{array}{c} j \neq N_\mathrm{X0}\,(1 + 2\,m) \quad \text{and} \\ j \neq N_\mathrm{Y0}\,(1 + 2\,l) \;\; \text{with } m,\; l \in \mathbb{N}_0 \end{array} \right\} . \tag{7.22}$$

In the following, a proof for the intersections happening at the subset S_I of the samples at t_j is derived and subsequently used for phase modulation design. The necessary half period shifts between two intersecting scan lines is first expressed as

$$n_{\mathrm{X}j} = N_\mathrm{X0} + (-1)^{N_\mathrm{X0}+j}\; j\, \frac{1 - L\, N_\mathrm{X0}}{K} , \tag{7.23}$$

where $L \in \mathbb{N}_0$ has to be chosen such that Eq. (7.20) is fulfilled. With the equality $f_\mathrm{X} N_\mathrm{Y0} = f_\mathrm{Y} N_\mathrm{X0}$ and Eq. (7.21), the second equation in Eq. (7.20) can be

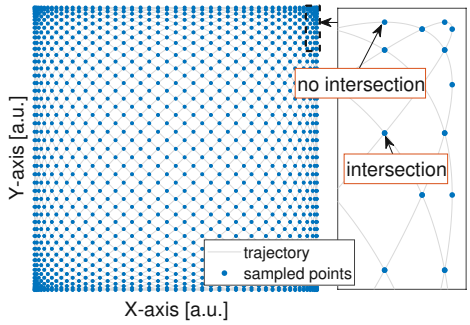

Figure 7.8.: Obtained samples of the Lissajous trajectory ($N_{\mathrm{X0}} = 26,\ N_{\mathrm{Y0}} = 25$) with a constant sampling time Δt_{S}. The samples mainly contain intersection points while also points on the edges of the FoV without an intersection.

rewritten as

$$\begin{aligned} \sin\left(j\frac{\pi}{2\,N_{\mathrm{X0}}}\right) &\overset{!}{=} \sin\left(n_{\mathrm{X}j}\pi\frac{N_{\mathrm{Y0}}}{N_{\mathrm{X0}}} + (-1)^{n_{\mathrm{X}j}}\,j\frac{\pi}{2\,N_{\mathrm{X0}}}\right) \\ &= \sin\left(n_{\mathrm{Y}j}\pi + (-1)^{n_{\mathrm{Y}j}}\,j\frac{\pi}{2\,N_{\mathrm{X0}}}\right), \end{aligned} \tag{7.24}$$

where $n_{\mathrm{Y}j} \in \mathbb{Z}$ is the corresponding Y-axis half periods shift and can be found to

$$n_{\mathrm{Y}j} = N_{\mathrm{Y0}} - (-1)^{N_{\mathrm{Y0}}+j}\ j\,\frac{1 - L\,N_{\mathrm{Y0}}}{K} = n_{\mathrm{X}j} - K - (-1)^{N_{\mathrm{Y0}}+j}\ j\,L\,. \tag{7.25}$$

The intersection condition is fulfilled for all j if L is chosen such that

$$\frac{1 - L\,N_{\mathrm{X0}}}{K} \quad \text{and} \quad \frac{1 - L\,N_{\mathrm{Y0}}}{K} = \frac{1 - L\,N_{\mathrm{X0}}}{K} + L \tag{7.26}$$

are odd integers. At least one L value can be found for each valid frequency ratio of an even and an odd integer. As K is then always odd, the above conditions reveal that L has to be even and results in the trivial solution $L = 0$ for the case $K = 1$. A proof is given in the Appendix.

Exceptionally the intersection condition with the used expressions is also fulfilled for the subset of the samples which actually are no intersection points, i.e. $S \backslash S_{\mathrm{I}}$. This is because for those samples both X-axis and Y-axis phases are shifted by a multiple of the Lissajous period, i.e. the points intersect with themselves. Hence, those samples do not have to be excluded or separately treated from the algorithm.

By shooting a pulsed laser on the scan lines between two adjacent samples, a

rectilinear high resolution pixel grid is obtained. In case of no modulation, this can be accomplished by a simple shift of the sample time t_j by half a sampling time, i.e.

$$t_{\mathrm{px}_j} = t_j + \frac{\Delta t_\mathrm{S}}{2} = \left(j + \frac{1}{2}\right) \Delta t_\mathrm{S} \,. \tag{7.27}$$

An example is shown in Fig. 7.9a, where the pixels are arranged in horizontal and vertical lines.

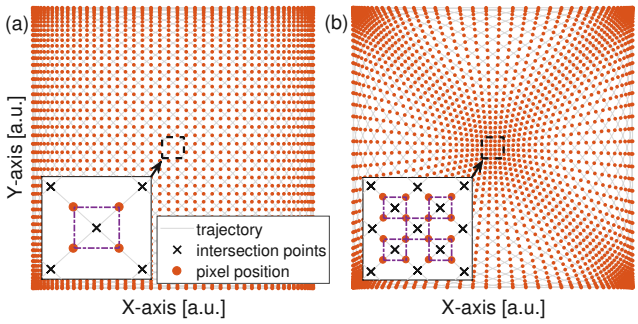

Figure 7.9.: Examples of pixel distributions and definition of polygon for resolution calculation (dashed rectangles in the insets). (a) No phase modulation, where a rectilinear grid with horizontal and vertical pixel lines is obtained. (b) Second order ($a_2 = 0.25\,\mathrm{rad}$) phase modulation, where the pixel lines are bent to obtain a high resolution at the center of the FoV.

In case of a modulated Y-axis as in Eq. (7.13), the intersection points do not happen at a constant sampling time. Hence, the sample times are expressed as

$$t_j = j\,\Delta t_\mathrm{S} + \Delta t_j \,, \tag{7.28}$$

where Δt_j has to be identified for all j and the new Y-axis intersection criterion is

$$\begin{aligned} &\sin\left(j\frac{\pi}{2N_{\mathrm{X0}}} + 2\pi\bar{f}_\mathrm{Y}\Delta t_j + \eta\left(t_j\right)\right) \\ &\overset{!}{=} \sin\left(n_{\mathrm{X}j}\pi\frac{N_{\mathrm{Y0}}}{N_{\mathrm{X0}}} + (-1)^{n_{\mathrm{X}j}}\left(j\frac{\pi}{2N_{\mathrm{X0}}} + 2\pi\bar{f}_\mathrm{Y}\Delta t_j\right) + \eta\left(\frac{n_{\mathrm{X}j}}{2f_\mathrm{X}} + (-1)^{n_{\mathrm{X}j}}\,t_j\right)\right). \end{aligned} \tag{7.29}$$

As the sampling time shifts are expected much smaller than a half period of the scanner, i.e. $\left|(-1)^{n_{\mathrm{X}j}}\,2\pi\bar{f}_\mathrm{Y}\Delta t_j + \eta\left(t_j\right)\right| \ll \pi$, a comparison with Eq. (7.24) shows that the previous calculation of $n_{\mathrm{X}j}$ and $n_{\mathrm{Y}j}$ fulfill the condition up to a small shift in phase. Hence, the shifts Δt_j can be calculated by compensating

the residual errors in the arguments of the sine functions, i.e.

$$2\pi\bar{f}_{\mathrm{Y}}\Delta t_j+\eta\left(t_j\right)\stackrel{!}{=}(-1)^{n_{\mathrm{Y}j}}\left((-1)^{n_{\mathrm{X}j}}\,2\pi\bar{f}_{\mathrm{Y}}\Delta t_j+\eta\left(\frac{n_{\mathrm{X}j}}{2f_{\mathrm{X}}}+(-1)^{n_{\mathrm{X}j}}\,t_j\right)\right), \tag{7.30}$$

where the sign dependency on $n_{\mathrm{Y}j}$ takes into account that the trajectory derivative is the same or different for both intersecting scan lines. Further simplification can be obtained by using the derived symmetry features of the phase modulation function as well as that $n_{\mathrm{X}j}$ and $n_{\mathrm{Y}j}$ are never both odd or both even, i.e.

$$2\pi\bar{f}_{\mathrm{Y}}\Delta t_j+\eta\left(t_j\right)\stackrel{!}{=}-2\pi\bar{f}_{\mathrm{Y}}\Delta t_j-\eta\left(\frac{N_{\mathrm{X0}}}{2f_{\mathrm{X}}}+j\frac{1-L\,N_{\mathrm{X0}}}{2f_{\mathrm{X}}K}+t_j\right). \tag{7.31}$$

A proof for the sign dependency elimination of the phase modulation function is given in the Appendix. As η is a nonlinear function, Eq. (7.31) cannot be analytically solved, while Δt_j can be approximated numerically by iterative refinement, i.e.

$$e=\frac{-1}{4\pi\bar{f}_{\mathrm{Y}}}\left(\eta\left(\hat{t}_j\right)+\eta\left(\frac{N_{\mathrm{X0}}}{2f_{\mathrm{X}}}+j\frac{1-L\,N_{\mathrm{X0}}}{2f_{\mathrm{X}}K}+\hat{t}_j\right)\right)-\Delta\hat{t}_j\,, \tag{7.32}$$

where $\hat{t}_j=j\,\Delta t_{\mathrm{S}}+\Delta\hat{t}_j$ and e is minimized by adding e to the estimate $\Delta\hat{t}_j$ in each iteration. Hence, with sufficient iterations the estimated time shifts $\Delta\hat{t}_j$ accurately match the exact solutions Δt_j and can be calculated for each intersection point. Again the samples without an intersection do not have to be excluded as the algorithm results in zero shift for those points.

Similar to the case without modulation, the high resolution pixel grid is obtained by interpolating between two adjacent samples, e.g. by linear interpolation

$$t_{\mathrm{px}_j}=\frac{1}{2}\left(t_j+t_{j+1}\right). \tag{7.33}$$

Fig. 7.9b shows an example of a resulting pixel grid with phase modulation. The original horizontal and vertical pixel lines in Fig. 7.9a are bent such that a high density of pixels is achieved at a certain position in the FoV, e.g. at the center.

The resolution of the pixel grid can be defined by the area spanned by the four pixels, which surround an intersection point, as illustrated in Fig. 7.9. Hence, for each intersection point at sampling time t_j the four vertices that define the

spanned area can be found at the times

$$\mathbf{t}_{\mathrm{V}_j} = \left[\, t_{\mathrm{px}_j},\quad t_{\mathrm{px}_l},\quad t_{\mathrm{px}_{j-1}},\quad t_{\mathrm{px}_{l-1}} \,\right],$$
$$\text{with}\quad l = \left\{ 2N_{\mathrm{X0}}N_{\mathrm{Y0}} + (-1)^{N_{\mathrm{X0}}+j}\, j \left(1 + 2N_{\mathrm{Y0}} \frac{1 - L\, N_{\mathrm{X0}}}{K} \right) \right\} \bmod 4N_{\mathrm{X0}}N_{\mathrm{Y0}}\,, \tag{7.34}$$

where mod is the modulus operator. The corresponding coordinates describe a polygon in the FoV whose spanned area $F\left(\mathbf{t}_{\mathrm{V}_j}\right)$ relates to the resolution, i.e. a large area corresponds to a low resolution. It has to be noted that the polygons can have various shapes and do not have to be rectangular. Fig. 7.10 shows a contour plot of the resulting spanned area for the case of conventional Lissajous scanning and a second order modulation. As expected, the modulation improves the resolution at the center of the FoV and shifts the low resolution regions towards the edges.

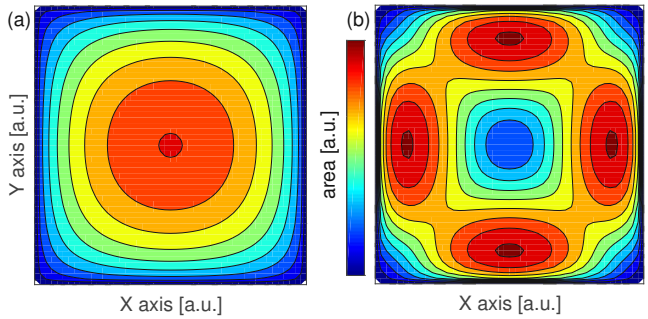

Figure 7.10.: Contour plot of the area spanned by the four pixels surrounding an intersection point. (a) Conventional Lissajous scanning. The resolution decreases towards the center of FoV. (b) Second order ($a_2 = 0.25\,\mathrm{rad}$) phase modulation. A high resolution is obtained at the center while other regions are sacrificed.

7.2.3. Compensation of amplitude variation

If no dedicated control is applied, the dynamic response of a scanning system can show an amplitude change if the scanning frequency is varied. Consequently the phase modulation causes variations in the scanning amplitude of the corresponding axis within a Lissajous frame and shifts the intersection points especially where both intersecting scan lines have different amplitude. This leads to a distorted pixel grid if no compensation is applied as shown in Fig. 7.11a. To account for the amplitude changes, the frequency dependent amplitude function $A(f)$ is

introduced and the trajectory of both axes are described as

$$x(t) = \sin\left(2\pi f_{\mathrm{X}}\, t\right) \quad \text{and} \quad y(t) = A\left(\bar{f}_{\mathrm{Y}} + \frac{\dot{\eta}\left(t\right)}{2\pi}\right) \cdot \sin\left(2\pi \bar{f}_{\mathrm{Y}}\, t + \eta\left(t\right)\right) . \tag{7.35}$$

Due to practical usefulness only relatively small amplitude variation need to be considered, which only lead to small additive compensation shifts $\Delta t_{\mathrm{A},j}$ of the sample timing, i.e.

$$t_j = j\,\Delta t_{\mathrm{S}} + \Delta t_j + \Delta t_{\mathrm{A},j}\,. \tag{7.36}$$

Hence, $\Delta t_{\mathrm{A},j}$ can be approximated by the Newton-Raphson method applied on the Y-axis trajectory as

$$y\left(\hat{t}_j\right) + \dot{y}\left(\hat{t}_j\right) e \stackrel{!}{=} y\left(\frac{n_{\mathrm{X}j}}{2f_{\mathrm{X}}} + (-1)^{n_{\mathrm{X}j}}\,\hat{t}_j\right) + (-1)^{n_{\mathrm{X}j}}\,\dot{y}\left(\frac{n_{\mathrm{X}j}}{2f_{\mathrm{X}}} + (-1)^{n_{\mathrm{X}j}}\,\hat{t}_j\right) e\,, \tag{7.37}$$

where e has to be zero at the actual intersection point. This leads to the iterative estimation algorithm

$$e = \frac{y\left(\frac{n_{\mathrm{X}j}}{2f_{\mathrm{X}}} + (-1)^{n_{\mathrm{X}j}}\,\hat{t}_j\right) - y\left(\hat{t}_j\right)}{\dot{y}\left(\hat{t}_j\right) - (-1)^{n_{\mathrm{X}j}}\,\dot{y}\left(\frac{n_{\mathrm{X}j}}{2f_{\mathrm{X}}} + (-1)^{n_{\mathrm{X}j}}\,\hat{t}_j\right)}\,, \tag{7.38}$$

where $\hat{t}_j = j\,\Delta t_{\mathrm{S}} + \Delta t_j + \Delta\hat{t}_{\mathrm{A},j}$ and has to be found to minimize e. Eq. (7.38) can be applied on all samples j except the subset where the Y-axis reaches its amplitude points, i.e. at $j = N_{\mathrm{X}0}\left(1 + 2\,m\right)$ with $m \in [0,\ 2N_{\mathrm{Y}0} - 1]$. At those points the trajectory only depends marginally on time and the algorithm is susceptible to numerical errors. Hence, the correct shift should be approximated by interpolating between the previous and the following sample point. Fig. 7.11b shows the corrected pixels by the proposed algorithm for an affine amplitude function $A(f) = A_0\left(1 + 0.1\,\left(f - \bar{f}_{\mathrm{Y}}\right)/f_0\right)$. It has to be noted that no assumptions are made for the amplitude function and it can be an arbitrary function of sufficient smoothness.

7.2.4. Phase modulation design

Using the derived resolution definition, the phase modulation function can be optimized for specific needs in application. One possibility is to define ROIs, where a high resolution is required while the rest of the FoV is of less interest, i.e. can have reduced resolution. In imaging applications, such as lidar, this allows detailed information where it is required, while still a coarse overall scan is provided. Hence, in this study a dedicated optimization procedure varies the parameters a_q of the phase modulation function to obtain the desired resolution in a defined ROI. To obtain this, the cost function penalizes the resolution at

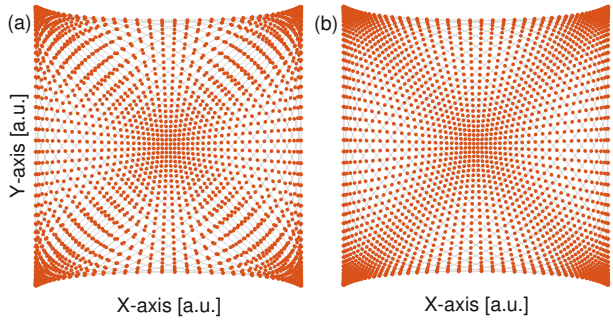

Figure 7.11.: Examples of pixel distributions for a second order ($a_2 = 0.25\,\mathrm{rad}$) phase modulation with and without amplitude compensation ($N_{\mathrm{X0}} = 26$, $N_{\mathrm{Y0}} = 25$, $A(f) = A_0\left(1 + 0.1\left(f - \bar{f}_{\mathrm{Y}}\right)/f_0\right)$). (a) No compensation. (b) Compensation based on the proposed algorithm.

the ROI the most using a spatial weighting. Besides judging the obtained grid resolution solely by the spanned area of neighboring pixels, also its aspect ratio can be taken into account, e.g. to prefer square shaped areas. Furthermore, the dynamic changes of the scanning frequency necessary for the modulation imposes input variations, which depends on the scanner dynamics. As an example, the necessary input amplitudes at the frequency components of the phase modulation function can be considered as a control effort, which might be limited.
The used algorithm can be described in the following steps:

1. Calculate the constant Lissajous parameters, such as N_{X0}, N_{Y0}, K, L, $n_{\mathrm{X}j}$, $n_{\mathrm{Y}j}$ (initialization).

2. Choose initial modulation parameters a_q with $1 \leq q \leq M$ for the initial starting point, where M is the maximum order considered for optimization.

3. Calculate sample time shifts $\Delta\hat{t}_j$ and $\Delta\hat{t}_{\mathrm{A},j}$ according to Eq. (7.32) and Eq. (7.38).

4. Calculate cost function terms, e.g. weighted spanned areas, aspect ratios, and control effort. An exemplary cost function is

$$J = \sum_{q=0}^{M} \overbrace{H_q}^{\text{control effort}} + \sum_{j=0}^{S_{\mathrm{I}}} \overbrace{W\left(x\left(t_j\right), y\left(t_j\right)\right)}^{\text{spatial weighting}} \cdot \left[\overbrace{F\left(\mathbf{t}_{\mathrm{V}_j}\right)}^{\text{spanned area}} - \bar{F}\right]^2 \cdot \overbrace{R\left(\mathbf{t}_{\mathrm{V}_j}\right)}^{\text{aspect ratio}}, \tag{7.39}$$

where $\bar{F}$ is the desired spanned area and $R\left(\mathbf{t}_{\mathrm{V}_j}\right) \geq 1$ which is equal to 1 for the desired aspect ratio, e.g. for a squared area.

5. If the cost function J has not reached a minimum, vary a_q and jump to (3.).

Fig. 7.12a-b shows two designs of ROI scan patterns using the proposed optimization procedure and the corresponding phase modulation functions in Fig. 7.12c. As can be seen, the straight pixel grid lines of conventional Lissajous scanning are bent to obtain a dense and almost square shaped pixel grid at the ROI. Due to the symmetry of the Lissajous scanning method, the ROI appears similarly in all four quadrants. Fig. 7.13 shows a conceptional illustration of a lidar scenario where the conventional and the proposed Lissajous scanning method are compared. As can be seen, the ROI is resolved with a higher resolution to maximize the information contained in the measured 3D point cloud, while neither the overall FoV nor the frame rate are sacrificed. In application the computation effort can be minimized by defining a discrete ROI grid in the FoV and to solve the optimization problem for each ROI beforehand. A system controller can then select the appropriate ROI on demand and the corresponding phase modulation function as well as the pixel timings are loaded. This allows fast switching between the ROIs to track objects or to re-scan sacrificed low resolution regions to guarantee that potentially dangerous objects are not missed. The ROI switching speed is then only limited by the ability of the scanner to follow the new modulation function.

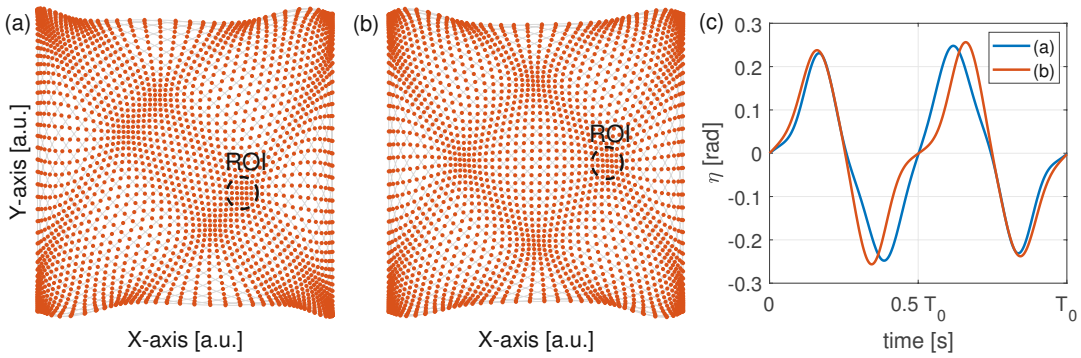

Figure 7.12.: Examples of ROI scan patterns obtained by the proposed optimization procedure (a-b) and corresponding phase modulation functions (c). The ROI appears in all four quadrants due to the symmetry of Lissajous scanning.

Figure 7.13.: Conceptional illustration of conventional Lissajous scanning (a) and ROI scanning using the proposed method (b) in a lidar scenario. Significantly more measurement points are created in the ROI compared to the conventional method.

7.2.5. Method demonstration

In this section the proposed modulation method is demonstrated by an extension of the Lissajous scanning system control blocks in Chapter 6 and using two single axis MEMS mirrors with a relatively large frequency tuning capability as shown in Fig. 7.14. The over-bending of the top response curve is advantageously used for the presented method as it provides a rather large frequency band where the amplitude changes are relatively low. This is different from conventional linear resonators, which would require a high damping for a reasonable tuning range, resulting in reduced energy efficiency, i.e. a low Q-factor. Hence, the used MEMS mirrors provide both, a high Q-factor as well as the possibility of frequency variation with a moderate change of amplitude. Around the nominal operation point, the amplitude function $A(f)$ can be approximated as an affine function of frequency as shown in the inset of the figure. To demonstrate the proposed method, the Y-axis MEMS mirror M1 of the Lissajous scanning system is forced to exhibit a desired phase modulation, which is discussed in the following paragraphs.

Adaption of synchronization concept

As the synchronization concept is based on aligning the MEMS mirror zero crossings with the received synchronization pulses derived from DCO phase slices, it has to be analyzed how a modulation effects the zero crossing timing. From the definition of the trajectories in Eq. (7.13) the zero crossing condition of the modulated Y-axis can be generally expressed as

$$2\pi \bar{f}_{\mathrm{Y}}\, t_i + \eta\,(t_i) \stackrel{!}{=} i\pi\,, \tag{7.40}$$

where $i \in \{0,\, 1, \cdots,\, 2N_{\mathrm{Y0}} - 1\}$ is the Y-axis half period index of a Lissajous frame and $t_i \in \mathbb{R}_0$ is the corresponding zero crossing time. As the modulation can be considered relatively small, i.e. $\eta\,(t_i) \ll \pi$, and with the nominal Y-axis

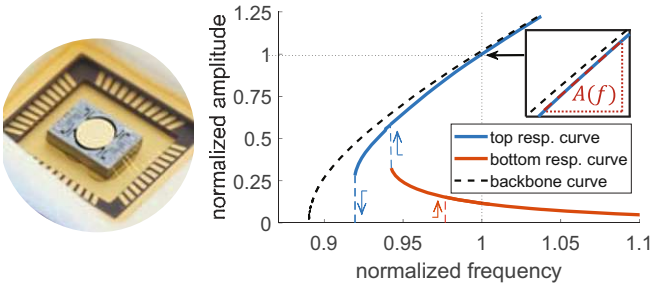

Figure 7.14.: (left) Picture of the used electrostatic actuated resonant MEMS mirrors in a glass covered ceramic package. (right) Measured steady state frequency response, normalized by the nominal operation point. The nonlinearities of the mirror lead to two stable branches, i.e. the bottom and the top response curve. The inset shows a linear relation between amplitude and frequency around the nominal operation point.

mirror half period $\bar{T}_{\mathrm{mh_Y}} = 0.5/\bar{f}_{\mathrm{Y}}$, the zero crossing times for each index i can be expressed as $t_i = i\,\bar{T}_{\mathrm{mh_Y}} + \Delta t_{\eta_i}$, with the modulation time shift Δt_{η_i}. Hence, above condition can be rewritten to

$$2\pi\,\bar{f}_{\mathrm{Y}}\,\Delta t_{\eta_i} + \eta\left(i\,\bar{T}_{\mathrm{mh_Y}} + \Delta t_{\eta_i}\right) \stackrel{!}{=} 0\,, \tag{7.41}$$

which is a nonlinear equation as $\eta\,(t)$ contains sine functions as in Eq. (7.18). From the symmetry analysis of the phase modulation function in Eq. (7.17) it is found that the modulation time shifts have to be zero at each half preview period. The other values can be obtained by a numerical approximation using iterative refinement of an estimate $\Delta\hat{t}_{\eta_i}$ that minimizes the error e defined by

$$e = \frac{-\eta\left(i\,\bar{T}_{\mathrm{mh_Y}} + \Delta\hat{t}_{\eta_i}\right)}{2\pi\,\bar{f}_{\mathrm{Y}}} - \Delta\hat{t}_{\eta_i}\,. \tag{7.42}$$

By this method the modulation time shifts can be calculated for each half period index of a Lissajous frame.

For example, in the M-SS Lissajous scanning control concept with decoupled axis, the synchronization pulse generator sends synchronization pulses to the Y-axis control block every $2^N + s_\Delta$ phase slices of the M-DCO, whose period is $\bar{T}_{\mathrm{mh_X}}$. The constant s_Δ results in a fixed frequency ratio between both axes. In case of a modulation, those pulses have to be shifted according to the corresponding modulation time shifts for proper synchronization control. Using a vector formulation of the modulation time shifts in one Lissajous frame as $\Delta\mathbf{t}_\eta = \begin{bmatrix}\Delta t_{\eta_0} & \Delta t_{\eta_1} & \cdots & \Delta t_{\eta_{2N_{\mathrm{Y0}}-1}}\end{bmatrix}^T$, the necessary phase slice shifts for the

synchronization pulse generator are given as

$$\bar{\mathbf{s}}_{\Delta} = \Delta \mathbf{t}_{\eta} \frac{2^N}{\bar{T}_{\mathrm{mh_X}}} \,. \tag{7.43}$$

With Eq. (7.18) and Eq. (7.41), Eq. (7.43) shows that the phase slice shifts solely depend on the frequency ratio and the phase modulation function, i.e. are independent of the actual scanning frequencies. Fig. 7.15 shows the proposed synchronization pulse signaling along the M-DCO phase slices for one frame. In contrast to conventional Lissajous scanning, the pulses are shifted according to the modulation. Hence, if the Y-axis control inputs are chosen such that it follows the desired phase modulation correctly, zero synchronization and phase errors are obtained. This allows the separated design of feedback control for non-repeating disturbance rejection such as external vibrations and feedforward modulation control to track the repeating modulation sequence. While the feedback control can be independent of the specific modulation function, the feedforward modulation control has to be tailored and necessities a memory in order to apply the corresponding sequence.

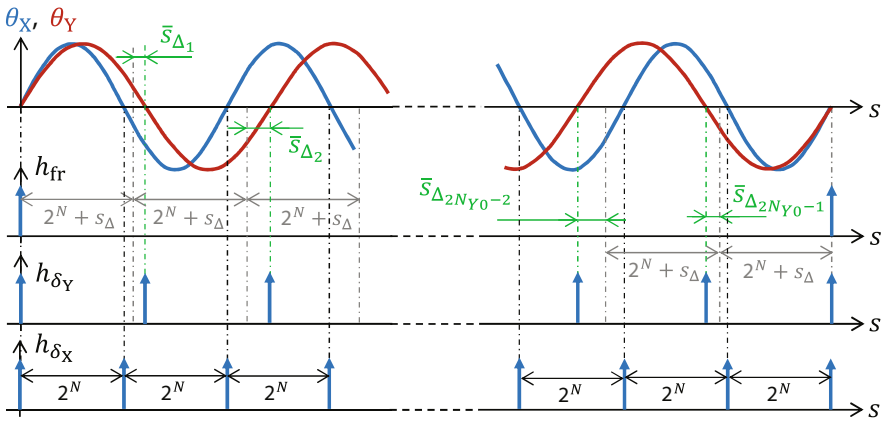

Figure 7.15.: Mirror trajectories and synchronization signals for adaptive Lissajous scanning along the M-DCO phase slices for one Lissajous frame. Synchronization pulses are sent at every frame start, i.e. h_{fr}, every zero crossing of the X-axis, i.e. h_{δ_X}, and at every necessary zero crossing of the Y-axis, i.e. h_{δ_Y}, for a correct modulated operation.

In the following, both the SISO and the MIMO control methods for Lissajous scanning discussed in Chapter 6 are extended to exhibit a desired phase modulation at the Y-axis MEMS mirror using feedforward modulation control. The feedforward input signals $\Delta\bar{s}_{\mathrm{off}_i}$ and $\Delta\bar{T}_{\mathrm{PLL}_i}$ are stored in a memory and precalculated based on the linearized MEMS mirror model, which however does not

account for the relatively large operation point variations due to the modulation, leading to residual synchronization and PLL phase errors. As those errors are repeating by the Lissajous period an iterative learning control (ILC) is used to adapt the feedforward signals in the memory, achieving precisely synchronized modulation once the sequence is learned. A model based SISO ILC with rather low computation effort is discussed, which adapts the switching off slice inputs based on the residual synchronization errors and suffices for the SISO control concept as PLL phase errors do not have to be zero for correct modulation tracking and are typically small. This is because a synchronization error means a misalignment of the desired and actual MEMS mirror phase, while a PLL phase error only represents a misalignment of the MEMS mirror and the corresponding PLL DCO, i.e. the driving signal, which can be tolerated. The MIMO controllers however strongly react on PLL phase errors and therefore necessitate a MIMO ILC, which adapts both inputs based on both outputs, resulting in zero modulation and PLL phase errors at the cost of computation effort.

Feedforward modulation control design

The aim of the feedforward modulation control design is to find appropriate input values $\Delta\bar{s}_{\mathrm{off}_i}$ and $\Delta\bar{T}_{\mathrm{PLL}_i}$ such that the synchronization error follows the desired modulation with zero phase error, i.e. $\Delta t_{\delta_i} = \Delta t_{\eta_i}$ and $\Delta t_{\phi_i} = 0$. Hence, then the used feedback controllers receive zero errors resulting in no additional control action. This can be obtained by solving the linearized MEMS mirror model given in Eq. (6.7) for the input vector as

$$\mathbf{u}_{\mathrm{S}_i} = \mathbf{B}_{\mathrm{S}}^{-1} \left(\mathbf{x}_{\mathrm{S}_{i+1}} - \mathbf{A}_{\mathrm{S}} \cdot \mathbf{x}_{\mathrm{S}_i} \right) . \tag{7.44}$$

However, since $\mathbf{B}_{\mathrm{S}}$ is non-square matrix, i.e. there are two inputs while three states, it cannot be directly inverted. By the phase modulation design, Δt_{δ} and Δt_{ϕ} are given for each period i, while ΔT_{Θ} cannot be independently chosen due to the limitation of only two inputs, i.e. $\bar{s}_{\mathrm{off}_i}$ and $\Delta\bar{T}_{\mathrm{PLL}_i}$. Therefore, a recursive method is used, which takes advantage of the fact that ΔT_{Θ_i} can be calculated from the previous periods using the linearized MEMS mirror model. Starting from $\Delta T_{\Theta_0} = 0$ and with the subscript notation that $\mathbf{A}_{\mathrm{S}_{rc}}$ is the entry of matrix $\mathbf{A}_{\mathrm{S}}$ in row r and column c, the procedure can be described by the following steps:

1. Calculate $\Delta\bar{s}_{\mathrm{off}_i}$ for the desired phase modulation (zero matrix entries are omitted)

$$\Delta\bar{s}_{\mathrm{off}_i} = \mathbf{B}_{\mathrm{S}_{31}}^{-1} \left(\Delta t_{\eta_{i+1}} - \mathbf{A}_{\mathrm{S}_{33}} \Delta t_{\eta_i} - \mathbf{A}_{\mathrm{S}_{32}} \Delta T_{\Theta_i} \right) . \tag{7.45}$$

2. Calculate $\Delta\bar{T}_{\mathrm{PLL}_i}$ for zero PLL phase error

$$\Delta\bar{T}_{\mathrm{PLL}_i} = \mathbf{B}_{\mathrm{S}_{12}}^{-1}\left(-\mathbf{A}_{\mathrm{S}_{12}}\,\Delta T_{\Theta_i} - \mathbf{B}_{\mathrm{S}_{11}}\,\Delta\bar{s}_{\mathrm{off}_i}\right). \tag{7.46}$$

3. Calculate $\Delta T_{\Theta_{i+1}}$ for use in next period

$$\Delta T_{\Theta_{i+1}} = \mathbf{A}_{\mathrm{S}_{22}}\,\Delta T_{\Theta_i} + \mathbf{B}_{\mathrm{S}_{21}}\,\Delta\bar{s}_{\mathrm{off}_i}. \tag{7.47}$$

4. Increase i and repeat from (1.).

By recursive manner the initial transients are vanished and the input values do not vary anymore from frame to frame. Hence, $2\,N_{\mathrm{Y0}}$ values are found for each input to obtain the desired modulation and are combined in the vectors $\Delta\bar{\mathbf{s}}_{\mathrm{off}}$ and $\Delta\bar{\mathbf{T}}_{\mathrm{PLL}}$, respectively. Fig. 7.16 shows the block diagram of the proposed feedforward modulation control concept with SISO feedback controllers. The synchronization pulse shifts $\bar{\mathbf{s}}_{\Delta}$ as well as the calculated input values are stored in memories, whose values are selected by multiplexer (MUX) according to the current period index within the Lissajous frame.

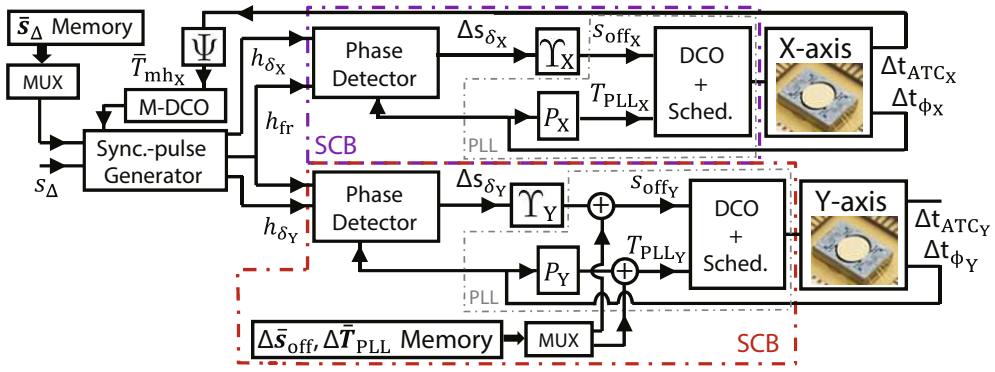

Figure 7.16.: Block diagram of the adaptive Lissajous scanning SISO control system with feedforward modulation control. The $2N_{\mathrm{Y0}} \times 1$ vectors $\bar{\mathbf{s}}_{\Delta}$, $\Delta\bar{\mathbf{s}}_{\mathrm{off}}$ and $\Delta\bar{\mathbf{T}}_{\mathrm{PLL}}$ are stored in memories and selected via multiplexer.

Experimental verification

The feedforward input values for a specific modulation function calculated based on the procedure above are shown in Fig. 7.17a and are applied in the adaptive Lissajous scanning system. The feedback controllers are not adapted for modulation control and have the same gain setting as in the case without modulation. As the linearized MEMS mirror model only describes the local dynamics accurately, while the modulation leads to rather large operation point variations, residual

synchronization and PLL phase errors are obtained as shown in Fig. 7.17b causing also feedback control action. Fig. 7.17c shows the resulting Lissajous scanning grid with a non-smooth scan line separation due to the modulation errors. Hence, a pure feedforward control with the input values calculated upfront and no tailored feedback controllers is not sufficient for accurate modulation tracking.

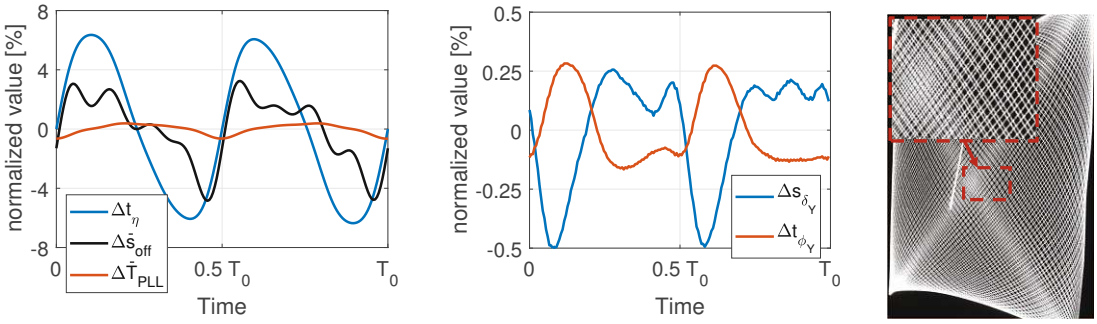

(a) (b) (c)

Figure 7.17.: (a) Calculated feedforward input signals for a desired modulation using the linearized MEMS mirror model. (b) Residual synchronization and PLL phase errors when the feedforward inputs are applied. Timing values are normalized by $\bar{T}_{\mathrm{mh_Y}}$ and phase slices by 2^N. (c) Resulting Lissajous scanning pattern with distorted regions as shown in the inset.

Iterative learning modulation control for SISO control system

Iterative learning control is widely used to compensate for errors in repeating tasks [132–134, 182] and mainly considered in this thesis, while alternative approaches such as repetitive control may achieve similar performance. In ILC the feedforward input signals are adapted based on the errors obtained from previous iterations, also called batches, using their repeating nature. The assumption of repeating errors allows also to adjust input values for compensation of errors in the future, i.e. non-causal control. In this context the relative degree $o \in \mathbb{N}_0$ of a discrete state space model is of importance, which is equal to the number of time steps it takes that an input shows action on an output. Hence, errors can only be compensated if the input is adapted at least o steps before the corresponding error. As the linearized MEMS mirror model in Eq. (6.7) has no direct feed-through of the inputs to the outputs, the relative degree is $o = 1$, which is the smallest number that fulfills the condition $\mathbf{C}_{\mathrm{S}}\mathbf{A}_{\mathrm{S}}^{o-1}\mathbf{B}_{\mathrm{S}} \neq 0$. Hence, any driving input change results in variations of the outputs in the next PLL period. A common formulation of the ILC exploits the lifted system representation, where the input and error values of the k-th iteration are combined in vectors of length

$2N_{\mathrm{Y0}}$, i.e. $\mathbf{u}_k$ and $\mathbf{e}_k$, and the update law is

$$\mathbf{u}_{k+1} = \mathbf{Q}\left(\mathbf{u}_k + \mathbf{L}\mathbf{e}_k\right) , \tag{7.48}$$

with the filter matrix $\mathbf{Q}$, the learning gain matrix $\mathbf{L}$ and $\mathbf{e}_k = \bar{\mathbf{y}} - \mathbf{y}_k$ as the difference of the desired and the actual output. Due to the nonzero relative degree the entries in $\mathbf{e}_k$ have to be shifted regarding that of $\mathbf{u}_k$. By using the subscript notation $u_{i|k}$ which is the input value corresponding to the PLL period i within iteration k, the vectors are given as

$$\begin{aligned}
\mathbf{u}_k &= \left[u_{0|k},\, u_{1|k}, \cdots, u_{2N_{\mathrm{Y0}}-1|k}\right]^{\mathrm{T}} , \\
\mathbf{e}_k &= \left[e_{o|k},\, e_{o+1|k}, \cdots, e_{o+2N_{\mathrm{Y0}}-1|k}\right]^{\mathrm{T}} , \\
\mathbf{y}_k &= \left[y_{o|k},\, y_{o+1|k}, \cdots, y_{o+2N_{\mathrm{Y0}}-1|k}\right]^{\mathrm{T}} .
\end{aligned} \tag{7.49}$$

The shift between inputs and outputs ensures that the system model matrix $\mathbf{G}$ defined as $\mathbf{y}_k = \mathbf{G}\mathbf{u}_k$ is Toeplitz and the diagonal entries are nonzero [134]. In the case of two inputs and outputs the individual entries of the vectors above are also 2×1 vectors, resulting in a total vector size of $4N_{\mathrm{Y0}} \times 1$. Let $\mathbf{A}_{\mathrm{FB}}$, $\mathbf{B}_{\mathrm{FB}}$ and $\mathbf{C}_{\mathrm{FB}}$ be the system matrix, the input matrix and the output matrix of the state space model representing the feedback controlled MEMS mirror, then the system model matrix can be expressed using the Markov parameters g_m defined as

$$\begin{aligned}
g_m &= \mathbf{C}_{\mathrm{FB}}\mathbf{A}_{\mathrm{FB}}^{m-1}\mathbf{B}_{\mathrm{FB}} \quad \text{with} \quad m = o,\, o+1,\, \ldots \infty , \\
\mathbf{G} &= \begin{bmatrix}
g_o & 0 & \cdots & 0 \\
g_{o+1} & g_o & \cdots & 0 \\
\vdots & \vdots & \ddots & 0 \\
g_{o+2N_{\mathrm{Y0}}-1} & g_{o+2N_{\mathrm{Y0}}-2} & \cdots & g_o
\end{bmatrix} .
\end{aligned} \tag{7.50}$$

Hence, the columns of the system model matrix represent the impulse response on the corresponding input shifted by the relative degree. Note that the Markov parameters are scalars if only one input and one output is considered in the ILC design, while they are matrices in the case of multiple inputs and outputs given by the columns in $\mathbf{B}_{\mathrm{FB}}$ and rows in $\mathbf{C}_{\mathrm{FB}}$, respectively.

Several approaches can be found in literature to design the matrices $\mathbf{Q}$ and $\mathbf{L}$. The filter matrix $\mathbf{Q}$ is typically designed to act as a low-pass filter and used to increase robustness against noise and non-repeating disturbances. However, a filter matrix different from the identity matrix, i.e. $\mathbf{Q} \neq \mathbf{I}$, effects the asymptotic error performance and typically does not achieve zero tracking error. Alternatively, as also suggested in [134] the errors can be averaged over several batches, i.e. Lissajous periods, before updating the inputs in order to avoid learning of noise and non-repeating disturbances. Hence, the error values corresponding to

the same Lissajous period index, i.e. a batch, are temporally filtered over several frames. In case of the synchronization error, the filtered synchronization error for the batch number j can be written in vector formulation as

$$\Delta\bar{\mathbf{s}}_{\delta_j} = \Delta\bar{\mathbf{s}}_{\delta_{j-1}} + G_{\mathrm{LP}} \left(\Delta\mathbf{s}_{\delta_{\mathrm{Y}}j} - \Delta\bar{\mathbf{s}}_{\delta_{j-1}} \right) , \tag{7.51}$$

where $\Delta\mathbf{s}_{\delta_{\mathrm{Y}},\mathrm{j}}$ denotes the measured synchronization errors and G_{LP} the scalar filter gain. Hence, if a new synchronization error is measured, the vector entry corresponding to the current Lissajous period index is updated. The ILC law is then executed after several batches passed in order to ensure convergence of the temporal filter and that transients caused by updates of the input vectors vanish. The corresponding settling time for a filter gain of $G_{\mathrm{LP}} = 0.1$ is 38 Lissajous periods, hence with a ILC update every 50 Lissajous periods the filter convergence is guaranteed. As a consequence, the convergence rate of the ILC is reduced, but has better stability and the filter matrix $\mathbf{Q}$ can be set to the identity matrix. This allows zero tracking error and reduces the complexity of the ILC as the temporal filters are simpler to implement than the filter matrix $\mathbf{Q}$. Furthermore, a reduced convergence rate is not problematic as the modulation functions have to be learned only once and would only necessitate an adaption if environmental conditions such as temperature or pressure change, which vary on a much larger time scale.

The entries of $\mathbf{L}$ at the left of the diagonal consider passed errors to update the corresponding input, while the right of the diagonal consider future errors. Hence, for example the first row does not take passed errors into account whereas the last row omits future errors within a batch. This is because for ILC it is typically assumed that the initial conditions are the same for each iteration, i.e. the system is reset to the same state before a new iteration is started [136]. Hence, the iteration can be treated independently from each other and influences of transient behaviors can be ignored. Even though the initial conditions are not always the same in this implementation, e.g. the start of an iteration is the end of the previous iteration, the transient independence is obtained as several batches pass until an update of the inputs is performed by the ILC, which allows transients to vanish. The learning gain matrix $\mathbf{L}$ can be of a simple PD-type exploiting a proportional and a differential part, e.g. $L = k_{\mathrm{p}}\mathbf{I} + k_{\mathrm{d}}\mathbf{D}$, with $\mathbf{D}$ as a derivative filter matrix and the gains k_{p} and k_{d} as tuning parameters [132, 134]. Alternatively it can be also designed based on a system model as for the inversion-based ILC, where the learning gain matrix corresponds to the inverse system model, i.e. $\mathbf{L} = \mathbf{G}^{-1}$ [134, 182]. Herein, a model-based design approach called norm-optimal ILC [133, 183] is applied, where the optimal gain and filter matrices are calculated to minimize a cost function with the system model as a constraint,

i.e.

$$J\left(\mathbf{u}_{k+1}\right) = \mathbf{e}_{k+1}^{\mathrm{T}}\mathbf{V}\mathbf{e}_{k+1} + \mathbf{u}_{k+1}^{\mathrm{T}}\mathbf{S}\mathbf{u}_{k+1} + \left(\mathbf{u}_{k+1} - \mathbf{u}_{k}\right)^{\mathrm{T}}\mathbf{R}\left(\mathbf{u}_{k+1} - \mathbf{u}_{k}\right) ,$$
$$\text{subject to} \quad \mathbf{e}_{k+1} = \bar{\mathbf{y}} - \mathbf{y}_{k+1} = \mathbf{e}_{k} + \mathbf{G}\mathbf{u}_{k} - \mathbf{G}\mathbf{u}_{k+1} , \tag{7.52}$$

with the weighting matrices $\mathbf{V}$, $\mathbf{S}$ and $\mathbf{R}$ and the ILC update law in Eq. (7.48). The solution of the minimization problem is given by

$$\mathbf{Q} = \left(\mathbf{G}^{\mathrm{T}}\mathbf{V}\mathbf{G} + \mathbf{S} + \mathbf{R}\right)^{-1}\left(\mathbf{G}^{\mathrm{T}}\mathbf{V}\mathbf{G} + \mathbf{R}\right) ,$$
$$\mathbf{L} = \left(\mathbf{G}^{\mathrm{T}}\mathbf{V}\mathbf{G} + \mathbf{R}\right)^{-1}\mathbf{G}^{\mathrm{T}}\mathbf{V} . \tag{7.53}$$

It can be seen that $\mathbf{S}$ defines the filter matrix $\mathbf{Q}$ and having $\mathbf{S} = 0$ results in an identity filter matrix while it does not influence the learning gain matrix. The weighting matrix $\mathbf{V}$ penalizes the residual errors and $\mathbf{R}$ the amount of change in the input vectors. With $\mathbf{V} = \mathbf{I}$ and $\mathbf{R} = 0$ the norm-optimal ILC is equal to the inversion based ILC without any restrictions on the inputs.

In the particular modulation control problem of the Y-axis MEMS mirror with SISO feedback control, it is only necessary to achieve zero synchronization errors. The PLL phase errors are assumed small enough to cause no serious misalignment between the DCO and the mirror oscillation, hence no effects on the sensing of phase, amplitude and scanning direction. By this assumption a simple SISO ILC can be used, which adjusts only the switching off input vector $\Delta\bar{\mathbf{s}}_{\mathrm{off}}$ according to the measured synchronization errors, while the feedforward PLL period vector $\Delta\bar{\mathbf{T}}_{\mathrm{PLL}}$ is not changed. Hence, the SISO ILC update law is

$$\Delta\bar{\mathbf{s}}_{\mathrm{off}_{k+1}} = \Delta\bar{\mathbf{s}}_{\mathrm{off}_{k}} - \mathbf{L}\,\Delta\bar{\mathbf{s}}_{\delta_{k}} , \tag{7.54}$$

with the learning gain matrix $\mathbf{L}$ obtained by Eq. (7.53) and the temporally filtered synchronization error $\Delta\bar{\mathbf{s}}_{\delta_k}$ in Eq. (7.51). Then the Markov parameters g_m are scalars and are calculated by Eq. (7.50) using only the entries in $\mathbf{B}_{\mathrm{FB}}$ and $\mathbf{C}_{\mathrm{FB}}$, which correspond to the inputs and outputs used by the ILC. Fig. 7.18 shows the block diagram of the adaptive Lissajous scanning system with SISO feedback control and the SISO ILC for the modulated axis. In contrast to the pure feedforward control method, the residual synchronization errors of the Y-axis are compensated by the ILC, which adapts the switching slices of the driving signal, i.e. the duty cycle, after enough Lissajous frames passed since the previous update.

SISO ILC design and implementation

The SISO ILC has only one input and output and each period index should be penalized equally. Therefore, the weighting matrices are typically set to diagonal

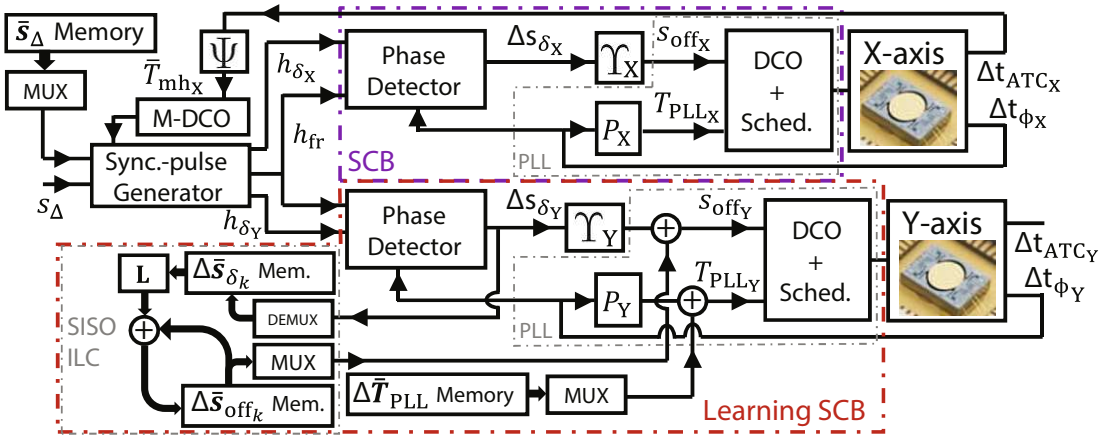

Figure 7.18.: Block diagram of the adaptive Lissajous scanning SISO control system with SISO ILC for feedforward modulation. The measured synchronization errors of each period are filtered according to Eq. (7.51) and stored in $\Delta\bar{\mathbf{s}}_{\delta_k}$. The feedforward switching slices $\Delta\bar{\mathbf{s}}_{\mathrm{off}_k}$ are updated using the learning gain matrix $\mathbf{L}$ after enough Lissajous frames passed since the previous update.

matrices defined by single scalar values, i.e. $\mathbf{V} = W_{\mathrm{s}_\delta}\,\mathbf{I}$ and $\mathbf{R} = W_{\mathrm{s_{off}}}\,\mathbf{I}$. For the design, only the relative value of W_{s_δ} and $W_{\mathrm{s_{off}}}$ matter. Hence, W_{s_δ} is arbitrarily chosen to 1 in order to penalize the residual errors and $W_{\mathrm{s_{off}}}$ is set to 0.5 to restrict the speed of the changes of the input vector and to enhance robustness. The SISO ILC law is then obtained as

$$\Delta\bar{\mathbf{s}}_{\mathrm{off}_{k+1}} = \Delta\bar{\mathbf{s}}_{\mathrm{off}_k} - \underbrace{\left(\mathbf{G}^{\mathrm{T}}\mathbf{G} + 0.5\,\mathbf{I}\right)^{-1}\mathbf{G}^{\mathrm{T}}}_{\mathbf{L}}\,\Delta\bar{\mathbf{s}}_{\delta_k}\,. \tag{7.55}$$

The state space model of the SISO feedback controlled MEMS mirrors defining the system model matrix $\mathbf{G}$ is obtained by combining the model in Eq. (6.7) and Eq. (6.8) with the feedback controllers in Eq. (6.9) and Eq. (6.10). The direct implementation of the learning gain matrix $\mathbf{L}$ would necessitate to store $2N_{\mathrm{Y0}} \times 2N_{\mathrm{Y0}}$ values and even shows bad performance at the start and end of the iteration as the repeating nature of the scanning reference is not utilized. For a perfect tracking of the repetitive modulation, both past and future errors should be considered for each input value. The proposed implementation of such a method is obtained by using a learning gain vector $\mathbf{l}$, which is the N_{Y0}-th row of $\mathbf{L}$ and the algorithm described in Alg. 1. The assumption is that most of the nonzero values in the learning gain matrix are around the diagonal and therefore the middle row, i.e. $\mathbf{l}$, considers equal numbers of passed and future errors. The other rows of the learning gain matrix can then be obtained by simply shifting the learning gain vector with zero padding, forming a Toeplitz matrix. Fig. 7.19

shows the obtained learning gain vector, where the nonzero values are concentrated around the center. The proposed algorithm given by the pseudo-code in Alg. 1 performs a convolution of the learning gain vector and the filtered synchronization errors, where the pointer *pntr* is also used to virtually expand the error vector for proper consideration of the start and end of the iteration.

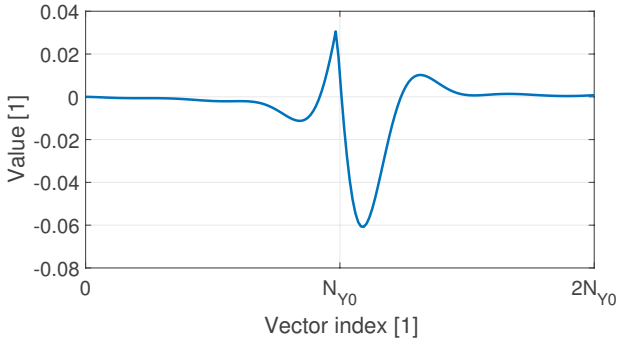

Figure 7.19.: Calculated values of the SISO ILC learning gain vector $\mathbf{l}$ over the vector index. The nonzero values are concentrated around the center index and approach zero towards both ends.

Algorithm 1 Pseudo-code for SISO ILC implementation to update the input vector $\Delta\bar{\mathbf{s}}_{\text{off}} \in \mathbb{R}^{2N_{\text{Y0}}}$ using the temporally filtered synchronization error vector $\Delta\bar{\mathbf{s}}_{\delta} \in \mathbb{R}^{2N_{\text{Y0}}}$, the learning gain vector $\mathbf{l} \in \mathbb{R}^{2N_{\text{Y0}}}$ and relative degree $o \in \mathbb{N}_0$. (Values in squared brackets represent vector indexes)

for $i \leftarrow 0$ **to** $2\,N_{\text{Y0}} - 1$ **do**
  $tmp \leftarrow 0$
  for $j \leftarrow 0$ **to** $2\,N_{\text{Y0}} - 1$ **do**
    $pntr \leftarrow i + j - N_{\text{Y0}} + o$
    if $pntr < 0$ **then**
      $pntr \leftarrow pntr + 2\,N_{\text{Y0}}$
    else if $pntr > 2\,N_{\text{Y0}} - 1$ **then**
      $pntr \leftarrow pntr - 2\,N_{\text{Y0}}$
    end if
    $tmp \leftarrow tmp - \mathbf{l}\,[j]\ \Delta\bar{\mathbf{s}}_{\delta}\,[pntr]$
  end for
  $\Delta\bar{\mathbf{s}}_{\text{off}}\,[i] \leftarrow \Delta\bar{\mathbf{s}}_{\text{off}}\,[i] + tmp$
end for

Experimental verification

The SISO ILC is implemented in the on-board CPU and executed every 50 Lissajous frames with $G_{\text{LP}} = 0.1$ allowing good noise suppression with enough

time for the filtered errors to follow the actual values between two ILC updates. Fig. 7.20 shows the synchronization error convergence when the ILC is turned on at $t = 0$ and executes 18 updates during 900 Lissajous periods. The error reduction every 50 Lissajous frames with the temporal filtering can be clearly observed and insets show the errors within a single Lissajous frame at the start and the end of the measurement. Fig. 7.21 shows the resulting scan patterns of the adaptive Lissajous scanning system at two different modulation functions only with feedforward control (a-b) and with the ILC (c-d). As can be seen, the initially distorted pattern is compensated and a proper smooth grid is obtained by the proposed ILC with a minimum rms synchronization error of only 0.0054% corresponding to an error reduction by a factor of 43 and is mainly limited by measurement noise. It has to be noted that in general each modulation function has to be learned only once for each MEMS mirror and allows immediate precise modulation tracking afterward if the values are stored in a memory.

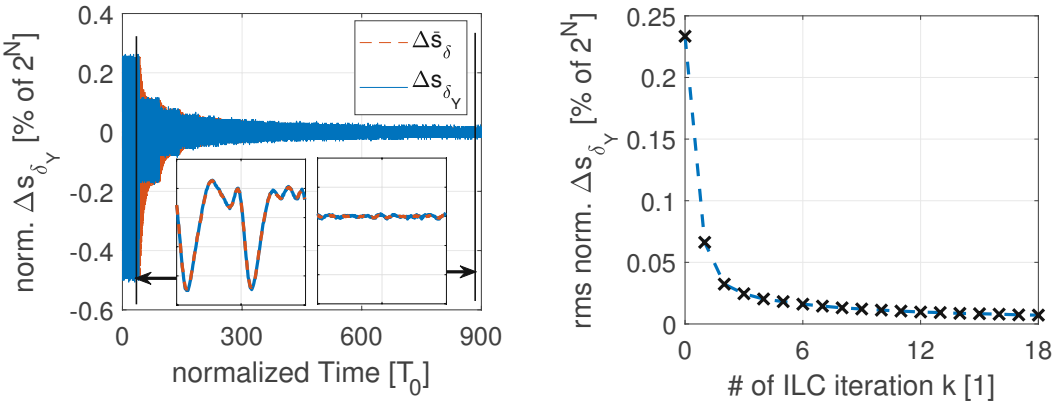

(a) (b)

Figure 7.20.: Convergence of the Y-axis synchronization error using the SISO ILC. The response over time in (a) shows steps every 50 Lissajous frames and the effect of the temporal filtering. Insets show the errors within a single Lissajous frame just before the first and the last ILC update. The time is normalized by the Lissajous period T_0. (b) The rms value of the synchronization error within a Lissajous frame and its reduction per ILC update, where a rms error of 0.0054% is reached as a minimum.

Fig. 7.22 shows a center ROI scan pattern compared to a conventional Lissajous scan with the corresponding pixel distribution derived by the proposed methods in this section. The amplitude variations are compensated based on the linear $A(f)$ relation obtained from the frequency response of the used MEMS mirror, resulting in a proper projection of the desired grid. Insets in the figure

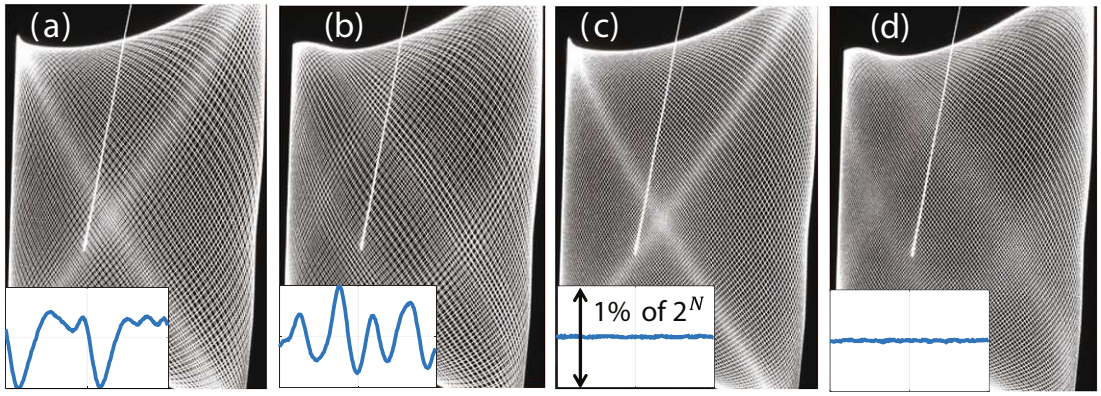

Figure 7.21.: Scan patterns of the adaptive Lissajous scanning system for two different modulation functions only with the feedforward control (a-b) and with the ILC (c-d). Insets show the corresponding synchronization errors within a single Lissajous frame.

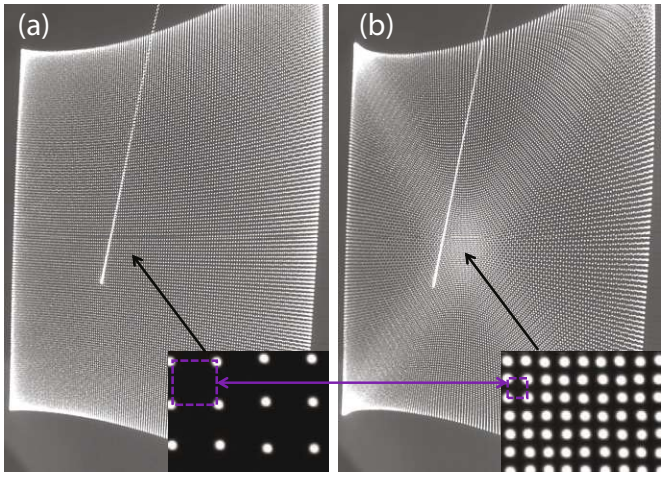

Figure 7.22.: Demonstration of pixel density improvement at ROI. (a) Conventional pixel distribution. (b) Proposed pixel distribution for a second order modulation. The insets show the pixel grid at the center of the FoV and demonstrate an improved resolution by a factor of 5 using the proposed modulation method.

show the zoomed center grids for both cases, where the modulated case provides a pixel distance reduced by 55%. This results in a resolution improvement by a factor of 5 due to the reduced area spanned by neighboring pixels.

Iterative learning modulation control for MIMO control system

As demonstrated in Chapter 6 the MIMO LQG controllers achieve superior performance in the suppression of external vibrations compared to SISO control. However, they are designed based on the linearized MEMS mirror model for fast compensation of any deviation from the nominal operation point, which is not desirable in case of modulation. Hence, as in the SISO controlled adaptive Lissajous scanning system, the LQG controllers should receive zero errors if the modulation is correctly followed and only compensate for deviations. As only two system inputs are considered, it is in general difficult to compensate for all three measured errors, i.e. PLL, amplitude and synchronization errors simultaneously during modulation and residual errors remain. Therefore, the $\mathrm{LQG_S}$ in Section 6.2.3 is slightly adapted, called $\mathrm{LQG_{AS}}$, not to receive amplitude error measurements, which are less critical for the modulation. The amplitude errors are also much less considered in the control, as can be seen by the integrator gains in Eq. (6.17) and the Kalman estimator gains in Eq. (6.19). This allows the use of a MIMO ILC, which updates the switching slices and the PLL period based on the measured PLL and synchronization errors, while ignoring the amplitude errors. Fig. 7.23 shows the block diagram of the adaptive Lissajous scanning system with MIMO feedback control and the MIMO ILC for the modulated axis. Both phase and synchronization errors, i.e. $\Delta t_{\phi_\mathrm{Y}}$ and $\Delta s_{\delta_\mathrm{Y}}$, are temporally filtered and stored in the memory, while the ILC law is executed again every 50 Lissajous frames for improved robustness and to allow $\mathbf{Q} = \mathbf{I}$ (i.e. $\mathbf{S} = 0$).

MIMO ILC design and implementation

As two inputs and two outputs are used for the MIMO ILC, the Markov parameters g_m are 2×2 matrices and the system model matrix $\mathbf{G} \in \mathbb{R}^{4N_{\mathrm{Y0}} \times 4N_{\mathrm{Y0}}}$ is block-wise Toeplitz. With the weighting values W_{t_ϕ} and W_{s_δ} for the PLL and synchronization error and $W_{\mathrm{s_{off}}}$ and $W_{\mathrm{T_{PLL}}}$ for the switching slices and PLL period inputs, respectively, the weighting matrices $\mathbf{V}$ and $\mathbf{R}$ in Eq. (7.52) have repeating values along the diagonal, i.e.

$$\begin{aligned} \mathbf{V} &= diag\left(W_{\mathrm{t}_\phi}, W_{\mathrm{s}_\delta}, W_{\mathrm{t}_\phi}, W_{\mathrm{s}_\delta}, \dots\right) \\ \mathbf{R} &= diag\left(W_{\mathrm{s_{off}}}, W_{\mathrm{T_{PLL}}}, W_{\mathrm{s_{off}}}, W_{\mathrm{T_{PLL}}}, \dots\right) . \end{aligned} \tag{7.56}$$

As only the relative relation of the weighting values is of importance, W_{s_δ} is again arbitrarily set to 1. The PLL phase error is of less importance and weighted by

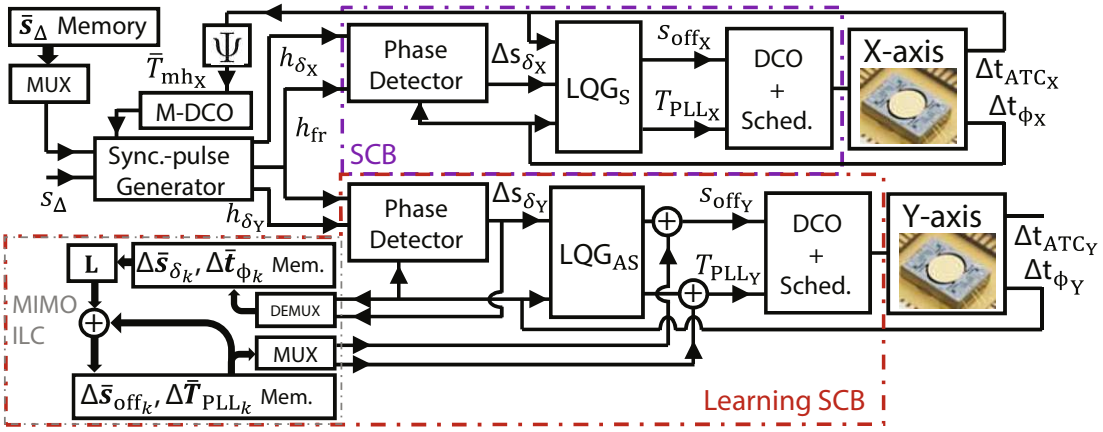

Figure 7.23.: Block diagram of the adaptive Lissajous scanning MIMO control system with MIMO ILC for feedforward modulation. The measured synchronization and PLL phase errors in each period are filtered and stored in $\Delta\bar{\mathbf{s}}_{\delta_k}$ and $\Delta\bar{\mathbf{t}}_{\phi_k}$. The feedforward inputs $\Delta\bar{\mathbf{s}}_{\mathrm{off}_k}$ and $\Delta\bar{\mathbf{T}}_{\mathrm{PLL}_k}$ are updated using the learning gain matrix $\mathbf{L}$ after enough Lissajous frames passed since the previous update.

$W_{\mathrm{t}_\phi} = 0.25\,\kappa_{\mathrm{t/s}}^{-2}$ considering the scaling between timing and phase slices. Similar to the LQG control design, the changes of the switching slices are allowed relatively fast while the PLL period is rather restricted, i.e. $W_{\mathrm{s_{off}}} = 0.1$ and $W_{\mathrm{T_{PLL}}} = 5\,\kappa_{\mathrm{t/s}}^{-2}$. This allows to calculate the learning gain matrix $\mathbf{L}$ using Eq. (7.53).

Again, an efficient implementation of the ILC can be obtained by extracting representative learning gain vectors from the obtained learning gain matrix and to perform a convolution with the measured errors. As two inputs and outputs are used, the effect of each input variation on both outputs should be considered. Hence, we define four learning gain vectors, which calculate the necessary change of an input due to an output error, i.e. $\mathbf{l}_{\Delta s_{\mathrm{off}}/\Delta s_\delta}, \mathbf{l}_{\Delta s_{\mathrm{off}}/\Delta t_\phi}, \mathbf{l}_{\Delta T_{\mathrm{PLL}}/\Delta s_\delta}$ and $\mathbf{l}_{\Delta T_{\mathrm{PLL}}/\Delta t_\phi}$. Similarly to the SISO ILC case, the same numbers of past and future errors should be considered for the compensation. Therefore, the corresponding learning gain vectors are extracted from the middle rows of the learning gain matrix $\mathbf{L}$, i.e. the $(2N_{\mathrm{Y0}}-1)$-th and $2N_{\mathrm{Y0}}$-th row, as

$$\begin{aligned}
\mathbf{l}_{\Delta s_{\mathrm{off}}/\Delta t_\phi} &= \mathbf{L}_{rc} \mid r = 2N_{\mathrm{Y0}} - 1 \quad \text{and} \quad c = 2\,i - 1 \\
\mathbf{l}_{\Delta s_{\mathrm{off}}/\Delta s_\delta} &= \mathbf{L}_{rc} \mid r = 2N_{\mathrm{Y0}} - 1 \quad \text{and} \quad c = 2\,i \\
\mathbf{l}_{\Delta T_{\mathrm{PLL}}/\Delta t_\phi} &= \mathbf{L}_{rc} \mid r = 2N_{\mathrm{Y0}} \quad \text{and} \quad c = 2\,i - 1 \\
\mathbf{l}_{\Delta T_{\mathrm{PLL}}/\Delta s_\delta} &= \mathbf{L}_{rc} \mid r = 2N_{\mathrm{Y0}} \quad \text{and} \quad c = 2\,i\,,
\end{aligned} \tag{7.57}$$

with the vector index $i \in [1,\, 2,\, \ldots,\, 2N_{\mathrm{Y0}}]$. Again by shifting the learning gain vec-

tors with zero padding, the learning gain matrix can be reconstructed. Fig. 7.24 shows the obtained learning gain vectors for the MIMO ILC implementation. An inset provides a close-up of the nonzero center values, while the entries get zero towards both ends. The pseudo-code shown in Alg. 2 performs the convolution for the MIMO ILC using the temporally filtered error values and the learning gain vectors.

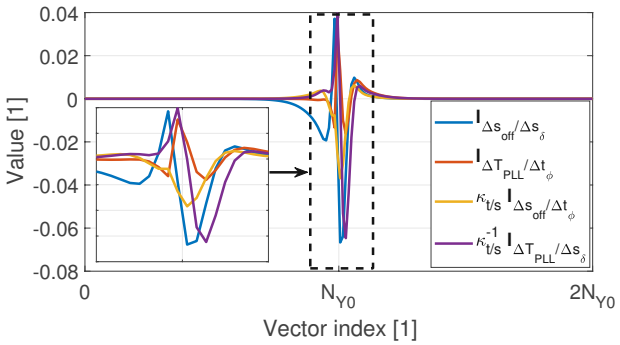

Figure 7.24.: Calculated values of the MIMO ILC learning gain vectors over the vector index. The nonzero values are concentrated around the center index and approach zero towards both ends. The learning gain vectors with different input and output domains are scaled by $\kappa_{\mathrm{t/s}} = \bar{T}_{\mathrm{mh_Y}}/2^N$ for visibility.

Experimental verification

Fig. 7.25 shows the final synchronization and PLL phase errors within one Lissajous period for the SISO ILC with SISO control and MIMO ILC with MIMO control, respectively. It can be observed that the MIMO ILC compensates for both errors caused by the modulation, resulting in no further control action of the MIMO controllers for modulation tracking.

To verify the vibration suppression performance for the modulated axis of the adaptive Lissajous scanning system, the Y-axis MEMS mirror is exposed to vibrations. Therefore, the experimental setup for vibration evaluation in Fig. 6.8 is used, where the MEMS mirror in the piezo-shaker (M2) is modulated and associated as Y-axis. Fig. 7.26a shows the comparison of the projected pixel grids using SISO ILC with SISO control (left) and MIMO ILC with MIMO control (right) when the vibration profile 2 in Fig. 5.22b is applied. The CCD exposure time is set to multiple Lissajous periods to visualize the errors by pixel blur. Insets provide close-ups of the image, showing that the pixels merge into another for the SISO control case, while the MIMO control provides clearly distinguishable pixels. As the axes are decoupled, only the disturbed axis shows pixel errors,

Algorithm 2 Pseudo-code for MIMO ILC implementation to update the input vectors $\Delta\bar{\mathbf{s}}_{\text{off}}$ and $\Delta\bar{\mathbf{T}}_{\text{PLL}} \in \mathbb{R}^{2N_{\text{Y0}}}$ using the temporally filtered error vectors $\Delta\bar{\mathbf{s}}_{\delta}$ and $\Delta\bar{\mathbf{t}}_{\phi} \in \mathbb{R}^{2N_{\text{Y0}}}$, the learning gain vectors $\mathbf{l}_{\Delta s_{\text{off}}/\Delta s_{\delta}}, \mathbf{l}_{\Delta s_{\text{off}}/\Delta t_{\phi}}, \mathbf{l}_{\Delta T_{\text{PLL}}/\Delta s_{\delta}}$ and $\mathbf{l}_{\Delta T_{\text{PLL}}/\Delta t_{\phi}} \in \mathbb{R}^{2N_{\text{Y0}}}$ and relative degree $o \in \mathbb{N}_0$. (Values in squared brackets represent vector indexes)

for $i \leftarrow 0$ **to** $2\,N_{\text{Y0}} - 1$ **do**
  $tmp\,[1] \leftarrow 0$
  $tmp\,[2] \leftarrow 0$
  for $j \leftarrow 0$ **to** $2\,N_{\text{Y0}} - 1$ **do**
    $pntr \leftarrow i + j - N_{\text{Y0}} + o$
    if $pntr < 0$ **then**
      $pntr \leftarrow pntr + 2\,N_{\text{Y0}}$
    else if $pntr > 2\,N_{\text{Y0}} - 1$ **then**
      $pntr \leftarrow pntr - 2\,N_{\text{Y0}}$
    end if
    $tmp\,[1] \leftarrow tmp\,[1] - \mathbf{l}_{\Delta s_{\text{off}}/\Delta s_{\delta}}\,[j]\ \Delta\bar{\mathbf{s}}_{\delta}\,[pntr] - \mathbf{l}_{\Delta s_{\text{off}}/\Delta t_{\phi}}\,[j]\ \Delta\bar{\mathbf{t}}_{\phi}\,[pntr]$
    $tmp\,[2] \leftarrow tmp\,[2] - \mathbf{l}_{\Delta T_{\text{PLL}}/\Delta s_{\delta}}\,[j]\ \Delta\bar{\mathbf{s}}_{\delta}\,[pntr] - \mathbf{l}_{\Delta T_{\text{PLL}}/\Delta t_{\phi}}\,[j]\ \Delta\bar{\mathbf{t}}_{\phi}\,[pntr]$
  end for
  $\Delta\bar{\mathbf{s}}_{\text{off}}\,[i] \leftarrow \Delta\bar{\mathbf{s}}_{\text{off}}\,[i] + tmp\,[1]$
  $\Delta\bar{\mathbf{T}}_{\text{PLL}}\,[i] \leftarrow \Delta\bar{\mathbf{T}}_{\text{PLL}}\,[i] + tmp\,[2]$
end for

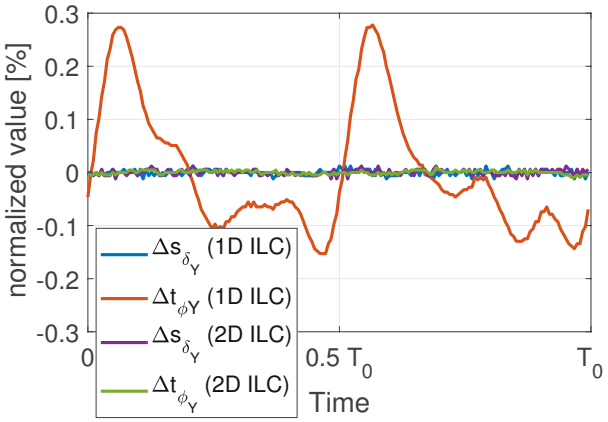

Figure 7.25.: Comparison of residual errors using SISO ILC with SISO control and MIMO ILC with MIMO control over one Lissajous period. Timing values are normalized by $\bar{T}_{\text{mh}_{\text{Y}}}$ and phase slices by 2^N.

while the other axis remains uninfluenced. Fig. 7.26b shows the resulting pointing uncertainty of the center and the corner pixel, proving the superior vibration performance of the MIMO control. The obtained optical pointing uncertainty of 22 mdeg for the MIMO control is only slightly higher, i.e. $\sim 7\%$, as compared to the case without modulation, which is mainly due to the switching slice input s_{off} has a limited range not to influence the sensing, e.g. the zero crossing detection. Hence, for adaptive Lissajous scanning using a MIMO ILC and MIMO LQG controllers for feedback control, the vibration suppression performance does not have to be compromised by modulation tracking requirements.

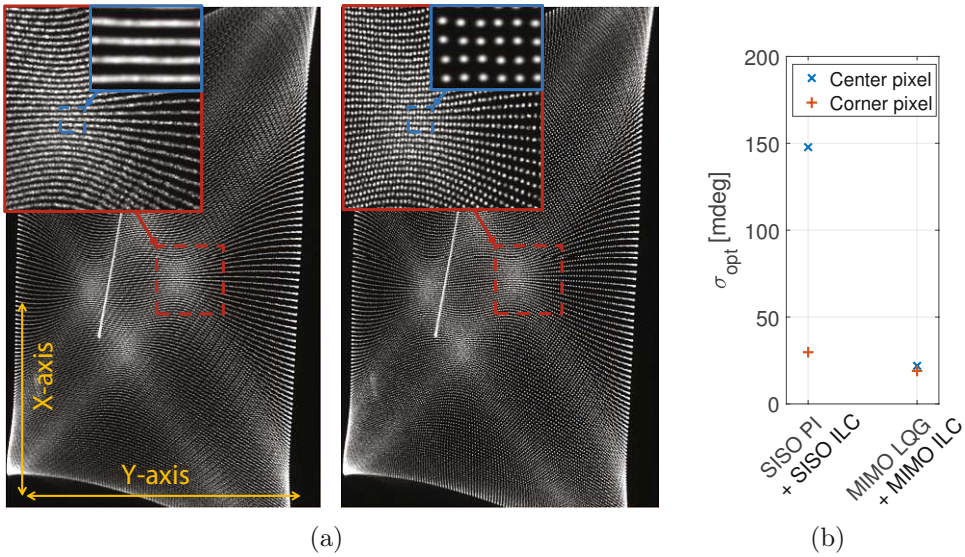

(a) (b)

Figure 7.26.: Pixel grid errors and pointing uncertainty of the adaptive Lissajous scanning system at exposure of vibration profile 2 to the modulated Y-axis MEMS mirror. (a) Comparison of pixel grid using SISO control (left) and MIMO control (right) with insets showing the resulting pixel blur. (b) Obtained pointing uncertainty of the center and the corner pixel in Y-axis direction.

7.3. Summary

Advanced scanning system concepts make use of the individual advantages of scanner design parameters, control method and pixel shooting as well as their interplay to achieve better overall system performance. In this chapter two advanced scanning concepts are discussed, the laser shot correction (ILC) for SISO and raster scanning systems and the adaptive Lissajous scanning using phase modulation.
The LSC is an advanced laser shot scheduling algorithm to correct pixel errors

caused by dynamic PLL phase and frequency mismatches as well as mirror amplitude errors. Based on a first order approximation of the trajectory at each pixel the corrections are calculated using two pixel position dependent parameters as well as estimates of the phase and amplitude errors. In order to predict the errors for the LSC in the following period, the Kalman estimator used in the LQG controller design is extended by a prediction output. An experimental verification reveals that the SISO control concept combined with the LSC shows similar performance to the LQG control concept during vibration exposure, providing a worst optical pointing uncertainty of 15 mdeg under harsh broadband vibrations.

The second presented concept is adaptive Lissajous scanning, which allows flexible scan pattern design by a dedicated modulation of the phase of at least one scanning axis. In conventional Lissajous scanning using constant frequencies the resolution has to be sacrificed with the frame rate and the scanning pattern shape is fixed, while adaptive Lissajous scanning provides an additional freedom in the pattern design to overcome this problem. The derived constraints of the phase modulation function reveal that it has to consist of sine waves with frequencies of multiples of the preview frame rate, i.e. the mean frequency difference of both axes. The proposed pixel calculation shows that the rectilinear grid lines of conventional Lissajous scanning can be bent such that a desired ROI has higher pixel density, while other regions are sacrificed. An optimization procedure results in a phase modulation function, which provides the desired scan pattern by judging the obtained resolution, i.e. the spanned area of neighboring pixels, its aspect ratios as well as the required control effort due to fast frequency changes. The implementation in the Lissajous scanning system based on MEMS mirrors demonstrates the feasibility of the proposed methods, showing cases of ROI scanning with a local resolution improvement by a factor of 5. Feedforward and iterative learning control are used for accurate modulation tracking, where the ILC is executed every 50 Lissajous frames to allow filtering of the errors for noise suppression. The ILC is implemented for both SISO and MIMO control concepts considering only one system input and output (SISO ILC) or both (MIMO ILC), demonstrating a fast convergence and reduced deterministic errors. Experimental results reveal that the modulation has only a negligible effect on the vibration suppression performance as long as the control does not reach a limit, achieving a worst optical pointing uncertainty of 22 mdeg at for ROI scan.

CHAPTER 8

Conclusion and Future Work

MEMS scanning systems promise versatile usability including automotive applications such as lidar, AR HUDs and adaptive headlights at a low cost. To be successful in the automotive market, enabling safety enhancing features up to fully automated cars, MEMS scanning systems have to achieve high performance even under harsh environmental conditions. In this thesis resonant electrostatic MEMS mirrors have been modeled and identified in detail and integrated into a scanning system including mirror synchronization methods for Lissajous scanning as well as optimal feedback control for external vibration suppression with tailored self-sensing concepts. Furthermore, novel methods to advance scanning systems are proposed, i.e. the laser shot correction enhancing 1D and raster scanning systems and adaptive Lissajous scanning to provide flexible scan pattern design, enabling ROI scanning. This chapter summarizes the findings of this thesis by addressing the research questions identified in Section 2.4 and provides an outlook with recommendations for future work.

8.1. Conclusion

To investigate the suitability of resonant MEMS mirrors for harsh automotive applications such as lidar, eight research questions have been formulated. These research questions are again successively given below and are answered one by one in the following.

Research Question 1:
Can the system dynamics of resonant electrostatic MEMS mirrors be accurately modeled and identified solely by measurement data in order to allow behavior prediction as well as monitoring of physical parameter variations?

Single axis MEMS mirrors can be typically designed such that the first mode is the desired scanning motion and the rotor is assumed rigid. Hence, in general only one DoF can be considered for the model, while several nonlinearities arise such as higher order stiffness, amplitude dependent damping and an angle dependent electrostatic torque. For the estimation of each physical parameter determining the MEMS mirror dynamics solely by measurements, the identification method needs to provide a separation of the parameters. In Section 3.2 the normalized nonlinear stiffness and damping are estimated from the mirror trajectory at a decay, where the low damping allows an independent stiffness estimation by the amplitude over frequency behavior. Subsequently, the comb-drive capacitance as well as the inertia are estimated from an actuated decay by simultaneously measuring the comb-dive current and the mirror trajectory, which allows a rescaling of the stiffness and the damping. A vibration measurement with a known acceleration amplitude also allows to estimate the vibration coupling parameter, completing the identification solely based on measurements. A damping realization function allows to correctly reproduce the amplitude dependent damping during simulation, resulting in an accurately matching frequency response and a period-based modified index of agreement of over 0.995 by comparing the decays. Hence, the first research question can be answered with: Yes.

Research Question 2:
Can the complex nonlinear dynamics of a resonant electrostatic MEMS mirror be accurately linearized at a nominal operation point, allowing linear system theory for simple and fast control design?

Conventional linearization methods of nonlinear equations of motion as proposed in literature, e.g. based on averaging, get complex as the order of nonlinearities increase, which hampers the analysis of closed loop control concepts. The method proposed in Section 3.3 is based on a period-to-period energy conservation, where the energy injection and dissipation of each driving period determines the change of the oscillation amplitude, i.e. the maximum potential energy stored in the springs, in the following period. A change in amplitude or phase varies the effective mechanical or electrostatic stiffness, respectively, leading to a change of the oscillation frequency and therefore the energy injection in the next period. The emerging dynamics are described by a linear second order state space model with the two states representing the phase and amplitude variations of the mirror oscillation at the nominal operation point. Furthermore, the system equation of the derived dynamic model can be fully identified by analyzing the obtained

phase error at an open loop period step allowing in-situ identification by the controller and is compared for different operation points. The correct scaling of the vibration disturbance input and the amplitude output necessitates a comb-drive current plateau and an amplitude measurement, respectively. The derived model accurately reproduces the local dynamics in time and frequency domain, verifying the proposed modeling approach. Hence, the second research question can be answered with: Yes.

Research Question 3:
What can be the consequences of a lightweight MEMS mirror design using reinforcement structures to the dynamics and robustness considering harsh automotive environments?

Lightweight MEMS mirror designs using reinforcement structures allow to increase the scanning speed without degrading the optical quality, while it has to be analyzed how such structures influence the dynamics and the robustness of the scanning system. Two major issues are identified and analyzed in this thesis, i.e. the influence of translational vibrations to the mirror oscillation and the R_X-T_Y mode coupling. Both are caused by the resulting center of mass displacement from the principal rotation axis and have the characteristic coupling parameter as the product of the rotor mass and the center of mass displacement.
Translational vibrations in the plane of rotation, i.e. in T_Y or T_Z direction, disturb the mirror oscillation, where it is found that the worst influence for T_Y is 10 times higher than that of T_Z. Furthermore, T_Y vibration frequencies close to the mirror frequency have the most influence, while for T_Z vibration frequencies close to twice the mirror frequency are most severe. This provides a rather good robustness against T_Z vibrations considering the frequency spectrum of the automotive standard LV124, while T_Y vibrations have to be considered by design of the scanning system. Hence, designers have to make a trade-off between scanning performance improvement by the reinforcement structure and vibration sensitivity. Possible circumventions are to increase the scanning frequency well above 2 kHz, to minimize the propagation of T_Y vibrations to the MEMS mirror by a dedicated housing or to use a high performance control.
The issue of R_X-T_Y mode coupling is occurring as the rotational acceleration of the mirror causes an acceleration of the center of mass in T_Y and vice versa, i.e. inertial coupling. As the dependency of the comb-drive capacitance on the translational mode is found to be negligible, only the inertial coupling is present between both modes. Hence, the rotational mode is electrostatically driven in parametric resonance, while the translational mode is driven as a conventional oscillator with a Duffing behavior due to its cubic stiffness. During a frequency sweep through the response curve of the MEMS mirror, a higher harmonic can hit the resonance of the translational mode, causing a significant distortion of the mirror trajectory due to the coupling ratio of $-0.029\,^{\circ}/\mu$m. However, by analyz-

ing the difference between left and right side comb-drive currents, the excitation of the translational mode can be detected and measures can be taken to reduce its amplitude, i.e. to cause a fallback. As due to the symmetric stiffness and comb-drive torque the mirror trajectory mainly includes only odd harmonics, those frequencies can be avoided by design for the translational mode resonance. Furthermore, if the resonance of the translational mode is not excited, the coupling enables a simple scanning direction detection by the current difference, which would be otherwise not possible for single-layer comb-drive designs. Hence to answer the third research question, the lightweight MEMS mirror design allows increased scanning performance and a self-sensing direction detection, while also errors caused by translational vibrations or a resonant mode coupling, which have to be considered by the scanning system design.

Research Question 4:
Is it possible to provide accurate and precise sensing signals for closed loop control solely based on a self-sensing concept using robust circuitry?

Self-sensing concepts have the benefit that the same structures are used for actuation and for sensing, reducing the complexity of the MEMS scanning system. In Chapter 4 two approaches of comb-drive designs are investigated, i.e. a single-layer and a double-layer design. The sensing concept is based on measuring the displacement current generated by the comb-drive movement and obtains phase, amplitude and scanning direction of the mirror by evaluating the timing of comparator threshold crossings. A precise phase measurement for both comb-drive designs is obtained at each mirror half period by a comparator as the current signal shows a sharp transition from positive to negative values when the mirror crosses the 0° position. It is found that the achievable optical resolution scales by the product of the driving voltage, the curvature of the comb-drive capacitance at 0°, the mirror amplitude and its maximum velocity. Amplitude measurements are obtained by the time between another comparator threshold crossing and the zero crossing of the mirror, where advantageous threshold settings are found to obtain a high sensitivity, i.e. about -2 ns per mdeg amplitude variation, at a low detection uncertainty. An analysis reveals that the normalization of the measured time by the mirror period provides a better robustness regarding mirror parameter variations due to manufacturing tolerances such as the stiffness. In case of the double-layer design, peaks in the current signals mark geometric features, i.e. the crossing of $\pm 6^{\circ}$ angle, which provides 50 times less uncertainty by threshold variations and 5 times less errors due to mirror parameter variations at the same sensitivity as compared to the single-layer design, while it is more complex in manufacturing. To detect the scanning direction for the single-layer design, the non-resonant R_X-T_Y mode coupling is utilized as it provides a direction dependent difference between left and right side comb-drive currents, while the double-layer design exploits intrinsic asymmetry. The self-sensing methods

use only simple circuitry comprising TIAs, adders, subtractors and comparators, providing high robustness and integrability. Hence, the fourth research question can be answered with: Yes.

Research Question 5:
Can a closed loop control be designed to start and stabilize resonant electrostatic MEMS mirrors with unknown stiffness nonlinearities in first-order parametric resonance and to provide precise pixel synchronization to evaluate the achievable resolution limits?

In contrast to MEMS mirrors with progressive springs as the ones used in this thesis, linear or degressive springs cause that operation points with positive phase delays are not stable in open loop. However, positive phase delays are necessary for the used self-sensing concept as the mirror zero crossing needs to happen when the driving voltage is on. The developed DAsPLL in Section 5.1 can stabilize open loop unstable operation points by immediate phase delay compensation. The driving voltage is always switched off with the detected zero crossing, while the switching on time, i.e. the duty cycle, is used to control the amplitude and calculated from previous zero crossings. A learning window technique allows the DAsPLL to track the mirror oscillation already during the transient beating of the mirror oscillation when started from rest, achieving a fast and reliable start-up to the maximum amplitude within less than 100 ms for various initial driving conditions. The pixel synchronization performance shows that it is not limited by the digital implementation but solely by the sensing noise according to the sensing concept analysis and results in an optical pointing uncertainty of 0.52 mdeg at the edges and 0.39 mdeg at the center of a 55° FoV. Hence, the fifth research question can be answered with: Yes.

Research Question 6:
Can the control strategies of resonant electrostatic MEMS mirrors be advanced in order to achieve stable scanning motion with the targeted 0.1° resolution considering harsh environmental conditions like in automotive lidar applications?

In automotive applications strong electromagnetic interference and vibrations have to be considered, increasing the sensing noise or disturbing the MEMS mirror motion, respectively. Hence, the control concept has to be optimized for vibration and noise robustness. In Section 5.2 an optimal PLL design is discussed comprising a time-normalized DCO based on phase slices and a model-based control design approach for 1D scanning and 2D Lissajous scanning. An optimal MIMO LQG servo controller is designed and compared to a SISO control concept using a PI loop filter. A worst case vibration test extending the automotive standard LV124 reveals the superior vibration suppression of the LQG control,

reducing the errors by 66% to stay within the targeted 0.1° resolution limit. For 2D Lissajous scanning, a synchronization concept is developed where a master DCO, i.e. either the DCO of one mirror (MS concept) or a separated DCO (M-SS concept), sends synchronization pulses to the slaves according to a desired frequency ratio between both axes. To align with the received synchronization pulses, a SISO PI control concept is used, where the gains are set based on an extended linear model of the MEMS mirror also including the synchronization error. Superior vibration suppression is again achieved by a MIMO LQG servo controller for the synchronization, resulting in an error reduction by 87% as compared to the SISO control. It is found, that the voltage of the driving signal can be used to compensate for small amplitude offsets of the MEMS mirrors, which is demonstrated by a compensation of 0.3° while the frequency ratio is kept constant. Hence, the sixth research question can be answered with: Yes.

Research Question 7:
Can the scheduling of the pixel trigger support the control concept to reduce the errors in application considering harsh environments?

Pixel errors of the scanning system can result from disturbances of the MEMS mirror motion due to external influences such as vibrations, causing misalignment of the PLL and mirror oscillation as well as variations in the scanning amplitude. An alternative to control the MEMS mirror oscillation can be to control the pixel timing directly, while the mirror oscillation is allowed to have increased errors. Hence, in Section 7.1 a laser shot correction approach based on the measured phase and amplitude errors is developed, while the MEMS mirror is controlled by a simple but low performance SISO control. For the correction, the phase and amplitude errors of the following period are predicted by utilizing a Kalman estimator. The pixel errors caused by the predicted amplitude variation is corrected based on a first order Taylor approximation of the mirror trajectory at the corresponding pixel position. The approach only needs two pixel position dependent parameters and achieves similar performance as the MIMO LQG servo control, while not influencing the dynamics of the closed loop controlled mirror. Hence, the seventh research question can be answered with: Yes.

Research Question 8:
Can Lissajous scanning provide flexible scan patterns with ROIs and which control concept is suitable to not compromise the robustness in harsh environments?

The inflexible scan pattern with fixed nonuniform resolution obtained by conventional Lissajous scanning is a major drawback compared to raster or random access scanning. An increase in resolution necessitates another scan frequency selection and typically reduces the frame rate if the selection range is limited.

However, an increase of the resolution in the total FoV is not always necessary, i.e. the ability to define high and low resolution areas can be beneficial.
In Section 7.2 adaptive Lissajous scanning is investigated exploiting a phase modulation between both scanning axes to shape the resulting scan pattern, e.g. to perform ROI scanning with a high resolution only in a specific area of the FoV, while the frame rate is kept constant. An analysis reveals that the phase modulation function has to consist of sine waves with frequencies that are multiples of the mean scanning frequency difference between both axes. A pixellation concept by shooting between scan line intersection points is adopted and extended for the phase modulation including the compensation of amplitude variations according to the scanner dynamics. The obtained pixels allow to design an optimized scan pattern to achieve the desired resolution grid. To accurately track the phase modulation by the MEMS mirror a norm optimal ILC is used, which successively adjusts the control inputs to minimize the errors over time. To also provide a high vibration robustness, the synchronization concept is adapted to only receive errors when the modulation is not correctly followed. This allows the separated design of modulation control by the ILC and vibration suppression by the LQG servo control, resulting in similar robustness as without modulation, which answers the last research question.

8.2. Outlook

This thesis has investigated 1D resonant electrostatic MEMS mirrors with progressive mechanical springs for their use in harsh automotive environments, including detailed modeling and tailored sensing as well as control concepts and also utilizing the implied frequency tuning capabilities. A natural extension of the presented work is to apply the same concepts or advances to MEMS mirrors with linear or degressive springs [126, 152].
2D Lissajous scanning is achieved by synchronizing two MEMS mirrors, which necessitates a rather bulky optical lens system to redirect the laser beam from the first to the second mirror, while it provides an ideal mechanical decoupling of both scanning axes. Hence, the proposed methods may be extended for a 2D MEMS mirror comprising a single mirror with two axes of rotation, reducing the optical system size, while several mechanical or electrostatic coupling mechanisms may arise. Modeling and identification of the rotational modes and their coupling as well as adapted robust sensing and control schemes to suppress undesired modes and external vibrations open many new research questions to be solved. Besides Lissajous scanning, raster scanning can be also investigated, where typical MEMS mirror designs utilize a fast resonant axis moving in an inner frame, representing the rotor of the rather slow non-resonant axis embedded in an outer frame [93]. For the slow axis, the proposed self-sensing concept based on the comb-drive current and simple comparators may not be feasible due to the

low oscillation frequency and as the driving signal is typically no square wave but a rather continuous signal. Hence, conventional or novel capacitive self-sensing methods as well as control concepts have to be evaluated regarding their robustness against harsh environments and parameter variations.

In order to evaluate the MEMS scanning system in the final application, appropriate transmitter and receiver units have to be developed. For example the projection unit in AR HUDs necessitates to convert a video data stream into pixels of the scanning system and corresponding RGB laser triggers. The lidar application needs a receiver unit with precision timing and a dedicated pulsed laser to measure the time-of-flight and to obtain a 3D point cloud. With those developments the performance at the final application can be analyzed and used to demonstrate the benefits of the concepts investigated in this thesis such as the advanced control and scanning concepts.

APPENDIX A

Response of Duffing Oscillator

The following analysis assumes a Duffing oscillator, whose equation of motion can be expressed as

$$m\,\ddot{x} + \gamma\,\dot{x} + k\left(x + \beta\,x^3\right) = A\,\cos\left(\omega t\right)\,. \tag{A.1}$$

with a cubic stiffness nonlinearity parametrized by β. First it is of interest how the resonance frequency f_0 shifts depending on the resulting amplitude $\hat{x}$. Assuming only a weakly nonlinear behavior, the actuation force at the resonance peak compensates for the damping force at any point in time. Hence, the total energy stored in the oscillator is constant. By introducing the potential and the kinetic energy as

$$E_{\mathrm{pot}}(x) = \int_0^x k\left(x + \beta\,x^3\right)\,\mathrm{d}x = \frac{x^2}{2} + \beta\,\frac{x^4}{4} \quad \text{and} \quad E_{\mathrm{kin}} = \frac{1}{2}\,m\,\dot{x}^2\,, \tag{A.2}$$

and the total energy as the sum of both and equal to the maximum potential energy $E_{\mathrm{pot}}\left(\hat{x}\right)$ at the amplitude $\hat{x}$, the velocity of the oscillator can be expressed as

$$\dot{x} = \sqrt{\frac{2}{m}\left(E_{\mathrm{pot}}\left(\hat{x}\right) - E_{\mathrm{pot}}\left(x\right)\right)} = \sqrt{\frac{2\,k}{m}\left(\frac{\hat{x}^2 - x^2}{2} + \beta\,\frac{\hat{x}^4 - x^4}{4}\right)}\,. \tag{A.3}$$

In general the oscillation period can be calculated by the integration of

$$T = 4\int_0^{\hat{x}} \frac{1}{\dot{x}}\,\mathrm{d}x\,, \tag{A.4}$$

where the symmetry of the trajectory is used. However according to Eq. (A.3) the integrand shows a division by zero at the integration limit $\hat{x}$. To overcome this, the trajectory is parametrized by a phase variable ϕ of a sine function as

$$x = \hat{x}\,\sin(\phi) \quad \text{and} \quad \mathrm{d}x = \hat{x}\,\cos(\phi)\,\mathrm{d}\phi \tag{A.5}$$

It is noteworthy that this parametrization does not assume a pure sine wave trajectory in time regarded as a single harmonic, it is only used to benefit from its trigonometric features. By using the identities

$$1 - \sin^2(\phi) = \cos(\phi)^2 \quad \text{and} \quad 1 - \sin(\phi)^4 = \cos(\phi)^2 \left(\frac{3}{2} - \frac{1}{2}\cos\left(2\phi\right)\right), \tag{A.6}$$

the oscillation period at the resonance peak can be calculated as

$$T_0 = 4\sqrt{\frac{m}{2\,k}} \int_0^{\frac{\pi}{2}} \frac{1}{\sqrt{\frac{1}{2} + \beta\,\frac{\hat{x}^2}{4}\left(\frac{3}{2} - \frac{1}{2}\cos\left(2\phi\right)\right)}}\,\mathrm{d}\phi \approx 2\pi\sqrt{\frac{m}{k}}\,\frac{1}{\sqrt{1 + \beta\,\frac{3}{4}\,\hat{x}^2}}, \tag{A.7}$$

where the $\cos\left(2\phi\right)$ term is neglected. Finally, the circular resonance frequency is obtained by

$$\omega_0(\hat{x}) = 2\pi\,\frac{1}{T_0} \approx \sqrt{\frac{k}{m}}\,\sqrt{1 + \beta\,\frac{3}{4}\,\hat{x}^2}\,. \tag{A.8}$$

Fig. A.1 shows the full simulated response of a Duffing oscillator according to Eq. (A.1) and the peak amplitude over frequency behavior calculated by Eq. (A.8).

A second interest is the dissipated energy per oscillation period, i.e.

$$\begin{aligned} E_{\mathrm{diss}}(T_0) &= \int_{x(0)}^{x(T_0)} \gamma\,\dot{x}\,\mathrm{d}x \\ &= \gamma\sqrt{\frac{2\,k}{m}}\,\hat{x}^2 \int_0^{2\pi} \sqrt{\frac{1}{2} + \beta\,\frac{\hat{x}^2}{4}\left(\frac{3}{2} - \frac{1}{2}\cos\left(2\phi\right)\right)}\,\cos(\phi)^2\,\mathrm{d}\phi \\ &\approx \gamma\,\pi\,\omega_0(\hat{x})\,\hat{x}^2\,, \end{aligned} \tag{A.9}$$

which is similar to a simple harmonic oscillator. Furthermore Eq. (A.9) is also valid for off resonance operation points, as long as the damping forces are relatively small, i.e. the trajectory is mainly defined by the springs and the mass. Hence, the dissipated energy per period for a given amplitude $\hat{x}$ and frequency f can be calculated by

$$E_{\mathrm{diss}}(T) \approx \gamma\,2\pi^2 f\,\hat{x}^2\,, \tag{A.10}$$

as shown in the right side of Fig. A.1.

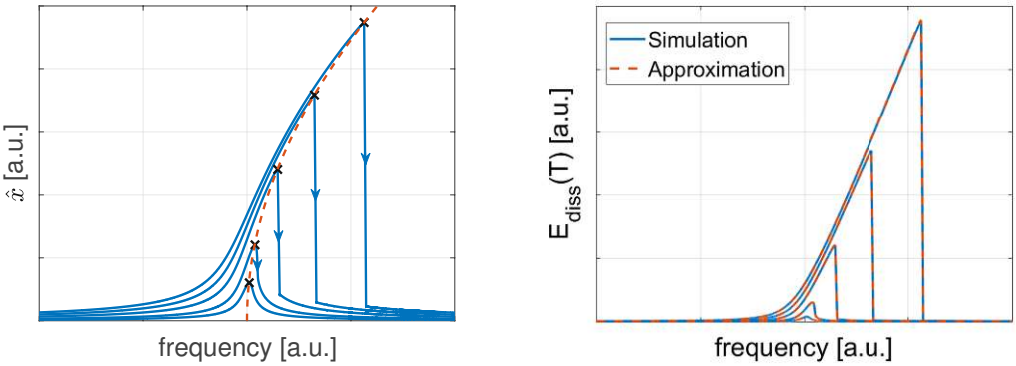

Figure A.1.: Simulated Duffing oscillator upsweep response of amplitude and dissipated energy per oscillation period. The obtained amplitude (Left) and dissipated energy (right) for different input amplitudes A (solid blue) are compared to the approximations Eq. (A.8) and Eq. (A.10) (dashed red), respectively. The maximum achieved amplitudes for different A are marked with black crosses and coincide with the approximation.

APPENDIX B

Collection of Proofs for Lissajous Scanning Analysis

In the following it is proven that

$$n_{\mathrm{X}j}\pi\frac{N_{\mathrm{Y0}}}{N_{\mathrm{X0}}} + (-1)^{n_{\mathrm{X}j}}\, j\frac{\pi}{2\,N_{\mathrm{X0}}} = n_{\mathrm{Y}j}\pi + (-1)^{n_{\mathrm{Y}j}}\, j\frac{\pi}{2\,N_{\mathrm{X0}}} \tag{B.1}$$

is fulfilled if L in Eq. (7.23) and Eq. (7.25) is an even and $\frac{1-L\,N_{\mathrm{X0}}}{K}$ is an odd integer. Inserting these two conditions into the expressions for $n_{\mathrm{X}j}$ and $n_{\mathrm{Y}j}$ yields

$$n_{\mathrm{X}j} = N_{\mathrm{X0}} + (-1)^{N_{\mathrm{X0}}+j}\; j\;\overbrace{\frac{1-L\,N_{\mathrm{X0}}}{K}}^{\text{odd}} \quad \text{and} \quad n_{\mathrm{Y}j} = n_{\mathrm{X}j} - K - \overbrace{(-1)^{N_{\mathrm{Y0}}+j}\; j\,L}^{\text{even}}\,. \tag{B.2}$$

With the above equations and $N_{\mathrm{Y0}} = N_{\mathrm{X0}} - K$, the left and the right hand side in Eq. (B.1) can be rewritten to

$$\begin{aligned} &-(-1)^{N_{\mathrm{X0}}+j}\, j\pi\left(\frac{1}{N_{\mathrm{X0}}} - L\right) + (-1)^{n_{\mathrm{X}j}}\, j\frac{\pi}{2\,N_{\mathrm{X0}}} \\ &\quad = -(-1)^{N_{\mathrm{Y0}}+j}\; j\pi\,L + (-1)^{n_{\mathrm{Y}j}}\, j\frac{\pi}{2\,N_{\mathrm{X0}}}\,, \end{aligned} \tag{B.3}$$

where common terms are eliminated. By analyzing Eq. (B.2) and that either N_{X0} or N_{Y0} is even while the other is odd (K is odd), the exponents in Eq. (B.3) can be equivalently written as

$$\begin{aligned} &(-1)^{N_{\mathrm{Y0}}+j} = -(-1)^{N_{\mathrm{X0}}+j}\;, \quad (-1)^{n_{\mathrm{Y}j}} = -(-1)^{n_{\mathrm{X}j}} \\ &\text{and} \quad (-1)^{n_{\mathrm{X}j}} = (-1)^{N_{\mathrm{X0}}+j}\;. \end{aligned} \tag{B.4}$$

Using this equivalences on both sides of Eq. (B.3) yields

$$-j\pi\left(\frac{1}{N_{\mathrm{X0}}}-L\right)+j\frac{\pi}{2\,N_{\mathrm{X0}}}=j\pi\,L-j\frac{\pi}{2\,N_{\mathrm{X0}}}\,, \tag{B.5}$$

which is true and therefore proves the equality of Eq. (B.1).

The equivalences in Eq. (B.4) are also used to proof the sign dependency elimination of the phase modulation function in Eq. (7.31). With the definition of $n_{\mathrm{X}j}$ it can be found that

$$\begin{aligned}&(-1)^{n_{\mathrm{Y}j}}\;\phi\left(\frac{n_{\mathrm{X}j}}{2f_{\mathrm{X}}}+(-1)^{n_{\mathrm{X}j}}\,t_j\right)\\&\quad=(-1)^{n_{\mathrm{Y}j}}\;\phi\left(\frac{N_{\mathrm{X0}}}{2f_{\mathrm{X}}}-(-1)^{n_{\mathrm{Y}j}}\left(j\frac{1-L\,N_{\mathrm{X0}}}{2f_{\mathrm{X}}K}+t_j\right)\right)\,.\end{aligned} \tag{B.6}$$

As the phase modulation function is anti-symmetric regarding half a Lissajous period shift, i.e.

$$\phi\left(\frac{N_{\mathrm{X0}}}{2f_{\mathrm{X}}}-t\right)=\phi\left(\frac{T_0}{2}-t\right)=-\phi\left(\frac{T_0}{2}+t\right)=-\phi\left(\frac{N_{\mathrm{X0}}}{2f_{\mathrm{X}}}+t\right)\,, \tag{B.7}$$

the sign dependency can be eliminated.

Bibliography

[1] P. A. Hancock, I. Nourbakhsh, and J. Stewart. On the future of transportation in an era of automated and autonomous vehicles. *Proceedings of the National Academy of Sciences*, 116(16):7684–7691, 2019.

[2] R. Munnig Schmidt, G. Schitter, A. Rankers, and J. van Eijk. *The Design of High Performance Mechatronics*. Delft University Press, 2nd edition, 2014.

[3] SAE International. Recommended practice J3016: Taxonomy and definitions for terms related to driving automation systems for on-road motor vehicles. 2014, revised 2018.

[4] Yole Développement. Smart automotive - latest trends in lidar and sensors. 2017.

[5] P. M. Knoll. Some pictures of the history of automotive instrumentation. *J. Soc. Inf. Disp.*, 25(1):44–52, 2017.

[6] Continental. Head-up displays. URL `https://conti-engineering.com/components/head-up-displays/`.

[7] Texas Instruments. Enabling the next generation of automotive head-up display systems. 2013, revised 2017.

[8] Audi OLED | Audi Future LAB. Audi matrix laser lights animation. URL `https://www.youtube.com/watch?v=wL3LSV3T4f4`.

[9] C. Reinert-Weiss and D. Duhme. High-resolution LCD headlamps for intelligent lighting. *Information Display*, 34(1):16–20, 2018.

[10] K. Braeckle. Eine revolution bei augmented reality (AR): der neue mems-scanner von infineon für brillen und head-up-displays, 2021. URL `https://www.infineon.com/cms/de/about-infineon/press/press-releases/2021/INFXX202108-091.html`.

[11] Z. Wendt and J. S. Cook. Saved by the sensor: Vehicle awareness in the self-driving age. URL `https://www.machinedesign.com/mechanical-motion-systems/article/21836344/saved-by-the-sensor-vehicle-awareness-in-the-selfdriving-age`.

[12] J. Hecht. Lidar for self-driving cars. *Optics and Photonics News*, 29(1): 26–33, 2018.

[13] Lidar: driving the future of autonomous navigation. Technical report, CA, USA, 2016.

[14] T. E. Laux and C.-I. Chen. 3D flash LIDAR vision systems for imaging in degraded visual environments. *Proc. SPIE*, 9087:14–25, 2014.

[15] R. H. Rasshofer and K. Gresser. Automotive radar and lidar systems for next generation driver assistance function. *Advanced in Radio Science*, 3: 205–209, 2005.

[16] R. Thakur. Scanning lidar in advanced driver assistance systems and beyond: Building a road map for next-generation lidar technology. *IEEE Consumer Electronics Magazine*, 5(3):48–54, 2016.

[17] J. R. McBride, J. C. Ivan, D. S. Rhode, J. D. Rupp, M. Y. Rupp, J. D. Higgins, D. D. Turner, and R. M. Eustice. A perspective on emerging automotive safety applications, derived from lessons learned through participation in the DARPA grand challenges. *J. Field Robot.*, 25:808–840, 2008.

[18] H. Wang, B. Wang, B. Liu, X. Meng, and G. Yang. Pedestrian recognition and tracking using 3D LiDAR for autonomous vehicle. *Robotics and Autonomous Systems*, 88:71–78, 2017.

[19] M. Himmelsbach, A. Müller, T. Lüttel, and H.-J. Wünsche. Lidar-based 3D object perception. *Computer Science*, 2008.

[20] Y. Yu, J. Li, H. Guan, C. Wang, and C. Wen. Bag of contextual-visual words for road scene object detection from mobile laser scanning data. *IEEE Trans. Intell. Transp. Syst.*, 17:3391 – 3406, 2016.

[21] Alberto Hata and Denis Wolf. Road marking detection using lidar reflective intensity data and its application to vehicle localization. *IEEE ITSC*, pages 584–589, 10 2014.

[22] S. L. Poczter and L. M. Jankovic. The Google car: Driving toward a better future? *Journal of Business Case Studies*, 10:7–14, 2014.

[23] E. Ackerman. Ford and Baidu invest $150 million in Velodyne for affordable lidar for self-driving cars. *IEEE Spectrum*, 2016.

[24] P. E. Ross. Volvo's self-driving program will have redundancy for everything. *IEEE Spectrum*, 2016.

[25] B. Berman. Lower-cost lidar is key to self-driving future. *Automotive Engineering*, 2015.

[26] D. J. Yeong, G. Velasco-Hernandez, J. Barry, and J. Walsh. Sensor and sensor fusion technology in autonomous vehicles: A review. *Sensors*, 21(6), 2021.

[27] AutonomouStuff. Lidar comparison chart. URL `https://www.techinsights.com/featured-reports/velodyne-lidar-puck`.

[28] Texas Instruments. DLP5530-Q1 0.55-inch 1.3-megapixel DMD for automotive interior display. 2016, revised 2019.

[29] R. Tamburo, E. Nurvitadhi, A. Chugh, M. Chen, A. Rowe, T. Kanade, and S. G. Narasimhan. Programmable automotive headlights. *Computer Vision – ECCV 2014*, pages 750–765, 2014.

[30] E. S. Cameron, R. P. Szumski, and J. K. West. Lidar scanning system, U.S. Patent 5006721 A, 1990.

[31] C. V. Poulton, M. J. Byrd, P. Russo, E. Timurdogan, M. Khandaker, D. Vermeulen, and M. R. Watts. Long-range LiDAR and free-space data communication with high-performance optical phased arrays. *IEEE J. Sel. Top. Quantum Electron.*, 25(5):1–8, 2019.

[32] C.-P. Hsu, B. Li, B. Solano-Rivas, A. R. Gohil, P. H. Chan, A. D. Moore, and V. Donzella. A review and perspective on optical phased array for automotive lidar. *IEEE J. Sel. Top. Quantum Electron.*, 27(1):1–16, 2021.

[33] K. Ito, C. Niclass, I. Aoyagi, H. Matsubara, M. Soga, S. Kato, M. Maeda, and M. Kagami. System design and performance characterization of a MEMS-based laser scanning time-of-flight sensor based on a 256x64-pixel single-photon imager. *IEEE Photonics Journal*, 5(2):6800114–6800114, 2013.

[34] H. W. Yoo, N. Druml, D. Brunner, C. Schwarzl, T. Thurner, M. Hennecke, and G. Schitter. MEMS-based lidar for autonomous driving. *e & i Elektrotechnik und Informationstechnik*, 135(6):408–415, 2018.

[35] D. Wang, C. Watkins, and H. Xie. MEMS mirrors for lidar: A review. *Micromachines*, 11(5), 2020.

[36] MicroVision. Short-throw interactive display module & starter kit (PSE-0407sti-421 & MV-2407sti-421). 2019.

[37] A. Kipman. How the HoloLens 2 works, explained by Microsoft's Alex Kipman, 2019. URL `https://www.youtube.com/watch?v=S0fEh4UdtT8&t=705s`.

[38] Renesas. Implementing laser scanned-MEMS projection in automotive head-up displays. 2017.

[39] J. Nakagawa, H. Yamaguchi, and T. Yasuda. Head up display with laser scanning unit. *Proc. SPIE*, 11125:28–34, 2019.

[40] Y.-H. Seo, K. Hwang, H. H. Kim, and K.-H. Jeong. Scanning MEMS mirror for high definition and high frame rate Lissajous patterns. *Micromachines*, 10(1):67, 2019.

[41] H. Baltes, O. Brand, G. Fedder, C. Hierold, J. Korvink, and O. Tabata (eds.). *Enabling Technology for MEMS and Nanodevices*. Weinheim, Germany: WILEY-â€‹VCH, 2004.

[42] T. Tsuchiya. MEMS mirrors for automotive applications. *2017 IEEE International Meeting for Future of Electron Devices, Kansai (IMFEDK)*, pages 82–83, 2017.

[43] A. Wolter, S.-T. Hsu, H. Schenk, and H. K. Lakner. Applications and requirements for MEMS scanner mirrors. *Proc. SPIE*, 5719:64–75, 2005.

[44] S. T. S. Holmström, U. Baran, and H. Urey. MEMS laser scanners: a review. *J. Microelectromech. Syst.*, 23(2):259–275, 2014.

[45] A. Bazaei, Y. K. Yong, and S. O. R. Moheimani. High-speed Lissajous-scan atomic force microscopy: Scan pattern planning and control design issues. *Review of Scientific Instruments*, 83(6):063701, 2012.

[46] E. Csencsics, S. Ito, J. Schlarp, and G. Schitter. System integration and control for 3D scanning laser metrology. *IEEJ J. Ind. Appl.*, 8(2):207–217, 2019.

[47] B. Ballard, V. Bhakta, M. Douglass, P. Gelabert, J. Kempf, W. McDonald, G. Pettitt, P. Rancuret, A. Rankin, J. Thompson, and P. I. Oden. 'steering' light with texas instruments digital micromirror device (DMD) - past, present & future. *SID Symposium Digest of Technical Papers*, 47(1):28–31, 2016.

[48] J. Rodriguez, B. Smith, B. Hellman, and Y. Takashima. Fast laser beam steering into multiple diffraction orders with a single digital micromirror device for time-of-flight lidar. *Appl. Opt.*, 59(22):G239–G248, 2020.

[49] T. Raj, F. H. Hashim, A. Ba. Huddin, M. F. Ibrahim, and A. Hussain. A survey on lidar scanning mechanisms. *Electronics*, 9(5), 2020.

[50] A. J. Fleming and A. G. Wills. Optimal periodic trajectories for band-limited systems. *IEEE Trans. Control Syst. Technol.*, 17(3):552–562, 2009.

[51] H. W. Yoo, S. Ito, and G. Schitter. High speed laser scanning microscopy by iterative learning control of a galvanometer scanner. *Control Engineering Practice*, 50:12–21, 2016.

[52] R. Aylward. Advanced galvanometer-based optical scanner design. *Sensor Review*, 23, 09 2003.

[53] E. Csencsics, J. Schlarp, T. Schopf, and G. Schitter. Compact high performance hybrid reluctance actuated fast steering mirror system. *Mechatronics*, 62:102251, 2019.

[54] P.M. Hagelin and O. Solgaard. Optical raster-scanning displays based on surface-micromachined polysilicon mirrors. *IEEE J. Sel. Top. Quantum Electron.*, 5(1):67–74, 1999.

[55] R. Schroedter, M. Roth, K. Janschek, and T. Sandner. Flatness-based open-loop and closed-loop control for electrostatic quasi-static microscanners using jerk-limited trajectory design. *Mechatronics*, 56:318–331, 2018.

[56] U. Hofmann, J. Janes, and H. Quenzer. High-Q MEMS resonators for laser beam scanning displays. *Micromachines*, 3:509–528, 2012.

[57] J. Wang, G. Zhang, and Z. You. Design rules for dense and rapid Lissajous scanning. *Microsyst. Nanoeng.*, 6(101), 2020.

[58] K. Hwang, Y.-H. Seo, J. Ahn, P. Kim, and K.-H. Jeong. Frequency selection rule for high definition and high frame rate Lissajous scanning. *Scientific Reports*, 7:14075, 2017.

[59] T. Tuma, J. Lygeros, A. Sebastian, and A. Pantazi. Analysis and design of multiresolution scan trajectories for high-speed scanning probe microscopy. *IFAC Proceedings Volumes*, 46(5):138–144, 2013. 6th IFAC Symposium on Mechatronic Systems.

[60] Q. A. A. Tanguy, O. Gaiffe, N. Passilly, J.-M. Cote, G. C., S. Bargiel, P. Lutz, H. Xie, and C. Gorecki. Real-time Lissajous imaging with a low-voltage 2-axis MEMS scanner based on electrothermal actuation. *Opt. Express*, 28(6):8512–8527, 2020.

[61] T. Tuma, J. Lygeros, A. Sebastian, and A. Pantazi. Optimal scan trajectories for high-speed scanning probe microscopy. *2012 American Control Conference (ACC)*, pages 3791–3796, 2012.

[62] H. Moriguchi, M. Wendt, and J. L. Duerk. Applying the uniform resampling (URS) algorithm to a Lissajous trajectory: Fast image reconstruction with optimal gridding. *Magnetic Resonance in Medicine*, 44(5):766–781, 2000.

[63] J. Kim, Y. Kawai, N. Inomata, and T. Ono. Parametrically driven resonant micro-mirror scanner with tunable springs. *IEEE 26th Int. Conf. Micro Electro Mech. Syst. (MEMS)*, pages 580–583, 2013.

[64] Y. Kawai, J.-H. Kim, N. Inomata, and T. Ono. Parametrically actuated resonant micromirror using stiffness tunable torsional springs. *Sensors and Materials*, 28:131–139, 01 2016.

[65] D. Brunner, H. W. Yoo, T. Thurner, and G. Schitter. Data based modelling and identification of nonlinear SDOF MOEMS mirror. *Proc. SPIE*, 10931: 269 – 278, 2019.

[66] W. O. Davis. Measuring quality factor from a nonlinear frequency response with jump discontinuities. *J. Microelectromech. Syst.*, 20(4):968–975, 2011.

[67] S. Z. Sullivan, R. D. Muir, J. A. Newman, M. S. Carlsen, S. Sreehari, C. Doerge, N. J. Begue, R. M. Everly, C. A. Bouman, and G. J. Simpson. High frame-rate multichannel beam-scanning microscopy based on Lissajous trajectories. *Opt. Express*, 22(20):24224–24234, 2014.

[68] P. F. McManamon, T. A. Dorschner, D. L. Corkum, L. J. Friedman, D. S. Hobbs, M. Holz, S. Liberman, H. Q. Nguyen, D. P. Resler, R. C. Sharp, and E. A. Watson. Optical phased array technology. *Proc. IEEE*, 84(2): 268–298, 1996.

[69] A. C. Lesina, D. Goodwill, E. Bernier, L. Ramunno, and P. Berini. On the performance of optical phased array technology for beam steering: effect of pixel limitations. *Opt. Express*, 28(21):31637–31657, 2020.

[70] P. A. Kirkby, K. M. N. S. Nadella, and R. A. Silver. A compact acousto-optic lens for 2D and 3D femtosecond based 2-photon microscopy. *Opt. Express*, 18(13):13720–13744, 2010.

[71] K. Nadella, H. Roš, C. Baragli, V. Griffiths, G. Konstantinou, T. Koimtzis, G. Evans, P. Kirkby, and R. Silver. Random-access scanning microscopy for 3D imaging in awake behaving animals. *Nature Methods*, 13(12):1001–1004, 10 2016.

[72] K. E. Petersen. Silicon as a mechanical material. *Proceedings of the IEEE*, 70(5):420–457, 1982.

[73] U. Nabholz, W. Heinzelmann, J. E. Mehner, and P. Degenfeld-Schonburg. Amplitude- and gas pressure-dependent nonlinear damping of high-Q oscillatory MEMS micro mirrors. *J. Microelectromech. Syst.*, 27(3):383–391, 2018.

[74] U. Hofmann, F. Senger, J. Janes, C. Mallas, V. Stenchly, T. Wantoch, H. Quenzer, and M. Weiss. Wafer-level vacuum-packaged two-axis MEMS scanning mirror for pico-projector application. *Proc. SPIE*, 8977:47–60, 2014.

[75] H. Xie, G. Fedder, and Y. Pan. MEMS-based endoscopic optical coherence tomography. *Proc. SPIE*, 5721:81–92, 2005.

[76] U. Hofmann, M. Aikio, J. Janes, F. Senger, V. Stenchly, M. Weiss, H.-J. Quenzer, B. Wagner, and W. Benecke. Resonant biaxial 7-mm MEMS mirror for omnidirectional scanning. *Proc. SPIE*, 8616:71–84, 2013.

[77] N. Druml, I. Maksymova, T. Thurner, D. Lierop, M. Hennecke, and A. Foroutan. 1D MEMS micro-scanning lidar. *In Int. Conf. on Sensor Device Technologies and Appl.*, 09 2018.

[78] H. Urey. MEMS scanners for display and imaging applications. *Proc. SPIE*, 5604:218–219, 2004.

[79] S. Gu-Stoppel, T. Giese, H.-J. Quenzer, U. Hofmann, and W. Benecke. Piezoelectrically driven and sensed micromirrors with extremely large scan angles and precise closed-loop control. *MikroSystemTechnik; Congress*, 1 (4), 2017.

[80] S. Tadigadapa and K. Mateti. Piezoelectric MEMS sensors: state-of-the-art and perspectives. *Measurement Science and Technology*, 20(9):092001, jul 2009.

[81] G. N. Nielson and G. Barbastathis. Dynamic pull-in of parallelplate and torsional electrostatic MEMS actuators. *J. Microelectromech. Syst.*, 15(4): 811–821, 2006.

[82] Y. Bai, J. T. W. Yeow, and B. C. Wilson. Design, fabrication, and characteristics of a MEMS micromirror with sidewall electrodes. *J. Microelectromech. Syst.*, 19(3):619–631, 2010.

[83] M. Ozdogan and S. Towfighian. Nonlinear dynamic behavior of a bi-axial torsional MEMS mirror with sidewall electrodes. *Micromachines*, 7(3), 2016.

[84] D. Hah, P. R. Patterson, H. D. Nguyen, H. Toshiyoshi, and M. C. Wu. Theory and experiments of angular vertical comb-drive actuators for scanning micromirrors. *IEEE J. Sel. Top. Quantum Electron*, 10(3):505–513, 2004.

[85] T. Sandner, T. Grasshoff, M. Schwarzenberg, R. Schroedter, and H. Schenk. Quasi-static microscanner with linearized scanning for an adaptive 3D laser camera. *Proc. SPIE*, 8977:299–308, 2014.

[86] T. Izawa, T. Sasaki, and K. Hane. Scanning micro-mirror with an electrostatic spring for compensation of hard-spring nonlinearity. *Micromachines*, 8(8):240, 2017.

[87] A. M. Elshurafa, K. Khirallah, H. H. Tawfik, A. Emira, A. K. S. Abdel Aziz, and S. M. Sedky. Nonlinear dynamics of spring softening and hardening in folded-MEMS comb drive resonators. *J. Microelectromech. Syst.*, 20(4): 943–958, 2011.

[88] T. Sandner, H. Schenk, and C. Drabe. Application specific micro scanning mirrors. *Proceedings SENSOR 2011*, pages 337–342, 2011.

[89] L. Ye, G. Zhang, and Z. You. Large-aperture khz operating frequency Ti-alloy based optical micro scanning mirror for lidar application. *Micromachines*, 8(4), 2017.

[90] A. Frangi, A. Guerrieri, N. Boni, R. Carminati, M. Soldo, and G. Mendicino. Mode coupling and parametric resonance in electrostatically actuated micromirrors. *IEEE Trans. Ind. Electron.*, 65(7):5962–5969, 2018.

[91] C. Xia, D. Qiao, Y. Zhang, X. Su, and Z. Guo. A position feedback solution based on the acoustic signal produced by electrostatically driven MEMS scanning mirror. *IEEE-NEMS*, pages 558–561, 2017.

[92] J. Grahmann, T. Graßhoff, H. Conrad, T. Sandner, and H. Schenk. Integrated piezoresistive position detection for electrostatic driven micro scanning mirrors. *Proc. SPIE*, 7930:260–267, 2011.

[93] R. Schroedter, T. Sandner, K. Janschek, M. Roth, and C. Hruschka. Real-time closed-loop control for micro mirrors with quasistatic comb drives. *Proc. SPIE*, 9760:28–40, 2016.

[94] U. Baran, D. Brown, S. Holmstrom, D. Balma, W. O. Davis, P. Muralt, and H. Urey. Resonant PZT MEMS scanner for high-resolution displays. *J. Microelectromech. Syst.*, 21:1303–1310, 2012.

[95] A. Tortschanoff, M. Lenzhofer, A. Frank, M. Wildenhain, T. Sandner, H. Schenk, W. Scherf, and A. Kenda. Position encoding and phase control of resonant MOEMS mirrors. *Sensors and Actuators A: Physical*, 162 (2):235–240, 2010.

[96] V. Milanović, A. Kasturi, J. Yang, and F. Hu. Closed-loop control of gimbal-less MEMS mirrors for increased bandwidth in lidar applications. *Proc. SPIE*, 10191:157–169, 2017.

[97] K.-U. Roscher, U. Fakesch, H. Schenk, H. K. Lakner, and D. Schlebusch. Driver ASIC for synchronized excitation of resonant micromirrors. *Proc. SPIE*, 4985:121–130, 2003.

[98] Baris Cagdaser, Anand Jog, Matt Last, Brian Leibowitz, L. Zhou, Eric Shelton, Kristofer Pister, and Bernhard Boser. Capacitive sense feedback control for MEMS beam steering mirrors. *Solid-State Sensor, Actuator and Microsystems Workshop*, pages 348–351, 2004.

[99] L. J. Chemmanda, C. C. Jianrong, R. P. Singh, and Y. Roterman. ASIC front-end for sensing MEMS-mirror position. *International Symposium on Integrated Circuits (ISIC)*, pages 396–399, 2014.

[100] A. C.-L. Hung, H. Y.-H. Lai, T.-W. Lin, S.-G. Fu, and M. S.-C. Lu. An electrostatically driven 2D micro-scanning mirror with capacitive sensing for projection display. *Sensors and Actuators A: Physical*, 222:122 – 129, 2015.

[101] J. Grahmann, A. Dreyhaupt, C. Drabe, R. Schroedter, J. Kamenz, and T. Sandner. MEMS-mirror based trajectory resolution and precision enabled by two different piezoresistive sensor technologies. *Proc. SPIE*, 9760: 157–169, 2016.

[102] S. Gu-Stoppel, T. Giese, H.-J. Quenzer, U. Hofmann, and W. Benecke. Pzt-actuated and -sensed resonant micromirrors with large scan angles applying mechanical leverage amplification for biaxial scanning. *Micromachines*, 8 (7), 2017.

[103] R. A. Wolf and S. Trolier-McKinstry. Temperature dependence of the piezoelectric response in lead zirconate titanate films. *Int. J. Appl. Phys.*, 95(3): 1397–1406, 2004.

[104] C.-H. Cho, R. C. Jaeger, and J. C. Suhling. Characterization of the temperature dependence of the piezoresistive coefficients of silicon from −150 °C to +125 °C. *IEEE Sensors Journal*, 8(8):1455–1468, 2008.

[105] R. Otmani, N. Benmoussa, and B. Benyoucef. The thermal drift characteristics of piezoresistive pressure sensor. *Physics Procedia*, 21:47–52, 2011.

[106] A. Tortschanoff, M. Lenzhofer, A. Frank, M. Wildenhain, T. Sandner, H. Schenk, and A. Kenda. Optical position feedback and phase control of MOEMS scanner mirrors. *Proc. SPIE*, 7594:168–178, 2010.

[107] B. Cagdaser and B. E. Boser. Low-voltage electrostatic actuation with inherent position feedback. *J. Microelectromech. Syst.*, 21(5):1187–1196, 2012.

[108] R. Schroedter, H. W. Yoo, D. Brunner, and G. Schitter. Capacitive charge-based self-sensing for resonant electrostatic MEMS mirrors. *IFAC-PapersOnLine*, 53(2):8553–8558, 2020. 21th IFAC World Congress.

[109] T. Sandner, T. Grasshoff, M. Wildenhain, and H. Schenk. Synchronized microscanner array for large aperture receiver optics of lidar systems. *Proc. SPIE*, 7594:107–118, 2010.

[110] H. Urey, D.d W. Wine, and T. D. Osborn. Optical performance requirements for MEMS-scanner-based microdisplays. *Proc. SPIE*, 4178:176–185, 2000.

[111] J. Nee, R. Conant, R. Muller, and K. Lau. Lightweight, optically flat micromirrors for fast beam steering. *IEEE/LEOS Int. Conf. on Opt. MEMS (Cat. No.00EX399)*, pages 9 – 10, 2000.

[112] V. Milanović, G.A. Matus, and D.T. McCormick. Gimbal-less monolithic silicon actuators for tip-tilt-piston micromirror applications. *IEEE J. Sel. Topics Quantum Electron.*, 10(3):462–471, 2004.

[113] S. Hsu, T. Klose, C. Drabe, and H. Schenk. Fabrication and characterization of a dynamically flat high resolution micro-scanner. *J. Opt. A: Pure Appl. Opt.*, 10(4):044005, 2008.

[114] U. Hofmann, M. Aikio, J. Janes, F. Senger, V. Stenchly, J. Hagge, H.-J. Quenzer, M. Weiss, T.v. Wantoch, C. Mallas, B. Wagner, and W. Benecke. Resonant biaxial 7-mm MEMS mirror for omnidirectional scanning. *J. Micro/Nanolith. MEMS MOEMS*, 13(1):011103, 2014.

[115] A.Z. Hajjaj, N. Jaber, S. Ilyas, F.K. Alfosail, and M.I. Younis. Linear and nonlinear dynamics of micro and nano-resonators: Review of recent advances. *Int. J. Non. Linear Mech.*, 119:103328, 2020.

[116] Rajashree Baskaran and Kimberly L Turner. Mechanical domain coupled mode parametric resonance and amplification in a torsional mode micro electro mechanical oscillator. *J. Micromech. Microeng.*, 13(5):701–707, 2003.

[117] J. F. Rhoads, S. W. Shaw, and K. L. Turner. Nonlinear Dynamics and Its Applications in Micro- and Nanoresonators. *J. Dyn. Syst. Meas. Control*, 132(3), 2010.

[118] H. v. Lierop and K. S. Khah. Mirror device comprising a leaf spring with openings, U.S. Patent 10877263B2 B2, 2020.

[119] W. O. Davis, O. M. O'Reilly, and A. P. Pisano. On the nonlinear dynamics of tether suspensions for MEMS. *J. Vib. Acoust.*, 126(3):326–331, 2004.

[120] C. Guo and G. K. Fedder. Bi-state control of parametric resonance. *Applied Physics Letters*, 103(18):183512, 2013.

[121] T. Klose, H. Conrad, T. Sandner, and H. Schenk. Fluidmechanical damping analysis of resonant micromirrors with out-of-plane comb drive. *Proc. COMSOL Conf.(Hannover)*, 2008.

[122] P. M. Polunin, Y. Yang, M. I. Dykman, T. W. Kenny, and S. W. Shaw. Characterization of MEMS resonator nonlinearities using the ringdown response. *J. Microelectromech. Syst.*, 25(2):297–303, 2016.

[123] J. M. Londono, S. A. Neild, and J. E. Cooper. Identification of backbone curves of nonlinear systems from resonance decay responses. *J. Sound Vib.*, 348:224 – 238, 2015.

[124] C. Ataman and H. Urey. Modeling and characterization of comb-actuated resonant microscanners. *J. Micromech. Microeng.*, 16(1):9–16, 2005.

[125] W. Shahid, Z. Qiu, X. Duan, H. Li, T. D. Wang, and K. R. Oldham. Modeling and simulation of a parametrically resonant micromirror with duty-cycled excitation. *J. Microelectromech. Syst.*, 23(6):1440–1453, 2014.

[126] A. Frangi, A. Guerrieri, R. Carminati, and G. Mendicino. Parametric resonance in electrostatically actuated micromirrors. *IEEE Trans. Ind. Electron.*, 64(2):1544–1551, 2017.

[127] A. Champneys. *Dynamics of Parametric Excitation*, pages 1–31. Springer New York, New York, NY, 2009.

[128] M. Fan, M. Clark, and Z.C. Feng. Implementation and stability study of phase-locked-loop nonlinear dynamic measurement systems. *J. Commun. Nonlinear Sci.*, 12(7):1302 – 1315, 2007.

[129] C. Wang, H.-H. Yu, M. Wu, and W. Fang. Implementation of phase-locked loop control for MEMS scanning mirror using DSP. *Sensors and Actuators A: Physical*, 133(1):243 – 249, 2007.

[130] M. Fan, M. Clark, and Z.C. Feng. Implementation and stability study of phase-locked-loop nonlinear dynamic measurement systems. *Commun. Nonlinear. Sci.*, 12(7):1302 – 1315, 2007.

[131] P. Dorato, C. Abdallah, and V. Cerone. *Linear Quadratic Control: An Introduction*. Florida, USA: Krieger Publishing Company, 2000.

[132] R. W. Longman. Iterative learning control and repetitive control for engineering practice. *Int. J. Control*, 73(10):930–954, 2000.

[133] J. H. Lee, K. S. Lee, and W. C. Kim. Model-based iterative learning control with a quadratic criterion for time-varying linear systems. *Automatica*, 36 (5):641–657, 2000.

[134] D. A. Bristow, M. Tharayil, and A. G. Alleyne. A survey of iterative learning control. *IEEE Control Systems Magazine*, 26(3):96–114, 2006.

[135] S. Hara, Y. Yamamoto, T. Omata, and M. Nakano. Repetitive control system: a new type servo system for periodic exogenous signals. *IEEE Transactions on Automatic Control*, 33(7):659–668, 1988.

[136] Youqing Wang, Furong Gao, and Francis J. Doyle. Survey on iterative learning control, repetitive control, and run-to-run control. *Journal of Process Control*, 19(10):1589–1600, 2009.

[137] Yik R. Teo, Yuen K. Yong, and Andrew J. Fleming. A review of scanning methods and control implications for scanning probe microscopy. In *American Control Conference (ACC)*, pages 7377–7383, 2016.

[138] Ying Wu, Qingze Zou, and Chanmin Su. A current cycle feedback iterative learning control approach for AFM imaging. *IEEE Transactions on Nanotechnology*, 8(4):515–527, 2009.

[139] Shengwen Xie and Juan Ren. High-speed AFM imaging via iterative learning-based model predictive control. *Mechatronics*, 57:86–94, 2019.

[140] Kyungjin Park, Jin Young Kim, Changho Lee, Seungwan Jeon, Geunbae Lim, and Chulhong Kim. Handheld photoacoustic microscopy probe. *Scientific Reports*, 7, 2017.

[141] Thomas Riel, Andreas Sinn, Christian Schwaer, Martin Ploner, and Georg Schitter. Iterative trajectory learning for highly accurate optical satellite tracking systems. *Acta Astronautica*, 164:121–129, 2019.

[142] Li-Wei Shih and Cheng-Wei Chen. Model-free repetitive control design and implementation for dynamical galvanometer-based raster scanning. *Control Engineering Practice*, 122:105124, 2022.

[143] Linlin Li, Wei-Wei Huang, Xiangyuan Wang, and LiMin Zhu. Dual-notch-based repetitive control for tracking lissajous scan trajectories with piezo-actuated nanoscanners. *IEEE Transactions on Instrumentation and Measurement*, 71:1–12, 2022.

[144] Zhao Feng, Min Ming, Jie Ling, Xiaohui Xiao, Zhi-Xin Yang, and Feng Wan. Fractional delay filter based repetitive control for precision tracking: Design and application to a piezoelectric nanopositioning stage. *Mechanical Systems and Signal Processing*, 164:108249, 2022.

[145] Linlin Li, Guoying Gu, and LiMin Zhu. Fractional repetitive control of nanopositioning stages for tracking high-frequency periodic inputs with non-synchronized sampling. *Review of Scientific Instruments*, 90:055108, 2019.

[146] Linlin Li, Guoying Gu, and Li-Min Zhu. Motion control of the piezoelectric tube scanner for Lissajous trajectories with modified repetitive control. In *International Conference on Manipulation, Automation and Robotics at Small Scales (MARSS)*, pages 1–6, 2018.

[147] Nastaran Nikooienejad, Mohammad Maroufi, and S. O. Reza Moheimani. Iterative learning control for video-rate atomic force microscopy. *IEEE/ASME Transactions on Mechatronics*, 26(4):2127–2138, 2021.

[148] Mohammad Maroufi and S. O. Reza Moheimani. A 2DOF SOI-MEMS nanopositioner with tilted flexure bulk piezoresistive displacement sensors. *IEEE Sensors Journal*, 16(7):1908–1917, 2016.

[149] V. Milanović, A. Kasturi, H. J. Kim, and F. Hu. Iterative learning control (ILC) algorithm for greatly increased bandwidth and linearity of MEMS mirrors in lidar and related imaging applications. In *MOEMS and Miniaturized Systems XVII*, volume 10545, page 1054513. SPIE, 2018.

[150] Richard Schroedter, Markus Schwarzenberg, Jan Grahmann, Thilo Sandner, and Klaus Janschek. Repetitive nonlinear control for linear scanning micro mirrors. In *MOEMS and Miniaturized Systems XVII*, volume 10545, pages 234 – 241. SPIE, 2018.

[151] T. Sandner, T. Grasshoff, M. Wildenhain, and M. Schwarzenberg. Hybrid assembled MEMS scanner array with large aperture for fast scanning LIDAR systems. *tm - Technisches Messen*, 86:151–163, 2019.

[152] T. Sandner, M. Wildenhain, C. Gerwig, H. Schenk, S. Schwarzer, and H. Wölfelschneider. Large aperture MEMS scanner module for 3D distance measurement. *Proc. SPIE*, 7594:119–129, 2010.

[153] L.-J. Yang, C.-W. Liu, and P. Chang. Phase synchronization of micromirror arrays using elastic linkages. *Sensors and Actuators A: Physical*, 95 (1):55 – 60, 2001.

[154] A. Tortschanoff, A. Frank, M. Wildenhain, T. Sandner, and A. Kenda. Optical position encoding and phase control of an electrostatically driven two-dimensional MOEMS scanner at two resonant modes. *J. Micro/Nanolith. MEMS MOEMS*, 10(3):1 – 10, 2011.

[155] A. Strasser, P. Stelzer, C. Steger, and N. Druml. Towards synchronous mode of multiple independently controlled MEMS mirrors. *IFAC-PapersOnLine*, 52(15):31 – 36, 2019.

[156] N. Ishikawa, K. Ikeda, and R. Sawada. Temperature dependence of the scanning performance of an electrostatic microscanner. *J. Micromech. Microeng.*, 26:035002, 2016.

[157] D. Brunner, H. W. Yoo, and G. Schitter. Linear modeling and control of comb-actuated resonant MEMS mirror with nonlinear dynamics. *IEEE Trans. Ind. Electron.*, 68(4):3315–3323, 2021.

[158] H. W. Yoo, R. Riegler, D. Brunner, S. G. Albert, T. Thurner, and G. Schitter. Experimental evaluation of vibration influence on a resonant MEMS scanning system for automotive lidars. *IEEE Trans. Ind. Electron.*, 69(3): 3099–3108, 2022.

[159] R. Schroedter, H. W. Yoo, D. Brunner, and G. Schitter. Charge-based capacitive self-sensing with continuous state observation for resonant electrostatic MEMS mirrors. *J. Microelectromech. Syst.*, 30(6):897–906, 2021.

[160] R. Farrugia, I. Grech, D. Camilleri, O. Casha, E. Gatt, and J. Micallef. Theoretical and finite element analysis of dynamic deformation in resonating micromirrors. *Microsyst. Technol.*, 24:1–11, 2017.

[161] H. W. Yoo, D. Brunner, T. Thurner, and G. Schitter. MEMS test bench and its uncertainty analysis for evaluation of MEMS mirrors. *IFAC-PapersOnLine*, 52(15):49–54, 2019.

[162] V. Kumar, Y. Yang, J. W. Boley, G. T. . Chiu, and J. F. Rhoads. Modeling, analysis, and experimental validation of a bifurcation-based microsensor. *J. Microelectromech. Syst.*, 21(3):549–558, 2012.

[163] H. Schenk, P. Durr, T. Haase, D. Kunze, U. Sobe, H. Lakner, and H. Kuck. Large deflection micromechanical scanning mirrors for linear scans and pattern generation. *IEEE J. Sel. Top. Quant.*, 6(5):715–722, 2000.

[164] A. K. Pandey, R. Pratap, and F. S. Chau. Effect of pressure on fluid damping in MEMS torsional resonators with flow ranging from continuum to molecular regime. *Experimental Mechanics*, 48(1):91–106, 2008.

[165] R. Farrugia, B. Portelli, I. Grech, D. Camilleri, O. Casha, J. Micallef, and E. Gatt. Air damping analysis in resonating micro-mirrors. *2018 Symposium on Design, Test, Integration Packaging of MEMS and MOEMS (DTIP)*, pages 1–5, 2018.

[166] J. Grahmann, R. Schroedter, O. Kiethe, and U. Todt. Vibration analysis of micro mirrors for lidar using on-chip piezo-resistive sensor. *Proc. SPIE*, 11293:34–45, 2020.

[167] LV 124: electric and electronic components in motor vehicles up to 3.5 t - general requirements, test conditions and tests (VW 80000). *Volkswagen AG*, Tech. Rep. 8MA00, 2013.

[168] C. J. Willmott. On the Validation of Models. *Physical Geography*, 2(2): 184–194, 1981.

[169] C. J. Willmott, S. G. Ackleson, R. E. Davis, J. J. Feddema, K. M. Klink, D. R. Legates, J. O'Donnell, and C. M. Rowe. Statistics for the evaluation and comparison of models. *J. Geophys. Res. Oceans*, 90(C5):8995–9005, 1985.

[170] D. R. Legates and G. J. McCabe. Evaluating the use of 'goodness-of-fit' Measures in hydrologic and hydroclimatic model validation. *Water Resources Research*, 35(1):233–241, 1999.

[171] H. Muroi and S. Adachi. Model validation criteria for system identification in time domain. *IFAC-PapersOnLine*, 48(28):86 – 91, 2015.

[172] D. Brunner, H. W. Yoo, and G. Schitter. Digital asynchronous phase locked loop for precision control of MOEMS scanning mirror. *IFAC-PapersOnLine*, 52(15):43 – 48, 2019.

[173] D. Brunner, H. W. Yoo, and G. Schitter. Precise phase control of resonant MOEMS mirrors by comb-drive current feedback. *Mechatronics*, 71:102420, 2020.

[174] D. Brunner, S. Albert, M. Hennecke, F. Darrer, and G. Schitter. Self-sensing control of resonant MEMS scanner by comb-drive current feedback. *Mechatronics*, 78:102631, 2021.

[175] I. Maksymova, P. Greiner, J. Wiesmeier, F. Darrer, and N. Druml. A MEMS mirror driver ASIC for beam-steering in scanning MEMS-based lidar. *Proc. SPIE*, 11107:64–71, 2019.

[176] A. Strasser, P. Stelzer, C. Steger, and N. Druml. Speed-up of MEMS mirror's transient start-up procedure. *IEEE Sensors Applications Symposium*, pages 1–5, 2019.

[177] S. Skogestad and I. Postlethwaite. *Multivariable Feedback Control: Analysis and Design*. John Wiley & Sons, Inc., Hoboken, NJ, USA, 2005.

[178] D. Brunner, H. W. Yoo, R. Schroedter, and G. Schitter. Adaptive Lissajous scanning pattern design by phase modulation. *Opt. Express*, 29(18):27989–28004, 2021.

[179] J. Rapp, J. Tachella, Y. Altmann, S. McLaughlin, and V. K. Goyal. Advances in single-photon lidar for autonomous vehicles: Working principles, challenges, and recent advances. *IEEE Signal Processing Magazine*, 37(4): 62–71, 2020.

[180] Z. Tasneem, C. Adhivarahan, D. Wang, H. Xie, K. Dantu, and S. J. Koppal. Adaptive fovea for scanning depth sensors. *Int. J. Robot. Res.*, 39(7):837–855, 2020.

[181] J. Wu, Y. Lin, Y. Lo, W. Liu, and L. Fu. Lissajous hierarchical local scanning to increase the speed of atomic force microscopy. *IEEE Trans. Nanotechnol.*, 14(5):810–819, 2015.

[182] T. J. Harte, J. Hätönen, and D. H. Owens *. Discrete-time inverse model-based iterative learning control: stability, monotonicity and robustness. *Int. J. Control*, 78(8):577–586, 2005.

[183] K. L. Barton and A. G. Alleyne. A norm optimal approach to time-varying ILC with application to a multi-axis robotic testbed. *IEEE Trans. Control Syst. Technol.*, 19(1):166–180, 2011.

Eidesstattliche Erklärung

Hiermit erkläre ich, dass die vorliegende Arbeit ohne unzulässige Hilfe Dritter und ohne Benutzung anderer als der angegebenen Hilfsmittel angefertigt wurde. Die aus anderen Quellen oder indirekt übernommenen Daten und Konzepte sind unter Angabe der Quelle gekennzeichnet.
Die Arbeit wurde bisher weder im In- noch im Ausland in gleicher oder in ähnlicher Form in anderen Prüfungsverfahren vorgelegt.

Wien, im August 2022

David Brunner

Author Information and Publication List

David Brunner is PhD student at the Automation and Control Institute (ACIN) of TU Wien. He received his M.Sc. degree in Energy Systems and Automation Technology from TU Wien, Austria, in 2017. His primary research interests include advanced identification and control concepts, high performance mechatronic systems and system integration.

Conferences

D. Brunner, H. W. Yoo, T. Thurner and G. Schitter. Data based modelling and identification of nonlinear SDOF MOEMS mirror. Proc. SPIE, 10931:269-278, 2019.

H. W. Yoo, D. Brunner, T. Thurner and G. Schitter. Compensation for temperature dependency of 1D position sensitive detector. Proc. SPIE, 10942:179-188, 2019.

D. Brunner, H. W. Yoo and G. Schitter. Digital asynchronous phase locked loop for precision control of MOEMS scanning mirror. IFAC, 52(15):43-48, 2019.

H. W. Yoo, D. Brunner, T. Thurner and G. Schitter. MEMS test bench and its uncertainty analysis for evaluation of MEMS mirrors. IFAC, 52(15):49-54, 2019.

R. Schroedter, H. W. Yoo, D. Brunner and G. Schitter. Capacitive charge-based self-sensing for resonant electrostatic MEMS mirrors. IFAC, 53(2):8553-8558, 2020.

Journals

H. W. Yoo, N. Druml, D. Brunner, C. Schwarzl, T. Thurner, M. Hennecke and G. Schitter. MEMS-based lidar for autonomous driving. e & i Elektrotechnik und

Informationstechnik, 135(6):408-415, 2018.

D. Brunner, H. W. Yoo and G. Schitter. Precise phase control of resonant MOEMS mirrors by comb-drive current feedback. Mechatronics, 71:102420, 2020.

D. Brunner, H. W. Yoo and G. Schitter. Linear modeling and control of comb-actuated resonant MEMS mirror with nonlinear dynamics. IEEE Trans. Ind. Electron., 68(4):3315-3323, 2021.

H. W. Yoo, R. Riegler, D. Brunner, S. G. Albert, T. Thurner and G. Schitter. Experimental evaluation of vibration influence on a resonant MEMS scanning system for automotive lidars. IEEE Trans. Ind. Electron., 69(3):3099-3108, 2022.

D. Brunner, S. Albert, M. Hennecke, F. Darrer and G. Schitter. Self-sensing control of resonant MEMS scanner by comb-drive current feedback. Mechatronics, 78:102631, 2021.

D. Brunner, H. W. Yoo, R. Schroedter and G. Schitter. Adaptive Lissajous scanning pattern design by phase modulation. Opt. Express, 29(18):27989-28004, 2021.

R. Schroedter, H. W. Yoo, D. Brunner and G. Schitter. Charge-based capacitive self-sensing with continuous state observation for resonant electrostatic MEMS mirrors. J. Microelectromech. Syst., 30(6):897-906, 2021.

Patents

T. Thurner, D. Brunner, M. E. Hennecke, G. Schitter, and H. W. Yoo, Lidar sensors and methods for lidar sensors, U.S. Patent, iss. US 2020/0150246 A1, 2020.

T. Thurner, D. Brunner, M. E. Hennecke, G. Schitter and H. W. Yoo, LiDAR-sensoren und verfahren für lidar-sensoren, Deutsches Patent- und Markenamt, iss. DE 10 2018 128 164 A1, 2020.

D. Brunner, H. W. Yoo, R. Schroedter, G. Schitter, Flexible Lissajous scanning pattern by phase modulation, Patent US 16/861,647 filed on 2020.04.29

R. Schroedter, D. Brunner, H. W. Yoo, G. Schitter, F. Darrer and M. E. Hennecke, Capacitive charge based self-sensing and position observer for electrostatic MEMS mirrors, Patent US 16/804,424 filed on 2020.02.28

D. Brunner, G. Schitter, F. Darrer, Control structure for oscillators with nonlinear frequency response, Patent US 16/749,270 filed on 2020.01.22

D. Brunner, H. W. Yoo, G. Schitter and F. Darrer, Laser scanning control system and method, Patent Germany 102019208386.2 filed on 2019.06.07

D. Brunner, H. W. Yoo and G. Schitter, Controlling an oscillating system, Patent Germany 102019210305.7 filed on 2019.07.11